



TECHNISCHE
UNIVERSITÄT
DARMSTADT

Nuclear Spectra and Strength Distributions from Importance-Truncated Configuration-Interaction Methods

Vom Fachbereich Physik
der Technischen Universität Darmstadt

zur Erlangung des Grades
Doctor rerum naturalium (Dr. rer. nat.)

genehmigte Dissertation von
Christina Stumpf

Referent: Prof. Dr. Robert Roth
Korreferent: Prof. Dr. Gabriel Martínez-Pinedo

Darmstadt 2018

Stumpf, Christina: Nuclear Spectra and Strength Distributions from Importance-Truncated Configuration-Interaction Methods

Darmstadt, Technische Universität Darmstadt

Jahr der Veröffentlichung der Dissertation auf TUprints: 2018

URN: urn:nbn:de:tuda-tuprints-75710

Tag der mündlichen Prüfung: 18. Juni 2018

Text



Figures



The text of this work is licensed under a Creative Commons BY-NC-ND 4.0 license.

All figures are licensed under a Creative Commons BY 4.0 license.

Visit <https://creativecommons.org/licenses/> for more information.

Abstract

In this work, we extend two successful nuclear-structure methods, the valence-space and the no-core shell model, to new domains of applications.

We address key developments for a realistic implementation of the valence-space shell model to enhance its predictive power and allow for a description of arbitrary nuclei, ranging from the valley of stability to the neutron-deficient or neutron-rich extremes of the Segrè chart. One essential step is the capability to deal with valence spaces that comprise more than a single major shell. We propose an importance-truncation scheme for the valence-space shell model based on a physics-driven and adaptive truncation that, in combination with refined extrapolation techniques, provides an efficient and accurate tool for the description of nuclei in large-scale model spaces. Additionally, we explore effective valence-space Hamiltonians derived from chiral interactions in the in-medium similarity renormalization group. These interactions are rooted in quantum chromodynamics and provide an excellent framework to describe nuclear properties from first principles. Using these interactions, we demonstrate the reliability of the approach in single-shell valence spaces; however, difficulties persist with the construction of effective Hamiltonians for multi-shell valence spaces. While an *ab initio* description of nuclei in the framework of the importance-truncated valence-space shell model is not yet feasible, we study ground and first excited states of neutron-deficient tin isotopes in the *gds* valence space based on effective Hamiltonians that are constrained by few-body data only. Our results highlight the need for a more rigorous and systematic approach for the construction of nuclear interactions.

Moreover, we present an *ab initio* approach for the description of collective excitations and transition-strength distributions by combining the importance-truncated no-core shell model with the Lanczos strength-function method. Due to its computational efficiency, this method can be applied to all nuclei that are feasible in the no-core shell model. It provides access to the full energy range from low-lying excitations to the giant-resonance region and beyond in a unified and consistent framework, including a complete description of fragmentation and fine structure. The method relies solely on the basis truncation, and we demonstrate convergence of the strength distributions with the truncation parameter. Starting from chiral effective-field-theory interactions, we explore the electric monopole, dipole, and quadrupole response of oxygen, carbon, and helium isotopes. We focus on the emergence and evolution of pygmy and giant resonances, as well as the systematics of dipole polarizabilities throughout the isotopic chains. Furthermore, we study transition densities of prominent transitions in the distributions, which provide valuable insights in their nature. The results underline the importance of collective modes for constraining nuclear interactions. In addition, we elaborate on the relation with approximate methods, such as the random-phase approximation, and shed new light on their deficiencies.

Zusammenfassung

In dieser Arbeit erweitern wir zwei erfolgreiche Kernstrukturmethoden, das Valenzraum-Schalenmodell und das No-Core Schalenmodell, um neue Anwendungsfelder.

Wir nehmen wesentliche Entwicklungen für eine realistische Implementierung des Valenzraum-Schalenmodells in Angriff, um dessen Vorhersagekraft zu verbessern und eine Beschreibung beliebiger Kerne, vom Tal der Stabilität bis zu den neutronenarmen und neutronenreichen Extremen der Segrè-Nuklidkarte, zu ermöglichen. Ein unverzichtbarer Schritt dabei ist die Erweiterung von Valenzräumen auf mehr als nur eine Hauptschale. Wir führen die Importance-Trunkierung für das Valenzraum-Schalenmodell ein, die auf einer physikalisch motivierten und adaptiven Trunkierung basiert. In Verbindung mit geeigneten Extrapolationsmethoden stellt sie ein effizientes und genaues Werkzeug zur Beschreibung von Kernen in sehr großen Modellräumen dar. Des Weiteren untersuchen wir effektive Valenzraum-Hamiltonians, die mittels der In-Medium Similarity Renormalization Group von chiralen Wechselwirkungen abgeleitet sind. Diese Wechselwirkungen bieten einen ausgezeichneten Rahmen, um Kerneigenschaften ausgehend von den Grundprinzipien der Quantenchromodynamik zu beschreiben. Wir nutzen diese effektiven Hamiltonians, um die Zuverlässigkeit des Importance-trunkierten Valenzraum-Schalenmodells für Valenzräume zu zeigen, die eine Hauptschale umfassen. Die Konstruktion entsprechender effektiver Hamiltonians für erweiterte Valenzräume ist derzeit allerdings noch problembehaftet. Solange eine *ab initio* Beschreibung von Kernen im Importance-trunkierten Valenzraum-Schalenmodell noch nicht möglich ist, untersuchen wir Grund- und Anregungszustände von neutronenarmen Zinn-Isotopen in der *gds* Schale ausgehend von effektiven Valenzraum-Wechselwirkungen, die nur von Daten aus Systemen mit wenig Teilchen abhängen. Unsere Ergebnisse hierzu stellen die Notwendigkeit eines strengeren und systematischeren Ansatzes zur Konstruktion von Kernwechselwirkungen heraus.

Außerdem präsentieren wir eine *ab initio* Methode zur Beschreibung von kollektiven Anregungen und Übergangsstärkeverteilungen, die aus der Kombination des Importance-trunkierten No-Core Schalenmodells mit der Lanczos-Stärkefunktionen-Methode hervorgeht. Aufgrund ihrer Recheneffizienz kann diese Methode auf alle Kerne angewendet werden, die auch im No-Core Schalenmodell realisierbar sind. Sie bietet einen vereinheitlichten und konsistenten Zugang zu Stärkeverteilungen im gesamten Energiebereich von niedrig liegenden Anregungen bis über die Riesenresonanzregion hinaus inklusive einer vollwertigen Beschreibung von Fragmentierung und Feinstruktur. Die Methode hängt ausschließlich von der Basistrunkierung ab und wir zeigen Konvergenz der Stärkeverteilungen mit dem Trunkierungsparameter. Ausgehend von Wechselwirkungen aus der chiralen effektiven Feldtheorie untersuchen wir Responsefunktionen von elektrischen Monopol-, Dipol- und Quadrupolübergängen für Sauerstoff-, Kohlenstoff- und Heliumisotope. Dabei legen wir den Schwerpunkt auf die Entstehung und Evolution von Pygmy-

und Riesenresonanzen, sowie auf die Systematik der Dipolpolarisierbarkeit durch die Isotopenketten hinweg. Zusätzlich untersuchen wir Übergangsdichten von besonders ausgeprägten Übergängen in den Stärkeverteilungen, da diese wertvolle Rückschlüsse auf deren Natur erlauben. Die Ergebnisse stellen heraus, wie wichtig kollektive Moden zur Bestimmung von Kernwechselwirkungen sind. Des Weiteren stellen wir eine Verbindung mit Näherungsmethoden, wie zum Beispiel der Random-Phase Approximation, her und geben neue Aufschlüsse über deren Defizite.

Contents

1. Introduction	1
2. Input Hamiltonians	5
2.1. Chiral Hamiltonians	5
2.2. Similarity Renormalization Group	7
2.3. Normal-Ordered Two-Body Approximation	8
3. Electromagnetic Moments and Transitions	11
3.1. Hamiltonian of a Nucleus in an Electromagnetic Field	11
3.2. Static Multipole Moments	13
3.3. Multipole Transitions	15
3.4. Single-Particle Matrix Elements of the Reduced Electromagnetic Multipole Operators	17
3.5. Isospin Decomposition	18
3.6. Translational Invariance	20
4. Configuration-Interaction Methods	23
4.1. General Concept	23
4.2. Valence-Space Shell Model	26
4.3. No-Core Shell Model	29
4.4. Computational Limitation	33
5. Importance-Truncated Configuration-Interaction Methods	35
5.1. Importance Truncation	35
5.2. Threshold Dependence and Threshold Extrapolation	38
5.3. Energy-Variance Extrapolation	42
6. Lanczos Strength Functions from the IT-NCSM	47
6.1. The Simple Lanczos Algorithm	47
6.2. Lanczos Strength-Function Method	52
6.3. Model-Space Convergence of Strength Distributions	57
7. Applications of the IT-VSSM	69
7.1. Effective Valence-Space Hamiltonians	69
7.2. IT-VSSM Benchmark with Phenomenological Interactions	71
7.3. Benchmark of Valence-Space Interactions from the IM-SRG	76
7.4. Structure of Neutron-Deficient Tin Isotopes	82

8. Applications of IT-NCSM Strength Functions	91
8.1. Validation of Strength Functions from RPA-Type Methods	91
8.2. Electric Strength Functions of Selected Isotopes	94
8.2.1. Oxygen Isotopes	95
8.2.2. Carbon Isotopes	101
8.2.3. Helium Isotopes	111
9. Conclusions	119
A. Derivation of Electromagnetic Quantities	123
A.1. Relevant Definitions and Notations	123
A.2. Vector Potential and Hamiltonian of the Electromagnetic Field	125
A.3. Static Multipole Operators	128
A.4. Electromagnetic Multipole Transition Operators	130
A.5. Single-Particle Matrix Elements of the Reduced Electric Multipole Operator	132
A.6. Translational Invariance of Electric Multipole Operators	135
B. Hartree-Fock Method	141
C. Multiconfigurational Perturbation Theory	145
D. Transition Density	149
Bibliography	151

List of Figures

4.1.	Schematic representation of single-particle orbits and magic numbers in a shell-model potential.	27
4.2.	Single-particle orbits of the HO potential.	31
4.3.	Schematic representation of single-particle orbits of an HF potential. . . .	32
4.4.	Model-space dimensions of even-mass silicon isotopes in the VSSM (<i>sdpf</i> shell) as a function of T_{\max} and of even-mass oxygen isotopes in the NCSM as a function of N_{\max}	34
5.1.	Energy of the ground and first excited state of ^{12}C in the IT-NCSM and of ^{56}Ni in the IT-VSSM as a function of the importance threshold for three reference thresholds.	40
5.2.	Threshold dependence and extrapolation of the quadrupole moment of the 2_1^+ state and the $B(E2 : 2_1^+ \rightarrow 0_1^+)$ transition strength of ^{12}C in the IT-NCSM and of ^{56}Ni in the IT-VSSM for three reference thresholds.	41
5.3.	Energy-variance extrapolation of the ground-state energy relative to the core for ^{56}Ni obtained in the IT-VSSM using the GXPF1A Hamiltonian. . .	45
5.4.	Energy-variance extrapolation of the quadrupole moment and the $B(E2 : 2_1^+ \rightarrow 0_1^+)$ transition strength of ^{56}Ni	46
6.1.	Convergence behavior of the lowest 15 energy eigenvalues in the Lanczos algorithm with full reorthogonalization and without reorthogonalization.	51
6.2.	Convergence of discrete isoscalar E2 strength distributions with the number of Lanczos vectors.	54
6.3.	Convergence of smoothed-out isoscalar E2 strength distributions with the number of Lanczos vectors.	55
6.4.	Discrete and smoothed-out isoscalar E2 strength distributions with full reorthogonalization and without reorthogonalization of the Lanczos basis.	56
6.5.	Dependence of isoscalar E0, isovector E1, and isoscalar E2 strength functions of ^{16}O and ^{24}O on the importance threshold κ_{\min}	58
6.6.	Dependence of isoscalar E0, isovector E1, and isoscalar E2 strength functions of ^{16}O and ^{24}O on the model-space truncation N_{\max} , using $\beta = 0$. . .	59
6.7.	Dependence of isoscalar E0, isovector E1, and isoscalar E2 strength functions of ^{16}O and ^{24}O on the model-space truncation N_{\max} , using $\beta = 0.5$. . .	59
6.8.	Dependence of isoscalar E0, isovector E1, and isoscalar E2 strength functions of ^{16}O and ^{24}O on the frequency $\hbar\Omega$	60
6.9.	Dependence of isoscalar E0, isovector E1, and isoscalar E2 strength functions of ^{16}O and ^{24}O on the single-particle basis truncation e_{\max}	61

6.10. Dependence of isoscalar E0, isovector E1, and isoscalar E2 strength functions of ^{16}O and ^{24}O obtained in the IT-NCSM using the SRG-evolved EMN400 interaction on the flow parameter α	62
6.11. Dependence of isoscalar E0, isovector E1, and isoscalar E2 strength functions of ^{16}O and ^{24}O obtained in the IT-NCSM using the SRG-evolved $\text{N}^2\text{LO}_{\text{sat}}$ interaction on the flow parameter α	62
6.12. Dependence of isoscalar E0, isovector E1, and isoscalar E2 strength functions of ^{16}O obtained in the IT-NCSM with HF basis on N_{max} and $\hbar\Omega$	64
6.13. Dependence of isoscalar E0, isovector E1, and isoscalar E2 strength functions of ^{16}O obtained in the IT-NCSM with HO basis on N_{max} and $\hbar\Omega$	64
6.14. Dependence of isoscalar E0, isovector E1, and isoscalar E2 strength functions of ^{16}O obtained in the IT-NCSM with natural-orbital basis on N_{max} and $\hbar\Omega$	65
6.15. N_{max} convergence of absolute and excitation energies of the 0^+ ground state and the first excited 1^- and 2^+ states in ^{16}O obtained in the IT-NCSM with HF basis.	66
6.16. N_{max} convergence of absolute and excitation energies of the 0^+ ground state and the first excited 1^- and 2^+ states in ^{16}O obtained in the IT-NCSM with HO basis.	67
7.1. Threshold and energy-variance extrapolation of the energies of the six lowest natural-parity states of ^{56}Ni for three reference thresholds.	72
7.2. Natural-parity spectrum of ^{56}Ni as a function of T_{max} in terms of absolute energies computed with the pf -shell valence-space Hamiltonian GXPf1A.	73
7.3. Threshold and energy-variance extrapolation of the energies of the lowest natural-parity states of ^{60}Zn and ^{64}Ge	74
7.4. Energies of the lowest natural-parity states of ^{60}Zn and ^{64}Ge obtained with the PFG9B3 valence-space Hamiltonian as a function of T_{max}	75
7.5. Energy of the ^{16}O core of an sd -shell valence-space Hamiltonian for $A = 18$ nuclei obtained in the IM-SRG as a function of the flow parameter.	77
7.6. Absolute and excitation energies of the lowest six natural-parity states of ^{18}O obtained in the VSSM and IT-NCSM using the same IM-SRG-evolved Hamiltonian as a function of the flow parameter.	78
7.7. Schematic matrix representation of the core, sd -shell valence, and excluded space in comparison to e_{max} -truncated model spaces.	79
7.8. Energy of the ^{16}O core of an $sdpf$ -shell valence-space Hamiltonian for $A = 18$ nuclei obtained in the IM-SRG as a function of the flow parameter.	80
7.9. Energies of the lowest two 0^+ and the lowest 6^+ states in ^{18}O obtained in the VSSM using an effective interaction from the IM-SRG with the imaginary-time generator for the $sdpf$ shell as a function of the flow parameter.	80
7.10. Energies of the ground and first excited states of $^{100-104}\text{Sn}$ as a function of T_{max} obtained with effective gds valence-space Hamiltonians derived from the 1.8/2.0(EM) and 2.0/2.0(EM) interactions.	83

7.11. Energies of the ground and first excited states of $^{105-109}\text{Sn}$ as a function of T_{max} obtained with effective gds valence-space Hamiltonians derived from the 1.8/2.0(EM) and 2.0/2.0(EM) interactions.	84
7.12. Energies of the ground and first excited states of $^{110-114}\text{Sn}$ as a function of T_{max} obtained with effective gds valence-space Hamiltonians derived from the 1.8/2.0(EM) and 2.0/2.0(EM) interactions.	85
7.13. Ground-state energies of $^{100-114}\text{Sn}$ obtained with effective gds valence-space Hamiltonians derived from the 1.8/2.0(EM) and 2.0/2.0(EM) interactions.	86
7.14. Excitation energies of the first 2^+ state of even- A tin isotopes obtained with effective gds -shell valence-space Hamiltonians derived from the 1.8/2.0(EM) and 2.0/2.0(EM) interactions.	87
7.15. Energy splitting between the lowest $7/2^+$ and $5/2^+$ states in light odd- A tin isotopes obtained with effective gds valence-space Hamiltonians derived from the 1.8/2.0(EM) and 2.0/2.0(EM) interactions.	88
8.1. Convergence behavior of isoscalar E0, isovector E1, and isoscalar E2 strength functions of ^{16}O obtained in the IT-NCSM with N_{max} truncation, IT-NCSM with T_{max} truncation, and the TDA, RPA, and SRPA.	92
8.2. Discrete isoscalar E0, isovector E1, and isoscalar E2 strength distributions for ^{16}O obtained in the IT-NCSM for $N_{\text{max}} = 8/9$, RPA, and SRPA.	94
8.3. Model-space convergence of the isoscalar E0, isovector E1, and isoscalar E2 strength functions of the even- A oxygen isotopes $^{16-24}\text{O}$ using the EMN400 interaction.	95
8.4. Model-space convergence of the isoscalar E0, isovector E1, and isoscalar E2 strength functions of the even- A oxygen isotopes $^{16-24}\text{O}$ using the $\text{N}^2\text{LO}_{\text{sat}}$ interaction.	96
8.5. Isoscalar E0, isovector E1, and isoscalar E2 strength functions of the even- A oxygen isotopes $^{16-24}\text{O}$ using the EM and EMN400 interactions.	97
8.6. Isoscalar E0, isovector E1, and isoscalar E2 strength functions of the even- A oxygen isotopes $^{16-24}\text{O}$ using the EMN400 and $\text{N}^2\text{LO}_{\text{sat}}$ interactions.	98
8.7. Discrete isoscalar E0, isovector E1, and isoscalar E2 strength functions of the even- A oxygen isotopes $^{16-24}\text{O}$ using the EMN400 and $\text{N}^2\text{LO}_{\text{sat}}$ interactions.	99
8.8. Comparison of the total E1 and E2 responses of $^{16-24}\text{O}$ with their isovector and isoscalar analog.	100
8.9. Model-space convergence of the isoscalar E0, isovector E1, and isoscalar E2 strength functions of the even- A carbon isotopes $^{10-18}\text{C}$ using the EMN400 interaction.	102
8.10. Model-space convergence of the isoscalar E0, isovector E1, and isoscalar E2 strength functions of the even- A carbon isotopes $^{10-18}\text{C}$ using the $\text{N}^2\text{LO}_{\text{sat}}$ interaction.	103
8.11. Isoscalar E0, isovector E1, and isoscalar E2 strength functions of the even- A carbon isotopes $^{10-18}\text{C}$ using the EMN400 and $\text{N}^2\text{LO}_{\text{sat}}$ interactions.	104
8.12. Comparison of the total E1 and E2 responses of $^{10-18}\text{C}$ with their isovector and isoscalar analog.	105

8.13. Discrete and folded isovector E1 strength functions of ^{10}C and ^{14}C	106
8.14. Radial proton and neutron transition densities from the 0^+ ground state of ^{10}C to 1^- states with dominant contributions to the isovector E1 response.	107
8.15. Radial proton and neutron transition densities from the 0^+ ground state of ^{14}C to 1^- states with dominant contributions to the isovector E1 response.	107
8.16. Discrete and folded isoscalar E2 strength functions of $^{10,14,16}\text{C}$	108
8.17. Radial proton and neutron transition densities from the 0^+ ground state of ^{10}C to 2^+ states with dominant contributions to the isoscalar E2 response.	109
8.18. Radial proton and neutron transition densities from the 0^+ ground state of ^{14}C to 2^+ states with dominant contributions to the isoscalar E2 response.	109
8.19. Radial proton and neutron transition densities from the 0^+ ground state of ^{16}C to 2^+ states with dominant contributions to the isoscalar E2 response.	110
8.20. Model-space convergence of the isoscalar E0, isovector E1, and isoscalar E2 strength functions of the helium isotopes $^{4,6,8}\text{He}$ using the EMN400 interaction.	111
8.21. Model-space convergence of the isoscalar E0, isovector E1, and isoscalar E2 strength functions of the helium isotopes $^{4,6,8}\text{He}$ using the $\text{N}^2\text{LO}_{\text{sat}}$ interaction.	112
8.22. Model-space convergence of the isoscalar E0, isovector E1, and isoscalar E2 strength functions of the helium isotopes $^{4,6,8}\text{He}$ using the EMN500 interaction.	112
8.23. Isoscalar E0, isovector E1, and isoscalar E2 strength functions of $^{4,6,8}\text{He}$ using the EMN400, $\text{N}^2\text{LO}_{\text{sat}}$, and EMN500 interactions.	113
8.24. Discrete isoscalar E0, isovector E1, and isoscalar E2 strength functions of $^{4,6,8}\text{He}$ using the EMN500 interaction.	113
8.25. Discrete and folded isovector E1 strength functions of $^{4,6,8}\text{He}$	115
8.26. Radial proton and neutron transition densities from the 0^+ ground state of ^4He to 1^- states with dominant contributions to the isovector E1 response.	116
8.27. Radial proton and neutron transition densities from the 0^+ ground state of ^6He to 1^- states with dominant contributions to the isovector E1 response.	116
8.28. Radial proton and neutron transition densities from the 0^+ ground state of ^8He to 1^- states with dominant contributions to the isovector E1 response.	117

List of Tables

8.1. Electric dipole polarizability for the even- A oxygen isotopes $^{16-24}\text{O}$ obtained for the EMN400 and $\text{N}^2\text{LO}_{\text{sat}}$ interactions.	100
8.2. Electric dipole polarizability for the even- A carbon isotopes $^{10-18}\text{C}$ obtained for the EMN400 and $\text{N}^2\text{LO}_{\text{sat}}$ interactions.	104
8.3. Electric dipole polarizability for $^{4,6,8}\text{He}$ obtained for the EMN400, $\text{N}^2\text{LO}_{\text{sat}}$, and EMN500 interactions.	114

Acronyms and Abbreviations

3N	three-nucleon
CC	coupled cluster
CCSD	coupled cluster with singles and doubles
CCSD(T)	CCSD with non-iterative triples corrections
CI	configuration interaction
EFT	effective field theory
EOM	equation-of-motion method
EOM-CCSD	EOM on top of a CCSD solution
EOM-CCSD(T)	EOM with triples corrections on top of a CCSD solution
HF	Hartree-Fock
HO	harmonic oscillator
IM-SRG	in-medium similarity renormalization group
IT-NCSM	importance-truncated no-core shell model
IT-VSSM	importance-truncated valence-space shell model
LIT	Lorentz-integral transform
LO	leading order
MCPT	multi-configurational perturbation theory
MCSM	Monte-Carlo shell model
NCSM	no-core shell model
NCSMC	no-core shell model with continuum
NLO	next-to-leading order
N ² LO	next-to-next-to-leading order
NN	nucleon-nucleon
NO2B	normal-ordered two-body
<i>npnh</i>	<i>n</i> -particle <i>n</i> -hole
QCD	quantum chromodynamics
RPA	random-phase approximation
SRG	similarity renormalization group
SRPA	second-order random-phase approximation
TDA	Tamm-Dancoff approximation
VSSM	valence-space shell model

1. Introduction

The fascination of nuclear physics results from its broadness, ranging from the most microscopic to cosmic scales, its impact on other fields, and the fast advances made since Chadwick's discovery of the neutron in 1932 [Cha32]. Before his seminal experiment, we only had a very basic understanding of atoms and were still ignorant regarding the complexity of their nuclei. Knowing about the existence of the neutron, it became evident that atomic nuclei—which are resolved by zooming in the atoms by a factor of 100 000—have a substructure of A nucleons interacting strongly with each other. Today, a wealth of theories and models are available that try to approximate the interactions inside nuclei so that experimental observations, e.g., binding and excitation energies, can be reproduced accurately. Only then can these models be used to provide quantitative predictions where no data is available and offer vital guidance for the design of future experiments. Several approaches exist to devise such models. Traditionally, phenomenological models provided the best description of nuclear observables. However, they typically involve adjustments to data, which is mainly available near the valley of stability. Since drastic changes in the nuclear structure happen when moving toward more exotic nuclei, e.g., for neutron-deficient or neutron-rich nuclei, extrapolations of phenomenological theories toward these regions often fail. Today, the goal of modern nuclear-structure theory is more ambitious. Since we have also learned that nucleons are not the fundamental building blocks of nuclei, but have a substructure of quarks and gluons, we wish to describe nuclei starting from these degrees of freedom. First attempts have been made for light nuclei [Bea+13; Bea+14], but are still in an early stage and suffer from large systematic errors. Therefore, we choose an intermediate approach and aim at the description of properties of stable and exotic nuclei using theories that are based on nucleons as degrees of freedom, but are rooted as much as possible in the fundamentals of quantum chromodynamics (QCD). Ideally, these theories rely on controllable approximations only, i.e., they can be improved systematically. Such theories are called *ab initio* theories.

Because of their relevance for this thesis, we outline the historical development of the nuclear valence-space shell model (VSSM) and no-core shell model (NCSM). Both theories have emerged from the naive shell model, also known as independent particle model, where the nucleus is, in a first approximation, described in terms of A independent particles moving in a central field. This central field accounts for the average action of all particles on one given particle, while the mutual interaction between the particles has to be considered explicitly via a residual interaction. The name “naive shell model” or “independent particle model” results from the fact that independent fermions in a central field exhibit some shell structure. At first glance, it is not evident that this simplified model can be applied to the atomic nucleus, a self-bound system consisting of A interacting nucleons without external potential. However, its validity has been confirmed experimentally. The observation of high-lying first excited states for some

nuclei in comparison with neighboring nuclei indicates relatively large energy gaps between the single-particle orbits for particular proton and neutron numbers, the magic numbers. In the 1950's, it became clear that the central potential must be modified to include a term accounting for spin-orbit splitting to reproduce higher magic numbers [May49; HJS49].

These observations and ideas form the basis of the more elaborate VSSM and NCSM. The VSSM assumes a closed-shell nucleus as inert core. All single-particle orbits of the core are fully occupied in a frozen configuration. The only degrees of freedom are the valence nucleons, the nucleons outside the core, restricted to one or several (sub-)shells. Once a suitable valence space is defined, the VSSM requires an effective interaction that accounts for interactions between core and valence nucleons and for effects of single-particle orbits above the valence space, which are excluded from the calculation. Traditionally, these interactions are constructed using renormalized nucleon-nucleon (NN) interactions combined with phenomenological fits of matrix elements to a subset of data. The eigenstates of a nucleus are obtained by solving the eigenvalue problem of the Hamilton matrix numerically. We note that the VSSM—though based on tight global truncations—has produced nuclear properties in remarkable agreement with experiment.

In 2000, advances in computer technology made new approaches such as the NCSM possible. The NCSM is conceptually simpler than the VSSM, as it does not require the artificial partitioning of the model space in core, valence, and excluded part, but considers all A nucleons as active degrees of freedom. This, however, restricts its applicability basically to s - and p -shell nuclei. The NCSM also allows to establish a connection to the underlying physics of quarks and gluons by using interactions derived in chiral effective field theory (EFT).

One major advantage of the VSSM and NCSM is that these methods provide the eigenstates, and thus, in principle, allow for the description of any observable of interest. In the VSSM, however, the phenomenological Hamiltonians are typically adjusted to nuclear spectra, and it is not clear *a priori* how other observables can be described in a consistent way. As a remedy for electromagnetic observables, e.g., effective charges are often introduced. In the NCSM with Hamiltonians from chiral EFT, it is possible to derive consistent operators and describe any observable on equal footing with the energies. Since different observables are sensitive to different aspects of the nuclear interaction, the study of various observables simultaneously provides valuable feedback on the quality of nuclear Hamiltonians.

Both, the VSSM and NCSM, are limited by model-space dimensions that increase combinatorially with the number of single-particle orbits and nucleons. The calculations are, thus, either restricted to systems with few particles in the active space or need to be carried out in severely truncated model spaces, which do not allow for reliable extrapolations. In order to extend the NCSM to larger model spaces and heavier nuclei, an importance-truncation scheme has been proposed and successfully implemented [RN07; Rot09]. The importance truncation is a conceptually simple approach based on a physics-driven, adaptive truncation of the many-body model space that allows to construct a reduced model space tailored specifically to the target eigenstates and Hamiltonian under consideration. Variations of this truncation further allow for an *a posteriori* extrapolation of the observables, which corrects for effects of the neglected basis states.

This thesis covers two major projects, with the goal to extend both, the VSSM as well as the NCSM, to new fields of applications. Within the first project, the importance-truncation scheme is applied to the VSSM, thus introducing the importance-truncated VSSM (IT-VSSM). In addition to the already established importance-threshold extrapolation, we explore extrapolations based on the energy variance. We demonstrate the efficiency and accuracy of the method by comparing to results in the full model space. With these developments, we aim at the description of new phenomena, as, e.g., intruder physics is captured in multi-shell valence spaces, and the domain of very neutron-deficient or neutron-rich nuclei becomes accessible. Recently, promising advances have been made in the derivation of effective valence-space Hamiltonians and operators in an *ab initio* framework [TBS12; Bog+14; Jan+14; Dik+15]. Within these approaches, we concentrate on the in-medium similarity renormalization group (IM-SRG) [TBS11; TBS12; Her+16; Her17] and benchmark effective valence-space Hamiltonians that are derived from chiral interactions for single- and multi-shell valence spaces. These developments represent important cornerstones toward an *ab initio* description of any medium-mass open-shell nucleus, starting from realistic interactions that are constrained by few-body data only.

The second project aims at the *ab initio* description of collective excitations and strength distributions in the framework of the importance-truncated no-core shell model (IT-NCSM). The study of collective modes, including the giant electric monopole, dipole, and quadrupole resonances, as well as the electromagnetic and weak response in general, has an extensive history in nuclear-structure physics [Spe91; HW01; Row10]. Many new aspects, e.g., the so-called pygmy dipole resonance, the fragmentation and fine structure of giant resonances, and the response of neutron-rich nuclei, are at the heart of ongoing experimental and theoretical investigations. These collective excitations serve as a magnifying glass for the internal dynamics of the nucleus and provide additional and complementary information on the effects of nuclear interactions. However, the theoretical description of collective excitations is still dominated by phenomenological models. First steps to describe collective excitations in an *ab initio* framework beyond the lightest nuclei have been made using the Lorentz-integral transform (LIT) method combined with the coupled-cluster (CC) method [Bac+13; Bac+14; Hag+16; Mio+16; Bir+17]. The LIT maps the continuum problem onto a bound-state problem, and, in this way, avoids the challenging calculations of final states in the continuum. However, the derivation of response functions requires a delicate inversion procedure, which only yields the gross structure of giant resonances above the particle threshold. We present an *ab initio* approach for the description of collective excitations and transition-strength distributions of arbitrary nuclei up into the *sd*-shell by combining the IT-NCSM with the Lanczos strength-function method. Our method describes electromagnetic strength distributions in the full energy range from low-lying excitations to the giant-resonance region and beyond in a unified and consistent framework, including a complete description of fragmentation and fine structure.

This thesis is organized as follows: Chapters 2 and 3 introduce the chiral Hamiltonians and electromagnetic quantities that are considered in the benchmarks and applications of the IT-VSSM and IT-NCSM. The concept of configuration-interaction (CI) methods and their relevant variants, the VSSM and NCSM, as well as their extension via the importance truncation and the different extrapolation techniques are presented in chapters 4 and 5.

Chapter 6 introduces the Lanczos strength-function method in the IT-NCSM and demonstrates its efficiency and accuracy in an extensive study of the model-space convergence behavior of the strength distributions. Finally, we show applications within the two projects covered in this thesis: Chapter 7 is dedicated to the first project. We validate the IT-VSSM by comparing results for nuclei in the pf and $pf g_{\frac{1}{2}}$ valence spaces using phenomenological interactions to available calculations in the full model spaces. In a second step, we address the performance of effective Hamiltonians derived in the IM-SRG for valence spaces comprising one major shell and two major shells. Finally, we apply this new method to the description of neutron-deficient tin isotopes, which have obtained recent attention in experimental and theoretical investigations. Applications in the framework of the second project are summarized in chapter 8. Here, we investigate the electric monopole, dipole, and quadrupole response of oxygen, carbon, and helium isotopes in the IT-NCSM and focus on their systematics throughout the isotopic chains. Additionally, we study the nature of pronounced individual transitions in the strength distributions by means of their transition densities and provide the dipole polarizabilities. We also compare our results to established approximate methods, such as the random-phase approximation (RPA) [RS80]. By imitating the truncations typically used in RPA-type methods in the IT-NCSM, we are able to shed new light on the deficiencies in these methods. Finally, we present conclusions and an outlook on future developments and research opportunities in chapter 9.

2. Input Hamiltonians

The quality of nuclear structure calculations is determined by the input Hamiltonian and the accuracy of the many-body method. This chapter is intended to present the Hamiltonians used in this thesis and to provide references for more details.

The translationally invariant nuclear Hamiltonian is given by

$$\begin{aligned} \mathbf{H} &= \mathbf{T}_{\text{int}} + \mathbf{V}^{[\text{NN}]} + \mathbf{V}^{[\text{3N}]} + \dots \\ &= \frac{1}{A} \sum_{i < j}^A \frac{(\vec{p}_i - \vec{p}_j)^2}{2m} + \sum_{i < j}^A \mathbf{v}_{ij}^{[\text{NN}]} + \sum_{i < j < k}^A \mathbf{v}_{ijk}^{[\text{3N}]} + \dots \end{aligned} \quad (2.1)$$

The first term denotes the intrinsic kinetic energy. It is obtained from the kinetic energy of all nucleons by subtracting the kinetic energy of the nucleus' center of mass and depends only on the relative momenta $\vec{p}_i - \vec{p}_j$ and the mass m of the nucleons. All other terms describe the interaction between the nucleons in hierarchical order. In general, up to A -body contributions can exist in an A -body system; however, we typically truncate the Hamiltonian at the three-body level at most.

Since a derivation of nuclear forces from QCD is currently not feasible because of its non-perturbative character in the low-energy regime relevant to nuclear structure theory, we resort to nuclear interactions derived in chiral EFT. Although these interactions are relatively soft compared to the traditionally used realistic nuclear potentials derived in meson-exchange theory [WSS95; Mac89], a prediagonalization via the similarity renormalization group (SRG) is vital to many-body methods to obtain observables which are either sufficiently converged or allow for a reliable extrapolation to infinite model spaces.

Many-body calculations with explicit three-nucleon (3N) interactions rapidly render unfeasible beyond the lightest nuclei because they come along with tremendously increased memory requirements compared to calculations including only NN forces. In order to limit the computational cost in the IT-NCSM, we often employ the normal-ordered two-body (NO2B) approximation. In the following, we give a brief overview of these topics.

2.1. Chiral Hamiltonians

Chiral EFT allows for the derivation of nuclear Hamiltonians in connection with the underlying physics of the strong interaction. In this framework, pions and nucleons are treated as degrees of freedom rather than quarks and gluons inherent to QCD. The basic idea of chiral EFT, as outlined by Weinberg in [Wei79], is to write down the most general Lagrangian consistent with the symmetry principles of QCD, in particular, the (broken) chiral symmetry. In principle, this Lagrangian consists of an infinite number of terms.

However, Weinberg showed that it can be expanded systematically in terms of $(Q/\Lambda_\chi)^\nu$, with a finite number of terms per order ν of the expansion. Here, Q is a typical nuclear momentum scale and Λ_χ the breakdown scale of the effective theory.

A great advantage of chiral interactions is that many-body forces emerge naturally in a hierarchical fashion. At order $\nu = 0$ and $\nu = 2$, commonly denoted by leading order (LO) and next-to-leading order (NLO), only two-body forces are present. Note that no contributions from order $\nu = 1$ exist. Starting from order $\nu = 3$, the next-to-next-to-leading order (N²LO), also three-body interactions arise, and so on. The interactions employed later are regularized using a momentum cutoff Λ_C , which is typically chosen around 500 MeV as a trade-off between the soft scale Q and the hard scale Λ_χ . Any physics at higher energies than Λ_C , which cannot be resolved in this theory, is absorbed into a set of low-energy constants. At present, they are determined from fits to experimental data, such as nucleon-nucleon and pion-nucleon scattering data and properties of two- and few-body systems, e.g., binding energies. First efforts regarding the determination of these low-energy constants in lattice QCD calculations have been made [EMN10], indicating a path for future developments.

Presently, interactions derived in chiral EFT include up to 3N forces, but research is ongoing to extend the available chiral potentials to the inclusion of four-body interactions and beyond [Epe07; Nog+10; Krü+13; Sch18]. Moreover, first efforts have been made to quantify theoretical uncertainties in chiral Hamiltonians [EKM15a; EKM15b; Bin+16; Car+16; EMN17; Bin+18]. We refer the reader to [ME11; EHM09] for reviews on chiral EFT and nuclear forces.

In applications of the methods developed in the framework of this thesis, we employ various chiral interactions: The interaction denoted “EM” is the chiral NN interaction at N³LO of Entem and Machleidt [EM03].

The “EMN500” interaction uses the EM interaction in combination with the 3N interaction at N²LO [Nav07], where the low-energy constants are fitted to the ground-state energy of $A = 3$ systems and the β -decay half-life of ${}^3\text{H}^1$ [GQN09]. The 3N interaction uses a cutoff $\Lambda_{3\text{N}} = 500$ MeV. As shown in [Rot+14], it has proven to yield ground-state energies in excellent agreement with data for light nuclei.

Furthermore, we employ the so-called “EMN400” interaction [Rot+12; Rot+14], obtained in the same way as the EMN500 interaction from the EM and the 3N interaction at N²LO [Nav07], but with a reduced 3N cutoff $\Lambda_{3\text{N}} = 400$ MeV. One low-energy constant is refitted so that the properties of two- and few-body systems are reproduced. This interaction—when SRG-evolved—performs better for medium-mass nuclei than the SRG-evolved EMN500 interaction because it suppresses SRG-induced contributions beyond the three-body level. The EMN400 interaction reproduces the experimental ground-state energies throughout the oxygen isotopic chain and describes the position of the dripline correctly.

The EMN500 and EMN400 interactions underestimate nuclear radii. To improve on that, the “N²LO_{sat}” interaction [Eks+15] was derived following a different approach. The NN and 3N forces at N²LO of the chiral expansion are optimized simultaneously to low-energy NN scattering data, as well as binding energies and radii of both, few-nucleon systems

¹Very recently, it was discovered that a factor of $-1/4$ was missing in the current-operator term relevant to the β decay. An updated set of low-energy constants is under way.

and selected carbon and oxygen isotopes. This interaction yields improved saturation properties of nuclear matter and accurately reproduces the binding energies and radii of sd -shell nuclei.

All of the above interactions are usually subjected to an SRG evolution before using them in a many-body method, e.g., the IT-NCSM, to enhance the convergence behavior.

Additionally, we use a different set of chiral interactions, denoted by “1.8/2.0(EM)” and “2.0/2.0(EM)” [Heb+11]. These interactions result from an SRG-evolved EM interaction, where the first value in the name labels the SRG cutoff, i.e., $\lambda = 1.8 \text{ fm}^{-1}$ and $\lambda = 2.0 \text{ fm}^{-1}$. Note that we use an alternative, but equivalent formulation of the SRG, where $\alpha = \lambda^{-4}$ is used as flow parameter. The 3N potential is taken as the leading 3N forces from chiral EFT with a momentum cutoff $\Lambda_{3N} = 2.0 \text{ fm}^{-1} \approx 395 \text{ MeV}$ —hence the second label in the name of these interactions—and is not SRG-evolved. Based on the assumption that the long-range part of the interaction remains approximately unchanged under the SRG transformation, only the low-energy constants of the short-range part of the 3N forces are refitted to reproduce the binding energy of ${}^3\text{H}$ and the radius of ${}^4\text{He}$, following [NBS04]. Particularly the 1.8/2.0(EM) interaction describes binding energies, two-neutron separation energies, and the energy of the first 2^+ states in nuclei up to the tin region successfully, while charge radii are too small [HJP16; Sim+17; Mor+18].

For practical calculations, we use matrix elements of the Hamiltonian provided in a JT -coupled basis of harmonic-oscillator (HO) single-particle states with some truncation. We cut the two-body matrix elements at a certain HO single-particle energy e_{\max} , in conformity with the truncation of the single-particle basis. If necessary, we introduce an additional truncation on the single-particle orbital angular momentum l_{\max} . The three-body matrix elements are further limited to orbits with a maximum HO single-particle energy $e_{3\max}$, and, additionally, with a maximum total energy $E_{3\max}$ i.e., $e_1 + e_2 + e_3 \leq E_{3\max} \leq 3e_{\max}$. Here, $e_1, e_2,$ and e_3 denote the HO single-particle energies of the nucleon orbits.

2.2. Similarity Renormalization Group

Nuclear interactions induce short-range correlations, which can only be accommodated in extremely large model spaces, thus slowing down the convergence behavior in the many-body calculations. In order to overcome this difficulty, we use the SRG [BFP07; HR07; BFS10; RNF10; Rot+14] to decouple low- and high-momentum modes in the chiral Hamiltonians via a continuous unitary transformation. The resulting Hamiltonian exhibits better convergence properties with respect to the model-space size than the bare Hamiltonian. This transformation of the Hamiltonian H and any operator O can be formally written as

$$H_\alpha = U_\alpha^\dagger H U_\alpha, \quad O_\alpha = U_\alpha^\dagger O U_\alpha. \quad (2.2)$$

The unitary operator U_α depends on a continuous parameter α , with the initial condition $U_{\alpha=0} = \mathbf{1}$. Accordingly, the initial nuclear Hamiltonian and the initial operator fulfill $H_{\alpha=0} = H$ and $O_{\alpha=0} = O$. By taking the derivative of (2.2) with respect to α , we obtain a

first-order differential equation for the evolved Hamiltonian and operator:

$$\frac{d}{d\alpha} \mathbf{H}_\alpha = [\boldsymbol{\eta}_\alpha, \mathbf{H}_\alpha], \quad \frac{d}{d\alpha} \mathbf{O}_\alpha = [\boldsymbol{\eta}_\alpha, \mathbf{O}_\alpha]. \quad (2.3)$$

This equation represents the so-called SRG flow equation. At the heart of the flow equation, there is the anti-Hermitian generator $\boldsymbol{\eta}_\alpha$, which governs the physics of the flow. In principle, several choices are possible [Weg94; BFP07; And+08; DON14], however, we typically define

$$\boldsymbol{\eta}_\alpha = m^2 [\mathbf{T}_{\text{int}}, \mathbf{H}_\alpha]. \quad (2.4)$$

This generator drives the Hamiltonian toward a diagonal form in the basis of eigenstates of the intrinsic kinetic energy. Note that any operator of relevance must be transformed simultaneously with the Hamiltonian for a consistent description of both, energies and other observables, because the generator depends on \mathbf{H}_α .

The major disadvantage of the SRG is that induced many-body contributions beyond the particle rank of the initial Hamiltonian emerge. In order to guarantee unitarity of the transformation, we need to keep all induced terms up to the A -body level. However, in practice, we have to truncate the transformation at a smaller particle rank—typically at the three-body level—and, thus, unitarity is formally violated. We can monitor the dependence of eigenvalues on the flow parameter α as a measure for the impact of discarded higher-order terms. A detailed study on the properties of SRG-evolved Hamiltonians is provided in [Rot+14].

In this thesis, we use the following variants of SRG-evolved Hamiltonians: By default, we employ the chiral Hamiltonians with initial two- and three-body interactions, SRG-evolved in three-body space. However, for benchmark purposes of the models developed, we occasionally use the chiral Hamiltonians evolved in two-body space only, i.e., neither initial nor induced three- and multi-particle interactions are taken into account. In order to assess the importance of initial 3N interactions, we also restrict the initial Hamiltonian to 2N interactions but carry out the SRG in three-body space.

2.3. Normal-Ordered Two-Body Approximation

The need for 3N interactions is evident from a series of applications, see, e.g., [ME11; EHM09; Ber+08; Ber+11; Epe+02]. However, for many large-scale many-body approaches, the computational cost increases tremendously by including 3N interactions explicitly. Often, these render calculations impractical which are routinely feasible using NN interactions only. By normal ordering a nuclear Hamiltonian with respect to a nucleus-specific reference state, a systematic lower-rank approximation of the 3N interaction is constructed, where some contributions of the 3N interaction are transferred to lower-particle ranks. The NO2B approximation [Rot+12]—obtained from this nucleus-specific Hamiltonian by omitting the remaining 3N term—represents a compromise between including 3N interactions explicitly while keeping the computational cost at the level of a calculation with NN interactions only. It has been found that the NO2B approximation works very well for energies of ground and excited states beyond the lightest nuclei and with the

exception of particularly fragile states [Rot+12; GCR16]. Energies typically deviate by less than 1% from the results obtained when including full 3N interactions.

A final technical remark: Although the initial Hamiltonian is translationally invariant, the NO2B approximation breaks this invariance explicitly because it couples the Hamiltonian to a localized density.

3. Electromagnetic Moments and Transitions

Electromagnetic moments and transitions are very sensitive to the detailed form of the nuclear wave function. Therefore, they play an important role in experimental and theoretical investigations of nuclei, and the possibility to directly compare these observables provides an excellent testing ground for *ab initio* theories. We introduce the fundamentals of electromagnetic moments and transitions following the discussion of [RS80]. Derivations of many of the following quantities can be found in appendix A.

3.1. Hamiltonian of a Nucleus in an Electromagnetic Field

A nucleus exposed to an external electromagnetic field is described by the Hamiltonian

$$\mathbf{H} = \mathbf{H}_{\text{nucl}} + \mathbf{H}_{\text{field}} + \mathbf{H}_{\text{int}} \quad (3.1)$$

composed of the Hamiltonians of the nucleus, the electromagnetic field, and the interaction between the two.

The nuclear Hamiltonian \mathbf{H}_{nucl} defines the eigenstates of the nucleus. In our calculations, it is given by one of the input Hamiltonians introduced in chapter 2, and we obtain its eigenstates by solving the many-body Schrödinger equation using one of the available many-body methods of chapters 4 and 5.

The electromagnetic radiation field can be expanded in multipoles and is quantized in terms of photons. In practice, we derive the vector potential

$$\vec{\mathbf{A}}(\vec{r}, t) = \sum_{\sigma k \lambda \mu} (\vec{\mathbf{A}}_{\sigma k \lambda \mu}(\vec{r}) e^{-i\omega_k t} \mathbf{a}_{\sigma k \lambda \mu}^\dagger + \vec{\mathbf{A}}_{\sigma k \lambda \mu}^*(\vec{r}) e^{i\omega_k t} \mathbf{a}_{\sigma k \lambda \mu}) \quad (3.2)$$

in transverse gauge, cf. appendix A.2, from which we can deduce the electric and magnetic fields. The operators $\mathbf{a}_{\sigma k \lambda \mu}^\dagger$ and $\mathbf{a}_{\sigma k \lambda \mu}$ create and annihilate a photon of electric ($\sigma = E$) or magnetic ($\sigma = M$) character with energy $E_k = \hbar\omega_k$, angular momentum λ , and projection μ , respectively. The coefficients contain all characteristics of the electromagnetic field and are given by

$$\begin{aligned} \vec{\mathbf{A}}_{Mk\lambda\mu}(\vec{r}) &= \mathcal{N} j_\lambda(kr) \vec{Y}_{\lambda\lambda\mu}(\Omega) \\ &= \frac{\mathcal{N}}{\sqrt{\lambda(\lambda+1)}} \frac{1}{i} (\vec{r} \times \vec{\nabla}) (j_\lambda(kr) Y_{\lambda\mu}(\Omega)) \end{aligned} \quad (3.3)$$

and

$$\begin{aligned} \vec{\mathbf{A}}_{Ek\lambda\mu}(\vec{r}) &= \frac{i}{k} (\vec{\nabla} \times \vec{\mathbf{A}}_{Mk\lambda\mu}(\vec{r})) \\ &= \frac{-\mathcal{N}}{\sqrt{\lambda(\lambda+1)}} \frac{1}{k} \left[\vec{\nabla} \left(Y_{\lambda\mu}(\Omega) \frac{\partial}{\partial r} (r j_\lambda(kr)) \right) + k^2 \vec{r} j_\lambda(kr) Y_{\lambda\mu}(\Omega) \right]. \end{aligned} \quad (3.4)$$

The quantity $\vec{Y}_{\lambda\lambda\mu}(\Omega)$ denotes the vector spherical harmonics of angular momentum $l = \lambda$, total angular momentum λ , and projection μ . The coefficients (3.3) and (3.4) depend on the spherical harmonics $Y_{\lambda\mu}(\Omega)$, the spherical Bessel function $j_\lambda(kr)$, and the absolute value of the photon momentum \vec{k} . The normalization constant

$$\mathcal{N} = \sqrt{\frac{4\pi\hbar\omega_k}{R}} \quad (3.5)$$

results from requiring the proper boundary conditions of an electromagnetic field at a perfectly conducting sphere with a large radius R compared to the nuclear radius. The Hamiltonian of the radiation field,

$$\mathbf{H}_{\text{field}} = \frac{1}{8\pi} \int d^3r (\vec{\mathbf{E}}^2(\vec{r}, t) + \vec{\mathbf{B}}^2(\vec{r}, t)), \quad (3.6)$$

can be rewritten in transverse gauge and in absence of radiation sources as

$$\begin{aligned} \mathbf{H}_{\text{field}} &= \frac{1}{8\pi} \int d^3r \left(\frac{1}{c^2} \dot{\vec{\mathbf{A}}}^2 + (\vec{\nabla} \times \vec{\mathbf{A}})^2 \right) \\ &= \sum_{\sigma k \lambda \mu} \hbar\omega_k \left(\mathbf{a}_{\sigma k \lambda \mu}^\dagger \mathbf{a}_{\sigma k \lambda \mu} + \frac{1}{2} \right). \end{aligned} \quad (3.7)$$

Its eigenstates in occupation-number representation are $|\dots n_{\sigma k \lambda \mu} \dots\rangle$.

The electromagnetic field couples to the nuclear charge density $\rho(\vec{r}, t)$ and nuclear current density $\vec{\mathbf{j}}(\vec{r}, t)$ via

$$\mathbf{H}_{\text{int}} = \int d^3r \left(\rho(\vec{r}, t) \Phi(\vec{r}, t) - \frac{1}{c} \vec{\mathbf{j}}(\vec{r}, t) \cdot \vec{\mathbf{A}}(\vec{r}, t) \right), \quad (3.8)$$

where $\Phi(\vec{r}, t)$ is the scalar potential of the field. This interaction can be treated perturbatively. In the definition of the nuclear charge density,

$$\rho(\vec{r}, t) = \sum_{i=1}^A e \left(\frac{1}{2} + \tau_i \right) \cdot \delta(\vec{r} - \vec{r}_i(t)), \quad (3.9)$$

we consider the nucleons as point-like particles for simplicity. The finite extension of the nucleons could, in principle, be taken into account by a form factor. The projector $(1/2 + \tau)$ ensures that only the protons contribute to the nuclear charge density. In our convention, protons have an isospin projection $\tau = +1/2$, neutrons have $\tau = -1/2$. The current density $\vec{\mathbf{j}}(\vec{r}, t)$ originates from the moving charges of protons and the spin magnetism of protons and neutrons. It is related to the density of the magnetic dipole moment $\vec{\mu}(\vec{r}, t)$ by

$$\vec{\mathbf{j}}(\vec{r}, t) = c \vec{\nabla} \times \vec{\mu}(\vec{r}, t). \quad (3.10)$$

The orbit part is given by

$$\vec{\mathbf{j}}^o(\vec{r}, t) = \sum_{i=1}^A e \left(\frac{1}{2} + \tau_i \right) \frac{1}{2} (\vec{v}_i \delta(\vec{r} - \vec{r}_i(t)) + h.c.). \quad (3.11)$$

Here, $\vec{v}_i = i[\mathbf{H}, \vec{r}_i]/\hbar$ is the nucleon velocity, which, according to (3.1), has contributions from the nuclear as well as from the interaction Hamiltonian. The spin part of the current density can be calculated from (3.10) and

$$\vec{\mu}(\vec{r}, t) = \sum_{i=1}^A \delta(\vec{r} - \vec{r}_i(t)) \mu_N \left[\left(\frac{1}{2} + \tau_i \right) g_p + \left(\frac{1}{2} - \tau_i \right) g_n \right] \vec{s}_i \quad (3.12)$$

with the nuclear magneton $\mu_N = e\hbar/(2mc)$. The g factors for free protons and neutrons are $g_p = 5.5856$ and $g_n = -3.8263$, respectively. In transverse gauge and for regions far from the sources of electromagnetic radiation, we obtain the interaction Hamiltonian

$$\mathbf{H}_{\text{int}} = -\frac{1}{c} \sum_{\sigma k \lambda \mu} \left[\mathbf{a}_{\sigma k \lambda \mu}^\dagger \int d^3r \vec{\mathbf{j}}(\vec{r}, t) \cdot \vec{A}_{\sigma k \lambda \mu}(\vec{r}) e^{-i\omega_k t} + h.c. \right]. \quad (3.13)$$

We note that the expressions (3.9) and (3.11) represent approximations because only one-body exchange terms are taken into account, and all other terms, e.g., the two-body currents describing pion exchange processes, are neglected. This approximation affects the form of the electromagnetic multipole operators as they are derived below and commonly employed in practical applications. However, we expect that the operators will be improved in future calculations. First efforts in this regard are made, in particular, two-body currents are subject to present investigations [Pas+13; Bar+16; KEM17].

3.2. Static Multipole Moments

The static multipole moments characterize specific configurations of the nucleus' protons and neutrons and are time independent. They are probed by exposing a nucleus to an external static electromagnetic field, e.g., created by the charged particles surrounding the nucleus or by some experimental setup in the laboratory.

In order to derive the static electric and magnetic multipole moments, we rewrite the interaction Hamiltonian (3.8) by using relation (3.10) and introducing the magnetic flux

$$\vec{\mathbf{B}}(\vec{r}) = \vec{\nabla} \times \vec{\mathbf{A}}(\vec{r}). \quad (3.14)$$

In this way, we obtain

$$\mathbf{H}_{\text{int}} = \int d^3r \left(\rho(\vec{r}) \Phi(\vec{r}) - \vec{\mu}(\vec{r}) \cdot \vec{\mathbf{B}}(\vec{r}) \right). \quad (3.15)$$

We assume that the sources of the electromagnetic field are far from the nucleus. Since the electromagnetic field exhibits no time dependence, the homogeneous Maxwell equations apply. Thus, both, the electric and magnetic field, can be written as gradients of scalar potentials:

$$\vec{\mathbf{E}}(\vec{r}) = -\vec{\nabla} \Phi(\vec{r}), \quad \vec{\mathbf{B}}(\vec{r}) = -\vec{\nabla} \Xi(\vec{r}). \quad (3.16)$$

3. Electromagnetic Moments and Transitions

By inserting these expressions into the homogeneous Maxwell equations, we obtain the Laplace equations

$$\Delta\Phi(\vec{r}) = 0, \quad \Delta\mathbf{E}(\vec{r}) = \mathbf{0}. \quad (3.17)$$

The most general solutions for these in spherical coordinates are

$$\Phi(\vec{r}) = \sum_{\lambda\mu} \mathbf{a}_{\lambda\mu} r^\lambda Y_{\lambda\mu}(\Omega), \quad (3.18a)$$

$$\mathbf{E}(\vec{r}) = \sum_{\lambda\mu} \mathbf{b}_{\lambda\mu} r^\lambda Y_{\lambda\mu}(\Omega), \quad (3.18b)$$

and, thus, the interaction Hamiltonian is given by

$$H_{\text{int}} = \sum_{\lambda\mu} (\mathbf{a}_{\lambda\mu} \mathbf{Q}_{\lambda\mu} + \mathbf{b}_{\lambda\mu} \mathbf{M}_{\lambda\mu}), \quad (3.19)$$

with the electric and magnetic multipole operators

$$\mathbf{Q}_{\lambda\mu} = \int d^3r \rho(\vec{r}) r^\lambda Y_{\lambda\mu}(\Omega), \quad (3.20)$$

$$\mathbf{M}_{\lambda\mu} = \int d^3r \vec{\mu}(\vec{r}) \cdot \vec{\nabla} (r^\lambda Y_{\lambda\mu}(\Omega)). \quad (3.21)$$

Inserting the expressions for the nuclear density and currents (3.9) to (3.12) into (3.20) and (3.21) yields the final expressions for the static electric and magnetic multipole operators

$$\mathbf{Q}_{\lambda\mu} = e \sum_{i=1}^A \left(\frac{1}{2} + \tau_i \right) \mathbf{r}_i^\lambda Y_{\lambda\mu}(\Omega_i), \quad (3.22)$$

$$\mathbf{M}_{\lambda\mu} = \mu_N \sum_{i=1}^A \left[g_s^{(i)} \vec{\mathbf{s}}_i + \frac{2}{\lambda+1} g_l^{(i)} \vec{\mathbf{l}}_i \right] \cdot (\vec{\nabla}_i r_i^\lambda Y_{\lambda\mu}(\Omega_i)). \quad (3.23)$$

The gyromagnetic ratios for proton and neutron spin are $g_s^{(i)} = g_p$ and $g_s^{(i)} = g_n$, respectively. The orbital factors are $g_l^{(i)} = 1$ for protons and $g_l^{(i)} = 0$ for neutrons. The derivation of (3.22) and (3.23) is sketched in appendix A.3.

The static electromagnetic moments of multipolarity λ and projection μ can be calculated from the expectation values of the operators (3.22) and (3.23) in a nuclear state $|\Psi_n\rangle = |\zeta JM\rangle$, where the index ζ collects all quantum numbers of the eigenstate except the total angular momentum J and its projection M :

$$Q_{\lambda\mu} = \langle \Psi_n | \mathbf{Q}_{\lambda\mu} | \Psi_n \rangle, \quad (3.24)$$

$$M_{\lambda\mu} = \langle \Psi_n | \mathbf{M}_{\lambda\mu} | \Psi_n \rangle. \quad (3.25)$$

Typically, the static multipole moments are calculated for the maximum value of the projected total angular momentum $M = J$. We note that, since the relevant quantities—the eigenstates as well as the operators $\mathbf{Q}_{\lambda\mu}$ and $\mathbf{M}_{\lambda\mu}$ —represent spherical tensors, it is easily

possible to obtain the static electromagnetic moments for arbitrary projection quantum numbers $M \neq J$ by applying the Wigner-Eckart theorem (A.10).

Typical examples of multipole moments addressed in nuclear structure theory are the magnetic dipole and electric quadrupole moments

$$\mu = \sqrt{\frac{4\pi}{3}} \langle \zeta JJ | \mathbf{M}_{10} | \zeta JJ \rangle, \quad (3.26)$$

$$Q = \sqrt{\frac{16\pi}{5}} \langle \zeta JJ | Q_{20} | \zeta JJ \rangle. \quad (3.27)$$

The prefactor of the electric multipole moment is defined to correct for the normalization of the spherical harmonics in (3.20) so that it matches the expression of its classical analog. For consistency, it is also introduced for the magnetic multipole moments.

Since the strong and electromagnetic interactions conserve parity, we can choose the nuclear eigenstate $|\Psi_n\rangle$ to be an eigenstate of the parity operator. By considering the behavior of (3.22) and (3.23) under parity transformations, we can deduce that the electric multipole operator has parity $(-1)^\lambda$ and the magnetic multipole operator has parity $(-1)^{\lambda+1}$. Therefore, the electric and magnetic moments vanish for $\lambda = 1, 3, 5, \dots$ and $\lambda = 0, 2, 4, \dots$, respectively.

3.3. Multipole Transitions

Nuclear radiative processes involve, in general, the absorption or emission of real photons. The eigenstates $\{|\Psi_n\rangle\}$ of the nuclear Hamiltonian H_{nucl} and the eigenstates

$$\{|\dots n_{\sigma k \lambda \mu} \dots\rangle\}$$

of the Hamiltonian of the electromagnetic field H_{field} define a complete set of eigenstates of the unperturbed Hamiltonian

$$\mathbf{H}_0 = \mathbf{H}_{\text{nucl}} + \mathbf{H}_{\text{field}}. \quad (3.28)$$

The interaction \mathbf{H}_{int} (3.13) does neither commute with the nuclear nor with the field Hamiltonian and, therefore, mediates transitions between the nuclear states $|\Psi_i\rangle$ and $|\Psi_f\rangle$ and the corresponding field eigenstates through absorption and emission of photons. We restrict ourselves to one-photon absorption processes

$$|i\rangle = |\Psi_i\rangle |\dots n_{\sigma k \lambda \mu} \dots\rangle \longrightarrow |f\rangle = |\Psi_f\rangle |\dots n_{\sigma k \lambda \mu} - 1 \dots\rangle. \quad (3.29)$$

One-photon emission processes can be treated analogously.

According to Fermi's golden rule [Fer50], the transition probability of an initial state of the system of nucleus plus electromagnetic field to a final state is given by

$$T_{fi} = \frac{2\pi}{\hbar} |\langle f | \mathbf{H}_{\text{int}} | i \rangle|^2 g(E_f). \quad (3.30)$$

3. Electromagnetic Moments and Transitions

The factor $g(E_f)$ is the density of final states with energy $E_f = E_i + \hbar\omega_k$. Inserting the interaction Hamiltonian (3.13) into (3.30) yields

$$T_{fi}(\sigma, k\lambda\mu) = \frac{8\pi(\lambda+1)}{\hbar\lambda((2\lambda+1)!!)^2} \left(\frac{E_k}{\hbar c}\right)^{2\lambda+1} |\langle \Psi_f | \mathbf{O}(\sigma, k\lambda\mu) | \Psi_i \rangle|^2, \quad (3.31)$$

with the electric and magnetic multipole transition operators

$$\begin{aligned} \mathbf{O}(E, k\lambda\mu) = \frac{(2\lambda+1)!!}{k^\lambda(\lambda+1)} \int d^3r \left(\boldsymbol{\rho}(\vec{r}, t) Y_{\lambda\mu}(\Omega) \frac{\partial}{\partial r} r j_\lambda(kr) \right. \\ \left. + i \frac{k}{c} \vec{\mathbf{j}}(\vec{r}, t) \cdot \vec{r} Y_{\lambda\mu}(\Omega) j_\lambda(kr) \right), \end{aligned} \quad (3.32)$$

$$\mathbf{O}(M, k\lambda\mu) = \frac{-(2\lambda+1)!!}{ck^\lambda(\lambda+1)} \int d^3r \vec{\mathbf{j}}(\vec{r}, t) \cdot (\vec{r} \times \vec{\nabla}) (j_\lambda(kr) Y_{\lambda\mu}(\Omega)). \quad (3.33)$$

The derivation is illustrated in appendix A.4.

We work in the long-wavelength limit, where we assume that the wavelength of the radiation $\Lambda \propto 1/k$ is large compared to the extension R_0 of the nucleus, i.e.,

$$kR_0 \ll 1. \quad (3.34)$$

This allows us to expand the spherical Bessel functions for small arguments:

$$j_\lambda(kr) \approx \frac{(kr)^\lambda}{(2\lambda+1)!!} \left(1 - \frac{1}{2} \frac{(kr)^2}{2\lambda+3} + \dots \right). \quad (3.35)$$

Substituting the leading term into (3.32), yields

$$\mathbf{O}(E, k\lambda\mu) = \int d^3r \boldsymbol{\rho}(\vec{r}, t) r^\lambda Y_{\lambda\mu}(\Omega) + \frac{ik}{\lambda+1} \int d^3r (\vec{r} \times \vec{\boldsymbol{\mu}}(\vec{r}, t)) \vec{\nabla} r^\lambda Y_{\lambda\mu}(\Omega) \quad (3.36)$$

$$\approx \int d^3r \boldsymbol{\rho}(\vec{r}, t) r^\lambda Y_{\lambda\mu}(\Omega) = \mathbf{Q}_{\lambda\mu} \quad (3.37)$$

for the electric multipole operator. The first term of (3.36) does not depend on k and can be identified with the static electric multipole operator $\mathbf{Q}_{\lambda\mu}$ (3.20). Since the integral in (3.36) is confined to the interior of the nucleus, the second term is of the order of kR_0 and is usually neglected.

This approximation can be used for all electric multipoles except for the electric monopole and isoscalar dipole operator. Regarding the electric monopole transition operator, the first term in (3.36) is constant—it is proportional to the charge of the nucleus—and the second term vanishes. In particular, the operator (3.36) cannot mediate intrinsic nuclear excitations for $\lambda = 0$. Therefore, we resort to the second-order term of (3.35) to derive an expression for the electric monopole transition operator:

$$\mathbf{Q}_{00} = e \sum_{i=1}^A \left(\frac{1}{2} + \tau_i \right) r_i^2 Y_{00}(\Omega_i). \quad (3.38)$$

3.4. Single-Particle Matrix Elements of the Reduced Electromagnetic Multipole Operators

For a discussion of the electric isoscalar dipole operator, we refer the reader to section 3.5.

An analogous procedure for the magnetic multipole operator results in

$$\mathbf{O}(M, k\lambda\mu) = \frac{1}{c(\lambda+1)} \int d^3r (\vec{r} \times \vec{j}(\vec{r}, t)) \cdot \vec{\nabla} (r^\lambda Y_{\lambda\mu}) = \mathbf{M}_{\lambda\mu}, \quad (3.39)$$

which is equivalent to the expression for the static magnetic multipole operator (3.21) (cf. (A.40)).

In general, the orientations of the angular momenta are not known in experiments except for polarization experiments. Therefore, we average over the initial projections M_i of the angular momenta and sum up all final projections M_f . In this way, we obtain the total transition probability

$$\begin{aligned} T_{fi}(\sigma, \lambda) &= \frac{1}{2J_i + 1} \sum_{M_i \mu M_f} T_{fi}(\sigma, k\lambda\mu) \\ &= \frac{8\pi(\lambda+1)}{\hbar\lambda((2\lambda+1)!!)^2} \left(\frac{E_k}{\hbar c} \right)^{2\lambda+1} B(\sigma\lambda, J_i \rightarrow J_f), \end{aligned} \quad (3.40)$$

where we have used the definition of the reduced transition probability

$$B(\sigma\lambda, J_i \rightarrow J_f) = \frac{1}{2J_i + 1} |\langle \Psi_f | \mathbf{O}_\lambda | \Psi_i \rangle|^2. \quad (3.41)$$

Here, \mathbf{O}_λ represents a placeholder for the electric or magnetic multipole operator. The reduced transition probability contains all relevant information about the nuclear wave function. Everything else is absorbed into kinematical factors.

Since real photons carry off at least one unit of angular momentum, no monopole transitions exist with real photons. For magnetic transitions, this is rooted fundamentally in the absence of magnetic monopoles. Electric monopole transitions are only possible with virtual photons, e.g., in internal conversion or electron-hadron scattering processes. Further selection rules are dictated by the structure of the multipole operators (3.37) and (3.39):

$$|J_i - J_f| \leq \lambda \leq J_i + J_f, \quad (3.42a)$$

$$M_f - M_i = \mu, \quad (3.42b)$$

$$\pi_i \pi_{\sigma\lambda\mu} \pi_f = 1. \quad (3.42c)$$

The parities of the transitions are given by $\pi_{E\lambda\mu} = (-1)^\lambda$ and $\pi_{M\lambda\mu} = (-1)^{\lambda+1}$. Usually, magnetic dipole and electric quadrupole radiation are of comparable importance, higher multipolarities are suppressed.

3.4. Single-Particle Matrix Elements of the Reduced Electromagnetic Multipole Operators

The matrix elements of the multipole operators can be evaluated, e.g., in a spherical single-particle basis defined by the HO potential. In the following, we exploit that we are dealing with nucleons, which have spin $s = 1/2$.

The reduced single-particle matrix elements of the electric multipole operators can be calculated via

$$\begin{aligned} \langle \psi_f \| \mathbf{Q}_\lambda \| \psi_i \rangle &= \langle n' s' l' j' \| e \mathbf{r}^\lambda Y_\lambda(\mathbf{\Omega}) \| n s l j \rangle \\ &= e \frac{1 + (-1)^{l'+\lambda+l}}{2} \langle n' l' | r^\lambda | n l \rangle \frac{\hat{j} \hat{\lambda} \hat{j}'}{\sqrt{4\pi}} (-1)^{j'-\frac{1}{2}} \begin{pmatrix} j' & \lambda & j \\ -\frac{1}{2} & 0 & \frac{1}{2} \end{pmatrix}, \end{aligned} \quad (3.43)$$

where we have introduced the shorthand notation

$$\hat{j} \equiv \sqrt{2j+1}. \quad (3.44)$$

The derivation of (3.43) is shown in appendix A.5.

The magnetic equivalent is given by

$$\begin{aligned} \langle \psi_f \| \mathbf{M}_\lambda \| \psi_i \rangle &= \langle n' s' l' j' \| \mu_N \left(g_s \vec{\mathbf{s}} + \frac{2}{\lambda+1} g_l \vec{\mathbf{l}} \right) \cdot (\nabla \mathbf{r}^\lambda Y_\lambda(\mathbf{\Omega})) \| n s l j \rangle \\ &= \mu_N \frac{1 - (-1)^{l'+\lambda+l}}{2} \langle n' l' | r^{\lambda-1} | n l \rangle \frac{\hat{j} \hat{\lambda} \hat{j}'}{\sqrt{4\pi}} \\ &\quad \times (-1)^{j'-\frac{1}{2}} \begin{pmatrix} j' & \lambda & j \\ -\frac{1}{2} & 0 & \frac{1}{2} \end{pmatrix} (\lambda - \kappa) \left[\frac{1}{2} g_s - g_l \left(1 + \frac{\kappa}{\lambda+1} \right) \right], \end{aligned} \quad (3.45)$$

with

$$\kappa = \left(j + \frac{1}{2} \right) (-1)^{l+j+\frac{1}{2}} + \left(j' + \frac{1}{2} \right) (-1)^{l'+j'+\frac{1}{2}}. \quad (3.46)$$

The radial integrals are defined as

$$\langle n' l' | r^\lambda | n l \rangle = \int dr r^2 R_{n'l'}(r) r^\lambda R_{nl}(r). \quad (3.47)$$

The radial wave functions $R_{nl}(r)$ and $R_{n'l'}(r)$ of the initial and final single-particle states must be evaluated in the respective basis, e.g., the HO or Hartree-Fock (HF) single-particle basis.

In CI calculations, we typically calculate the matrix elements of the electromagnetic operators on the fly using the above expressions. We note that a consistent description of both, spectra and electromagnetic observables, in the IT-NCSM, where we use SRG-evolved Hamiltonians, requires also the SRG evolution for the electromagnetic operator [RNF10; Sch+14; Sch+15]. Since the effect of the consistently evolved operators has been found to be small, their use is important in precision calculations only.

3.5. Isospin Decomposition

In isospin formalism, the electric multipole operator (3.22) reads

$$\mathbf{Q}_{\lambda\mu} = \frac{1}{2} e \sum_{i=1}^A \mathbf{r}_i^\lambda Y_{\lambda\mu}(\mathbf{\Omega}_i) + e \sum_{i=1}^A \boldsymbol{\tau}_i \mathbf{r}_i^\lambda Y_{\lambda\mu}(\mathbf{\Omega}_i), \quad (3.48)$$

where the first term has no dependence on the isospin. Consequently, it can only lead to isoscalar excitations, which do not change the isospin T of the nuclear state, i.e., $\Delta T = 0$. The second term is proportional to the z-projection of the isospin and gives rise to isovector transitions with $\Delta T = 1$.

We define the electric multipole operator as the sum of its isoscalar and isovector part,

$$\mathcal{Q}_{\lambda\mu} \equiv \mathcal{Q}_{\lambda\mu}^{\text{IS}} + \mathcal{Q}_{\lambda\mu}^{\text{IV}} \quad (3.49)$$

with

$$\mathcal{Q}_{\lambda\mu}^{\text{IS}} = \frac{1}{2}e \sum_{\pi=1}^Z r_{\pi}^{\lambda} Y_{\lambda\mu}(\mathbf{\Omega}_{\pi}) + \frac{1}{2}e \sum_{\nu=1}^N r_{\nu}^{\lambda} Y_{\lambda\mu}(\mathbf{\Omega}_{\nu}), \quad (3.50)$$

$$\mathcal{Q}_{\lambda\mu}^{\text{IV}} = \frac{1}{2}e \sum_{\pi=1}^Z r_{\pi}^{\lambda} Y_{\lambda\mu}(\mathbf{\Omega}_{\pi}) - \frac{1}{2}e \sum_{\nu=1}^N r_{\nu}^{\lambda} Y_{\lambda\mu}(\mathbf{\Omega}_{\nu}). \quad (3.51)$$

In this definition, we carry out the sums over protons and neutrons separately. We have, furthermore, introduced the electric charge e for both, protons and neutrons, in accordance with the macroscopic picture of protons and neutrons contributing equally to oscillations in and out of phase, see discussion below.

We point out one peculiarity: The isoscalar dipole operator is proportional to the center-of-mass coordinate; thus, it causes translations of the nucleus as a whole but cannot induce intrinsic excitations. This is similar to the electric monopole operator, for which the leading term in the expansion of the spherical Bessel function (3.35) leads to an operator proportional to the charge of the nucleus. Again, higher-order contributions of (3.35) are required to allow for intrinsic nuclear transitions. We define the isoscalar dipole transition operator as

$$\mathcal{Q}_{1\mu}^{\text{IS}} = \frac{1}{4}e \sum_{i=1}^A r_i^3 Y_{1\mu}(\mathbf{\Omega}_i). \quad (3.52)$$

The magnetic multipole operator can be separated into isoscalar and isovector operators analogously. To this aim, we substitute $g_s^{(i)}$ and $g_l^{(i)}$ in (3.23) by their respective values in terms of isospin:

$$\begin{aligned} \mathbf{M}_{\lambda\mu} = & \mu_N \sum_{i=1}^A \left[\frac{1}{2}(g_p + g_n)\vec{s}_i + \frac{1}{\lambda+1}\vec{l}_i \right] \cdot (\vec{\nabla}_i r_i^{\lambda} Y_{\lambda\mu}(\mathbf{\Omega}_i)) \\ & + \mu_N \sum_{i=1}^A \left[\tau_i(g_p - g_n)\vec{s}_i + \frac{2}{\lambda+1}\tau_i\vec{l}_i \right] \cdot (\vec{\nabla}_i r_i^{\lambda} Y_{\lambda\mu}(\mathbf{\Omega}_i)). \end{aligned} \quad (3.53)$$

The first term corresponds to the isoscalar magnetic multipole operator and the second term to the isovector magnetic multipole operator. The isoscalar and isovector components

are

$$\begin{aligned} \mathbf{M}_{\lambda\mu}^{\text{IS}} = & \mu_N \sum_{\pi=1}^Z \left[\frac{1}{2}(g_p + g_n)\vec{s}_{\pi} + \frac{1}{\lambda+1}\vec{l}_{\pi} \right] \cdot (\vec{\nabla}_{\pi} r_{\pi}^{\lambda} Y_{\lambda\mu}(\mathbf{\Omega}_{\pi})) \\ & + \mu_N \sum_{\nu=1}^N \left[\frac{1}{2}(g_p + g_n)\vec{s}_{\nu} + \frac{1}{\lambda+1}\vec{l}_{\nu} \right] \cdot (\vec{\nabla}_{\nu} r_{\nu}^{\lambda} Y_{\lambda\mu}(\mathbf{\Omega}_{\nu})), \end{aligned} \quad (3.54)$$

$$\begin{aligned} \mathbf{M}_{\lambda\mu}^{\text{IV}} = & \mu_N \sum_{\pi=1}^Z \left[\frac{1}{2}(g_p - g_n)\vec{s}_{\pi} + \frac{1}{\lambda+1}\vec{l}_{\pi} \right] \cdot (\vec{\nabla}_{\pi} r_{\pi}^{\lambda} Y_{\lambda\mu}(\mathbf{\Omega}_{\pi})) \\ & - \mu_N \sum_{\nu=1}^N \left[\frac{1}{2}(g_p - g_n)\vec{s}_{\nu} + \frac{1}{\lambda+1}\vec{l}_{\nu} \right] \cdot (\vec{\nabla}_{\nu} r_{\nu}^{\lambda} Y_{\lambda\mu}(\mathbf{\Omega}_{\nu})). \end{aligned} \quad (3.55)$$

Here, we have used the bare values for the gyromagnetic ratios and orbit g factors.

Collective excitations typically involve many or all nucleons. In the macroscopic picture of isoscalar and isovector electric transitions, protons and neutrons oscillate in and out of phase, respectively, according to a specific multipole pattern defined by λ . The isoscalar electric monopole mode, e.g., corresponds to a radial oscillation of the nucleus as a whole and is, therefore, often referred to as a “breathing” or “compressional” mode. The isovector electric dipole mode, in contrast, is characterized by a one-dimensional collective oscillation of all neutrons against all protons, which results in a separation of the center of mass and center of charge of the nucleus. In the isoscalar electric quadrupole mode, the nucleus is deformed alternately into an oblate and prolate shape by in-phase oscillations of the nucleons. The isoscalar magnetic dipole mode can be interpreted macroscopically as the oscillation of spin-up nucleons against spin-down nucleons, whereas the isovector magnetic dipole mode is understood as the out-of-phase oscillation of spin-up (spin-down) neutrons against spin-down (spin-up) protons. More details on electromagnetic transitions and their macroscopic picture can be found, e.g., in [HW01] and references therein.

We remark that, in general, isovector modes for the same multipolarity are at higher energies compared to their isoscalar partners, because extra energy is required to separate protons and neutrons.

3.6. Translational Invariance

We point out that all expressions for the electromagnetic operators are derived in the reference system of the nucleus, i.e., the coordinates of the electromagnetic operators are defined relative to the center of mass of the nucleus. In principle, we need to substitute \vec{r} by $\vec{r} - \vec{R}_{\text{cm}}$ at the operator level for practical calculations to ensure translational invariance. Consequently, the operators are not one-body but A -body operators.

The translationally invariant expressions for the electric monopole, dipole, and quadru-

pole operators are

$$\mathbf{Q}_{00} = e \sum_{i=1}^A \left(\frac{1}{2} + \boldsymbol{\tau}_i \right) (\vec{\mathbf{r}}_i - \vec{\mathbf{R}}_{\text{cm}})^2 Y_{00}(\vec{\boldsymbol{\omega}}_i) \quad (3.56)$$

$$= \frac{1}{\sqrt{4\pi}} e \frac{1}{A} \sum_{i>j=1}^A \left(\Pi_i^\pi + \Pi_j^\nu - \frac{Z}{A} \right) \vec{\mathbf{r}}_{ij}^2, \quad (3.57)$$

$$\mathbf{Q}_{10} = e \sum_{i=1}^A \left(\frac{1}{2} + \boldsymbol{\tau}_i \right) |\vec{\mathbf{r}}_i - \vec{\mathbf{R}}_{\text{cm}}| Y_{10}(\vec{\boldsymbol{\omega}}_i) \quad (3.58)$$

$$= e \frac{2}{A} \sum_{i>j=1}^A \left(\Pi_i^\pi \Pi_j^\pi + \Pi_i^\pi \Pi_j^\nu \right) |\vec{\mathbf{r}}_{ij}| Y_{10}(\vec{\boldsymbol{\omega}}_{ij}), \quad (3.59)$$

$$\mathbf{Q}_{20} = e \sum_{i=1}^A \left(\frac{1}{2} + \boldsymbol{\tau}_i \right) (\vec{\mathbf{r}}_i - \vec{\mathbf{R}}_{\text{cm}})^2 Y_{20}(\vec{\boldsymbol{\omega}}_i) \quad (3.60)$$

$$= e \frac{1}{A} \sum_{i>j=1}^A \left(\Pi_i^\pi + \Pi_j^\nu - \frac{Z}{A} \right) \vec{\mathbf{r}}_{ij}^2 Y_{20}(\vec{\boldsymbol{\omega}}_{ij}). \quad (3.61)$$

Here, we have introduced the angle $\vec{\boldsymbol{\omega}}$ defined in the reference frame of the nucleus' center of mass and the relative coordinate $\vec{\mathbf{r}}_{ij} = \vec{\mathbf{r}}_i - \vec{\mathbf{r}}_j$. We have further used the shorthands

$$\begin{aligned} \Pi_i^\pi &= \frac{1}{2} + \boldsymbol{\tau}_i, \\ \Pi_i^\nu &= \frac{1}{2} - \boldsymbol{\tau}_i \end{aligned}$$

for the projection operators for protons and neutrons. Note that we could use the expressions for the single-particle matrix elements of the reduced electric multipole operators of section 3.4 without need for modifications to evaluate the matrix elements of the reduced electric multipole operators in a relative basis, e.g., the relative HO basis.

In the following, we will often consider the isoscalar electric monopole, isovector electric dipole, and isoscalar electric quadrupole mode. The respective operators are obtained by applying the prescription for the isospin decomposition given in section 3.5 to (3.56), (3.58) and (3.60):

$$\mathbf{Q}_{00}^{\text{IS}} = \frac{1}{\sqrt{4\pi}} e \frac{1}{2A} \sum_{i>j=1}^A \vec{\mathbf{r}}_{ij}^2, \quad (3.62)$$

$$\mathbf{Q}_{10}^{\text{IV}} = e \frac{1}{A} \sum_{i>j=1}^A \left(\Pi_i^\pi \Pi_j^\pi - \Pi_i^\nu \Pi_j^\nu + \Pi_i^\pi \Pi_j^\nu - \Pi_i^\nu \Pi_j^\pi \right) |\vec{\mathbf{r}}_{ij}| Y_{10}(\vec{\boldsymbol{\omega}}_{ij}), \quad (3.63)$$

$$\mathbf{Q}_{20}^{\text{IS}} = e \frac{1}{2A} \sum_{i>j=1}^A \vec{\mathbf{r}}_{ij}^2 Y_{20}(\vec{\boldsymbol{\omega}}_{ij}). \quad (3.64)$$

In present applications, the operators are commonly used in the one-body form, where the coordinates in (3.22) and (3.23) are interpreted as single-particle coordinates in the

laboratory frame. As indicated in [Ste+05] and shown in appendix A.6, this approximation, however, yields correct results for the electric dipole and quadrupole operators if the basis used in the calculations factorizes exactly into relative and center-of-mass parts and if the center-of-mass component is in its ground state. This is guaranteed in the NCSM if the HO basis is used in combination with the N_{\max} truncation. We have further checked the error of using the isoscalar electric monopole operators in one-body form by comparing the $B(E0 : 0_1^+ \rightarrow 0_2^+)$ transition strengths in ^{16}O to results where the electromagnetic multipole operators have been treated correctly. The respective transition strengths, $0.585 e^2 \text{fm}^4$ and $0.520 e^2 \text{fm}^4$, have been calculated in the IT-NCSM with HO basis using the EMN400 interaction, SRG-evolved up to $\alpha = 0.08 \text{fm}^4$, for $N_{\max} = 8$ and $\hbar\Omega = 16 \text{MeV}$. Here, this approximation affects the result by about 10%, which is significant if one is interested in precision calculations. Therefore, the latter require, besides the inclusion of currents and a consistent treatment of the operators in the SRG, the use of the translationally invariant form of the electric monopole operator. In this thesis, we calculate electromagnetic observables from the respective operators in one-body form as we are mainly interested in strength distributions, where the absolute strength of the transitions is of minor importance.

4. Configuration-Interaction Methods

In a first approximation, the atomic nucleus can be described by its nucleons moving independently in an average potential. This picture is, however, too simplistic; correlations between the nucleons must be taken into account for a correct description of the nucleus. Therefore, a variety of CI methods has been developed, which have proven of value in the solution of the nuclear many-body eigenvalue problem. They all share the same simple concept but differ formally in the choice of the single-particle potential that defines the reference basis and the different truncation schemes applied. Particularly, the truncation scheme confines the applicability of the different variants to specific mass ranges of nuclei.

We first present the general concept of the CI method. We then restrict a detailed introduction to the CI approaches employed in this thesis, the VSSM and the NCSM. The VSSM assumes that a few valence nucleons on top of a fully-occupied closed shell are the only active degrees of freedom needed to obtain reasonable approximations for nuclear observables. This basis restriction allows for applications to medium-mass nuclei. The NCSM, in contrast, is an exact *ab initio* method that treats all nucleons as active degrees of freedom, and applications are limited to light nuclei.

4.1. General Concept

All CI approaches are based on the expansion of the eigenstates of the Hamiltonian \mathbf{H} in a basis of A -body Slater determinants $\{|\Phi_j\rangle\}$ spanning the Hilbert space:

$$|\Psi_n\rangle = \sum_j c_j^{(n)} |\Phi_j\rangle = \sum_j \langle \Phi_j | \Psi_n \rangle |\Phi_j\rangle. \quad (4.1)$$

The Slater determinants are constructed from single-particle states in some reference basis, e.g., the HO, HF, or natural-orbitals basis. These single-particle states have a spatial, spin, and isospin component. With (4.1), the eigenvalue problem

$$\mathbf{H} |\Psi_n\rangle = E_n |\Psi_n\rangle \quad (4.2)$$

can be written as

$$\sum_j \langle \Phi_i | \mathbf{H} | \Phi_j \rangle \langle \Phi_j | \Psi_n \rangle = E_n \langle \Phi_i | \Psi_n \rangle, \quad (4.3)$$

and the eigenvalues E_n and the coefficients $c_j^{(n)}$ of the energy eigenstates (4.1) are obtained by numerically calculating the eigenvalues and eigenvectors of the A -body Hamilton matrix with matrix elements $\langle \Phi_i | \mathbf{H} | \Phi_j \rangle$. One major advantage of CI methods is that energies of ground and excited states are treated on equal footing and that other observables

4. Configuration-Interaction Methods

can be calculated consistently. Once the eigenstates are determined, any observable of the nucleus under consideration can be computed by evaluating expectation values and matrix elements of the corresponding operator.

We can express the basis states $|\Phi_j\rangle$ as particle-hole excitations with respect to some reference determinant $|\Phi\rangle$ such that the expansion of the eigenstates (4.1) can alternatively be written as

$$|\Psi_n\rangle = c_n |\Phi\rangle + \sum_{a,p} c_{n,a}^p |\Phi_a^p\rangle + \sum_{\substack{a<b \\ p<q}} c_{n,ab}^{pq} |\Phi_{ab}^{pq}\rangle + \sum_{\substack{a<b<c \\ p<q<r}} c_{n,abc}^{pqr} |\Phi_{abc}^{pqr}\rangle + \dots \quad (4.4)$$

Here, the singly-excited basis states $|\Phi_a^p\rangle$ are generated by replacing the single-particle (hole) state a in the reference determinant $|\Phi\rangle$ by the single-particle (particle) state p not occupied in $|\Phi\rangle$. Basis states of higher particle-hole rank with respect to $|\Phi\rangle$ can be formed analogously. We remark that the restrictions on the summation indices ensure that each basis state is included in the sum only once. The reference determinant $|\Phi\rangle$ is usually chosen to be any of the lowest-possible configurations of the nucleus under consideration obtained in a mean-field picture and is, therefore, often referred to as unperturbed Slater determinant. For closed-shell nuclei, there is only one such configuration, the ground state.

In practice, we have to resort to finite bases by introducing truncations. To this aim, we typically restrict the number of HO single-particle orbits used to construct the many-body basis by introducing a maximum HO principal quantum number $l_{\max} = (2n + l)_{\max}$, and, optionally, an additional truncation l_{\max} on the single-particle orbital angular momentum. Such a truncated basis spans the model space \mathcal{M} . The energies obtained by diagonalizing the Hamilton matrix in a truncated space are no longer exact. They represent approximations to the exact energies, and we can check their quality by a systematic variation of the truncation.

One can show that the solution of the Schrödinger equation is equivalent to the determination of the stationary points in the method of linear variations [Rit09]. Consequently, the variational principle applies, and it is guaranteed that the energies represent upper bounds to the exact energies. The inclusion of more and more basis states in the model space, thus, causes the energy eigenvalues to drop monotonically. We expect convergence of energies and other observables for sufficiently large model spaces. We note that the variational principle is only fulfilled for the energies and that not all observables converge at the same rate as the energies with respect to model-space size.

However, even finite single-particle bases often render the CI method impractical because of the vast number of A -body basis states that can be constructed combinatorially from the single-particle states. Furthermore, numerical eigenvalue solutions of the Hamilton matrix are limited to linear dimensions of about 10^{10} when only a few low-lying eigenstates are calculated using sophisticated algorithms, e.g., the Lanczos algorithm [Lan50]. Consequently, additional truncation schemes need to be introduced that, in combination with the choice of single-particle basis, define the particular variants of CI suited for application to different nuclear mass regions.

As all many-body methods in nuclear structure theory, CI faces the challenge to properly describe a finite, self-bound system. Since the nucleus is not located in an external potential,

no natural reference point for the single-particle coordinates of the nucleons is available. The eigenstates $|\Psi_n\rangle$ depend on the coordinates and momenta of the A nucleons. For the description of the intrinsic properties of a nucleus, one needs the relative positions and momenta of the nucleons, i.e., $3A - 3$ coordinates and $3A - 3$ momenta. The redundant coordinates and momenta account for the motion of the center of mass. Since any intrinsic operator \mathbf{O} exhibits translational and Galilean invariance, it commutes with the center-of-mass momentum operator $\vec{\mathbf{P}}$ and the center-of-mass coordinate $\vec{\mathbf{R}}$. Thus, any physical operator \mathbf{O} , in particular the intrinsic nuclear Hamiltonian \mathbf{H}_{nucl} , and any operator acting solely on the center of mass of the nucleus possess a common eigenbasis, and the many-body eigenstate factorizes:

$$|\Psi_n\rangle = |\Psi_{n,\text{int}}\rangle \otimes |\Psi_{n,\text{cm}}\rangle. \quad (4.5)$$

The components $|\Psi_{n,\text{int}}\rangle$ and $|\Psi_{n,\text{cm}}\rangle$ depend only on relative and center-of-mass coordinates and momenta, respectively. When solving the eigenvalue problem for \mathbf{H}_{nucl} , eigenstates with the same intrinsic component $|\Psi_{n,\text{int}}\rangle$ but different center-of-mass component $|\Psi_{n,\text{cm}}\rangle$ are degenerate.

If the model space allows for the decoupling of intrinsic and center-of-mass components as in (4.5), the appearance of eigenstates with an excited center-of-mass component in the spectra can be avoided by solving the nuclear eigenvalue problem for the Hamiltonian

$$\mathbf{H} = \mathbf{H}_{\text{nucl}} + \beta \mathbf{H}_{\text{cm}} \quad (4.6)$$

composed of the intrinsic nuclear Hamiltonian \mathbf{H}_{nucl} and a Hamiltonian \mathbf{H}_{cm} acting exclusively on the nucleus' center of mass. The use of this modified Hamiltonian dates back to Gloeckner and Lawson [GL74], however, unlike initially proposed, we choose finite values for the control parameter β . This procedure leaves the intrinsic properties of the eigenstates unchanged but confines the center-of-mass components to a specific state. When using the HO single-particle basis, the center-of-mass Hamiltonian is an HO potential:

$$\mathbf{H}_{\text{cm}} = \frac{\mathbf{P}^2}{2Am} + \frac{m\Omega^2 A}{2} \mathbf{R}^2 - \frac{3}{2} \hbar \Omega. \quad (4.7)$$

Here, m and $\hbar\Omega$ denote the nucleon mass and HO frequency, respectively. The last term shifts the ground-state energy of \mathbf{H}_{cm} to zero. By solving the eigenvalue problem using the Hamiltonian (4.6) with $\beta > 0$, the degeneracy of the intrinsic states with respect to their center-of-mass component is lifted. Center-of-mass excitations are pushed upward in energy and are removed from the relevant part of the spectrum.

We remark that truncated model spaces allow for an exact decoupling of intrinsic and center-of-mass components only if the HO basis is used in combination with the N_{max} truncation, cf. section 4.3. In all other cases, the eigenstates may contain mixtures of intrinsic and center-of-mass components. Such eigenstates are denoted as spurious or center-of-mass contaminated states, and the above prescription can be applied only as an approximation.

The starting point of CI calculations is the nuclear Hamiltonian

$$\mathbf{H}_{\text{nucl}} = \mathbf{H}_{0\text{B}} + \mathbf{H}_{1\text{B}} + \mathbf{H}_{2\text{B}} + \mathbf{H}_{3\text{B}}, \quad (4.8)$$

where we consider zero-, one-, two-, and three-body operators at most. Depending on the CI variant, some of them vanish from the outset or are neglected.

4.2. Valence-Space Shell Model

The VSSM [KB66; Cau+05; Cor+14] is the pioneering CI method in nuclear physics. Recently, it has gained renewed interest as methods have become available that derive effective valence-space Hamiltonians and operators in an *ab initio* framework [TBS12; Bog+14; Jan+14; Dik+15; Jan+16; Str+16; Str+17; Par+17; Sim+17].

Originally, the VSSM has been motivated by the success of the naive shell model, which approximates the nucleus by a system of A nucleons confined in a single-particle potential in combination with a spin-orbit term [May49; HJS49]. The single-particle orbits $0s_{1/2}$, $0p_{3/2}$, $0p_{1/2}$, \dots are grouped in shells according to their single-particle energy in such a way that energy differences between orbits within one shell are much smaller than energy differences between orbits of two different shells. The spin-orbit term causes a lowering in energy of orbits with large coupled total angular momentum $j = l + 1/2$, e.g., $0f_{7/2}$ and $0g_{7/2}$ in figure 4.1, and gives rise to shell closures that reproduce the experimentally observed magic numbers 2, 8, 20, 28, 50, 82, and 126. Nuclei with magic neutron and proton numbers are especially stable. In absence of the mutual interaction, all nucleons occupy the lowest single-particle orbits allowed according to the Pauli principle up to a shell gap at a magic number, and excitations are only possible if one or more nucleons are excited to a higher shell.

The VSSM is based on the classification of a core, valence, and excluded space, often separated by a shell gap. The core is composed of fully-occupied shells, which can be different for protons and neutrons, and has total angular momentum and parity $J^\pi = 0^+$. The nucleons of the core are considered to be inert; they are not considered explicitly in VSSM calculations. The only active degrees of freedom are the valence nucleons, which are restricted to one or a few (sub-)shells above the core. The explicit form of their wave functions is not known. We identify the *ls*-coupled single-particle states of the valence nucleons by the set of quantum numbers (n, l, j, m, τ) , where we omit the trivial quantum numbers spin $s = 1/2$ and isospin $t = 1/2$. The quantum numbers m and τ represent the z -projection of the total angular momentum and the isospin, respectively. Single-particle orbits with higher single-particle energy than the valence orbits belong to the excluded space.

The restrictions assumed in the single-particle basis, i.e., the omission of excitations of core nucleons to arbitrary orbits or excitations of valence nucleons to the excluded space, as well as interactions between core and valence nucleons, are accounted for implicitly by the effective valence-space Hamiltonian. This Hamiltonian is, thus, a crucial input for VSSM calculations and has, generally, the form (4.8). The zero-body term represents the energy of the core. When using phenomenological interactions, it is typically set to the experimental binding energy of the corresponding nucleus. For valence-space Hamiltonians derived in an *ab initio* approach, the zero-body term is determined consistently along with the interaction matrix elements. All observables calculated in the VSSM are defined relative to the core. The operators \mathbf{H}_{1B} and \mathbf{H}_{2B} provide the single-particle energies and the

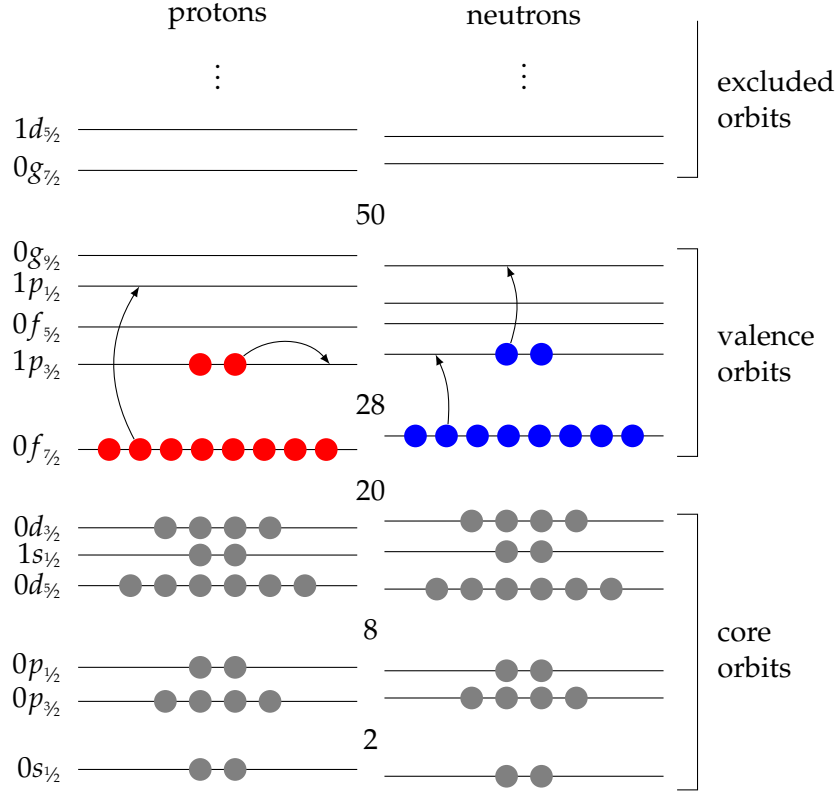


Figure 4.1.: Schematic representation of single-particle orbits and magic numbers for protons and neutrons in a shell-model potential. The basis generation from the unperturbed Slater determinant is illustrated for ^{60}Zn in a valence space comprising the orbits $0f_{7/2}$, $1p_{3/2}$, $0f_{5/2}$, $1p_{1/2}$, and $0g_{7/2}$. See text for details.

effective one- and two-body interaction of the valence nucleons. At present, shell-model calculations including explicit three-body terms in the Hamiltonian are not available.

The model space is spanned by m -scheme Slater determinants $\{|\Phi_{j,\text{val}}\rangle\}$ built from the single-particle states of the A_v valence nucleons. We can write the corresponding A -body basis state as

$$|\Phi_j\rangle = |\Phi_{j,\text{core}}\rangle \otimes |\Phi_{j,\text{val}}\rangle, \quad (4.9)$$

where the core component $|\Phi_{j,\text{core}}\rangle$ is identical for all configurations. As it is not taken into account explicitly in shell-model calculations, we only consider the valence-space component $|\Phi_{j,\text{val}}\rangle$ of the Slater determinants and define the VSSM results relative to the core. In the following, we drop the subscript 'val'. Furthermore, since the nuclear Hamiltonian is not sensitive to the z -projection of the single-particle states, we restrict the model space to basis states with conserved quantum numbers $M = \sum_{j=1}^{A_v} m_j$, parity π and $M_T = \sum_{j=1}^{A_v} \tau_j$. Working in the m -scheme allows for a straightforward definition

of many-body operators in terms of second quantization, which makes the evaluation of matrix elements convenient.

Model-space dimensions increase rapidly when heavier nuclei are considered or more single-particle orbits are included in the valence space, and shell-model calculations become intractable. In standard shell-model calculations, the so-called T_{\max} truncation is introduced to cope with this problem. Each configuration has an assigned value t which denotes the number of nucleons in previously unoccupied orbits. In the T_{\max} -truncated model space, we only include basis states with $t \leq T_{\max}$.

In figure 4.1, we illustrate the core, valence, and excluded space for a single-particle potential that is different for protons and neutrons. In this example, we consider ^{60}Zn , where 20 protons and 20 neutrons form the ^{40}Ca core and 10 protons and 10 neutrons occupy the valence orbits $0f_{7/2}$, $1p_{3/2}$, $0f_{5/2}$, $1p_{1/2}$ and $0g_{7/2}$. The basis states can be generated from the unperturbed Slater determinant by particle-hole excitations. The configuration resulting from the unperturbed Slater determinant by replacing single-particle states as indicated by the arrows represents a $t = 2$ configuration. One proton and one neutron are excited to valence orbits which are not occupied in the unperturbed configuration, each contributing with $t = 1$. Arbitrary redistributions of nucleons within the orbits occupied by the reference determinant do not change t .

The structure of the basis states (4.9) implies that the eigenstates do not factorize into relative and center-of-mass parts whenever more than one major HO shell is employed as valence space. Only if an $N_{\max} = 0$ model space is used, where all nucleons occupy the lowest possible HO levels, the nucleus' center of mass is guaranteed to be in its ground state and a decoupling of relative and center-of-mass components is achieved. Furthermore, the nuclear Hamiltonian is not translationally invariant. Thus, the action of the nuclear Hamiltonian on an eigenstate of the nucleus also affects the center-of-mass component, which, in return, can cause a change in the energies. There is no exact solution for the decoupling of relative and center-of-mass components in the VSSM. Nevertheless, we solve the eigenvalue problem for the Hamiltonian (4.6), where we choose fairly small values for β , e.g., $\beta = 1$ [Whi+77]. In this way, eigenstates with large spurious component are artificially shifted to higher energies while non-spurious ones are left relatively unchanged. It is expected that most of the mixing of relative and center-of-mass components can be removed in this way.

The center-of-mass Hamiltonian (4.7) can be expressed in terms of core and valence nucleons for the use in the VSSM:

$$\begin{aligned} \mathbf{H}_{\text{cm}} = & \frac{N_c}{A} \left(\frac{1}{2N_c m} \bar{\mathbf{p}}_c^2 + \frac{1}{2} m \Omega^2 N_c \bar{\mathbf{r}}_c^2 \right) \\ & + \sum_{v=N_c+1}^A \left(\frac{\mathbf{p}_v^2}{2m} + \frac{m \Omega^2}{2} \mathbf{r}_v^2 \right) \\ & + \frac{A_v}{A} \sum_{c=1}^{N_c} \left(\frac{\bar{\mathbf{p}}_c^2}{2m} + \frac{m \Omega^2}{2} \bar{\mathbf{r}}_c^2 \right) \\ & - \frac{1}{A} \sum_{c=1}^{N_c} \sum_{v=N_c+1}^A \left(\frac{1}{2m} (\bar{\mathbf{p}}_c - \bar{\mathbf{p}}_v)^2 + \frac{m \Omega^2}{2} (\bar{\mathbf{r}}_c - \bar{\mathbf{r}}_v)^2 \right) \end{aligned}$$

$$\begin{aligned}
& - \frac{1}{A} \sum_{v>v'=N_c+1}^A \left(\frac{1}{2m} (\vec{p}_v - \vec{p}_{v'})^2 + \frac{m\Omega^2}{2} (\vec{r}_v - \vec{r}_{v'})^2 \right) \\
& - \frac{3}{2} \hbar\Omega.
\end{aligned} \tag{4.10}$$

Here, the indices c, c' and v, v' refer to core and valence nucleons, respectively. The sum over core indices is over the N_c core nucleons and the sum over valence nucleons is over the remaining $A_v = A - N_c$ nucleons. The first term of (4.10) corresponds to the HO potential. The third term is a sum over HO potentials of the single-particle states of the core nucleons. These terms and the last term of (4.10) can be classified as zero-body terms because they involve no or only core nucleons and are constant. The second and fourth term represent one-body operators, where the latter can be identified with an effective interaction of the valence nucleons with the core. The fifth term constitutes a two-body operator acting between the valence nucleons.

4.3. No-Core Shell Model

The NCSM [NVB00a; NVB00b; NKB00; NO02; NO03; Nav+09; BNV13] has been introduced as a method for the exact solution of the nuclear many-body problem, where all A nucleons are treated as active degrees of freedom. Two equivalent formulations exist; one uses antisymmetrized HO Jacobi states and the other Slater determinants as many-body basis states. The latter has proven to be more efficient for nuclear systems with $A \gtrsim 4$. Possible choices for the reference basis are, e.g., the HO, HF, Woods-Saxon, or natural-orbital single-particle basis. The combination of choice of reference basis and truncation scheme gives rise to a variety of NCSM approaches. Their performance differs, e.g., in the convergence behavior with respect to model-space size.

The starting point of the NCSM is a Hamiltonian of the form (4.8) containing the kinetic energy and the interactions between the nucleons up to the three-body level. In order to remove states with excited center-of-mass component from the relevant part of the spectrum, we use the modified Hamiltonian (4.6) for the solution of the eigenvalue problem. We recall that this approach is exact in the NCSM with HO basis and N_{\max} truncation, which allows for a factorization of relative and center-of-mass components, and it is used as an approximation otherwise.

In this thesis, we mainly employ the NCSM using the HO and HF basis. In the following, we present the two variants and discuss some differences.

No-Core Shell Model with Harmonic Oscillator Basis

Traditionally, the NCSM employs the HO single-particle basis $\{|nljm\tau\rangle\}$ as reference basis, where the angular momentum and spin is coupled to total angular momentum j with projection m . The energy of the single-particle states is given by

$$\epsilon(n, l) = \left(2n + l + \frac{3}{2} \right) \hbar\Omega, \tag{4.11}$$

4. Configuration-Interaction Methods

and the convention for the quantum numbers is

$$n = 0, 1, 2, \dots, \quad (4.12a)$$

$$e = 2n + l = 0, 1, 2, \dots \quad (4.12b)$$

From these single-particle states, we build A -body m -scheme Slater determinants with conserved quantum numbers $M = \sum_{j=1}^A m_j$, parity π , and $M_T = \sum_{j=1}^A \tau_j$. This allows us to apply the powerful second-quantization technique to many-body operators for the evaluation of matrix elements.

In order to restrict the model space to a manageable size, we introduce the N_{\max} truncation and include only those many-body basis states in the model space with a maximum HO excitation energy above the unperturbed Slater determinant:

$$\sum_{j=1}^A (\epsilon_j - \epsilon_{0,j}) = \sum_{j=1}^A (e_j - e_{0,j}) \hbar\Omega \leq N_{\max} \hbar\Omega. \quad (4.13)$$

Here, the sum is over the single-particle energies of the A nucleons defining a basis Slater determinant relative to the unperturbed Slater determinant with energy $\sum_{j=1}^A \epsilon_{0,j}$.

In figure 4.2, we show the single-particle orbits of the HO potential with principal quantum number e . The stiffness of the HO potential is controlled by the basis parameter $\hbar\Omega$. We consider the basis generation for ^{18}O starting from a reference determinant, where the neutrons are in one of the degenerate lowest possible configurations. By promoting protons and neutrons from this unperturbed configuration to other single-particle states, the model space can be built systematically. The excitation of, e.g., one proton from the $e = 1$ orbit to the $e = 5$ orbit as indicated by the arrow, yields a new basis state with $4\hbar\Omega$ excitation energy compared to the unperturbed configuration. If we additionally consider one proton from the $e = 0$ orbit and one neutron from the $e = 1$ orbit to be excited to the $e = 3$ and $e = 4$ orbit, respectively, the resulting basis state has a total excitation energy of $10\hbar\Omega$ compared to the unperturbed configuration. Such a basis state is contained in the model space for truncation parameters $N_{\max} \geq 10$.

The combination of Slater determinants constructed from HO single-particle states with the N_{\max} truncation is a very convenient choice of many-body basis as it retains the translational invariance of the Hamiltonian and, thus, ensures the exact factorization of the eigenstates (4.5). Consequently, the use of (4.6) for finite values of β removes eigenstates with excited center-of-mass components from the relevant low-lying part of the spectrum. We remark that, in general, the oscillator frequency of the center-of-mass Hamiltonian and the HO single-particle potential must not necessarily be chosen equal.

In practice, convergence of observables with respect to model-space size is often not reached due to computational limitations. Therefore, we carry out NCSM calculations for a series of N_{\max} values and use extrapolations to obtain estimates for the observables in the infinite model space. Various extrapolation techniques [Coo+12; FHP12; Mor+13; Rot+14] are available that yield robust approximations. In particular for absolute energies, where the variational principle applies, we typically use decreasing exponential functions to extrapolate to $N_{\max} \rightarrow \infty$. Furthermore, converged results for observables are independent of the oscillator frequency $\hbar\Omega$. In order to obtain the best approximation to the exact result,

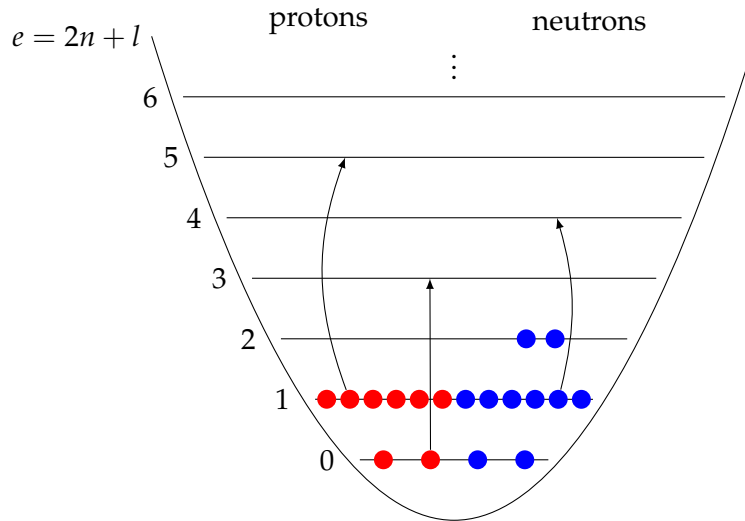


Figure 4.2.: Single-particle orbits of the HO potential. The basis generation in the NCSM from the unperturbed Slater determinant is illustrated for ^{18}O . See text for details.

we need to increase N_{max} until the observable shows a flat trend as a function of $\hbar\Omega$. In practice, we often choose an optimal value for $\hbar\Omega$ such that the energy is minimized.

We remark that the HO single-particle states exhibit a Gaussian fall-off. This wrong asymptotic behavior causes long-range observables to converge extremely slowly. Therefore, the description of loosely bound systems, such as halo nuclei, is problematic. A possible remedy is the use of a different basis set which is better suited for the description of long-range observables, e.g., the HF or Woods-Saxon basis.

Furthermore, the NCSM does not include continuum degrees of freedom, which are essential for the description of resonances and continuum states. Improvements regarding this issue are possible via extensions of the NCSM, e.g., by an explicit inclusion of continuum physics in the NCSM, as implemented in the NCSM with continuum (NCSMC) [BNQ13; Cal+16], or by resorting to another reference basis that implicitly includes continuum degrees of freedom, e.g., the Berggren basis [Ber68; Pap+13].

No-Core Shell Model with Hartree-Fock Basis

More recently, the HF basis has been employed in the context of the NCSM [Geb+17]. The motivation for using the HF basis as reference basis is that the HF potential already incorporates a part of the relevant physics for the given nucleus and that the correct asymptotic behavior of the single-particle wave functions, which fall off exponentially, improves convergence of long-range observables.

We start from a nucleus-dependent single-particle potential generated in an HF calculation in equal-filling approximation [PR08]. The ls -coupled single-particle states carry quantum numbers (n, l, j, m, τ) . An overview of the HF method is given in appendix B.

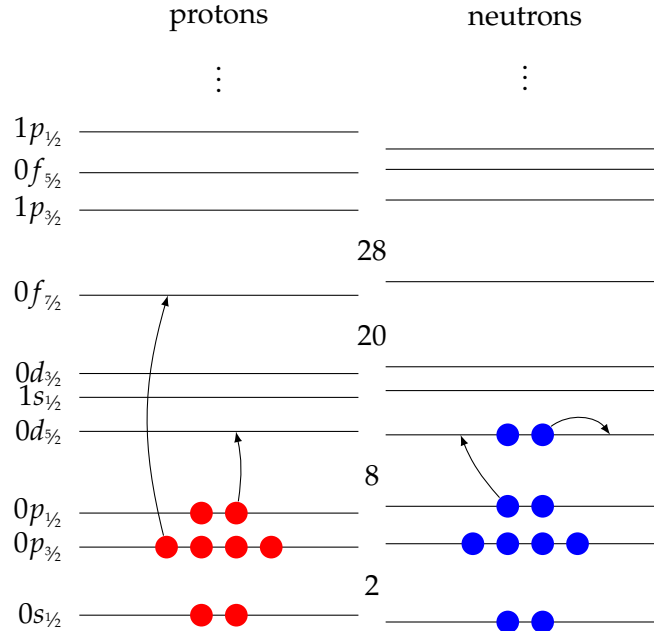


Figure 4.3.: Schematic representation of single-particle orbits of an HF potential for ^{18}O . The basis generation from the unperturbed Slater determinant is illustrated. See text for details.

Although a finite HF basis breaks translational invariance (4.8), we add the Lawson-type term $\beta\mathbf{H}_{\text{cm}}$ to the nuclear Hamiltonian for the numerical solution of the eigenvalue problem as an approximate remedy to the center-of-mass problem. In practice, we often apply the NO2B approximation to the Hamiltonian (4.8), which further introduces an explicit dependence on center-of-mass coordinates.

The many-body basis is constructed in the same way as in the NCSM with HO basis, however, we employ two many-body truncation schemes. We routinely use the N_{max} truncation (4.13) as introduced for the NCSM. To this aim, we associate each HF orbit with quantum numbers (n, l, j) with the HO orbit with $e = 2n + l$. The example in figure 4.3 for ^{18}O illustrates the basis generation from the unperturbed Slater determinant. The configuration shown in the example is contained in the N_{max} -truncated model space for $N_{\text{max}} \geq 4$.

For some benchmark calculations, we restrict the number of particle-hole excitations from the unperturbed HF Slater determinant. We use the T_{max} truncation as introduced in the VSSM and allow at most T_{max} nucleons to be excited to previously unoccupied orbits. Redistributions of nucleons within the orbits populated by the unperturbed Slater determinant contribute with $t = 0$. Therefore, the example for ^{18}O shown in figure 4.3

yields, in total, a $t = 2$ configuration driven by the protons only.

Although the convergence of absolute energies with N_{\max} seems to be worse in the NCSM when an HF basis is used, excitation energies are stable and practically independent of $\hbar\Omega$.

Recently, a similar approach, where a natural-orbital single-particle basis derived to better match the physical structure of the many-body wave function was used in the NCSM. It has been applied successfully to the halo nucleus ${}^6\text{He}$ and has demonstrated improved convergence properties compared to the NCSM using the HO basis [Con+17].

4.4. Computational Limitation

From a computational point of view, the nuclear eigenvalue problem represents a large-scale eigenvalue problem of a sparse matrix. It is particularly challenging because of the strong interaction, where many-nucleon forces are important. Furthermore, collective phenomena play a crucial role in nuclear physics. Therefore, results close to converged with respect to model-space truncations—prerequisite for reliable extrapolations—are, in general, only obtained for extremely large model spaces.

If we start from an e_{\max} -truncated single-particle basis, the m -scheme model-space dimension d of a nucleus is proportional to

$$\binom{n_N}{N} \binom{n_Z}{Z},$$

where N (Z) denotes the number of neutrons (protons) that can be distributed among n_N (n_Z) neutron (proton) single-particle states. This dimension is reduced by about one order of magnitude by imposing constraints on the quantum numbers of the eigenstates. Furthermore, the many-body truncation parameters T_{\max} and N_{\max} are applied and control the model-space dimensions. In the VSSM, the number of neutron and proton single-particle states is relatively small, e.g., $n_N = n_Z = 32$ in the $sdpf$ shell, and the model-space dimension becomes maximal at mid-shell, where $N_v = n_N/2$ and $Z_v = n_Z/2$. In contrary, the NCSM with single-particle truncation $e_{\max} = 12$ provides already 910 neutron and 910 proton single-particle states to construct the many-body basis from. This illustrates why heavy nuclei, such as ${}^{208}\text{Pb}$, will remain unfeasible in the NCSM also in the future, albeit the additional many-body truncations.

Figure 4.4 shows model-space dimensions of VSSM calculations in the $sdpf$ shell for several silicon isotopes and of NCSM calculations for even- A oxygen isotopes as a function of the truncation parameters T_{\max} and N_{\max} , respectively. In the VSSM, the model-space dimension of a nucleus typically saturates for $T_{\max} \gtrsim 8$ for isotopes not too close to the shell closures limiting the valence space and reaches its maximum for isotopes around mid-shell. The NCSM exhibits a factorial growth of the basis dimension with N_{\max} and mass number $A = N + Z$. Considering that we, typically, need to choose the model-space truncation parameter N_{\max} not smaller than 8 to 10 [BNV13] to reasonably extrapolate the energies, figure 4.4 illustrates why heavier systems rapidly reach the present computational limits and, thus, become prohibitive. The most challenging diagonalizations have been carried out for nuclei in model spaces comprising around 10^{10} basis states [Len+10; BNV13]. We

4. Configuration-Interaction Methods

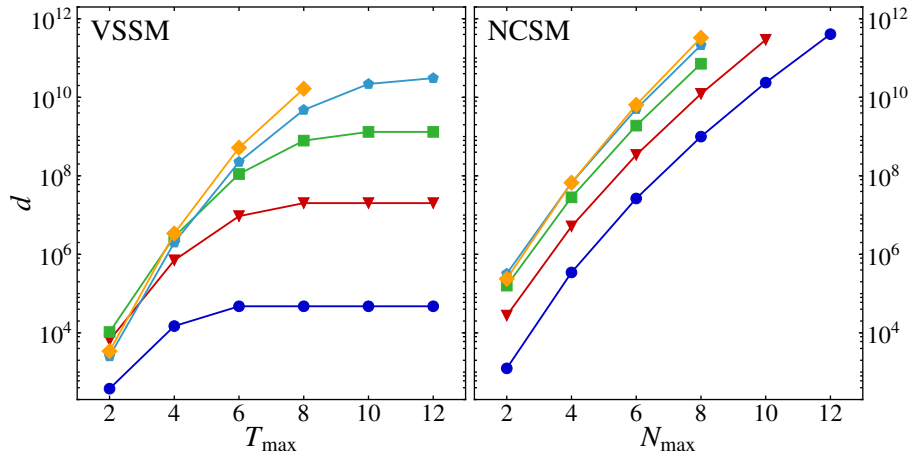


Figure 4.4.: Model-space dimensions of the silicon isotopes ^{22}Si (\bullet), ^{24}Si (\blacktriangledown), ^{26}Si (\blacksquare), ^{28}Si (\blacklozenge), and ^{30}Si (\blacklozenge) in the VSSM ($sdpf$ shell) as a function of T_{\max} and of the oxygen isotopes ^{16}O (\bullet), ^{18}O (\blacktriangledown), ^{20}O (\blacksquare), ^{22}O (\blacklozenge), and ^{24}O (\blacklozenge) in the NCSM as a function of N_{\max} .

routinely carry out CI calculations with model-space dimensions of the order of 10^8 using two-body interactions or 10^7 when also three-body interactions are taken into account.

The bottle neck of CI calculations is the number of non-zero matrix elements of the A -body Hamilton matrix, which governs the computational cost of their calculation and storage, as well as the numerical solution of the eigenvalue problem. Even though we are dealing with sparse matrices and only store non-zero matrix elements, we typically need terabytes of memory for the Hamilton matrix. We remark that the inclusion of three-body interactions significantly increases the number of non-zero matrix elements compared to CI calculations using only two-body interactions, and, thus, pushes storage demands. In practice, we use massively parallelized codes capable of distributing the matrix elements on several nodes and, potentially, on disc. We employ the sophisticated implicitly restarted Arnoldi algorithm [LSY98] for the matrix diagonalization, which requires some additional memory for the vectors. We note that an alternative to keeping all matrix elements in memory is their on-the-fly recalculation [JOK13], which, however, tremendously increases computing times. Although enormous advances in computer technology have been made (see [BNV13, appendix] for a brief overview) and further development is ongoing, many nuclei remain out of reach of present and future investigations using standard CI approaches.

5. Importance-Truncated Configuration-Interaction Methods

In order to overcome the limitations of the CI methods of chapter 4, we propose an importance-truncation scheme, which has been applied successfully to the NCSM [RN07; Rot09] for some time, and recently to the VSSM [SBR16]. The importance truncation is a physics-driven, adaptive truncation criterion for the many-body model space based on a measure for the importance of individual basis states for the description of a few target eigenstates of a given Hamiltonian. We impose a threshold on this importance measure to define the importance-truncated model space tailored to the specific set of eigenstates and the Hamiltonian. Variations of the importance threshold can be used to extract observables in the limit of the full model space. Together, importance truncation and extrapolation provide an accurate and efficient tool for nuclei and model spaces beyond the reach of standard CI calculations.

We first introduce the concept of importance truncation and define the importance measure. Then, we present the implementation of the importance-truncation selection procedure via an iterative scheme. Sections 5.2 and 5.3 are devoted to extrapolation methods that correct the observables for effects of excluded basis states and approximate the results in the limit of vanishing thresholds.

5.1. Importance Truncation

For the solution of the nuclear eigenvalue problem (4.2) of a Hamiltonian H in large-scale model spaces, CI methods are routinely used. Systematic model-space truncation schemes exist, both, on the single-particle and many-body level (see chapter 4 for details); however, they are not motivated by the physical features of the specific system provided by the Hamiltonian. We refer to such globally truncated model spaces as full model spaces. The importance truncation is based on the observation that—if one is interested in only a few eigenstates of a Hamiltonian—a large fraction of the basis states $\{|\Phi_j\rangle\}$ contributes only with very small or vanishing amplitudes $c_j^{(n)}$ to the basis expansion of the target eigenstates

$$|\Psi_n\rangle = \sum_{j=1}^d c_j^{(n)} |\Phi_j\rangle. \quad (5.1)$$

Here, d denotes the full m -scheme dimension of the model space. The idea of the importance truncation is to identify and select the important basis states for the basis expansion (5.1) without solving the eigenvalue problem in the full model space. For this purpose, we

introduce an importance measure derived in multi-configurational perturbation theory (MCPT) [SO96] to assess the relevance of the individual basis states for the description of a target eigenstate using the information provided by the Hamiltonian: We estimate the amplitudes $c_j^{(n)}$ in (5.1) by means of the first-order perturbative correction to an initial approximation of the respective target state. We impose an importance threshold to decide whether or not a basis state is included in the importance-truncated model space based on its importance measure. The thus constructed model space is, therefore, tailored to the description of a set of target eigenstates. The solution of the eigenvalue problem in the importance-truncated model space requires the calculation and diagonalization of the Hamilton matrix in a model space with typically much smaller dimension than the full model space, while the observables calculated from the eigenstates remain almost unchanged. The quality of the eigenstates can be controlled by variation of the importance threshold. In the limit of vanishing importance threshold, the results in the full model space are recovered.

Importance Measure

The construction of the importance-truncated model space is based on a set of reference states

$$|\Psi_{\text{ref}}^{(n)}\rangle = \sum_{j \in \mathcal{M}_{\text{ref}}} c_{j,\text{ref}}^{(n)} |\Phi_j\rangle, \quad (5.2)$$

which represent initial approximations of the target eigenstates carrying the correct quantum numbers. They are obtained from a previous diagonalization in a small space. The basis states that contribute to the reference states span the reference space \mathcal{M}_{ref} . We estimate the importance of basis states outside \mathcal{M}_{ref} for the target eigenstates by means of the amplitudes

$$\begin{aligned} \kappa_j^{(n)} &= -\frac{\langle \Phi_j | \mathbf{H} | \Psi_{\text{ref}}^{(n)} \rangle}{\Delta \epsilon_j} \\ &= \sum_{i \in \mathcal{M}_{\text{ref}}} c_{i,\text{ref}}^{(n)} \frac{\langle \Phi_j | \mathbf{H} | \Phi_i \rangle}{\Delta \epsilon_j} \end{aligned} \quad (5.3)$$

of the first-order perturbative correction to $|\Psi_{\text{ref}}^{(n)}\rangle$. We use the simple Møller-Plesset-type formulation of MCPT, where the energy denominator $\Delta \epsilon_j$ corresponds to the excitation energy of the basis state $|\Phi_j\rangle$ calculated from the unperturbed single-particle energies of the nucleons. A brief overview of MCPT and the derivation of the importance measure is given in appendix C. Only basis states with an absolute value of the importance measure larger than a given importance threshold, i.e.,

$$|\kappa_j^{(n)}| \geq \kappa_{\text{min}},$$

for at least one reference state $|\Psi_{\text{ref}}^{(n)}\rangle$ are included in the importance-truncated model space \mathcal{M}_{IT} . As a result, we obtain an importance-truncated model space tailored to the simultaneous description of all target eigenstates.

We note that an importance measure defined in this way assesses the relevance of basis states for the basis expansion of the eigenstates, which, in turn, can be used to calculate any observable. This choice of importance measure is not biased with respect to a specific observable; however, some observables might be more sensitive to small components of the wave function. This manifests itself in a slow convergence behavior with the model-space truncation.

Alternative importance measures can be derived, e.g., from the second-order energy correction in MCPT:

$$\zeta_j = -\frac{\left| \langle \Phi_j | \mathbf{H} | \Psi_{\text{ref}}^{(n)} \rangle \right|^2}{\Delta \epsilon_j}. \quad (5.4)$$

This definition of importance measure assesses the relevance of the basis states outside \mathcal{M}_{ref} for the computation of the energy.

Both importance measures yield similar results for the energies [Rot09]. Since we are interested in an optimum description of the eigenstates, we employ the simple first-order importance measure (5.3) in standard applications.

We note that this importance measure cannot probe basis states that differ by more than two-particle two-hole (2p2h) (three-particle three-hole (3p3h)) excitations from any state in \mathcal{M}_{ref} if the Hamiltonian consists of up to two-body (three-body) operators. One possibility to access particle-hole excitations of higher particle rank is to consider amplitudes of perturbative state corrections of higher order. Fortunately, it is possible to avoid their computationally demanding evaluation by embedding the construction of the importance-truncated model space into an iterative scheme.

Iterative Model-Space Construction

We adopt a universal iterative scheme to extend the reference space to arbitrary $npnh$ excitations. In the NCSM, we can, e.g., start from a model space truncated at $N_{\text{max}} = 0$. All Slater determinants with nucleons distributed in the lowest accessible orbits are in this model space. For $N_{\text{max}} = 2$, up to two nucleons are promoted to higher-lying orbits—this model space can be generated through one-particle one-hole (1p1h) and 2p2h excitations on top of the $N_{\text{max}} = 0$ space. In the same way, a $T_{\text{max}} = 2$ model space can be generated in the VSSM or NCSM by systematically creating all 1p1h and 2p2h excitations on top of a $T_{\text{max}} = 0$ space. It is, thus, possible to combine a sequential increase of the truncation parameter with the importance-selection procedure [Rot09; SBR16]. This scheme is general and can be applied to the CI methods introduced in chapter 4 with T_{max} or N_{max} truncations. In the following, we explain the procedure exemplarily for the IT-NCSM with N_{max} truncation.

A complete IT-NCSM calculation typically proceeds as follows: We start with a conventional NCSM calculation for small N_{max} , e.g., $N_{\text{max}} = 2$, and select a set of target eigenstates. We define the reference states by filtering the important components of these eigenstates through a so-called reference threshold C_{min} with respect to the amplitudes

from the NCSM calculation:

$$|\Psi_{\text{ref}}^{(n)}\rangle = \mathcal{N}_{\text{ref}}^{(n)} \sum_{j \in \mathcal{M}_{\text{ref}}}^{|c_{j,\text{ref}}^{(n)}| \geq C_{\text{min}}} c_{j,\text{ref}}^{(n)} |\Phi_j\rangle. \quad (5.5)$$

Here, the factor $\mathcal{N}_{\text{ref}}^{(n)}$ ensures the norm of the reference states. We note that the reference threshold is of pure technical purpose. It can typically be chosen an order of magnitude larger than the importance measure without affecting the results; however, it accelerates the evaluation of the importance measure significantly. Starting from these reference states, we construct importance-truncated model spaces with $N_{\text{max}} = 4$ for a sequence of importance thresholds by generating 1p1h and 2p2h excitations on top of the reference space and probing them against the importance thresholds. In each space $\mathcal{M}_{\text{IT}}(\kappa_{\text{min}})$, we solve the eigenvalue problem and compute the relevant observables. The eigenvectors for the largest importance-truncated model space define the new reference states, again imposing the reference threshold C_{min} , for constructing the importance-truncated model spaces with $N_{\text{max}} = 6$. The previous steps are repeated until the desired N_{max} is reached. The basis states are reassessed in each iteration with respect to their relevance for the description of the target eigenstates using the most recent reference states. In this way, the coupling of basis states with few $npnh$ excitations to basis states with higher orders of $npnh$ excitations is established in the importance-truncated model space. In the limit $(\kappa_{\text{min}}, C_{\text{min}}) \rightarrow 0$, the algorithm is guaranteed to reproduce the results corresponding to the full model space at each N_{max} . This provides the possibility to carry out extrapolations to vanishing thresholds.

Analogously, we can apply the T_{max} truncation instead of the N_{max} truncation in the IT-NCSM, or we can transfer the procedure to the IT-VSSM, where the iteration can be carried out until T_{max} reaches the number of valence nucleons.

In practice, we always generate importance-truncated model spaces for various importance thresholds. In order to minimize the computational cost, we employ a filtering method: We construct \mathcal{M}_{IT} for the smallest importance threshold of the sequence and solve the eigenvalue problem in this space. The importance-truncated model space corresponding to the next-larger importance threshold is obtained from the previous one by removing the basis states with importance measure smaller than the new importance threshold. After deleting the rows and columns of the Hamilton matrix associated with these discarded basis states, the eigenvalue problem is solved again. This procedure is repeated until the eigenvalue problem has been solved in the importance-truncated model space corresponding to the largest importance threshold of the sequence. In this way, we carry out the computationally demanding and time-consuming construction of the importance-truncated model space and Hamilton matrix only once per κ_{min} sequence.

5.2. Threshold Dependence and Threshold Extrapolation

The variation of the importance threshold probes the quality of the importance truncation, and it provides the basis for extrapolations, which approximately correct the observables for effects of excluded basis states. We note that the importance truncation represents

a strictly variational approach. The energies are determined by solving the eigenvalue problem in a reduced model space, where, for each eigenstate, the smallest eigenvalue provides an upper bound for the exact energy. Furthermore, the Hylleraas-Undheim theorem [HU30] applies, i.e., the energies of all states are guaranteed to drop monotonically with decreasing κ_{\min} and reach their exact values in the limit of the full model space:

$$E_{n,\text{exact}} \leq E_n(\kappa_{\min}) \leq E_n(\kappa'_{\min}) \text{ for } \kappa_{\min} < \kappa'_{\min}. \quad (5.6)$$

Since the full model space is recovered in the limit of vanishing thresholds, i.e., $\kappa_{\min} \rightarrow 0$ and $C_{\min} \rightarrow 0$, extrapolations to $\kappa_{\min} \rightarrow 0$ are used to approximate the result in the full model space. We note that no such rule exists for other observables. In the following, we illustrate the threshold dependence and extrapolation in the IT-NCSM and IT-VSSM for energies and electromagnetic observables.

For the benchmark of the IT-NCSM, we consider ^{12}C in an $N_{\max} = 8$ model space, for which full NCSM results are available [Mar+14]. We employ the chiral two- and three-body interaction EMN500, SRG-evolved up to $\alpha = 0.0625 \text{ fm}^4$, and an HO frequency $\hbar\Omega = 20 \text{ MeV}$. The full m -scheme dimension of the model space is $5.94 \cdot 10^8$. Such an NCSM calculation is computationally demanding, in particular, when three-body interactions are included. Note that an HO single-particle basis is used in the IT-NCSM here.

As test case of the IT-VSSM, we consider ^{56}Ni in a pf valence space using the phenomenological GXPF1A Hamiltonian [Hon+05]. The full m -scheme dimension is $1.09 \cdot 10^9$, which is at the limit of routine VSSM calculations.

Figure 5.1 shows the energy eigenvalues of the ground and first excited state and the model-space dimensions of ^{12}C and ^{56}Ni as a function of κ_{\min} for a set of reference thresholds C_{\min} . We remark that the energy axis in panel (b) is extremely magnified and spans only 80 keV. The dimensions of the importance-truncated model spaces are reduced drastically as compared to the full m -scheme dimensions, by more than one order of magnitude in the test case for the IT-NCSM and by about two orders of magnitude in the test case for the IT-VSSM. For decreasing κ_{\min} , the energies decrease monotonically and approach the exact results. In the IT-NCSM, the energies and dimensions of the importance-truncated spaces are approximately independent of C_{\min} for the smallest κ_{\min} data points. It is, however, peculiar that for the smallest C_{\min} , the larger κ_{\min} values yield smaller model spaces and higher energies as compared to the respective results with larger C_{\min} . The absolute ground-state energies corresponding to the smallest κ_{\min} threshold differ by only about 1 MeV from the result in the full model space, i.e., the IT-NCSM without extrapolation determines the energy within 1% of the exact energy. Note the expanded energy axis in panel (c) compared to panel (a)—excitation energies in the IT-NCSM typically show a smaller dependence on κ_{\min} than absolute energies. Here, the energy of the first excited state for the smallest κ_{\min} value deviates by less than 100 keV from the result in the full model space. In the IT-VSSM, the variation of C_{\min} results in a small, but constant offset of the κ_{\min} sequence for the dimensions and energies. The absolute energies in the largest importance-truncated model spaces, corresponding to the smallest κ_{\min} and C_{\min} thresholds, differ by only about 10 keV from the results in the full model space. The agreement with the exact result is further improved for

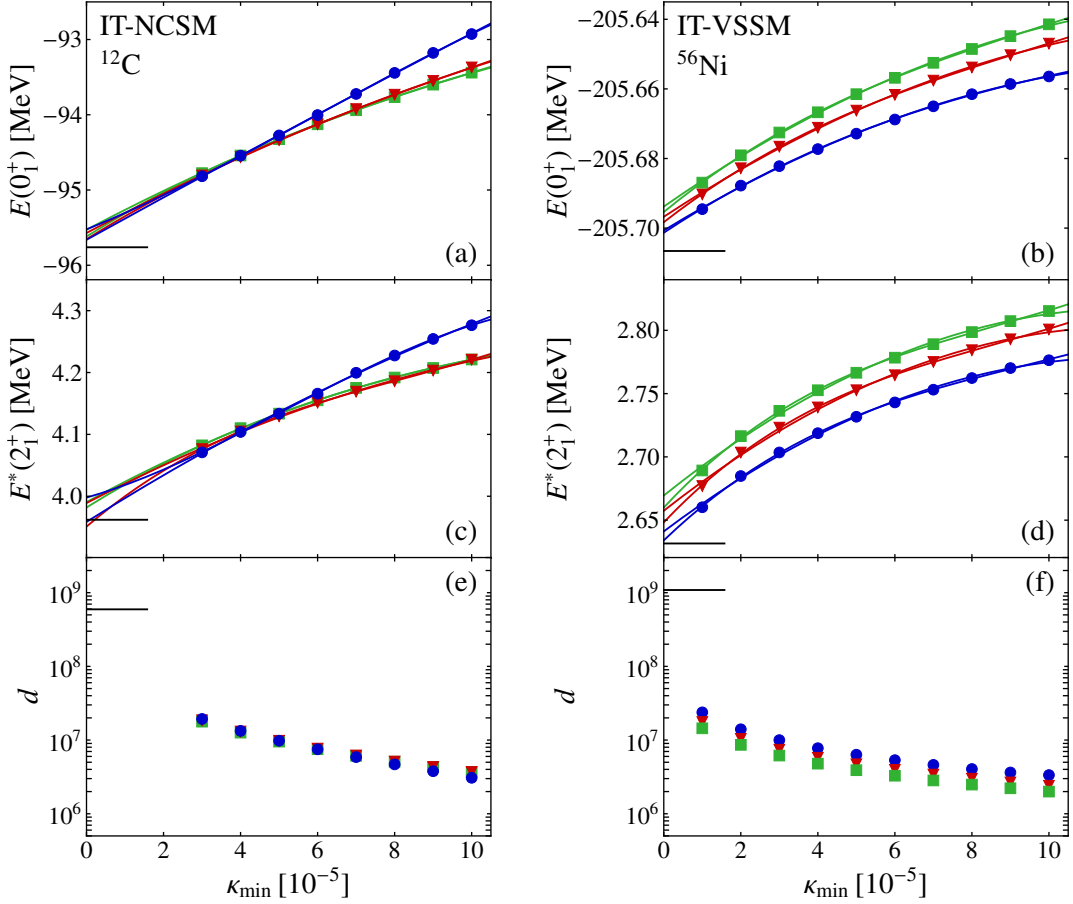


Figure 5.1.: Energy of the ground and first excited state of ^{12}C in the IT-NCSM ((a) and (c)) and of ^{56}Ni in the IT-VSSM ((b) and (d)) as a function of the importance threshold for the reference thresholds $C_{\min} = \{1(\bullet), 2(\blacktriangledown), 3(\blacksquare)\} \cdot 10^{-4}$. In the IT-NCSM, the EMN500 interaction, SRG-evolved up to $\alpha = 0.0625 \text{ fm}^4$, is used. The oscillator frequency is $\hbar\Omega = 20 \text{ MeV}$, and the model-space truncation parameter is $N_{\max} = 8$. In the IT-VSSM, the model space is constructed up to $T_{\max} = 16$ for a pf valence space using the GXPF1A Hamiltonian. Also shown are the respective dimensions d of the IT model spaces ((e) and (f)). The horizontal lines denote the energies (taken from [Mar+14] and extracted from [Hor+06]) and the dimensions of the full model spaces.

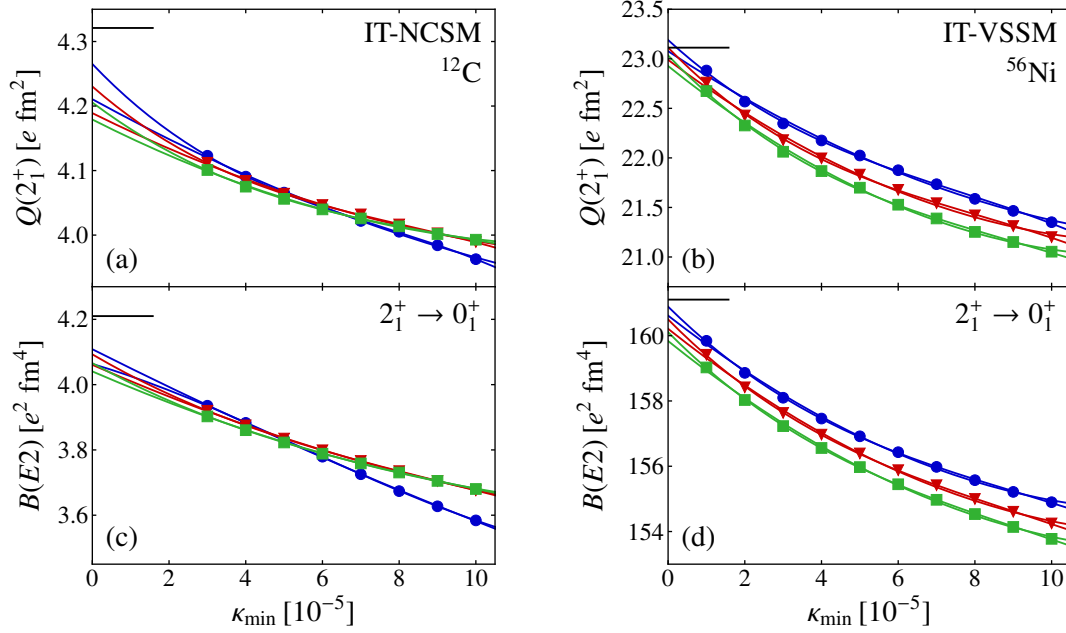


Figure 5.2.: Threshold dependence and extrapolation of the quadrupole moment of the 2_1^+ state and the $B(E2 : 2_1^+ \rightarrow 0_1^+)$ transition strength of ^{12}C ((a) and (c)) in the IT-NCSM and of ^{56}Ni in the IT-VSSM ((b) and (d)) for a set of reference thresholds $C_{\min} = \{1(\bullet), 2(\blacktriangledown), 3(\blacksquare)\} \cdot 10^{-4}$. In the IT-NCSM, the EMN500 interaction, SRG-evolved up to $\alpha = 0.0625 \text{ fm}^4$, is used. The oscillator frequency is $\hbar\Omega = 20 \text{ MeV}$, and the model-space truncation parameter is $N_{\max} = 8$. In the IT-VSSM, the model space is constructed for $T_{\max} = 8$ using the GXPF1A Hamiltonian. The horizontal lines denote the results obtained for the full model spaces. The NCSM results are taken from [Mar+14], the VSSM results have been obtained in a calculation using the ANTOINE code [Cau+05; CN99].

the excitation energy of the first excited state. This demonstrates the efficiency of the importance truncation—it identifies the 10^7 basis states that determine the bulk of energy among the approximately 10^9 basis states in the full space that are responsible for the residual 1 MeV and accordingly 10 keV, with improved results for excitation energies.

We recover the effects of basis configurations excluded from the importance-truncated model spaces by a simple extrapolation of the observables based on the importance threshold κ_{\min} . The energy eigenvalues depend smoothly on κ_{\min} and we can fit simple functions to the set of energies obtained for different importance thresholds and extract the energies for $\kappa_{\min} \rightarrow 0$. Since we do not have a theoretical model for the functional dependence on the importance thresholds, we use simple polynomials, typically of order two to four. Varying the order of the polynomials gives an estimate for the uncertainty of this threshold extrapolation.

Figure 5.1 includes examples for fits with second- and third-order polynomials for the IT-NCSM and IT-VSSM energies of ^{12}C and ^{56}Ni , respectively. In the IT-NCSM, the

extrapolated energies using the two polynomials as fit functions span the same energy range for all reference thresholds C_{\min} . This proves the efficiency of the reference threshold; it accelerates the evaluation of the importance measure for basis states outside the reference space, while the threshold-extrapolated results are independent of its particular value. In the IT-VSSM, a small residual dependence of the extrapolated energies on C_{\min} is found. Note that the uncertainty of the κ_{\min} extrapolation is small compared to the dependence on C_{\min} .

Since the IT-NCSM and IT-VSSM provide the eigenstates in the importance-truncated model spaces, we have access to all other observables, particularly to electromagnetic moments and transition strengths relevant for spectroscopy. For each κ_{\min} , we compute the observable of interest using the respective eigenvector.

Figure 5.2 illustrates the threshold dependence of the quadrupole moment of the first excited 2_1^+ state of ^{12}C and ^{56}Ni and the $B(E2)$ transition strength from this state to the ground state. Also these observables show a smooth dependence on κ_{\min} , allowing for simple polynomial extrapolations to vanishing importance threshold. The κ_{\min} -extrapolated results show a mild dependence on C_{\min} for the test cases considered here, which is of the same magnitude as the uncertainty of the threshold extrapolation. For ^{12}C , the extrapolated quadrupole moment and $B(E2)$ transition strength agree well with the results obtained in a full NCSM calculation. In the IT-VSSM, the agreement with the results in the full model space is excellent. This proves that the importance truncation provides also direct access to spectroscopic observables.

5.3. Energy-Variance Extrapolation

The simple threshold extrapolation does not require additional computations and can be applied to all observables on equal footing. However, it exclusively addresses the importance threshold κ_{\min} , and uncertainties of the polynomial extrapolations can be sizable. The description of deformed nuclei is particularly challenging in the importance truncation because many basis states contribute with small amplitudes, which in sum are important. This can result in a stronger bending of the energy eigenvalues as a function of κ_{\min} , making the threshold extrapolation less precise. In these cases, it is possible to reduce the extrapolation uncertainties by including additional information on the excluded basis states in the fitting procedure, e.g., through a second-order perturbative estimate of their contribution to the energy, as done successfully in the IT-NCSM [Rot09].

We propose an alternative approach and consider a more elaborate extrapolation scheme based on the energy variance

$$\Delta E_n^2 = \langle \Psi_n | \mathbf{H}^2 | \Psi_n \rangle - \langle \Psi_n | \mathbf{H} | \Psi_n \rangle^2, \quad (5.7)$$

which was used in the NCSM and VSSM context before [Zha+04; Miz04; Shi+10; Shi+12]. By construction, the energy variance (5.7) vanishes for the exact eigenstates in the full model space. This is seen explicitly by assuming that $|\Psi_n\rangle$ is an exact eigenstate of \mathbf{H} and exploiting the eigenvalue relation. Therefore, for approximate eigenstates obtained in a truncated subspace, the energy variance serves as a measure for the distance of this state from the energy eigenstate in the full space. Based on a perturbative expansion, the

functional dependence of approximate energy eigenvalues on the energy variance has been shown to be predominantly linear with sub-leading quadratic terms [MI03]. We thus have a simple model, predicting the behavior of the energies in the extrapolated region, and a robust two- or three-parameter fit function at hand that provide reliable and accurate extrapolations.

The calculation of the energy variance implies the explicit evaluation of the expectation value $\langle \Psi_n | \mathbf{H}^2 | \Psi_n \rangle$. If we start from a Hamiltonian of the form

$$\begin{aligned} \mathbf{H} &= \mathbf{H}_{0B} + \mathbf{H}_{1B} + \mathbf{H}_{2B} \\ &= h_0 + \sum_{ij} h_j^i \mathbf{A}_j^i + \frac{1}{4} \sum_{ijkl} h_{kl}^{ij} \mathbf{A}_{kl}^{ij}, \end{aligned} \quad (5.8)$$

where we have introduced the shorthand notation

$$\mathbf{A}_j^i = \mathbf{a}_i^\dagger \mathbf{a}_j, \quad (5.9a)$$

$$\mathbf{A}_{kl}^{ij} = \mathbf{a}_i^\dagger \mathbf{a}_j^\dagger \mathbf{a}_l \mathbf{a}_k, \quad (5.9b)$$

$$\mathbf{A}_{kl\dots}^{ij\dots} = \mathbf{a}_i^\dagger \mathbf{a}_j^\dagger \dots \mathbf{a}_l \mathbf{a}_k \quad (5.9c)$$

for the product of creation and annihilation operators and h_0 , h_j^i , and h_{kl}^{ij} for the corresponding zero-, one-, and two-body matrix elements, we can write the operator \mathbf{H}^2 as

$$\begin{aligned} \mathbf{H}^2 &= h_0^2 + 2h_0 \sum_{ij} \mathbf{A}_j^i h_j^i + \sum_{ijk} \mathbf{A}_j^i h_k^i h_j^k \\ &\quad + 2h_0 \sum_{\substack{i<j \\ k<l}} \mathbf{A}_{kl}^{ij} h_{kl}^{ij} + \sum_{\substack{i<j \\ k<l}} \mathbf{A}_{kl}^{ij} [2h_k^i h_l^j - h_k^j h_l^i - h_l^i h_k^j] \\ &\quad + \sum_{\substack{m \\ i<j \\ k<l}} \mathbf{A}_{kl}^{ij} [h_m^i h_{kl}^{mj} - h_m^j h_{kl}^{mi} - h_l^m h_{mk}^{ij} - h_k^m h_{lm}^{ij}] \\ &\quad + \sum_{\substack{i<j \\ k<l \\ m<n}} \mathbf{A}_{kl}^{ij} h_{mn}^{ij} h_{kl}^{mn} \\ &\quad + 2 \sum_{\substack{i<j<k \\ l<m<n}} \mathbf{A}_{lmn}^{ijk} [h_l^i h_{mn}^{jk} - h_l^j h_{mn}^{ik} + h_l^k h_{mn}^{ij} - h_m^i h_{ln}^{jk} + h_m^j h_{ln}^{ik} \\ &\quad \quad - h_m^k h_{ln}^{ij} + h_n^i h_{lm}^{jk} - h_n^j h_{lm}^{ik} + h_n^k h_{lm}^{ij}] \\ &\quad + \sum_{\substack{0 \\ i<j<k \\ l<m<n}} \mathbf{A}_{lmn}^{ijk} [h_{ol}^{ij} h_{mn}^{ko} + h_{ol}^{kj} h_{mn}^{io} - h_{ol}^{ik} h_{mn}^{jo} - h_{om}^{ij} h_{ln}^{ko} - h_{om}^{kj} h_{ln}^{io} \\ &\quad \quad + h_{om}^{ik} h_{ln}^{jo} + h_{on}^{ij} h_{ml}^{ko} + h_{on}^{kj} h_{ml}^{io} - h_{on}^{ik} h_{ml}^{jo}] \\ &\quad + \sum_{\substack{i<j<k<l \\ m<n<o<p}} \mathbf{A}_{mnop}^{ijkl} [h_{mn}^{ij} h_{op}^{kl} - h_{mn}^{ik} h_{op}^{jl} + h_{mn}^{il} h_{op}^{jk} - h_{mn}^{kj} h_{op}^{il} + h_{mn}^{lj} h_{op}^{ik} + h_{mn}^{kl} h_{op}^{ij}] \end{aligned}$$

5. Importance-Truncated Configuration-Interaction Methods

$$\begin{aligned}
& -h_{mo}^{ij}h_{np}^{kl} + h_{mo}^{ik}h_{np}^{jl} - h_{mo}^{il}h_{np}^{jk} + h_{mo}^{kj}h_{np}^{il} - h_{mo}^{lj}h_{np}^{ik} - h_{mo}^{kl}h_{np}^{ij} \\
& + h_{mp}^{ij}h_{no}^{kl} - h_{mp}^{ik}h_{no}^{jl} + h_{mp}^{il}h_{no}^{jk} - h_{mp}^{kj}h_{no}^{il} + h_{mp}^{lj}h_{no}^{ik} + h_{mp}^{kl}h_{no}^{ij} \\
& + h_{no}^{ij}h_{mp}^{kl} - h_{no}^{ik}h_{mp}^{jl} + h_{no}^{il}h_{mp}^{jk} - h_{no}^{kj}h_{mp}^{il} + h_{no}^{lj}h_{mp}^{ik} + h_{no}^{kl}h_{mp}^{ij} \\
& - h_{po}^{ij}h_{mn}^{kl} + h_{po}^{ik}h_{mn}^{jl} - h_{po}^{il}h_{mn}^{jk} + h_{po}^{kj}h_{mn}^{il} - h_{po}^{lj}h_{mn}^{ik} - h_{po}^{kl}h_{mn}^{ij} \\
& - h_{np}^{ij}h_{mo}^{kl} + h_{np}^{ik}h_{mo}^{jl} - h_{np}^{il}h_{mo}^{jk} + h_{np}^{kj}h_{mo}^{il} - h_{np}^{lj}h_{mo}^{ik} - h_{np}^{kl}h_{mo}^{ij} \Big], \quad (5.10)
\end{aligned}$$

obtaining zero- to four-body contributions. Note that the above expression can be obtained by either using the anti-commutation relations of creation and annihilation operators or, more elegantly, by using normal-ordering techniques.

The energy variance captures nontrivial information on the full model space through the expectation value $\langle \Psi_n | \mathbf{H}^2 | \Psi_n \rangle$. This is seen explicitly by inserting the identity operator

$$\mathbf{1} = \sum_{|\Phi_j\rangle \in \mathcal{M}_{\text{full}}} |\Phi_j\rangle \langle \Phi_j| \quad (5.11)$$

represented in the full model space in between the product of the two Hamiltonians—the variance probes the coupling to basis states outside of the truncated subspace.

In the IT-VSSM, this allows to extrapolate to the full model space defined by the valence orbits without any additional truncation. In this way, the variance extrapolation remedies all truncations used in the IT-VSSM, i.e., the κ_{min} , C_{min} , and T_{max} truncations. In this respect, the variance extrapolation is much more powerful than the simple threshold extrapolation. However, other target spaces are possible using an alternative implementation for the calculation of the energy variance. By choosing a specific identity operator (5.11), e.g., for a T_{max} -truncated many-body space, for insertion in between the product of the two Hamiltonians, we can circumvent the evaluation of up to four-body contributions and evaluate products of two-body matrix elements instead. In this case, the variance extrapolation will only account for the κ_{min} and C_{min} truncations. We usually compute the \mathbf{H}^2 operator to correct the approximate energy eigenvalues for all truncations applied in the IT-VSSM. The individual contributions of (5.10) are calculated on the fly, where the four-body part is the costliest. The limiting factor for the calculation of the energy variance is not memory but computing time, which, for typical applications, is an order of magnitude larger than the computing time of the corresponding IT-VSSM calculation.

The expression (5.10) illustrates why the evaluation of the expectation value of \mathbf{H}^2 becomes prohibitive for large model spaces, in particular if 3N interactions are included additionally, resulting in up to six-body contributions. In the (IT-)VSSM, the full model space is always finite because the valence orbits naturally restrict the number of many-body basis states. No such constraint exists in the (IT-)NCSM, rendering the full model space infinite. Furthermore, the energy variance is not sensitive to the model-space truncation parameter. This poses a conceptual problem for the applicability of the variance extrapolation in the IT-NCSM. We have tried to overcome this difficulty using the alternative implementation based on the identity operator in a full model space defined by N_{max} . However, the computing time scales approximately linearly with the size of the full model space, and can, thus, become immense. Therefore, we employ the variance extrapolation only in the context of the IT-VSSM.

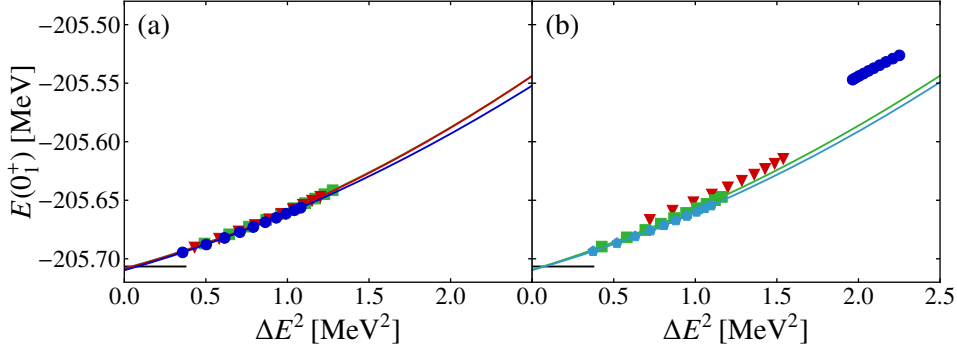


Figure 5.3.: Energy-variance extrapolation of the ground-state energy relative to the core for ^{56}Ni obtained in the IT-VSSM using the GXPF1A Hamiltonian. Panel (a) shows results for different reference thresholds $C_{\min} = \{1(\bullet), 2(\blacktriangledown), 3(\blacksquare)\} \cdot 10^{-4}$ for $T_{\max} = 16$. In panel (b), calculations for different truncations $T_{\max} = \{4(\bullet), 6(\blacktriangledown), 8(\blacksquare), 10(\circ)\}$ with $C_{\min} = 1 \cdot 10^{-4}$ are depicted. The horizontal lines denote the results of the full model spaces obtained in a calculation using the ANTOINE code [Cau+05; CN99].

In figure 5.3, the ground-state energy of ^{56}Ni is illustrated as a function of the energy variance. Panel (a) shows κ_{\min} sequences for $T_{\max} = 16$ and different reference thresholds C_{\min} , while panel (b) displays κ_{\min} sequences for different T_{\max} and fixed C_{\min} . The first remarkable observation is that the κ_{\min} sequences for different C_{\min} fall onto one curve. Consequently, the respective variance extrapolations yield the same result. The variance-extrapolated energy is in excellent agreement with the result for the full space reported in [Hor+06]. Even with an additional T_{\max} truncation, as shown in panel (b), the results beyond $T_{\max} = 6$ fall onto the same line. For severe truncations, e.g., $T_{\max} = 4$, we observe larger energy variances that cannot be extrapolated reliably.

The advantages of the variance extrapolation are that a simple and robust fit model is available and that the extrapolation remedies all truncations inherent to an IT-VSSM calculation. The disadvantage is that substantial computational effort goes into the evaluation of the energy variance. Typically, the computation of the variance needs more computing time than the complete IT-VSSM calculation.

Based on the success of the variance extrapolation for energies, we tentatively apply the same approach to other observables. Figure 5.4 illustrates the dependence of the quadrupole moment of the first 2^+ state in ^{56}Ni and the $B(E2)$ transition strength to the ground state on the energy variance. We find that the variance extrapolation using linear and quadratic fit functions do not improve the results obtained by the threshold extrapolation, cf. figure 5.2. The variance extrapolation for electromagnetic observables is lacking the rigorous formal foundation that it has for energies and a simple linear dependence is neither guaranteed nor observed. Moreover, for electromagnetic transitions, the energy variances of two states need to be combined into one control parameter for the extrapolation in a heuristic way. As in [Miz04], we use the mean of the energy variances of the two states as control parameter. It is evident from figure 5.4 that the sequences for

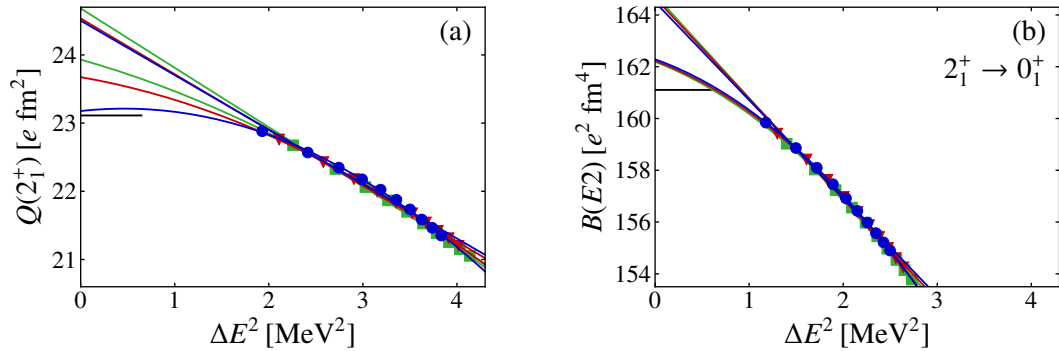


Figure 5.4.: Energy-variance extrapolation of the quadrupole moment (a) and the $B(E2 : 2_1^+ \rightarrow 0_1^+)$ transition strength (b) of ^{56}Ni using linear and quadratic fit functions. The wave functions have been obtained in an IT-VSSM calculation using the GXPF1A Hamiltonian for $T_{\max} = 8$ and the reference thresholds $C_{\min} = \{1(\bullet), 2(\blacktriangledown), 3(\blacksquare)\} \cdot 10^{-4}$. For the transition strength, the mean energy variance of the states considered is used. The horizontal lines denote the results of the full model spaces obtained in a VSSM calculation using the ANTOINE code [Cau+05; CN99].

different C_{\min} approximately collapse onto one line; however, the systematic deviations are larger than for the energies. A linear fit does not yield an adequate reproduction of the points and clearly misses the exact result. The quadratic fit reveals a strong dependence on C_{\min} for the quadrupole moment and also overestimates the result. Therefore, we conclude that the variance extrapolation for electromagnetic observables is less robust and accurate than the simple threshold extrapolation. Since it is also computationally more expensive, we restrict ourselves to using the threshold extrapolation for observables other than energies.

6. Lanczos Strength Functions from the IT-NCSM

We present a new approach for the *ab initio* description of collective excitations and nuclear response functions. We combine the IT-NCSM with the Lanczos strength-function method proposed by Whitehead [Whi80] for the efficient computation of transition strengths and their distributions. This enables direct *ab initio* calculations of all relevant strength distributions for all nuclei that are feasible in the IT-NCSM. The method is based on the Lanczos algorithm [Lan50; Pai71] in its simplest form. We first introduce the Lanczos algorithm in exact arithmetic. Since practical calculations are carried out with finite precision, we further discuss effects of round-off errors on the performance of the algorithm. We then present the Lanczos strength-function method, which emerges from the Lanczos method by choosing a specific start vector and allows for the efficient computation of strength distributions in the IT-NCSM. Finally, we apply this new approach to electromagnetic strength distributions and investigate their convergence behavior.

6.1. The Simple Lanczos Algorithm

The Lanczos algorithm is an iterative method for the computation of extreme eigenpairs of a Hermitian matrix A . It transforms the matrix A into tridiagonal form, making a subsequent diagonalization an easy task using standard diagonalization techniques, e.g., the QR algorithm. The Lanczos algorithm [Lan50] was originally introduced in 1950 as a method for the solution of the eigenvalue problem of a $d \times d$ symmetric matrix A via the construction of a convergent expansion for the eigenvectors, yielding the exact eigenvectors after at most d iterations. At that time, however, the common perception was that this method could be used for the reduction of a whole matrix to tridiagonal form. This is, in practice, hampered by effects of finite precision arithmetic unless computationally demanding modifications are incorporated. Later, C. C. Paige demonstrated that the algorithm in its simplest form can be used for the efficient calculation of a few extreme eigenpairs of a symmetric matrix, despite its sensitivity to round-off errors [Pai71].

We present two approaches to the algorithm in the ideal case of exact arithmetic and discuss how the results are affected by finite precision arithmetic afterward. Note that we are interested in diagonalizing Hamilton matrices, which are real Hermitian and, thus, real symmetric. In the overview of the formalism, we restrict the notation to the relevant case of real symmetric matrices. We remark, however, that generalizations of the Lanczos algorithm to complex and non-Hermitian matrices exist [Saa11].

Approach via Krylov Spaces

Formally, the simple Lanczos algorithm is based on orthogonal projections onto Krylov spaces \mathcal{K} [Pai71; Par98; Saa11]. Here, we give a brief outline to motivate why the Lanczos algorithm transforms a symmetric $d \times d$ matrix A into tridiagonal form. For more details on projection methods and Krylov spaces, we refer the reader to the literature, e.g., [Par98; Saa11].

The Krylov space \mathcal{K}_p can be constructed recursively by repeated multiplication of the matrix A with a d -dimensional start vector \vec{k} , i.e., it is spanned by the basis vectors $K_p = (\vec{k}, A\vec{k}, \dots, A^{p-1}\vec{k})$ written in matrix representation, where each column corresponds to one basis vector. By applying the Gram-Schmidt orthonormalization procedure to the columns of the Krylov matrix K_p in natural order, an orthonormal basis $V_p = (\vec{v}_1, \vec{v}_2, \dots, \vec{v}_p)$ of \mathcal{K}_p , which we denote Lanczos basis in the following, is obtained. We assume that the matrix K_p has full rank $p \leq d$, i.e., its p basis vectors are linearly independent. In this case, the matrix A can be transformed into tridiagonal form via

$$V_p^T A V_p = T_p. \quad (6.1)$$

This becomes evident from the following considerations [Par98]: A characteristic property of Krylov spaces, rooted in their recursive setup, is $A\mathcal{K}_j \subseteq \mathcal{K}_{j+1}$ for all $j \leq p$. In particular, $\vec{v}_i \perp \mathcal{K}_{i-1}$ and $A\vec{v}_j \in \mathcal{K}_{j+1}$. By combining this with the symmetry of A , we conclude that $\vec{v}_i^T A \vec{v}_j = \vec{v}_j^T A \vec{v}_i = 0$ for all $i > j + 1$. This demonstrates that T_p must have tridiagonal form. Furthermore, if K_p has full rank and $j < p$, then $A\vec{v}_j$ and \vec{v}_{j+1} cannot be orthogonal, i.e., $\vec{v}_{j+1}^T A \vec{v}_j \neq 0$.

Instead of orthonormalizing a given set of p Krylov vectors, it is more efficient to embed the construction of the Lanczos basis into an iterative scheme. At iteration step j , the Lanczos algorithm can be summarized by the two equations:

$$A V_j - V_j T_j = \vec{v}_{j+1} \beta_j \vec{e}_j^T, \quad (6.2a)$$

$$V_j^T V_j = \mathbb{1}. \quad (6.2b)$$

Here, we have introduced $\beta_j = \vec{v}_{j+1}^T A \vec{v}_j$ and added the subscript j to indicate the current number of Lanczos vectors and the dimension of the matrix T_j . The vector \vec{e}_j is a unit vector with entry 1 at position j , and $\mathbb{1}$ is the identity matrix. Due to the symmetry of A , a newly generated Lanczos vector has to be orthonormalized only against the two preceding ones.

Since the columns of V_p are orthonormal, the transformation (6.1) resembles a similarity transformation, and, thus, the diagonalization of T_p yields approximations for the eigenpairs of A , which become the exact ones for $p = d$.

Approach via Matrix Reduction to Tridiagonal Form

It is evident from the above discussion that, after p iterative steps, the Lanczos method yields a tridiagonal matrix

$$T_p = \begin{pmatrix} \alpha_1 & \beta_1 & & & \\ \beta_1 & \alpha_2 & \beta_2 & & \\ & \ddots & \ddots & \ddots & \\ & & & \beta_{p-1} & \alpha_p \\ & & & \beta_{p-1} & \alpha_p \end{pmatrix} \quad (6.3)$$

starting from a symmetric $d \times d$ matrix A . Therefore, the method can be translated into an iterative algorithm for the matrix reduction of a symmetric matrix to tridiagonal form via the three-term recurrence:

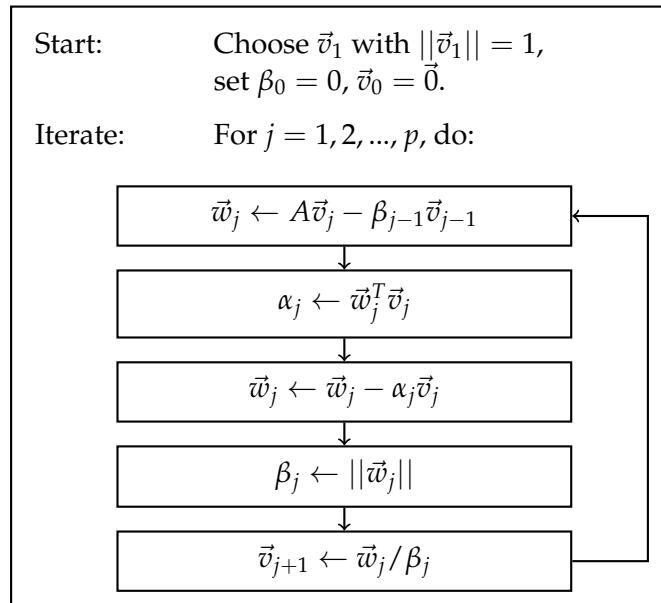
$$\vec{v}_{j+1} = (A\vec{v}_j - \beta_{j-1}\vec{v}_{j-1} - \alpha_j\vec{v}_j) / \beta_j. \quad (6.4)$$

Here, we have defined

$$\alpha_j = \vec{v}_j^T A \vec{v}_j, \quad (6.5a)$$

$$\beta_j = \|A\vec{v}_j - \beta_{j-1}\vec{v}_{j-1} - \alpha_j\vec{v}_j\|. \quad (6.5b)$$

There are several equivalent formulations of the algorithm in accordance with this recurrence. We employ the version denoted by "A2" in [Pai71], which has been found to be the most reliable because it best maintains orthogonality of consecutive Lanczos vectors \vec{v}_j in finite precision. An outline of the algorithm is:



The algorithm requires as input a symmetric matrix A , a non-zero, normalized pivot vector \vec{v}_1 , and the number of iterations p . Note that, in general, \vec{v}_1 can be chosen arbitrarily. It may,

however, be convenient to choose the pivot vector to embody any available knowledge about the target eigenvectors. In each iteration, the matrix elements α_j and β_j of the tridiagonal matrix T_p are computed. Since the Lanczos vectors are not needed if we are not interested in the approximate eigenvectors of A , only the two most recent Lanczos vectors and the temporary vector \vec{w}_j have to be kept in storage. The algorithm is particularly suited for large sparse matrices because the matrix A appears only once per iteration step in a matrix-vector multiplication, where one can take advantage of the sparsity. All other operations involve only simple vector arithmetic.

Besides its simplicity and memory efficiency, the Lanczos algorithm generates a tridiagonal matrix T_p whose extreme eigenvalues converge rapidly with p to the extreme eigenvalues of A . If the approximate eigenvectors of A are needed, also the storage of the Lanczos vectors is required. The former are obtained from the eigenvectors of T_p , represented in the Lanczos basis, by transformation into the original basis using the unitary matrix V_p , where each column corresponds to a Lanczos vector.

Orthogonality Loss of the Lanczos Basis

In practice, calculations are carried out with finite precision, and the results are affected by round-off errors. The simple Lanczos algorithm, thus, yields in each iteration the matrix elements α_j and β_j and a new Lanczos vector \vec{v}_{j+1} , which carry some error. Eventually, this results in a loss of orthogonality among the Lanczos vectors, manifesting itself in the appearance of degeneracies in the eigenvalue spectrum of T_p . We note that the matrix $V_p^T A V_p$ is not tridiagonal when round-off errors are present. However, the algorithm still computes a tridiagonal matrix T_p , which is not the projection of A onto the Krylov space, and, thus, the matrix T_p is not guaranteed to be similar to A for $p = d$.

C. C. Paige has proven a close relationship between the loss of orthogonality in the Lanczos basis and the convergence of an approximate eigenpair [Pai71]. He demonstrated that a new Lanczos vector remains almost orthogonal to all approximate eigenvectors that are not yet fully converged, but that orthogonality is lost with those approximate eigenvectors whose corresponding approximate eigenvalues have converged to an exact eigenvalue of A . Consequently, the simple Lanczos algorithm provides accurate approximations of the eigenvalues of A .

Nevertheless, the loss of orthogonality was commonly interpreted as a severe drawback of the Lanczos method. Therefore, full Gram-Schmidt reorthogonalization procedures were typically incorporated into the algorithm. This represents a straight-forward, but computationally expensive cure to this issue, because the complete Lanczos basis needs to be kept in store.

Many cheaper reorthogonalization schemes were proposed in the following years, e.g., the Lanczos algorithm with selective or partial reorthogonalization, see, e.g., [PS79; Sim84]. In contrast, Cullum and Willoughby [CW81] advocated to use the simple Lanczos algorithm without any reorthogonalization technique to obtain a required number of distinct eigenvalues by increasing the number of iterations—in many cases, the number of iterations significantly exceeds the dimensionality of the problem. We note that, in general applications, it may be difficult to distinguish between situations where several close eigenvalues correspond to degenerate exact eigenvalues of A or to copies of one

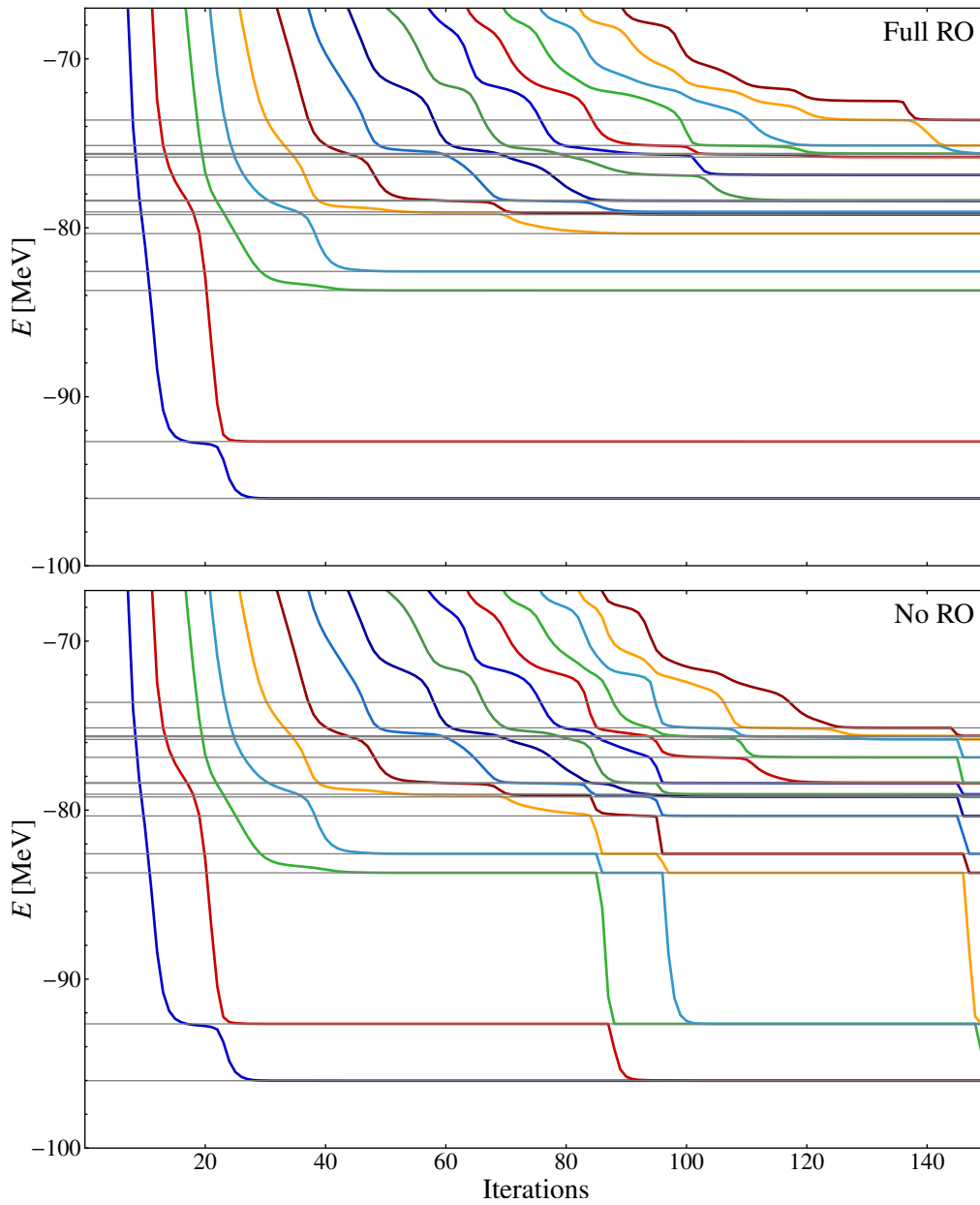


Figure 6.1.: Convergence behavior of the lowest 15 energy eigenvalues in the Lanczos algorithm with full reorthogonalization (Full RO) and without reorthogonalization (No RO). The Hamilton matrix has been calculated in the NCSM with HO basis for ^{12}C using the EM interaction, SRG-evolved up to $\alpha = 0.08 \text{ fm}^4$ in the two-body space, for $N_{\text{max}} = 4$ and $\hbar\Omega = 20 \text{ MeV}$. The gray lines denote the exact eigenvalues.

eigenvalue due to orthogonality loss. Nowadays, the trend is to use restarted methods for matrix diagonalizations, e.g., the implicitly restarted Arnoldi algorithm [LSY98].

More details on effects of finite-precision arithmetic in the Lanczos algorithm can be found in [Pai71; Par98; Meu06].

Figure 6.1 illustrates the convergence behavior of the low-lying part of the eigenvalue spectrum of a symmetric matrix calculated using the Lanczos algorithm with full and without reorthogonalization of the Lanczos basis. The matrix is the Hamilton matrix of ^{12}C calculated in the NCSM with HO basis using the EM interaction, SRG-evolved up to $\alpha = 0.08 \text{ fm}^4$ in the two-body space, for $N_{\text{max}} = 4$ and $\hbar\Omega = 20 \text{ MeV}$.

The upper panel of figure 6.1 shows results for the 15 lowest energy eigenvalues obtained with the Lanczos algorithm with full reorthogonalization of the Lanczos basis. As expected, the extreme eigenvalues—here the ground state and the first few excited states—converge fast to the exact values indicated by the gray lines. We find that the ground state is determined to very good accuracy after less than 30 Lanczos iterations, and that the excited states follow the same pattern but require more iterations. Note that it is possible that the energies of some states first seem to converge to the energies of some higher-lying states before collapsing on the exact energies, as observed, e.g., for the ground state.

The results displayed in the lower panel illustrate the convergence behavior of the Lanczos algorithm when used in its simplest form. During the first iterative steps, the convergence pattern is indistinguishable from the process where the orthogonality of the Lanczos basis is enforced. However, at some point—after about 90 iterations—the algorithm starts to produce copies of approximate eigenvalues that have been computed previously. This becomes evident when eigenvalues collapse onto already existing lower eigenvalues.

6.2. Lanczos Strength-Function Method

The Lanczos strength-function method, proposed by R. R. Whitehead [Whi80], allows the construction of fast-converging approximations of transition strength distributions for any observable using the Lanczos algorithm in its simplest form. This method has been used successfully for the calculation of electromagnetic or weak responses in the VSSM for some time [Cau+05; CPZ90; EHV92; Cau+94; CPZ95; GDJ00; SJ03; HNZ05; Loe+12; SMY18].

We follow a similar approach and present a new method for the *ab initio* description of the nuclear response by combining the IT-NCSM with the Lanczos strength-function method [SWR17]. The calculation involves two steps: First, we solve the eigenvalue problem of the Hamiltonian using the IT-NCSM within a certain many-body model space. One of the eigenstates—typically the ground state $|\Psi_0\rangle$ —serves as input for the next step of the calculation.

We note that, unlike in section 6.1, where we have used the matrix-vector formalism as a natural way to describe the Lanczos algorithm, we use the more general Dirac notation in the following for convenience. Since practical applications are always restricted to finite basis representations, both notations are equivalent.

We construct a normalized pivot vector $|v_1\rangle$ by applying the transition operator \mathbf{O}_λ , e.g.,

an electromagnetic multipole operator of type σ (electric or magnetic) with multipolarity λ and projection μ (suppressed for brevity in the following), to the ground-state eigenvector $|\Psi_0\rangle$ obtained in the first step:

$$|v_1\rangle = \frac{1}{\sqrt{S}} \mathbf{O}_\lambda |\Psi_0\rangle. \quad (6.6)$$

The normalization factor

$$S = \langle \Psi_0 | \mathbf{O}_\lambda^\dagger \mathbf{O}_\lambda | \Psi_0 \rangle \quad (6.7)$$

corresponds to the total transition strength from the ground state $|\Psi_0\rangle$ to any excited state. This is seen explicitly by inserting a completeness relation in between the two operators:

$$\begin{aligned} S &= \sum_n \langle \Psi_0 | \mathbf{O}_\lambda^\dagger | \Psi_n \rangle \langle \Psi_n | \mathbf{O}_\lambda | \Psi_0 \rangle \\ &= \sum_n |\langle \Psi_n | \mathbf{O}_\lambda | \Psi_0 \rangle|^2. \end{aligned} \quad (6.8)$$

Starting from $|v_1\rangle$, we use the simple Lanczos algorithm with the Hamiltonian to reduce the Hamilton matrix to tridiagonal form in p iterations. By diagonalizing this tridiagonal matrix T_p , we obtain its eigenvalues E_n and the coefficients $c_j^{(n)}$, which define its eigenvectors $|E_n\rangle$. The latter represent approximations for p eigenstates of the Hamiltonian via

$$|E_n\rangle = \sum_{j=1}^p c_j^{(n)} |v_j\rangle. \quad (6.9)$$

In standard applications, we would continue the iterations until the eigenvalues and eigenstates of interest are converged.

For evaluating transition strengths, the first coefficient in each eigenvector of the matrix T_p plays an important role. Due to the special definition of $|v_1\rangle$ in (6.6), we obtain

$$\begin{aligned} c_1^{(n)} &= \langle E_n | v_1 \rangle \\ &= \frac{1}{\sqrt{S}} \langle E_n | \mathbf{O}_\lambda | \Psi_0 \rangle. \end{aligned} \quad (6.10)$$

We can thus calculate the transition matrix element $\langle E_n | \mathbf{O}_\lambda | \Psi_0 \rangle$ from the coefficients $c_1^{(n)}$ —a product of the simple Lanczos algorithm—and the total strength S of the pivot state.

We are mainly interested in distributions of reduced transition strengths

$$R(E^*; \sigma\lambda) = \sum_n |\langle E_n | \mathbf{O}_\lambda | \Psi_0 \rangle|^2 \delta(E^* - (E_n - E_0)), \quad (6.11)$$

where the reduced transition matrix element $\langle E_n | \mathbf{O}_\lambda | \Psi_0 \rangle$ needs to be computed from $\langle E_n | \mathbf{O}_\lambda | \Psi_0 \rangle$ using the Wigner-Eckart theorem. In this thesis, we only consider transitions between a $J_0 = 0$ ground state $|\Psi_0\rangle$ and the Lanczos approximation for an excited state

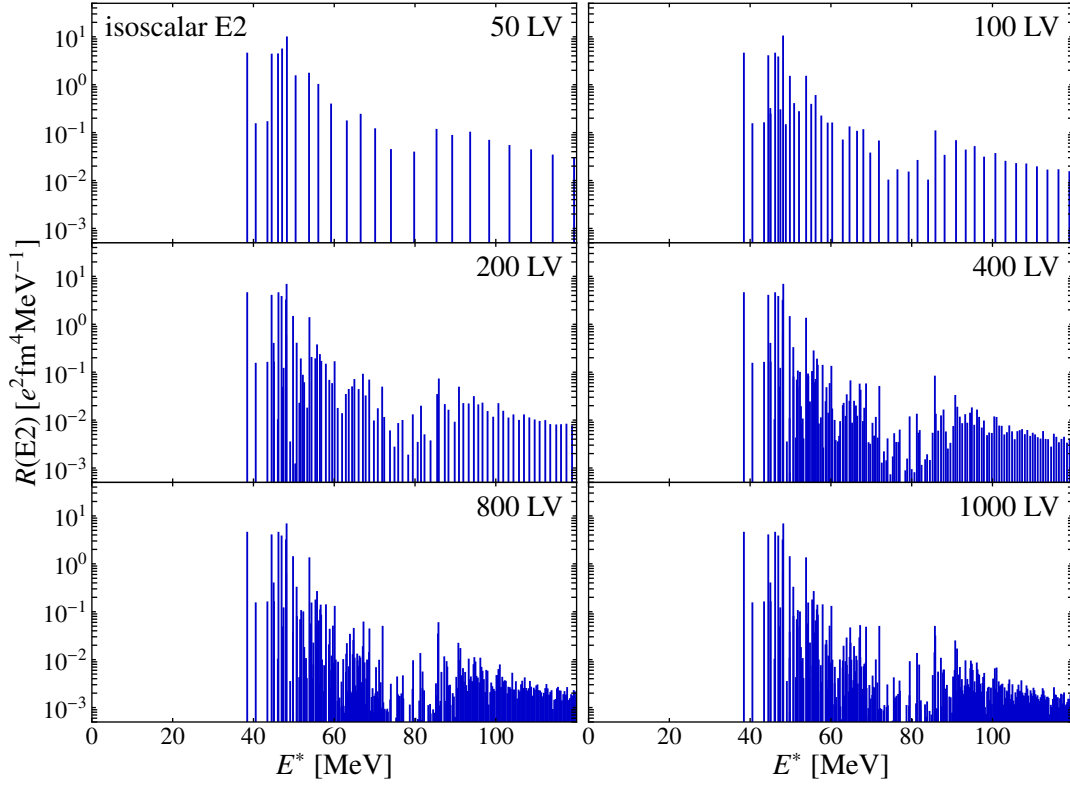


Figure 6.2.: Convergence of discrete isoscalar E2 strength distributions with the number of Lanczos vectors (LV) for ^{16}O obtained in the NCSM with HO basis, using the EM interaction, SRG-evolved in two-body space up to $\alpha = 0.08 \text{ fm}^4$. The oscillator frequency is $\hbar\Omega = 20 \text{ MeV}$, the center-of-mass control parameter is $\beta = 1$, and the model space is truncated at $N_{\text{max}} = 4$. The Lanczos basis has been fully reorthogonalized.

$|E_n\rangle$, for which then follows $J_n = \lambda$. The reduced transition matrix element is simply given by

$$\langle E_n || \mathbf{O}_\lambda || \Psi_0 \rangle = \sqrt{(2\lambda + 1)S} c_1^{(n)}. \quad (6.12)$$

The fact that we obtain a discrete excitation spectrum results from the use of a bound-state method, the IT-NCSM. The coupling to the continuum and the resulting escape width are not captured, however, all correlation effects are explicitly taken into account. In practical applications, we are often interested in smoothed-out distributions, lending themselves to an easy comparison with experimental data. Therefore, we mainly discuss continuous strength functions obtained by folding $R(E^*; \sigma\lambda)$ with a Lorentzian:

$$\tilde{R}(E^*; \sigma\lambda) = \sum_n \frac{\Gamma}{\pi} \frac{|\langle E_n || \mathbf{O}_\lambda || \Psi_0 \rangle|^2}{(E^* - (E_n - E_0))^2 + \Gamma^2}. \quad (6.13)$$

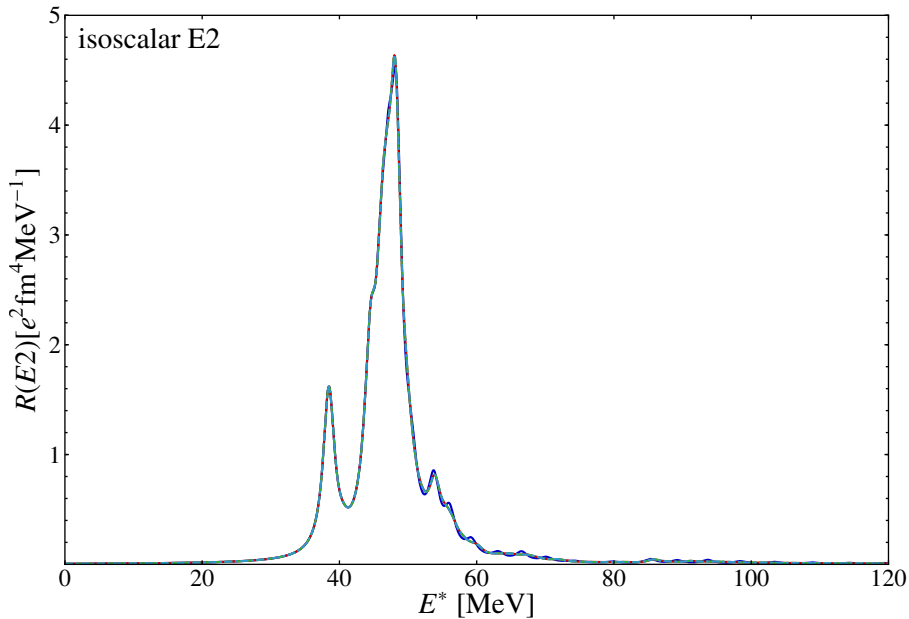


Figure 6.3.: Convergence of smoothed-out isoscalar E2 strength distributions with the number of Lanczos vectors $LV = \{50$ (—), 200 (—), 400 (---), and 1000 (---)} for ^{16}O obtained in the NCSM with HO basis, using the EM interaction, SRG-evolved in two-body space up to $\alpha = 0.08 \text{ fm}^4$. The oscillator frequency is $\hbar\Omega = 20 \text{ MeV}$, the center-of-mass control parameter is $\beta = 1$, and the model space is truncated at $N_{\text{max}} = 4$. The Lanczos basis has been fully reorthogonalized.

The parameter Γ denotes the width of the Lorentzian function, which we choose $\Gamma = 1 \text{ MeV}$ if not stated otherwise. Since a clear distinction between discrete and convolved strength functions is always possible from the context, both variants are denoted by $R(E^*; \sigma\lambda)$ in the following.

Figures 6.2 and 6.3 illustrate the convergence behavior of discrete and smoothed-out strength functions with the number of Lanczos iterations. As a test case, we consider isoscalar E2 strength distributions of ^{16}O . The strength functions are obtained in the NCSM with an HO basis, using the EM interaction, SRG-evolved up to $\alpha = 0.08 \text{ fm}^4$ in two-body space, for a model space truncated at $N_{\text{max}} = 4$. The strength functions have been obtained with the Lanczos strength-function method with full reorthogonalization. We observe fast convergence of the discrete strength functions with the number of Lanczos iterations, as shown in figure 6.2. Note that convergence takes place gradually, as expected from the Lanczos algorithm, with individual transition strengths to low-lying excited states converging first. The overall shape of the strength distribution—particularly in the relevant energy region up to 60 MeV —is evident already for a few hundred Lanczos iterations. No obvious changes in the discrete strength distributions obtained after 800 and 1000 Lanczos iterations are visible to the naked eye. For smoothed-out strength functions, the convergence behavior is even more remarkable. Figure 6.3 shows the

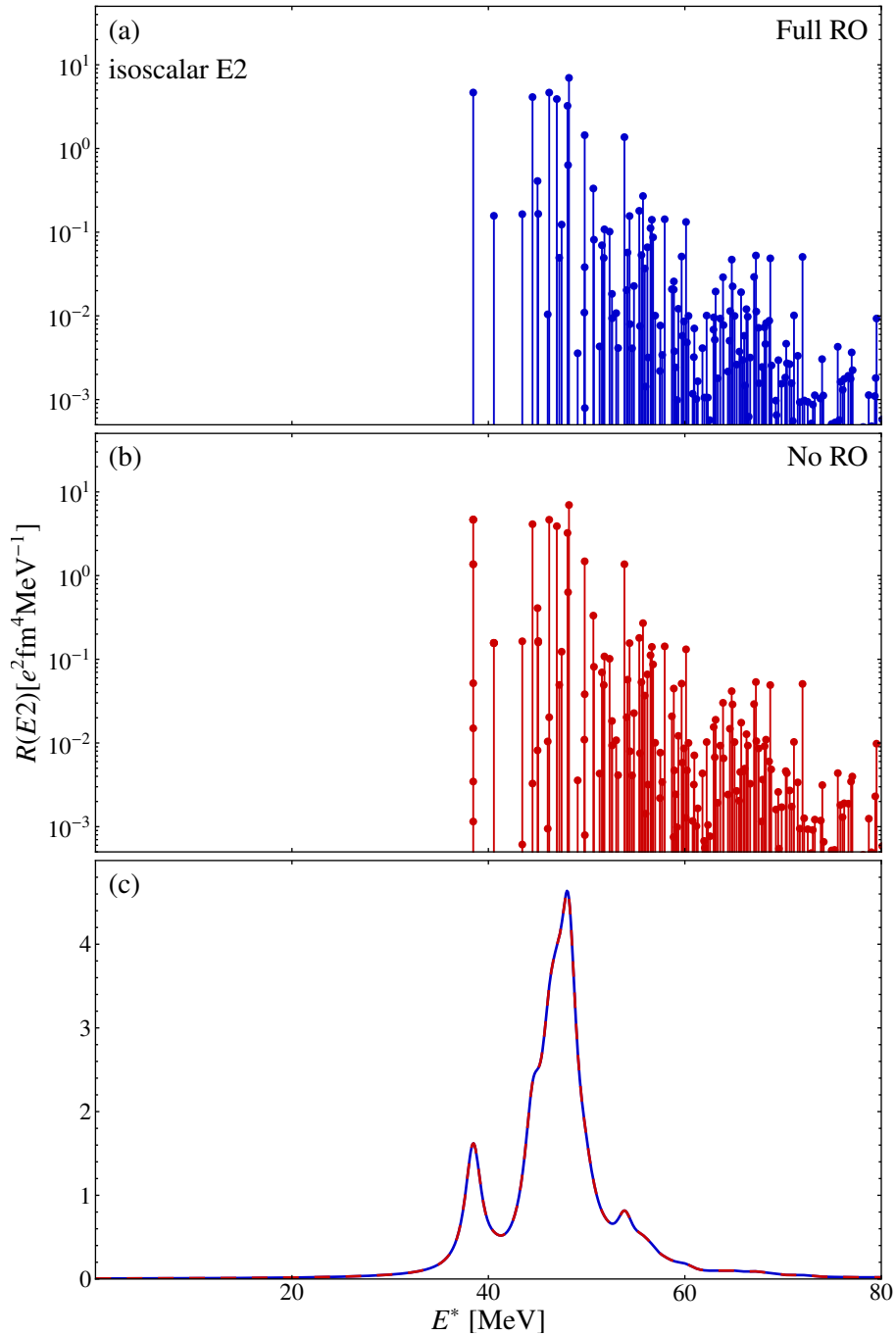


Figure 6.4.: Discrete and smoothed-out isoscalar E2 strength distributions for ^{16}O obtained in the NCSM with HO basis, using the EM interaction, SRG-evolved in two-body space up to $\alpha = 0.08 \text{ fm}^4$. The oscillator frequency is $\hbar\Omega = 20 \text{ MeV}$, the center-of-mass control parameter is $\beta = 1$, and the model space is truncated at $N_{\text{max}} = 4$. Panels (a) and (b) contrast the discrete strength functions obtained by using the Lanczos algorithm with full and without reorthogonalization of the Lanczos basis. Panel (c) shows the corresponding smoothed-out strength functions ((—) and (---), respectively).

strength functions of figure 6.2 for 50, 200, 400, and 1000 Lanczos iterations, convolved with a Lorentzian of width 1 MeV. The strength distributions are all on top of each other, with negligible deviations only for the one obtained after 50 Lanczos iterations. We conclude that a few hundred Lanczos iterations are generally sufficient to fully converge the strength functions.

This underlines the efficiency of the calculation of strength distributions using the IT-NCSM in combination with the Lanczos strength-function method. Generally, if the IT-NCSM calculation for the ground state is feasible, then we can also compute the strength distribution. Since we work with the simplest possible version of the Lanczos algorithm, where only three Lanczos vectors need to be stored, memory requirements are no limiting factor.

As already discussed in the previous section, a disadvantage of the simple Lanczos algorithm is the loss of orthogonality of the Lanczos basis due to round-off errors for finite precision. However, the resulting duplicates in the energy spectrum do not affect the strength distributions, as (6.11) implies a summation of strength corresponding to the same energy. Figure 6.4 shows that discrete and smoothed-out strength functions for the test case obtained with full and without reorthogonalization of the Lanczos basis are identical. The summation of strength to the same energy is indicated in panel (b), where the plot markers represent the individual contributions.

6.3. Model-Space Convergence of Strength Distributions

We study the robustness of the isoscalar electric monopole (E0), isovector electric dipole (E1), and isoscalar electric quadrupole (E2) strength distributions of ^{16}O and ^{24}O obtained in the IT-NCSM by varying the different model-space parameters and truncations. All strength functions are completely converged with respect to the size of the Lanczos basis. Throughout this thesis, we show results obtained for at least 400 Lanczos iterations.

For the following benchmark, we use the SRG-evolved EMN400 interaction with $\alpha = 0.08 \text{ fm}^4$ in NO2B approximation if not stated otherwise. We always employ the HF basis for the calculation of strength functions because of the superior convergence and reduced frequency dependence. We demonstrate this in a direct comparison of the convergence of energy eigenvalues for selected states and strength functions for the IT-NCSM with HF and HO basis. Furthermore, we use a standard set of model-space parameters and truncations, which we vary one by one. The single-particle basis is truncated at $e_{\text{max}} = 12$ with an additional cut on the orbital angular momentum $l_{\text{max}} = 10$. We use the importance-truncation scheme with reference threshold $C_{\text{min}} = 2 \cdot 10^{-4}$ and default importance threshold $\kappa_{\text{min}} = 3 \cdot 10^{-5}$. The model space is truncated at $N_{\text{max}} = 8$ and $N_{\text{max}} = 9$ for natural- and unnatural-parity states, respectively. The oscillator frequency is $\hbar\Omega = 20 \text{ MeV}$, and the center-of-mass control parameter is $\beta = 0.5$.

Note that we restrict the following discussion to the study of the model-space convergence and refer the reader to chapter 8 for applications.

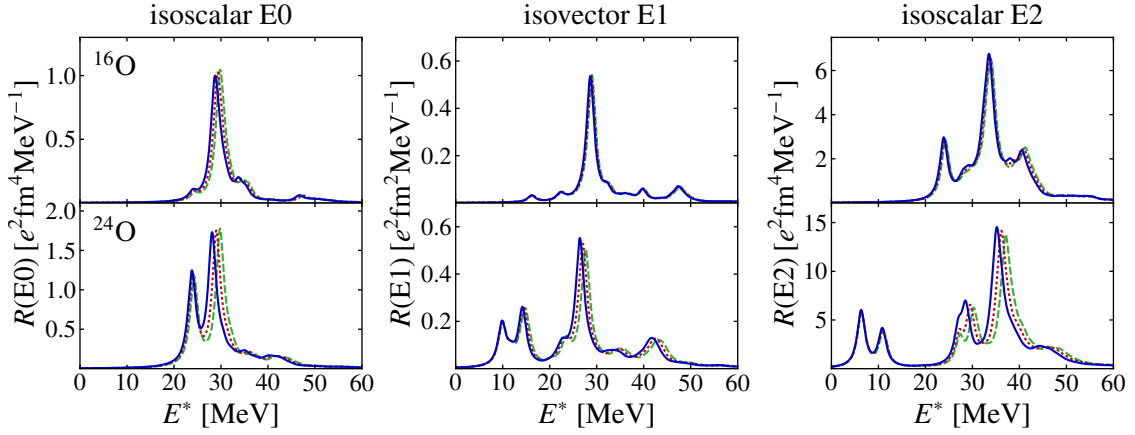


Figure 6.5.: Isoscalar E0, isovector E1, and isoscalar E2 strength functions of ^{16}O and ^{24}O for the importance thresholds $\kappa_{\min} = \{3 \cdot 10^{-5} (\text{—}), 4 \cdot 10^{-5} (\text{⋯}), 5 \cdot 10^{-5} (\text{- - -})\}$. See text for more details.

Importance Threshold

Since most applications in this thesis rely on the use of the importance-truncation scheme in the NCSM, we investigate the dependence of strength functions on the importance threshold. Figure 6.5 shows isoscalar E0, isovector E1, and isoscalar E2 strength functions of ^{16}O and ^{24}O for the importance thresholds $\kappa_{\min} = 3 \cdot 10^{-5}, 4 \cdot 10^{-5}$, and $5 \cdot 10^{-5}$. The overall dependence of the strength functions on the importance threshold is small. In all cases, the variation of the importance threshold does not affect the shape of the strength distributions, it merely shifts the peaks to slightly lower excitation energies for smaller values of κ_{\min} . In particular for ^{16}O and the energy region below 25 MeV in ^{24}O , the strength functions are remarkably stable. We conclude that the importance truncation has only minor effects on the strength distributions, which are less significant than the dependence on the other model-space parameters and truncations as shown below. Consequently, there is no need for an extrapolation of the strength functions to vanishing importance threshold.

Model-Space Truncation N_{\max}

We study the convergence of isoscalar E0, isovector E1, and isoscalar E2 strength functions of ^{16}O and ^{24}O as a function of the model-space truncation N_{\max} . Since we employ an HF single-particle basis and a Hamiltonian in NO2B approximation, both breaking the translational invariance in the many-body basis, we expect the strength functions and their convergence behavior to depend on the center-of-mass control parameter β . Therefore, we compare the convergence of the strength functions for $\beta = 0$, where center-of-mass contaminations are not considered, and for $\beta = 0.5$, which we use as default parameter, in figures 6.6 and 6.7. For ^{16}O , we find that already for moderate model-space sizes, the results are remarkably stable, both, for the prominent giant resonance features and

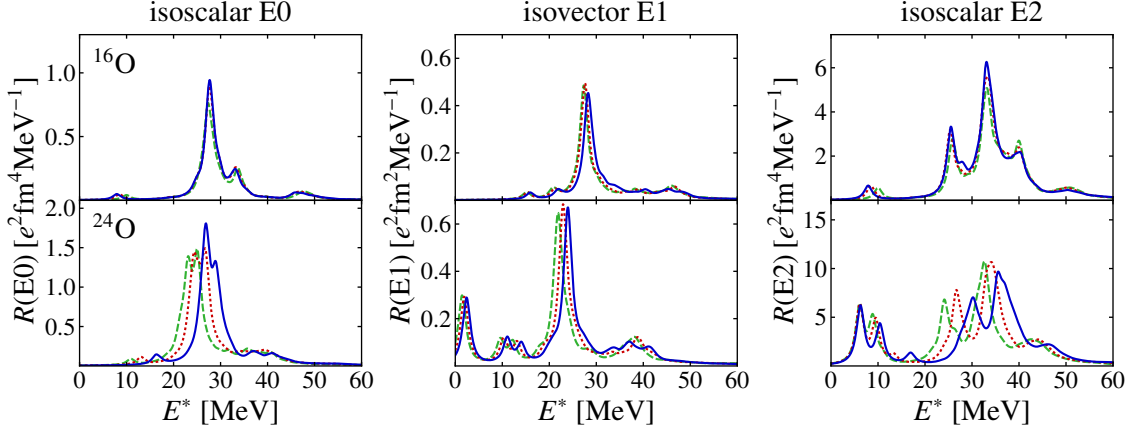


Figure 6.6.: Isoscalar E0, isovector E1, and isoscalar E2 strength functions of ^{16}O and ^{24}O for the model-space truncations $N_{\max} = \{4/5(\text{---}), 6/7(\text{...}), 8/9(\text{—})\}$. The center-of-mass control parameter is $\beta = 0$. See text for more details.

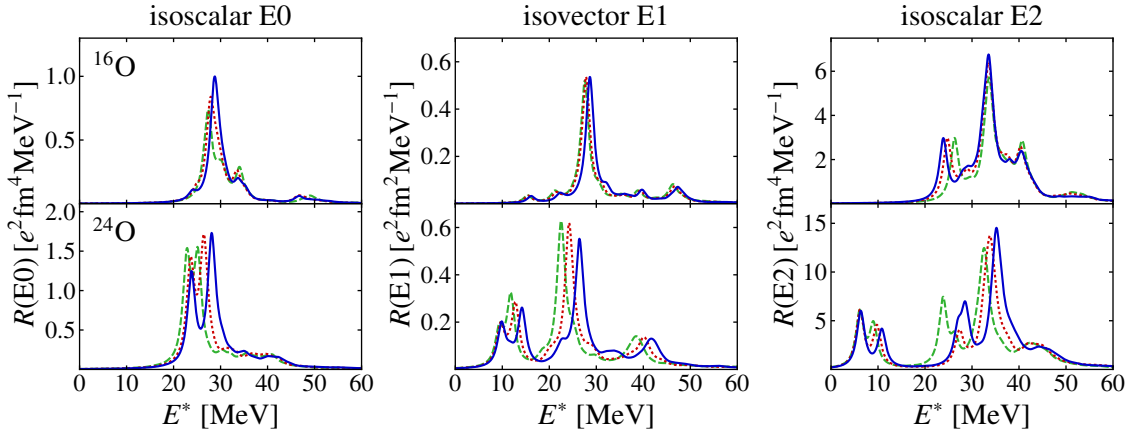


Figure 6.7.: Isoscalar E0, isovector E1, and isoscalar E2 strength functions of ^{16}O and ^{24}O for the model-space truncations $N_{\max} = \{4/5(\text{---}), 6/7(\text{...}), 8/9(\text{—})\}$. The center-of-mass control parameter is $\beta = 0.5$. See text for more details.

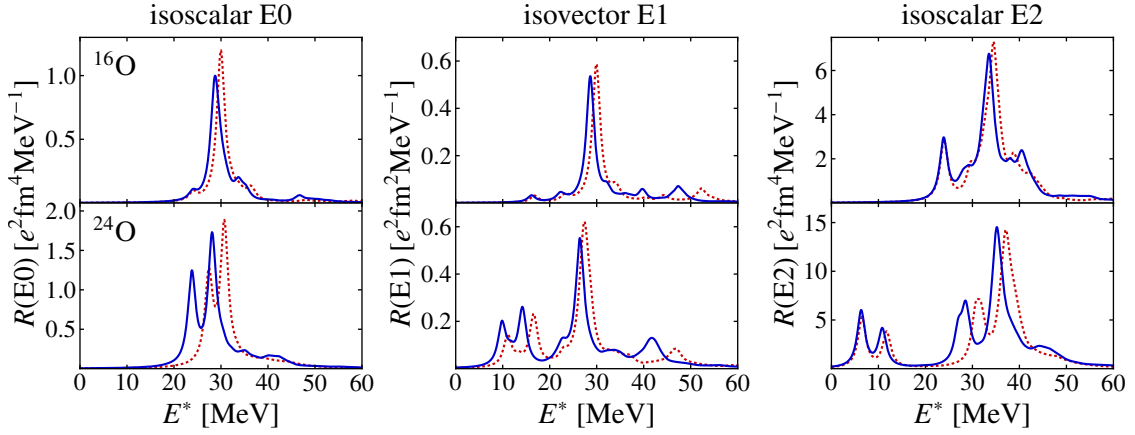


Figure 6.8.: Isoscalar E0, isovector E1, and isoscalar E2 strength functions of ^{16}O and ^{24}O for the frequencies $\hbar\Omega = 20$ MeV (—) and $\hbar\Omega = 24$ MeV (⋯). See text for more details.

for the smaller structures. The largest systematic dependence on N_{\max} appears for the isovector E1 transitions that connect the $J^\pi = 0^+$ ground state to 1^- unnatural-parity states, which are known to exhibit slowly converging excitation energies in the IT-NCSM. The low-lying strength around 7-8 MeV in the isoscalar E0 and E2 strength distributions is due to center-of-mass contaminations and vanishes if a Lawson-type center-of-mass term βH_{cm} is added, as discussed in chapter 4 and shown in figure 6.7. However, the center-of-mass Hamiltonian induces a small dependence of the strength functions on N_{\max} , and, thus, affects the convergence behavior observed in figure 6.6. In practice, we choose small values for β as a compromise between the removal of strength resulting from center-of-mass contaminated states and the favorable convergence with respect to N_{\max} observed for $\beta = 0$. Both, the dependence on N_{\max} as well as on β , are more pronounced in the strength functions of ^{24}O . Also here, the isoscalar E0 and E2 strength around 17 MeV and the isovector E1 strength below 10 MeV found in figure 6.6 disappear for $\beta = 0.5$. Furthermore, the strength functions vary in magnitude for the two values of β , in particular for the isoscalar E2 strength.

We note that no dependence on β is expected for strength functions calculated in the (IT-)NCSM with HO basis because it allows for an (almost) exact factorization of intrinsic and center-of-mass components, providing a possibility to remove center-of-mass contaminations.

Frequency Dependence

For sufficiently large model spaces, the results are expected to be independent of the HO frequency $\hbar\Omega$. We investigate the dependence of the isoscalar E0, isovector E1, and isoscalar E2 strength functions, calculated in the IT-NCSM using an HF basis, on $\hbar\Omega$ as a further indicator of model-space convergence. In figure 6.8, we compare strength functions of ^{16}O and ^{24}O obtained for $\hbar\Omega = 20$ MeV and 24 MeV. We observe a shift of strength in

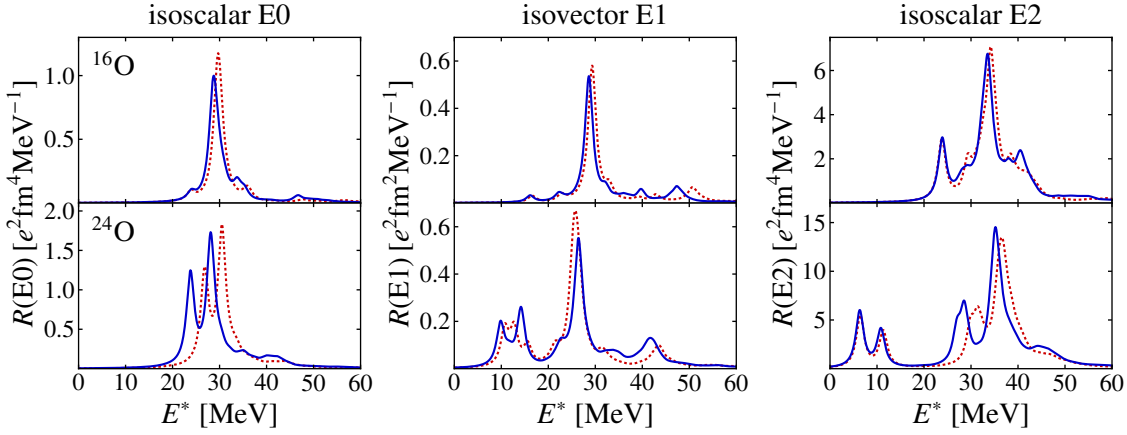


Figure 6.9.: Isoscalar E0, isovector E1, and isoscalar E2 strength functions of ^{16}O and ^{24}O for the single-particle basis truncations $e_{\max} = 12$, $l_{\max} = 10$ (—) and $e_{\max} = 10$ (.....). See text for more details.

the strength distributions for the two frequencies, which is small for ^{16}O and amounts up to 5 MeV for ^{24}O . Additionally, the strength is slightly increased for $\hbar\Omega = 24$ MeV. We note that the low-lying part of the isoscalar E2 strength distributions represents an exception as it remains stable for varying $\hbar\Omega$.

Single-Particle Truncation e_{\max}

Ideally, the strength functions should not depend on the truncations of the single-particle basis. When using the HO basis, this is guaranteed provided that the maximum single-particle energy e_{\max} is chosen sufficiently large such that this truncation is not resolved by the N_{\max} truncation. However, we use the HF single-particle basis by default, which is specific not only for any nucleus but also for any single-particle truncation. Therefore, we assess the effect of different single-particle truncations in figure 6.9, where we compare results for the isoscalar E0, isovector E1, and isoscalar E2 strength distributions of ^{16}O and ^{24}O for single-particle bases truncated at $e_{\max} = 12$ with additional orbital angular momentum cut $l_{\max} = 10$ and $e_{\max} = 10$. The overall structure of the strength distributions remains the same, with robust results in the case of ^{16}O and small effects on the peak positions for ^{24}O . The strength functions obtained in the larger single-particle truncated model space exhibit strength at slightly lower energies, consistent with an improved convergence. We note that the dependence on e_{\max} is of similar magnitude as for the variation of the frequency, as illustrated in figure 6.8.

We note that we should be able to remove all dependencies on $\hbar\Omega$, e_{\max} , and N_{\max} once more computing power becomes available.

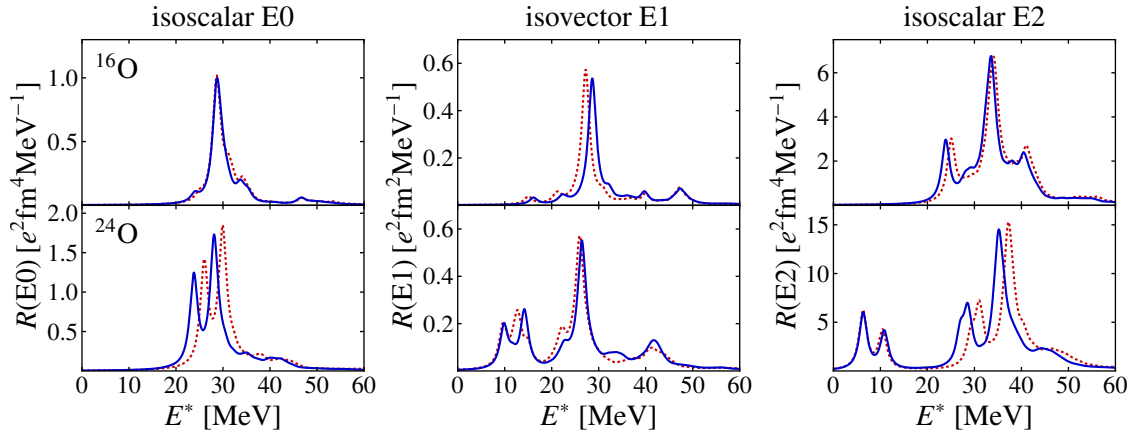


Figure 6.10.: Isoscalar E0, isovector E1, and isoscalar E2 strength functions of ^{16}O and ^{24}O obtained in the IT-NCSM using the EMN400 interaction, SRG-evolved up to $\alpha = 0.08 \text{ fm}^4$ (—) and $\alpha = 0.04 \text{ fm}^4$ (.....). See text for more details.

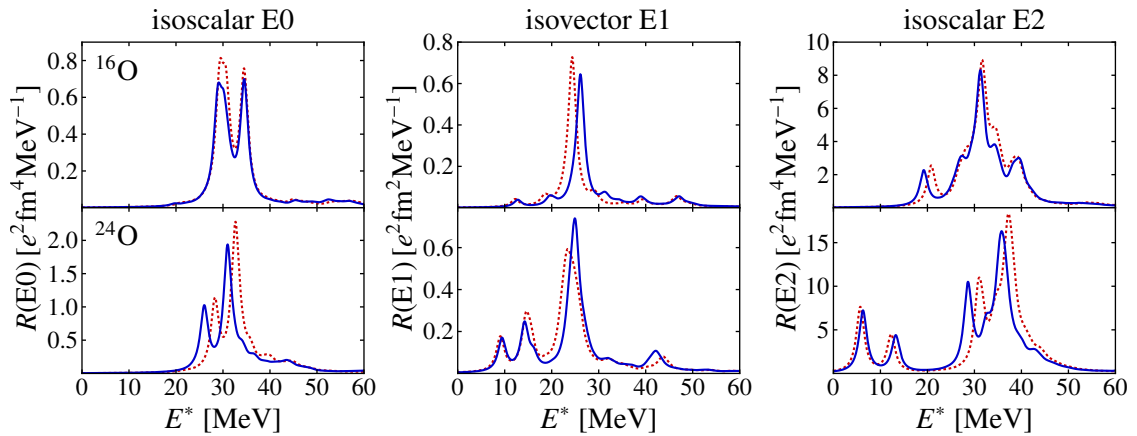


Figure 6.11.: Isoscalar E0, isovector E1, and isoscalar E2 strength functions of ^{16}O and ^{24}O obtained in the IT-NCSM using the $\text{N}^2\text{LO}_{\text{sat}}$ interaction, SRG-evolved up to $\alpha = 0.08 \text{ fm}^4$ (—) and $\alpha = 0.04 \text{ fm}^4$ (.....). See text for more details.

SRG Dependence

In order to enhance the convergence in the IT-NCSM, we use SRG-evolved Hamiltonians. Induced many-body forces are included consistently up to the three-body level, contributions beyond that level are neglected. In order to assess their significance, we study the dependence of the isoscalar E0, isovector E1, and isoscalar E2 strength functions of ^{16}O and ^{24}O on the SRG flow parameter α for the EMN400 and $\text{N}^2\text{LO}_{\text{sat}}$ interactions, see figures 6.10 and 6.11, respectively. We find robust results for the flow parameters $\alpha = 0.04 \text{ fm}^4$ and $\alpha = 0.08 \text{ fm}^4$. The isoscalar E0 and E2 strength functions are shifted to slightly lower energies for $\alpha = 0.08 \text{ fm}^4$, indicating an improved model-space convergence behavior due to the softer Hamiltonian. Only the isovector E1 strengths are moved to somewhat higher energies because of the different convergence rates of the unnatural-parity states with respect to the natural-parity ground state. We note that the dependence of the strength functions on the SRG flow parameter is of the same magnitude for both interactions and comparable to the effects observed in the variation of the single-particle basis truncation e_{max} and the frequency $\hbar\Omega$, cf. figures 6.8 and 6.9.

Choice of Single-Particle Basis

In the following, we demonstrate that the convergence of strength distributions is enhanced when an HF single-particle basis is used instead of the HO single-particle basis. Figures 6.12 and 6.13 display the N_{max} convergence of strength functions of ^{16}O obtained in the IT-NCSM with HF and HO single-particle basis, respectively, using the SRG-evolved EMN400 interaction for two frequencies. Note that the 3N interaction has been included explicitly in the case of the IT-NCSM with HO basis, and the center-of-mass control parameter is set to $\beta = 1$. We have already seen in the previous discussion that the strength distributions obtained in the IT-NCSM with HF single-particle basis are remarkably robust with respect to variation of N_{max} and $\hbar\Omega$. This is seen even more clearly in figure 6.12, where each row shows the N_{max} convergence of the strength functions for one of the frequencies, allowing for a direct comparison of their shape and location. However, when using the HO single-particle basis, the convergence of the strength functions with respect to N_{max} is significantly worse, see figure 6.13. Although the structure of the strength distributions is already present for the smaller model spaces, their positions exhibit a sizable dependence on the model-space truncation, in particular for the isoscalar E0 and E2 transition strengths. Moreover, the results depend notably on $\hbar\Omega$.

As an outlook to possible future applications, we additionally show strength functions obtained in the IT-NCSM with a natural-orbital single-particle basis in figure 6.14 employing the EMN400 interaction, SRG-evolved up to $\alpha = 0.08 \text{ fm}^4$, in NO2B approximation. The center-of-mass control parameter is chosen $\beta = 0.5$. Only recently, the IT-NCSM has been extended to using this basis [Tic+18], which is generated from an HF basis by including perturbative corrections for the one-body density matrix. First applications in the conventional IT-NCSM have proven that this basis yields fast converging absolute energies, similar to that obtained in the IT-NCSM with HO basis, but the frequency dependence is completely removed. This behavior is also observed in the strength distributions: The N_{max} dependence of the strength functions resembles the one of figure 6.13, with

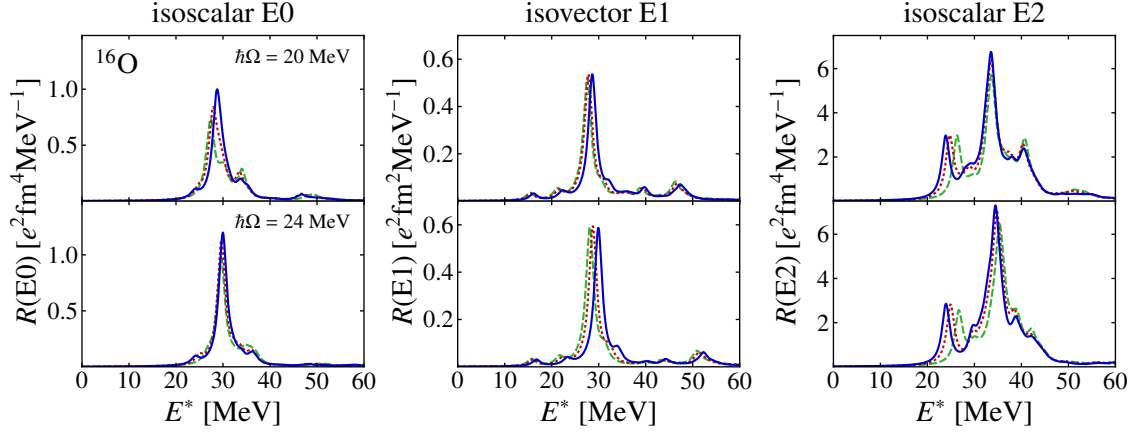


Figure 6.12.: Isoscalar E0, isovector E1, and isoscalar E2 strength functions of ^{16}O obtained in the IT-NCSM with HF basis for $N_{\text{max}} = \{4/5(\text{---}), 6/7(\text{...}), 8/9(\text{—})\}$. The two rows correspond to the frequencies $\hbar\Omega = 20\text{ MeV}$ and $\hbar\Omega = 24\text{ MeV}$. See text for more details.

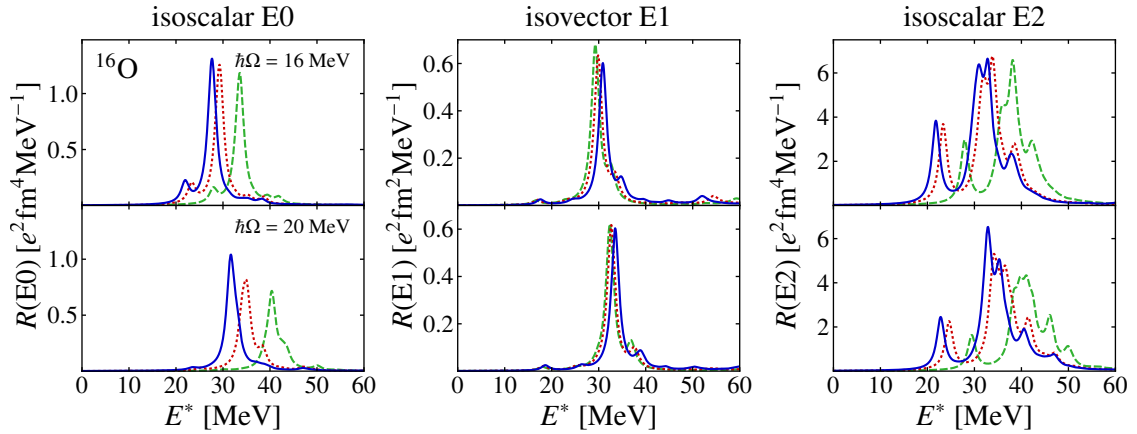


Figure 6.13.: Isoscalar E0, isovector E1, and isoscalar E2 strength functions of ^{16}O obtained in the IT-NCSM with HO basis for $N_{\text{max}} = \{4/5(\text{---}), 6/7(\text{...}), 8/9(\text{—})\}$ using the SRG-evolved EMN400 interaction with explicitly included 3N interaction. The center-of-mass control parameter is $\beta = 1$. The two rows correspond to the frequencies $\hbar\Omega = 16\text{ MeV}$ and $\hbar\Omega = 20\text{ MeV}$. See text for more details.

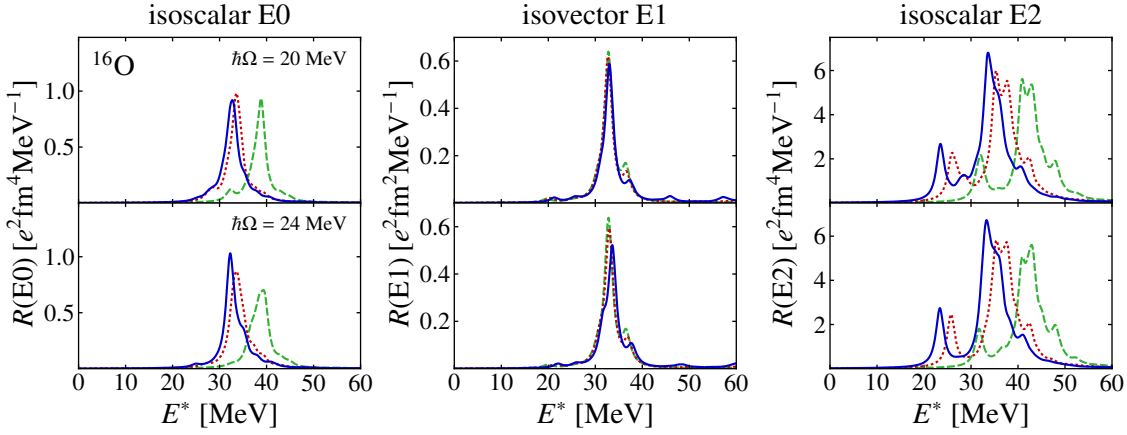


Figure 6.14.: Isoscalar E0, isovector E1, and isoscalar E2 strength functions of ^{16}O obtained in the IT-NCSM with natural-orbital basis for $N_{\max} = \{4/5(\text{---}), 6/7(\text{...}), 8/9(\text{—})\}$ using the SRG-evolved EMN400 interaction. The center-of-mass control parameter is $\beta = 0.5$. The two rows correspond to the frequencies $\hbar\Omega = 20$ MeV and $\hbar\Omega = 24$ MeV. See text for more details.

improved convergence in case of the isoscalar E0 and isovector E1 strength and slightly worse convergence in case of the isoscalar E2 strength. However, the strength distributions are located at the same energies for the two frequencies.

The convergence pattern of the strength functions obtained in the IT-NCSM with HF and HO basis can be understood from the corresponding convergence of the excitation energies, which are shown along with the absolute energies for the 0^+ ground state and the lowest 1^- and 2^+ states in figures 6.15 and 6.16. In the IT-NCSM with HF basis, the absolute energies of the ground state and the low-lying excited states decrease by a certain constant value in each N_{\max} step and, thus, show no signs of convergence nor allow for a reliable extrapolation to an infinite model space. This behavior is observed for the two frequencies considered and is characteristic for the IT-NCSM with HF basis, where convergence with respect to N_{\max} is only reached for N_{\max} large enough to resolve the limits on the available matrix elements. However, this particular dependence of the absolute energies on N_{\max} results in stable excitation energies, which are also approximately independent of $\hbar\Omega$. Since the convergence behavior of the strength functions is driven primarily by the convergence of the excitation energies, the HF basis represents an excellent choice for the calculation of strength functions in the IT-NCSM. In contrast, the absolute energies of the ground and low-lying excited states in the IT-NCSM with HO basis show improved convergence, allowing for an N_{\max} extrapolation using exponential functions. However, ground and excited states do not converge at the same rate, resulting in a significant dependence of the excitation energies on N_{\max} and also on $\hbar\Omega$, manifesting itself in the disadvantageous convergence pattern of the strength functions.

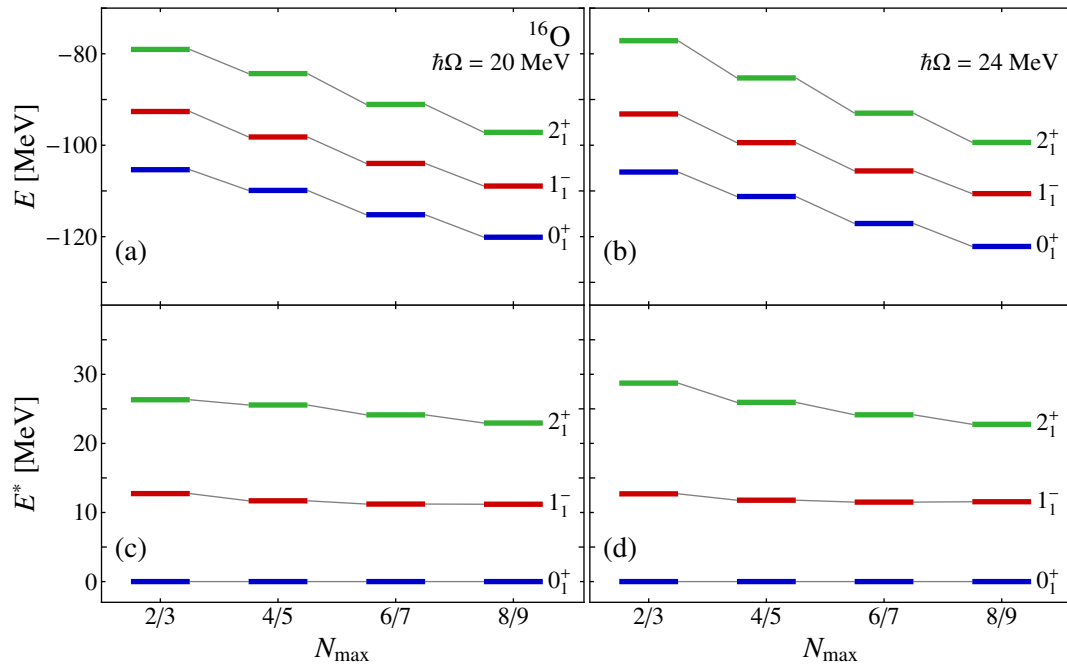


Figure 6.15.: N_{\max} convergence of absolute and excitation energies of the 0^+ ground state and the first excited 1^- and 2^+ states in ^{16}O obtained in the IT-NCSM with HF basis. The columns correspond to the frequencies $\hbar\Omega = 20$ MeV ((a) and (c)) and $\hbar\Omega = 24$ MeV ((b) and (d)). See text for more details.

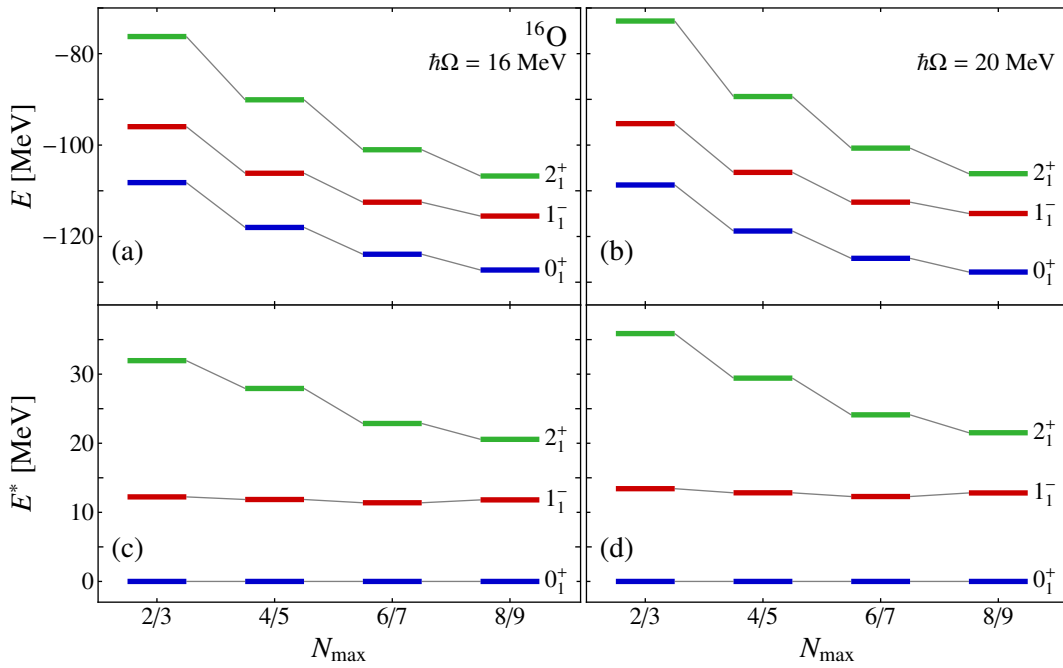


Figure 6.16.: N_{max} convergence of absolute and excitation energies of the 0^+ ground state and the first excited 1^- and 2^+ states in ^{16}O obtained in the IT-NCSM with HO basis using the SRG-evolved EMN400 interaction with explicitly included 3N interaction. The columns correspond to the frequencies $\hbar\Omega = 16$ MeV ((a) and (c)) and $\hbar\Omega = 20$ MeV ((b) and (d)), the center-of-mass control parameter is $\beta = 1$. See text for more details.

7. Applications of the IT-VSSM

Using the IT-VSSM with importance-threshold and energy-variance extrapolation, we discuss spectra of several medium-mass nuclei. The effective valence-space interactions employed are presented in section 7.1. In section 7.2, we benchmark the IT-VSSM by comparing energies of ground and excited states of pf -shell nuclei to available results from exact diagonalizations and the Monte-Carlo shell model (MCSM). Section 7.3 is dedicated to a study of the performance of effective valence-space Hamiltonians derived in the IM-SRG for single- and multi-shell valence spaces. These new developments offer unique perspectives for detailed nuclear-structure investigations beyond the reach of the conventional VSSM as they allow for the description of any open-shell medium-mass nucleus in extended valence spaces based on chiral Hamiltonians, which are constrained by few-body data only. Finally, we study the structure of neutron-deficient tin isotopes as a first application of the IT-VSSM in a large-scale valence space, the gds shell, in conjunction with these modern effective Hamiltonians. The importance-truncation scheme allows us to obtain converged results. In contrast, previous VSSM calculations were restricted to using phenomenological interactions and severe particle-hole truncations.

7.1. Effective Valence-Space Hamiltonians

The IT-VSSM requires effective Hamiltonians tailored to the specific valence spaces as input. The ones we use are either of phenomenological origin—these allow for a benchmark of the IT-VSSM against available results—or are derived in the IM-SRG starting from SRG-evolved chiral Hamiltonians. This section overviews the phenomenological valence-space Hamiltonians used and how the IM-SRG can be adapted to produce such effective Hamiltonians.

Traditionally, effective valence-space interactions are constructed using renormalized NN interactions combined with phenomenological fits of matrix elements to nuclei within the valence space [Cau+05; Cor+09; KB66; HKO95]. Though this phenomenological approach allows for a rather accurate description, it lacks a rigorous connection to the underlying nuclear interaction and does not provide a consistent framework for the treatment of observables other than the energy.

Recently, a set of novel approaches to systematically derive valence-space Hamiltonians and operators has been proposed [TBS12; Bog+14; Jan+14; Dik+15]. They offer new insights into valence-space Hamiltonians and can be linked to *ab initio* calculations.

In the following, we provide an overview of the phenomenological valence-space interactions we use in this thesis for benchmark purposes of the IT-VSSM. Then, we outline the IM-SRG and how this *ab initio* approach can be used for the construction of effective valence-space Hamiltonians.

Phenomenological Interactions

For the description of some pf -shell nuclei in the IT-VSSM, we use the effective interaction “GXPF1A” [Hon+05]. It has been derived from a realistic G -matrix interaction with core-polarization corrections based on the Bonn-C potential [HKO95] by adjusting both, single-particle and two-body matrix elements to energy data of a wide range of pf -shell nuclei in a refined fitting procedure. The latter implies a successive variation of the interaction parameters followed by the numerical solution of the nuclear eigenvalue problem, using the most recent Hamiltonian resulting from the variation. These steps are repeated until the total squared deviation of the calculated eigenvalues from the experimental set of energy data is minimized. The GXPF1A interaction successfully reproduces spectra of nuclei almost all over the entire pf shell, with difficulties only close to the borders of the valence space. These nuclei require an extension of the valence space out of the pf shell.

Such an extension is realized in the “PFG9B3” interaction [Ots; Hon+], which is built on the GXPF1A interaction with additional G -matrix elements describing the interaction between the pf orbits and the $g_{7/2}$ orbit. Additionally, the single-particle energy of the $g_{7/2}$ orbit has been modified. This interaction has been used before for the description of ^{64}Ge in the MCSM [Shi+10; Shi+12].

Valence-Space Interactions from the In-Medium Similarity Renormalization Group

The IM-SRG [TBS11; Her+13; Her+16] is an *ab initio* approach for the calculation of nuclear ground states, where the Hamiltonian is at the heart of the method. As the free-space SRG, the IM-SRG is based on a flow equation (2.3), but, in contrast, is solved directly in the A -body system of interest. To this aim, all operators are normal ordered with respect to a given reference, e.g., the HF ground state. Then, a continuous unitary transformation is performed for the normal-ordered nuclear many-body Hamiltonian that decouples the reference state from all particle-hole excitations. Typically, the reference state becomes the ground state once the Hamiltonian is fully evolved, and the ground-state energy of the nucleus under consideration can be extracted. Note that the flow parameter in the IM-SRG is typically denoted by s . In principle, the IM-SRG needs to be carried out in A -body space because higher-order contributions appear as the commutator on the right-hand side of (2.3) is evaluated. For practical purposes, the IM-SRG needs to be truncated at a given rank of normal-ordered operators $n \leq A$, presently at $n = 2$, and unitarity is therefore formally violated. Induced many-body contributions are, however, taken into account partly by the normal-ordered zero-, one-, and two-body terms.

In its basic formulation, the IM-SRG is restricted to the description of closed-shell nuclei only. One possible, straight-forward extension is to generate non-empirical valence-space Hamiltonians and operators, which can then be fed as input into subsequent VSSM calculations [TBS11; TBS12; Bog+14; Str+16; Her+16; Str+17; Par+17; Her17], providing access to energies of ground and excited states of both, open- and closed-shell nuclei, as well as other observables, such as transitions. Here, the valence space is decoupled simultaneously from the inert core and the excluded space. This is accomplished by defining a reference state for the inert core and dividing the single-particle basis into hole, valence, and non-valence states. Treating all nucleons, i.e., core and valence nucleons,

as active degrees of freedom, we suppress all matrix elements that couple the reference state to excitations, and, additionally, matrix elements that connect states consisting of the reference state plus A_{val} particles in the valence space from states containing non-valence states.

Since the nuclear Hamiltonian is, in the simplest formulation, a normal-ordered two-body operator, effects of 3N forces between the valence nucleons are not taken into account. They are, however, vital to obtain satisfactory agreement with experiment and *ab initio* calculations that are performed directly for the nucleus under consideration. As a remedy, targeted [Str+16] and ensemble [Str+17] normal-ordering techniques have been introduced. Targeted normal ordering uses a reference state that is normal ordered with respect to the nearest closed subshell, whereas ensemble normal ordering employs an ensemble reference built from fractionally filled orbitals. In both cases, the IM-SRG decoupling is carried out with respect to the specific reference state and the interaction is re-normal ordered afterward with respect to the core for use in the (IT-)VSSM.

7.2. IT-VSSM Benchmark with Phenomenological Interactions

We aim to validate the IT-VSSM by comparing spectra of *pf*-shell nuclei at the limit of routine VSSM calculations and beyond against results from exact diagonalizations and the MCSM [Ots+01]. As a first test case, we consider ^{56}Ni in a valence space comprising the *pf* shell, using the GXPF1A Hamiltonian [SBR16]. The full *m*-scheme dimension amounts to $1.09 \cdot 10^9$ and is feasible in large-scale VSSM calculations. The same nucleus, valence space, and Hamiltonian has been considered in [Hor+06], where the convergence of the first three 0^+ , 2^+ , 4^+ , and 6^+ states has been studied as a function of the model-space truncation parameter T_{max} using exact diagonalizations carried out with the ANTOINE [Cau04; CN99] and CMICHSM [HBZ03] codes. These results provide an excellent reference for benchmarking the IT-VSSM. We note that the lowest excitation energies found in [Hor+06] agree very well with experiment. This is not surprising because the fitting procedure in the derivation of this Hamiltonian includes some states of ^{56}Ni .

Figure 7.1 shows the absolute energies of the lowest six natural-parity states of ^{56}Ni relative to the ^{40}Ca core for three reference thresholds C_{min} as a function of the importance threshold κ_{min} and the energy variance ΔE^2 . Note that the κ_{min} axis is reversed. Compared to typical excitation energies, which are of the order of 1 MeV, the κ_{min} and C_{min} dependence—spanning typically about 100 keV—is very weak. Both, the threshold- and variance-extrapolated energies, are in excellent agreement with results of the full VSSM, where available. The second 0^+ state, however, shows a quite distinct behavior. Its dependence on κ_{min} and C_{min} is stronger than for all other states and the energy variances are significantly larger. This indicates a particularly complicated structure, in this case due to deformation, resulting in many small components in the basis expansion of the eigenstate and, thus, a less accurate approximation in the IT model space. The simple threshold extrapolation does not capture the contribution of all these small components and cannot correct for the sizable C_{min} dependence. The variance extrapolation, however, yields a reliable result—independent of C_{min} —and even restores the correct level ordering in excellent agreement with the full VSSM. This demonstrates that the variance

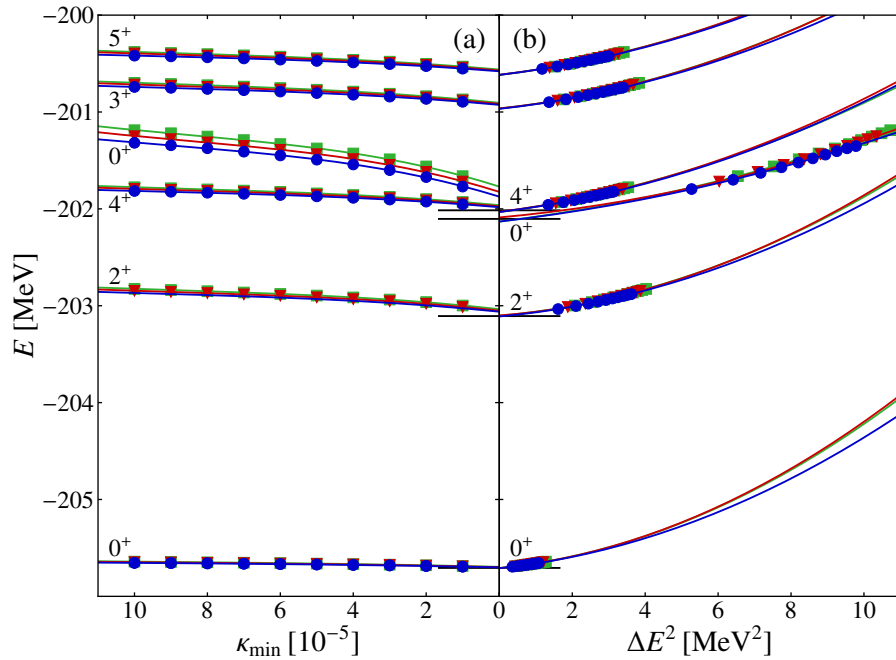


Figure 7.1.: Threshold (a) and energy-variance (b) extrapolation of the energies of the six lowest natural-parity states of ^{56}Ni relative to the ^{40}Ca core obtained in the IT-VSSM for the reference thresholds $C_{\min} = \{1(\bullet), 2(\blacktriangledown), 3(\blacksquare)\} \cdot 10^{-4}$. We use the GXPF1A valence-space Hamiltonian for the pf shell and $T_{\max} = 16$. For the threshold and variance extrapolations, polynomials of order three and two have been employed, respectively. The horizontal lines denote the results of the full model spaces extracted from [Hor+06].

extrapolation offers significant advantages, particularly for the description of these fragile states.

Figure 7.2 summarizes the extrapolated energies for the lowest six natural-parity states of ^{56}Ni relative to the ^{40}Ca core. The threshold-extrapolated results for a sequence of T_{\max} -truncated calculations are shown in the main part of the plot, followed by the spectrum obtained from the variance extrapolation for $T_{\max} = 8$ and the full VSSM result. Starting from $T_{\max} = 8$, the spectrum is rather stable and in good agreement with the full VSSM results, except for the second 0^+ state discussed above. The energy-variance extrapolation for $T_{\max} = 8$ yields excellent agreement with the full VSSM for all states.

A first application of the IT-VSSM in a valence space covering more than one major shell was also published in [SBR16]. We consider a $pf g_{7/2}$ valence space using the effective PFG9B3 Hamiltonian and study ^{60}Zn and ^{64}Ge . The full m -scheme dimensions are $2.2 \cdot 10^{13}$ and $1.7 \cdot 10^{14}$, respectively. These extended model spaces are susceptible to center-of-mass spuriousities. Therefore, we use the Lawson-type prescription to diagnose center-of-mass contaminations, i.e., we use the Hamiltonian (4.6) in combination with (4.10) for the solution of the eigenvalue problem. Particularly, ^{64}Ge has been studied before in the

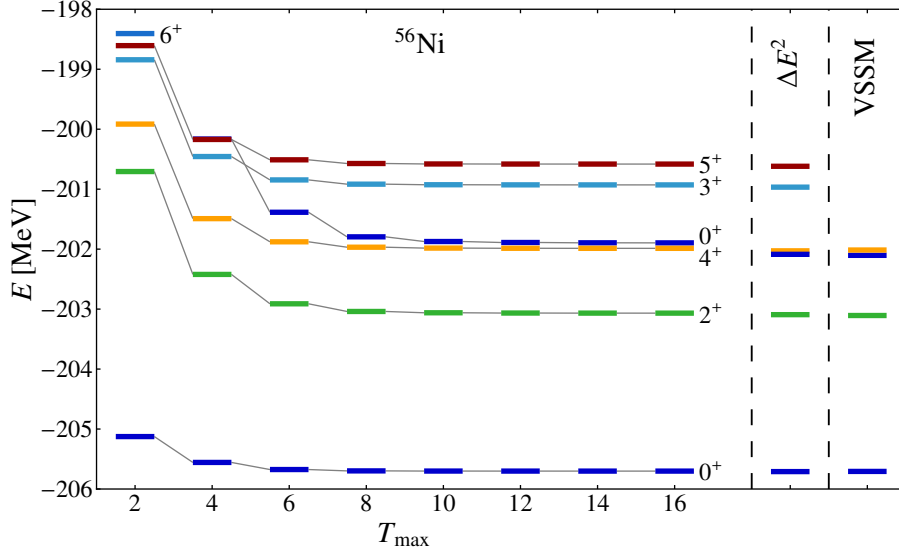


Figure 7.2.: Natural-parity spectrum of ^{56}Ni as a function of T_{\max} in terms of absolute energies relative to the ^{40}Ca core computed in the IT-VSSM with $C_{\min} = 1 \cdot 10^{-4}$ using the GXPF1A valence-space Hamiltonian for the pf shell. The right-hand columns show the results of an energy-variance extrapolation (ΔE^2) and the full VSSM energies extracted from [Hor+06].

MCSM using the same interaction [Shi+10; Shi+12]. The MCSM follows a different approach to extend the conventional VSSM to larger model spaces. By generating a deformed many-body basis in a refined stochastic-sampling procedure with subsequent symmetry restoration, extremely reduced basis dimensions—of the order of ten to 100—are sufficient to obtain good approximations of the exact energy eigenvalues. Recently, a study using the density-matrix renormalization group with the VSSM targeted the same nucleus and valence space [Leg+15]. These competing approaches highlight the difficulty of these calculations.

Figure 7.3 shows the absolute energies of the few lowest states of ^{60}Zn and ^{64}Ge relative to the ^{40}Ca core as a function of the importance threshold and the energy variance as well as the respective extrapolations, for which we employ polynomials of order three and two. The results for the κ_{\min} and ΔE^2 sequences are obtained in IT-VSSM calculations using the reference threshold $C_{\min} = 2 \cdot 10^{-4}$ and truncations $T_{\max} = 10$ and $T_{\max} = 6$, respectively. The first excited state of ^{64}Ge exhibits an ill-behaved dependence on the energy variance and is not shown. The dependence of the energies on the importance threshold and the energy variance is very smooth for ^{60}Zn , and the extrapolations yield similar results. However, for ^{64}Ge , we observe a distinct bending toward lower energies around $\kappa_{\min} = 4 \cdot 10^{-5}$ for the two states considered, indicating that basis states contributing with small absolute amplitudes to the basis expansion of the eigenstates significantly affect the energies. Evidently, a variation of the polynomial degree—we show extrapolations using polynomials of order two and three here—or the omission of selected data points (not

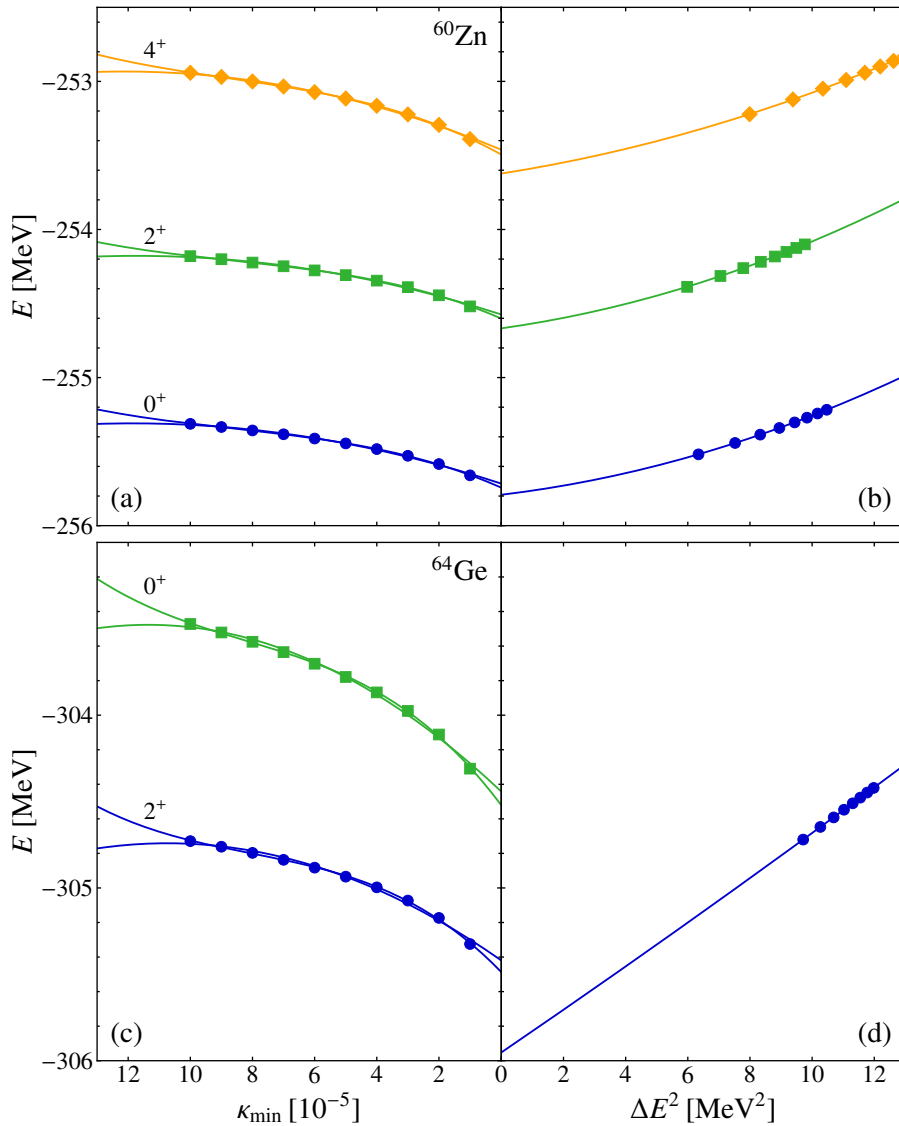


Figure 7.3.: Threshold ((a) and (c)) and energy-variance ((b) and (d)) extrapolation of the energies of the lowest natural-parity states of ^{60}Zn and ^{64}Ge relative to the ^{40}Ca core obtained in the IT-VSSM with $C_{\min} = 2 \cdot 10^{-4}$. We use the PFG9B3 Hamiltonian for the $pf g_{7/2}$ valence space. The results in panels (a) and (c) have been determined for $T_{\max} = 10$, and the results in panels (b) and (d) for $T_{\max} = 6$. For the threshold extrapolations, polynomials of order two and three have been employed, while a polynomial of order two has been used for the variance extrapolation. For ^{64}Ge , the energy-variance extrapolation is shown for the ground state only.

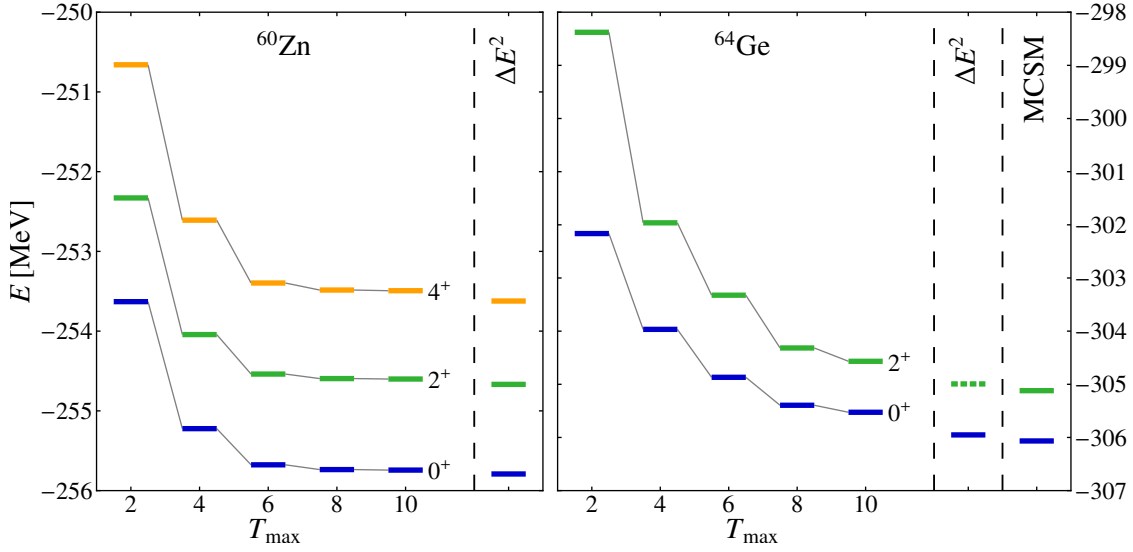


Figure 7.4.: Energies of the lowest natural-parity states of ^{60}Zn and ^{64}Ge relative to the ^{40}Ca core computed in the IT-VSSM with $C_{\min} = 2 \cdot 10^{-4}$ using the PFG9B3 valence-space Hamiltonian as a function of T_{\max} . The right-hand columns show the results from the energy-variance extrapolation (ΔE^2) of the $T_{\max} = 6$ results. The dashed bar shows an approximation for the energy of the 2^+ state calculated from the excitation energy obtained in the IT-VSSM for $T_{\max} = 10$ and the ΔE^2 -extrapolated ground-state energy. For ^{64}Ge , the MCSM results [Shi+10; Shi+12] are shown for comparison.

shown) would notably impact the threshold extrapolation and its uncertainties. The variance extrapolation for the ground state yields an energy of about 0.5 MeV lower than the threshold-extrapolated result, due to effects of the C_{\min} and T_{\max} truncations not captured in the threshold extrapolation.

The absolute energies of the lowest states in ^{60}Zn and ^{64}Ge extracted from the above threshold extrapolation for a sequence of T_{\max} -truncated spaces and from the energy-variance extrapolation for $T_{\max} = 6$ are summarized in figure 7.4. Whereas the spectra seem converged at $T_{\max} = 8$ for ^{60}Zn and agree well with the variance-extrapolated results, there is still some dependence on T_{\max} for ^{64}Ge . The variance extrapolation efficiently corrects for the missing 0.5 MeV in the ground-state energy obtained in the simple threshold extrapolation, yielding agreement with the MCSM result. The dashed bar indicates an approximation for the energy of the first excited state in ^{64}Ge , determined from the variance-extrapolated result for the ground-state energy and the threshold-extrapolated excitation energy for $T_{\max} = 10$. The sensitivity of the threshold-extrapolated energies on the various truncations, i.e., C_{\min} , κ_{\min} , and T_{\max} , is due to the strong deformation of ^{64}Ge , whose description requires many small components in the basis expansion. The variance extrapolation captures these subtle effects and yields excellent agreement with the MCSM results, where the very small remaining deviation is due to the

treatment of center-of-mass contaminations, not taken into account in the MCSM.

These applications demonstrate the robustness of the IT-VSSM and its ability to deal with extremely large valence spaces.

7.3. Benchmark of Valence-Space Interactions from the IM-SRG

Based on the reliability of the IT-VSSM for the description of nuclei in large-scale valence spaces, we study effective valence-space Hamiltonians derived in the IM-SRG. Alternative approaches to derive effective valence-space Hamiltonians in an *ab initio* framework, e.g., within the CC method, have been proposed recently [Jan+14; Jan+16; Dik+15]. In a first step, we employ an *sd*-shell valence space and demonstrate the robustness of the IM-SRG approach to valence spaces comprising a single major HO shell. Then, we illustrate problems arising for multi-shell valence spaces.

We note that, up to now, all energies calculated in the IT-VSSM were determined using phenomenological valence-space Hamiltonians, which are adjusted to experimental data of the nuclei they are built to describe, and are given relative to the core. In contrast, the IM-SRG computes the valence-space Hamiltonian from a realistic nucleonic potential that is fitted to few-body data only. It also provides the core energy, allowing for the calculation of energies without need for empirical adjustments.

Single-Shell Valence Spaces

In a first step, we benchmark effective valence-space Hamiltonians from the IM-SRG in a single HO major shell. Such valence spaces and Hamiltonians have already been used successfully to calculate spectra of light and medium-mass nuclei, and the results agreed well with those from the NCSM and other many-body methods, the VSSM using established phenomenological Hamiltonians, and experiment [TBS12; Bog+14; Str+16; Str+17]. By monitoring the eigenstates as a function of the IM-SRG flow parameter and comparing to exact calculations, where all nucleons are treated as active degrees of freedom, we validate the decoupling of the valence space from the core and excluded space. As a test case, we consider ^{18}O in a valence space comprising the orbits of the *sd* shell. The effective valence-space Hamiltonian is calculated in the IM-SRG using the White generator [TBS11; Whi02; Her+16] from the free-space SRG-evolved EMN400 interaction with flow parameter $\alpha = 0.08 \text{ fm}^4$ [VR16].

As a first indicator of the robustness of the IM-SRG flow, we show the ^{16}O core energy for the effective valence-space Hamiltonian for $A = 18$ nuclei in the *sd* shell in figure 7.5. The core energy corresponds to the expectation value of the A -dependent IM-SRG-evolved Hamiltonian with respect to the Slater determinant of the core. It is typically different from the ground-state energy of the core nucleus because the intrinsic kinetic energy in the initial Hamiltonian is adjusted to the particle number of the target nucleus. The core energy displayed in figure 7.5 exhibits a fast and monotonous convergence behavior as a function of the IM-SRG flow parameter s , and the results are stable from $s \approx 0.1$ on.

The left column of figure 7.6 shows the absolute and excitation energies of the lowest six natural-parity states of ^{18}O obtained in the VSSM using this effective *sd*-shell Hamiltonian.

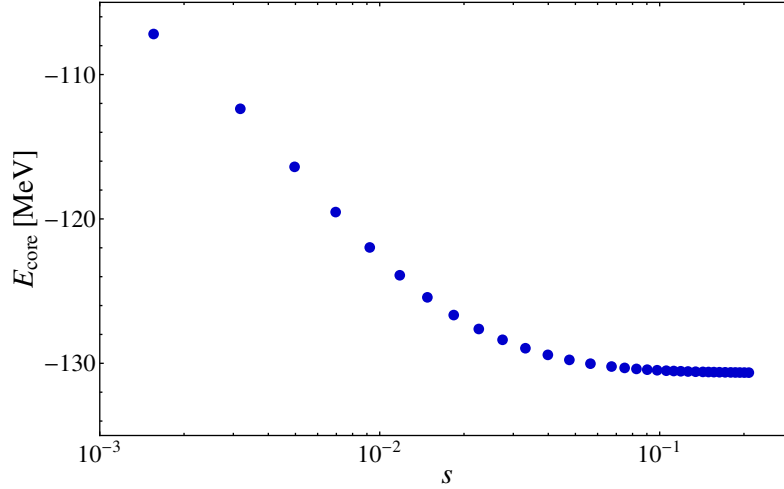


Figure 7.5.: Energy of the ^{16}O core of an sd -shell valence-space Hamiltonian for $A = 18$ nuclei obtained in the IM-SRG with the White generator as a function of the flow parameter s . The initial Hamiltonian uses the EMN400 interaction, SRG-evolved up to $\alpha = 0.08 \text{ fm}^4$.

As for the core energy, we observe stable results for all states for IM-SRG flow parameters $s \gtrsim 0.1$. The convergence pattern of the absolute energies with respect to s is similar to that of the core energy. The middle and right columns illustrate the respective energies obtained in the IT-NCSM using the same IM-SRG-evolved Hamiltonian in $e_{\text{max}} = 2$ and $e_{\text{max}} = 3$ model spaces. We have used $C_{\text{min}} = 2 \cdot 10^{-4}$ and have ensured that all energies are converged with respect to N_{max} . Note that we show the dependence of the IT-NCSM results on the IM-SRG flow parameter only for the calculations in the $e_{\text{max}} = 2$ model space, and limit the results in the $e_{\text{max}} = 3$ model space to the results for $s = 0.21$.

The comparison of the VSSM results to these calculations allows for a direct validation of the decoupling of the valence space from the core and excluded space. Figure 7.7 sketches the matrix representation in an ideal situation, where the matrix elements coupling the core, valence, and excluded space vanish. The IT-NCSM model space for $e_{\text{max}} = 2$ just comprises all core and valence orbits but treats all nucleons as active degrees of freedom. Thus, a comparison of these results against those obtained in the VSSM provides a direct test of the decoupling of the valence space from the core. Including higher orbits in the IT-NCSM model space additionally probes the decoupling of the valence space from the excluded space. We observe a very similar convergence behavior of both, absolute and excitation energies obtained in the VSSM and IT-NCSM in the $e_{\text{max}} = 2$ model space, as a function of s . A slight difference is visible for small values of s , where, e.g., the absolute energies obtained in the IT-NCSM are about 5 MeV lower than in the VSSM, reflecting the larger IT-NCSM model space, where the nucleons are not subject to restrictions on particle-hole excitations. The results are, furthermore, in excellent agreement with those obtained in the larger IT-NCSM model space. Since the flow-parameter dependence is very similar, we only show the spectrum for the largest value of s . Altogether, we conclude that

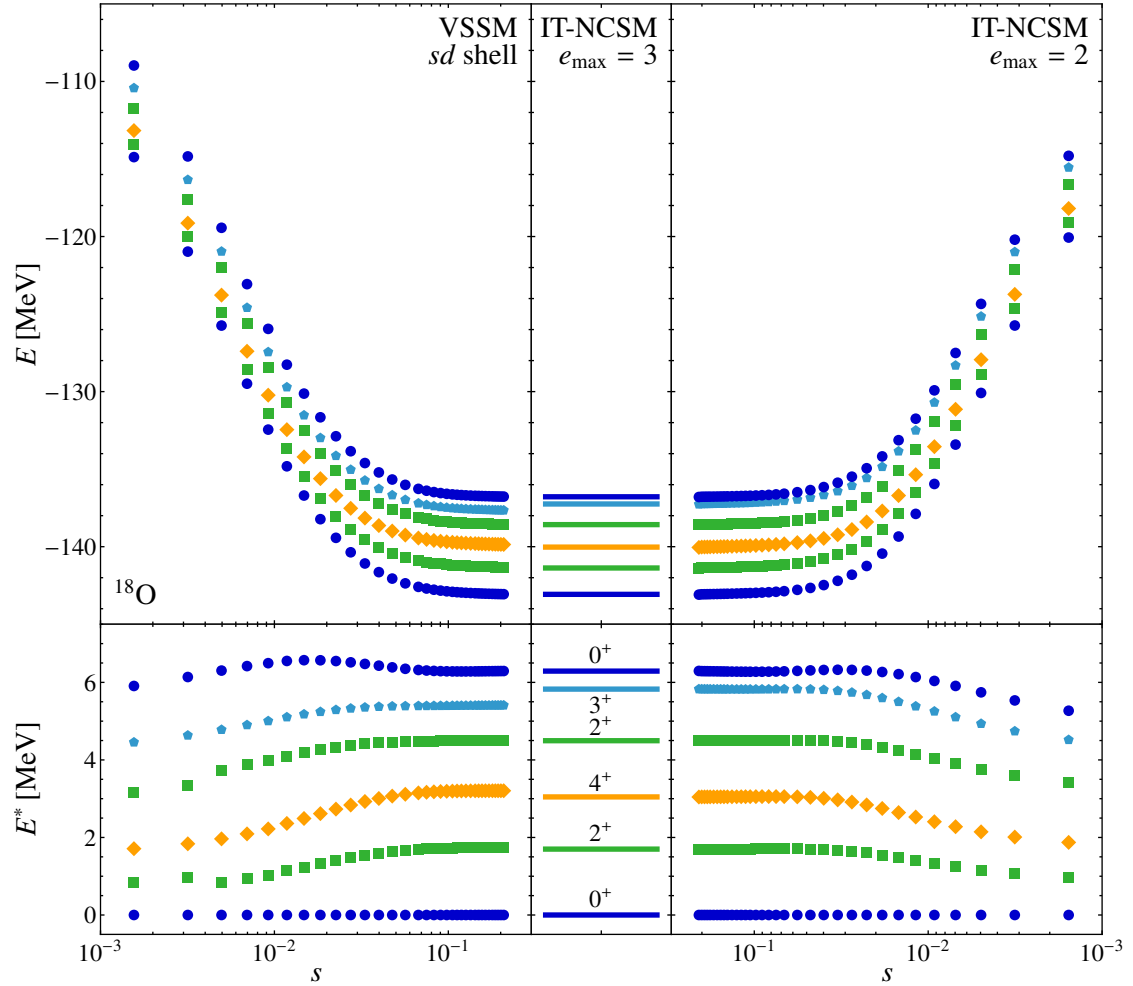


Figure 7.6.: Absolute and excitation energies of the lowest six natural-parity states of ^{18}O obtained in the VSSM and IT-NCSM using the same IM-SRG-evolved Hamiltonian as a function of the flow parameter s . The IM-SRG employs the White generator and the initial Hamiltonian contains the EMN400 interaction, SRG-evolved up to $\alpha = 0.08 \text{ fm}^4$. The left and right columns show the flow-parameter dependence of the energies in the VSSM using the sd shell as valence space and in the IT-NCSM with $e_{\text{max}} = 2$ truncation. The middle column shows IT-NCSM results for $e_{\text{max}} = 3$ for $s = 0.21$.

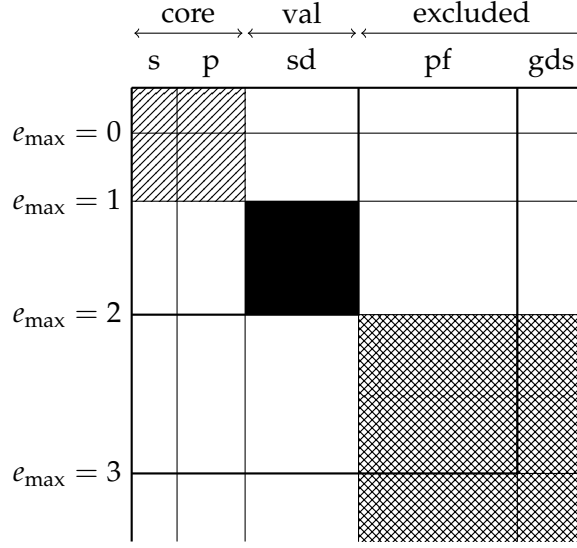


Figure 7.7.: Schematic matrix representation of the core, sd -shell valence, and excluded space in comparison to e_{\max} -truncated model spaces. The simply-hatched square denotes the core space, the black square the valence space, and the cross-hatched square the excluded space. A decoupled valence space requires vanishing off-diagonal blocks.

the IM-SRG successfully decouples single-shell valence spaces from core and excluded spaces as demonstrated here for the sd shell.

Multi-Shell Valence Spaces

Based on the observation that the IT-NCSM results remain unchanged when going from an $e_{\max} = 2$ to an $e_{\max} = 3$ model space in figure 7.6, we expect that a VSSM calculation in an extended valence space, comprising the $sdpf$ shell, should not affect the low-lying part of the natural-parity spectrum of ^{18}O . We employ an effective Hamiltonian for the $sdpf$ valence space [VR16] computed in the IM-SRG from the same SRG-evolved EMN400 interaction as for the sd shell, but using the imaginary-time generator [Her+14; Her+16]. This generator has proven to be advantageous with respect to numerical stability in the IM-SRG flow compared to the White generator.

Again, we first study the flow-parameter dependence of the ^{16}O core energy in figure 7.8. The core energy evolves over a larger range of s values during the IM-SRG flow than when using the White generator, but also stabilizes around $s \gtrsim 0.1 \text{ MeV}^{-1}$. After convergence is obtained, the core energy is lower than the ^{16}O ground-state energy, and we expect a repulsive contribution from the effective one- and two-body matrix elements.

In figure 7.9, the energies of the lowest two 0^+ and the lowest 6^+ states of ^{18}O obtained in the VSSM are shown as a function of the flow parameter s . This lowest 6^+ state is a mixture of $(f_{7/2})^2$ and $(f_{7/2})^1(f_{5/2})^1$ neutron configurations, where the neutron orbits $f_{7/2}$ and $f_{5/2}$ come down as intruders during the IM-SRG flow, making it an erroneous ground state.

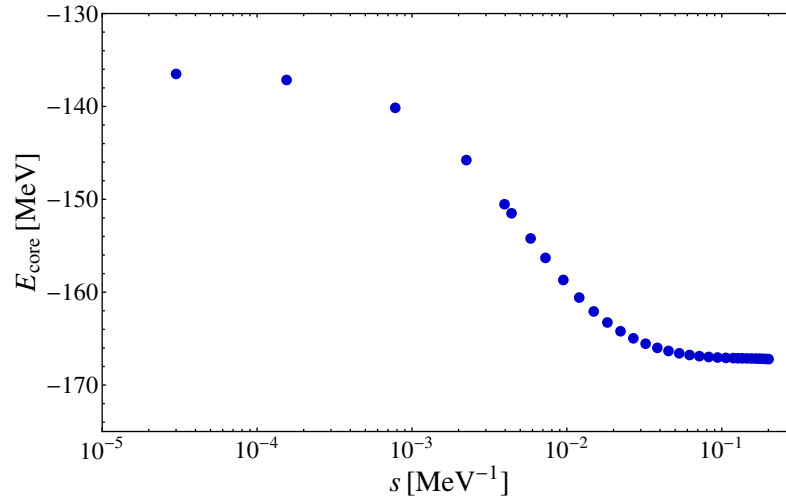


Figure 7.8.: Energy of the ^{16}O core of an $sdpf$ -shell valence-space Hamiltonian for $A = 18$ nuclei obtained in the IM-SRG with the imaginary-time generator as a function of the flow parameter s . The initial Hamiltonian employs the EMN400 interaction, SRG-evolved up to $\alpha = 0.08 \text{ fm}^4$.

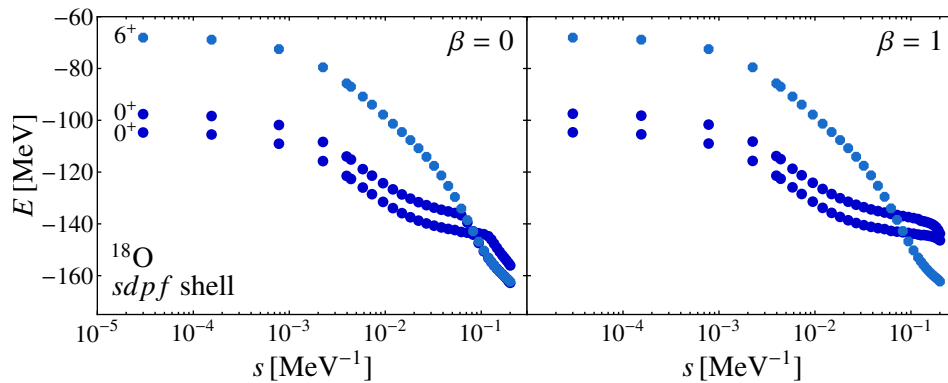


Figure 7.9.: Energies of the lowest two 0^+ and the lowest 6^+ states in ^{18}O obtained in the VSSM using an effective interaction from the IM-SRG with the imaginary-time generator for the $sdpf$ shell as a function of the flow parameter s . The initial Hamiltonian contains the EMN400 interaction, SRG-evolved up to $\alpha = 0.08 \text{ fm}^4$. The left and right columns compare the IM-SRG flow of the energies for the center-of-mass control parameters $\beta = 0$ and $\beta = 1$.

Since this extended valence space can give rise to center-of-mass spuriousities, we compare the IM-SRG flows of the energies calculated without and with Lawson-type center-of-mass Hamiltonian for $\beta = 1$. In the left panel of figure 7.9, where we have set $\beta = 0$, we observe an extreme drop of the energies of the two 0^+ states starting around $s \approx 0.07 \text{ MeV}^{-1}$. We note that several other low-lying states with different J^π quantum numbers are found in between these two states, all exhibiting a similar behavior. Furthermore, the 6^+ state—also here, we show only the lowest of a group of states with a similar behavior—shows a peculiar dependence on s . This initially high-lying state dives down during the IM-SRG flow and even passes the low-lying states, thus becoming an erroneous ground state. Our first suspicion, based on the large expectation value of the center-of-mass Hamiltonian with respect to this state, was that center-of-mass contaminations cause the IM-SRG flow to fail. An attempt to remedy this by adding a Lawson-type center-of-mass Hamiltonian to the valence-space Hamiltonian for the solution of the eigenvalue problem in the VSSM is illustrated in the right panel of figure 7.9. The general picture improves only slightly: The failure of the IM-SRG flow is delayed and the nonphysical fall-off of the energies of the 0^+ states sets in at larger values of s . However, the dependence of the 6^+ state on the flow parameter remains the same. Consequently, the approximate removal of intruding spurious states by setting $\beta = 1$ is not sufficient to remedy the IM-SRG Hamiltonians for extended valence spaces such as the *sdpf* shell. One possible reason is the truncation of the IM-SRG at the level of normal-ordered two-body operators, which cannot accommodate for a simultaneous suppression of all off-diagonal parts of the Hamiltonian as they are feeding into each other during the decoupling process, thus inducing significant higher-order terms, which eventually destroy the IM-SRG flow. This problem seems to be connected with intruder states, which can appear in valence spaces comprising multiple major shells. The details are not yet fully understood, and no remedy is presently available. We note that these problems persist also for different choices of IM-SRG generators. Thus, such multi-shell valence spaces remain subject to future investigations.

We add a final remark: Work is not only ongoing regarding the construction of valence-space Hamiltonians in the IM-SRG, but also other observables have been considered [Par+17], e.g., for the description of electromagnetic transitions.

Comparison to the In-Medium No-Core Shell Model

Recently, a new approach has been developed that shares some similarities with the use of IM-SRG effective Hamiltonians in the VSSM: By merging the multi-reference IM-SRG with the NCSM, a new *ab initio* method, the in-medium no-core shell model (IM-NCSM) has been implemented for the description of light to medium-heavy nuclei with even mass number [Geb+17; Geb17]. The method starts from a reference state for the target nucleus with the appropriate quantum numbers obtained in a previous NCSM calculation in a small model space, typically for $N_{\text{max}} = 0$. During the multi-reference IM-SRG flow, the Hamiltonian, normal-ordered with respect to this reference state, is evolved. Thereby, the reference state is decoupled from all particle-hole excitations. The eigenvalue problem of the evolved Hamiltonian is solved in the NCSM afterward. Thus, remaining couplings within the reference space, remnants of the IM-SRG truncations, are handled, and ground and excited states as well as their energies are obtained. The IM-SRG decoupling of the

Hamiltonian dramatically enhances the convergence properties in the NCSM, extending its applicability to an unprecedented range of nuclei. One advantage of this method over the use of effective Hamiltonians from the IM-SRG in the IT-VSSM results from the choice of a multi-determinantal reference state, which avoids the artificial definition of ensemble references for the construction of valence-space Hamiltonians for nuclei with increasing nucleon number in the valence spaces. Additionally, the IM-NCSM naturally captures intruder physics in the model spaces typically used. These interesting phenomena cannot be addressed when single-shell valence spaces are employed. Still, many nuclei remain out of reach of the IM-NCSM, e.g., if the computation of the reference state in the NCSM is already prohibitive for $N_{\max} = 0$. Therefore, the need to pursue investigations for the derivation of multi-shell valence-space interactions for use in the IT-VSSM in *ab initio* approaches remains.

7.4. Structure of Neutron-Deficient Tin Isotopes

We study neutron-deficient tin isotopes in the IT-VSSM using effective valence-space Hamiltonians derived in the IM-SRG from chiral potentials. The tin isotopic chain provides an excellent playground for theoretical and experimental shell-structure investigations because it comprises many isotopes, including the two doubly-magic nuclei ^{100}Sn [Hin+12] and ^{132}Sn [Bjö+80; Jon+10]. Particularly the neutron-deficient tin isotopes, i.e., ^{100}Sn and neighbors, have received recent attention in experimental and theoretical investigations, see [FGG13] for a review. To date, no excited states of ^{100}Sn , the heaviest $N = Z$ nucleus stable against ground-state proton decay [Lew+94], have been measured, and the nuclear spins of the first excited states of $^{101,103,105}\text{Sn}$ have not yet been assigned definitely, while their excitation energies are known. In the near future, laser-spectroscopy measurements will help to shed light on these controversies [Gar+16]. Theoretical predictions on the spectroscopy of ^{100}Sn and some of its neighbors were obtained in large-scale VSSM calculations using a phenomenological interaction for the *gds* valence space [Now02; FGG13]. However, severe particle-hole truncations were necessary to make these calculations computationally feasible. Furthermore, compared to other phenomenological Hamiltonians, e.g., for the *sd* or *pf* shell, which are adjusted to a wealth of experimental data and allow for an accurate description of nuclear spectra, the quality of the phenomenological Hamiltonian for the *gds* shell is uncertain as only scarce data is available to constrain it.

We present first converged results for the ground and first excited states of all tin isotopes in the mass range 100 to 114 obtained in the IT-VSSM using the *gds* shell on top of a ^{80}Zr core as valence space. We employ two effective Hamiltonians, both constructed in the IM-SRG from the chiral interactions 1.8/2.0(EM) and 2.0/2.0(EM). All calculations exploit the importance truncation and are carried out for a reference threshold $C_{\min} = 2 \cdot 10^{-4}$. The results are extrapolated using the simple threshold extrapolation. Figures 7.10 to 7.12 show the T_{\max} dependence of the absolute energies of the ground and first excited states of ^{100}Sn to ^{114}Sn . If not shown, no state with corresponding quantum numbers is among the calculated lowest natural-parity eigenstates. Typically, these states appear only for higher T_{\max} values, e.g., the 2^+ state obtained for ^{100}Sn using the 1.8/2.0(EM) interaction for $T_{\max} \geq 6$. Note that we have carried out most IT-VSSM calculations up to $T_{\max} = 12$,

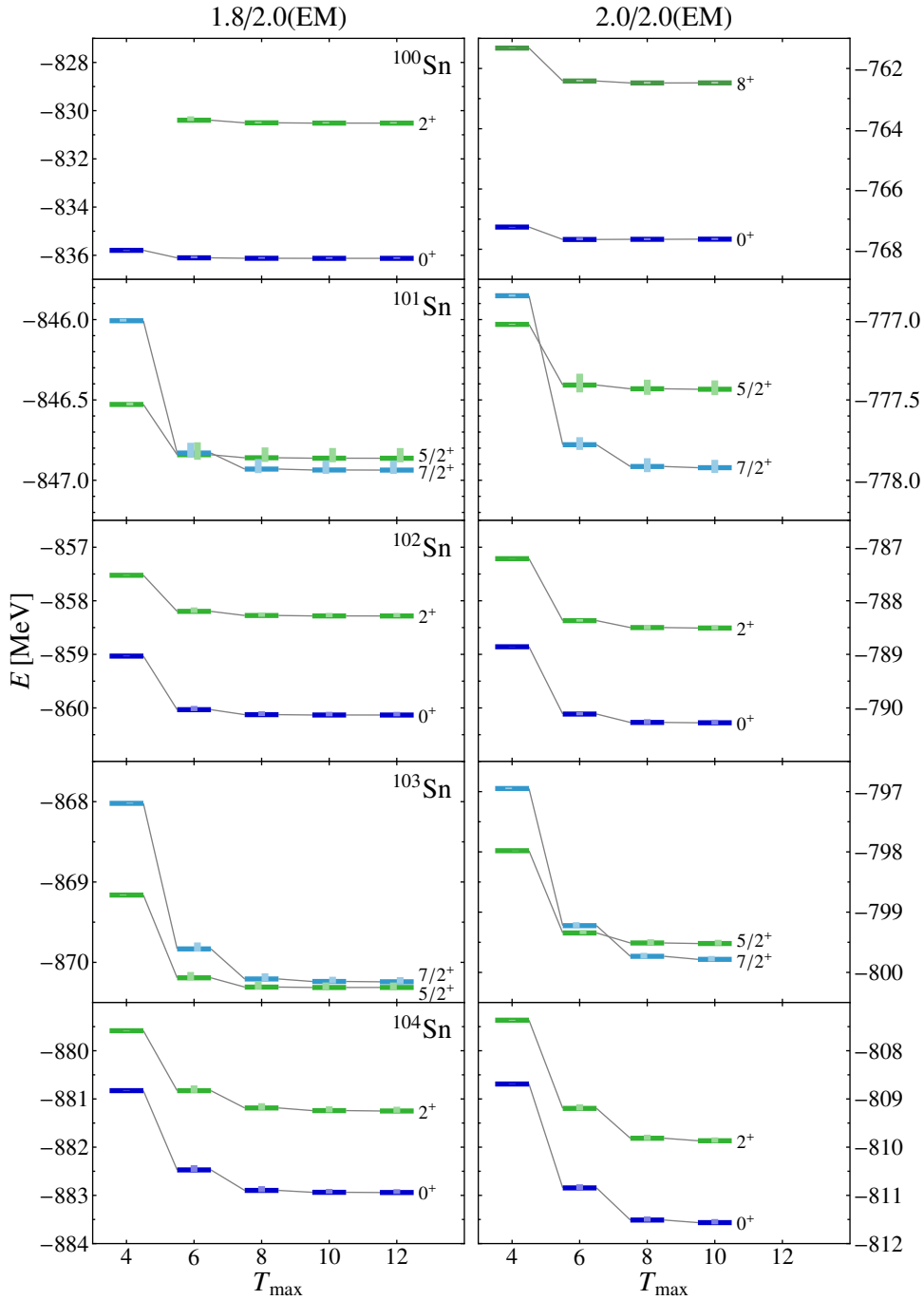


Figure 7.10.: Energies of the ground and first excited states of $^{100-104}\text{Sn}$ as a function of T_{max} obtained in the IT-VSSM for $C_{\text{min}} = 2 \cdot 10^{-4}$ using effective gds valence-space Hamiltonians derived in the IM-SRG from the 1.8/2.0(EM) and 2.0/2.0(EM) interactions. The light-colored rectangles represent the uncertainty of the κ_{min} extrapolations.

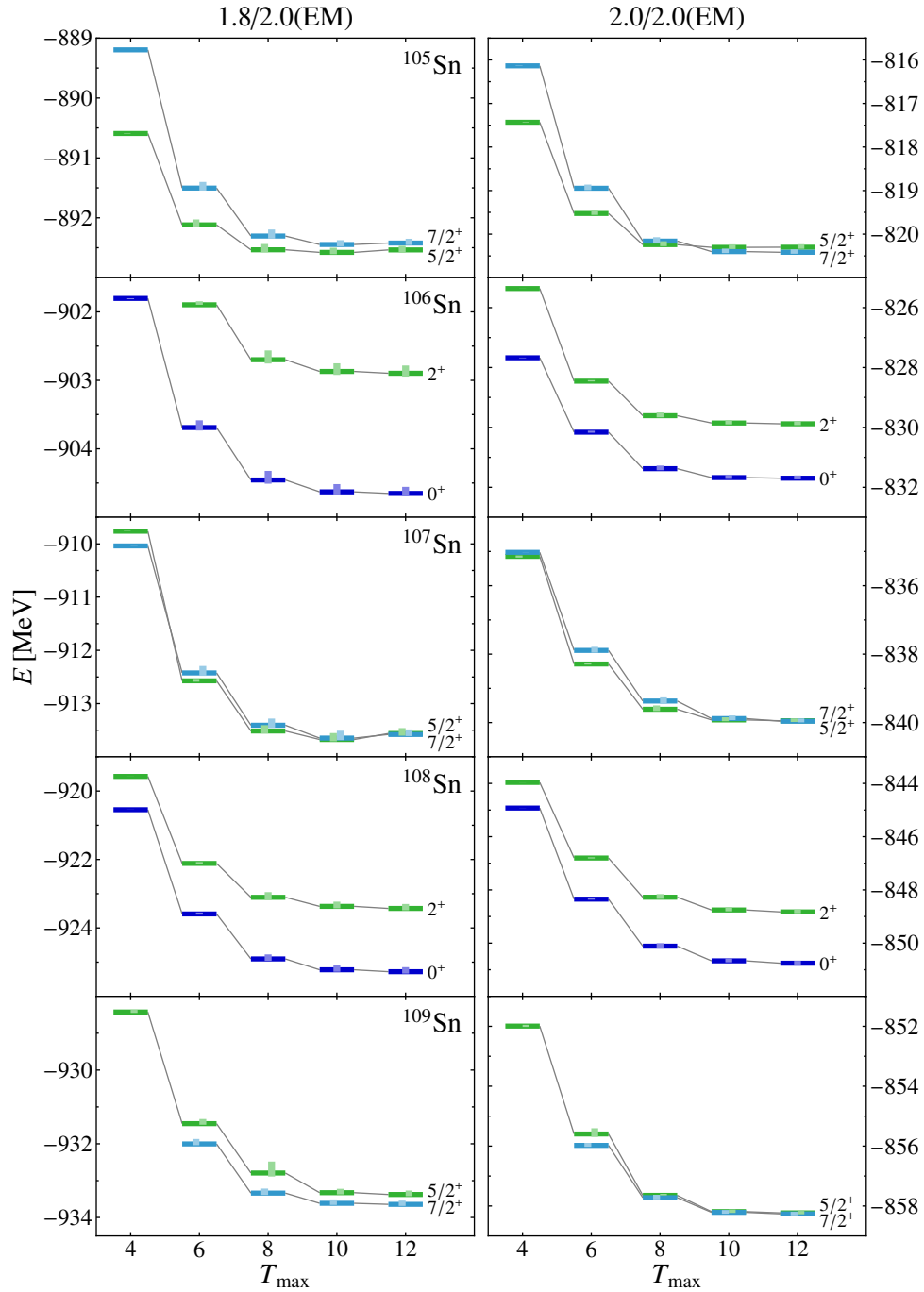


Figure 7.11.: Energies of the ground and first excited states of $^{105-109}\text{Sn}$ as a function of T_{max} obtained in the IT-VSSM for $C_{\text{min}} = 2 \cdot 10^{-4}$ using effective gds valence-space Hamiltonians derived in the IM-SRG from the 1.8/2.0(EM) and 2.0/2.0(EM) interactions. The light-colored rectangles represent the uncertainty of the κ_{min} extrapolations.

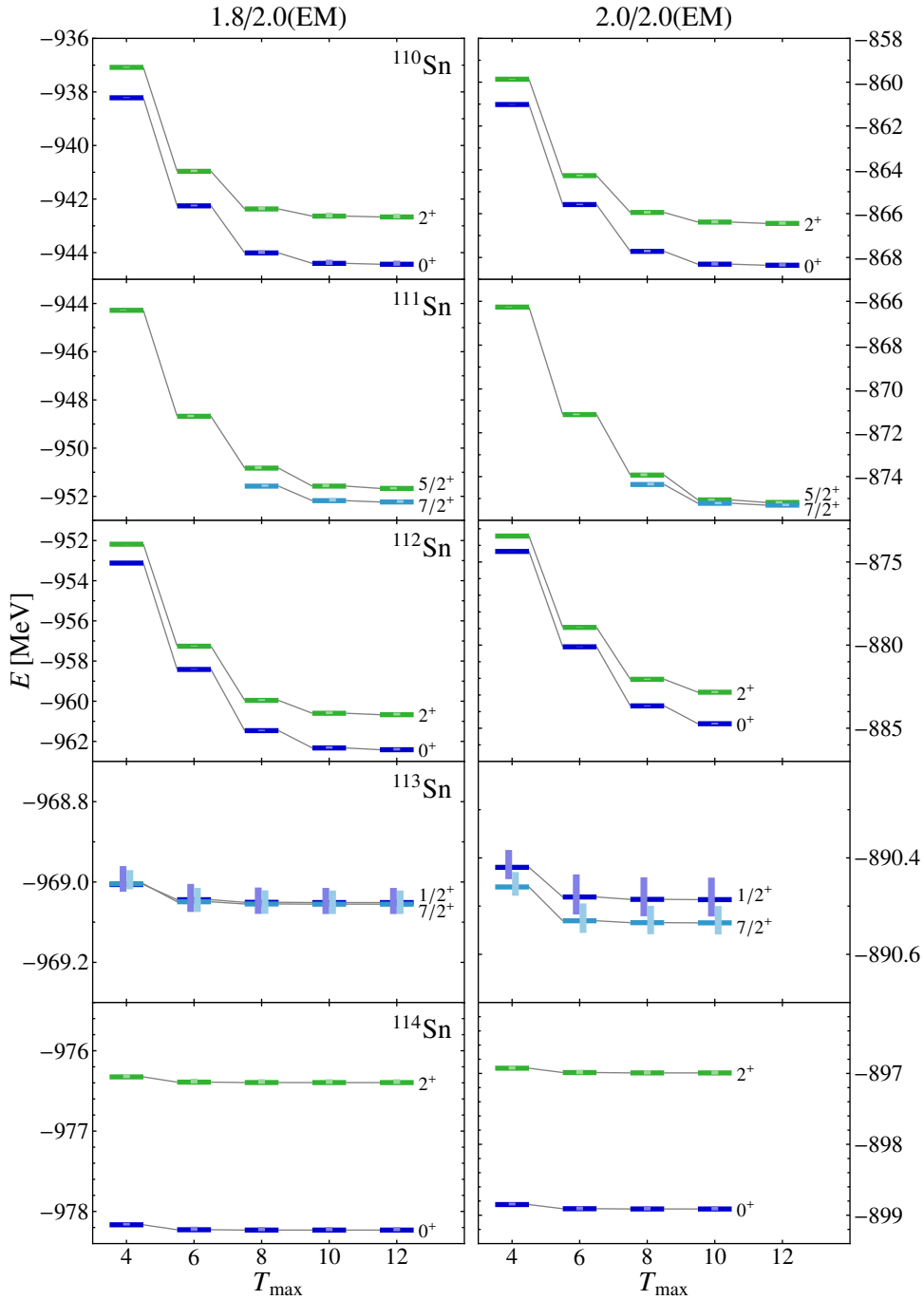


Figure 7.12.: Energies of the ground and first excited states of $^{110-114}\text{Sn}$ as a function of T_{max} obtained in the IT-VSSM for $C_{\text{min}} = 2 \cdot 10^{-4}$ using effective gds valence-space Hamiltonians derived in the IM-SRG from the 1.8/2.0(EM) and 2.0/2.0(EM) interactions. The light-colored rectangles represent the uncertainty of the κ_{min} extrapolations.

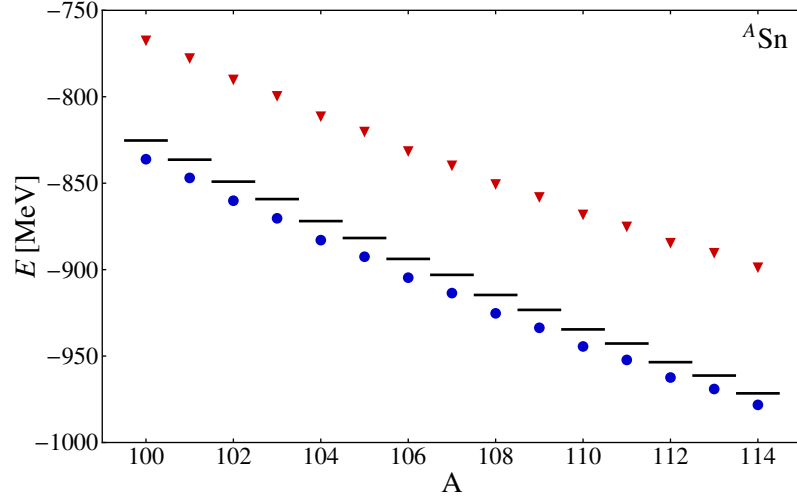


Figure 7.13.: Ground-state energies of $^{100-114}\text{Sn}$ obtained in the IT-VSSM for $C_{\min} = 2 \cdot 10^{-4}$ using effective gds valence-space Hamiltonians derived in the IM-SRG from the 1.8/2.0(EM) (●) and 2.0/2.0(EM) (▼) interactions. The black bars show the experimental ground-state energies [NNDC].

with some exceptions using the 2.0/2.0(EM) potential, where results are available only up to $T_{\max} = 10$. Besides for the ^{112}Sn results obtained for the 2.0/2.0(EM) Hamiltonian, convergence with T_{\max} is evident for all energies of the ground and first excited states. We note that the energies obtained for ^{107}Sn using the 1.8/2.0(EM) interaction increase slightly from $T_{\max} = 10$ to $T_{\max} = 12$ as a consequence of truncation effects from the importance truncation. In principle, a more precise result, which avoids this problem, could be obtained by reducing the reference threshold. However, compared to the difference in the energies resulting from the specific choice of Hamiltonian, this effect is small. The uncertainties resulting from the threshold extrapolations, indicated in figures 7.10 to 7.12 as rectangles of the respective heights in the same color but a lighter tone, are also small for all tin isotopes and interactions, with a maximum deviation of about 100 keV. We conclude that the main source of uncertainty in the results is due to the Hamiltonians used. Typically, the ground and first excited states of even- A tin isotopes carry the quantum numbers 0^+ and 2^+ , respectively, in agreement with the experimentally observed nuclear spins. Only for ^{100}Sn , where no experimental data on excited states is available, the 2.0/2.0(EM) predicts a first excited 8^+ state. This is unexpected and indicates that this interaction is not suited for the spectroscopy of ^{100}Sn . The ground and first excited states of odd- A tin isotopes are degenerate. In many cases, any of the states is consistent with the ground state within the threshold-extrapolation uncertainty, impeding a statement on their level ordering. Up to ^{111}Sn , the two lowest states carry the quantum numbers $5/2^+$ and $7/2^+$, whereas for ^{113}Sn , a $7/2^+$ and a $1/2^+$ state is predicted. We remark, however, that a $5/2^+$ state—not shown here—is in their close vicinity.

In figure 7.13, we compare our results for the ground-state energies of $^{100-114}\text{Sn}$ with experiment. Both interactions reproduce the trend of the experimental energies, but the

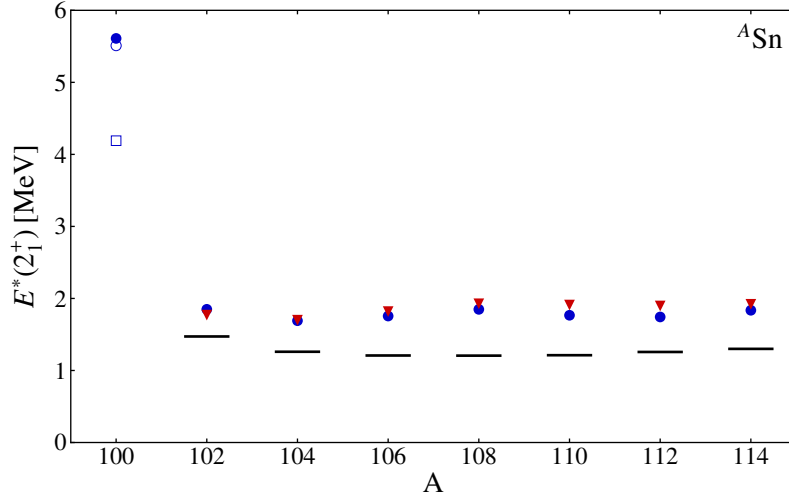


Figure 7.14.: Excitation energies of the first 2^+ state of even- A tin isotopes obtained in the IT-VSSM for $C_{\min} = 2 \cdot 10^{-4}$ using effective gds valence-space Hamiltonians derived in the IM-SRG from the 1.8/2.0(EM) (\bullet) and 2.0/2.0(EM) (\blacktriangledown) interactions. For ^{100}Sn , results from the EOM-CCSD (\circ) and EOM-CCSD(T) (\square) employing the 1.8/2.0(EM) interaction are shown [Mor+18]. The black bars denote the experimental data [NNDC].

1.8/2.0(EM) interaction is superior in the description of the absolute ground-state energies. It is, however, not clear what distinguishes this interaction, which yields a surprising agreement with experimental binding energies, from other interactions that are derived in a similar way. Thus, the discrepancies in the results can be interpreted conservatively in terms of uncertainties of the nuclear Hamiltonians.

We investigate the systematics of the excitation energy of the first 2^+ state in the even- A tin isotopes $^{100-114}\text{Sn}$ obtained in the IT-VSSM and from experiment in figure 7.14 [Mor+18]. The trend of the computed 2^+ energies in the tin isotopes suggests that ^{100}Sn is doubly magic. We predict an excitation energy of 5.67 MeV for the first 2^+ state in ^{100}Sn , which is large compared to the excitation energies of about 2 MeV calculated for the first 2^+ states of the neighboring tin isotopes. Both interactions used predict approximately the same excitation energies for all tin isotopes considered. We recall that no 2^+ state is found for ^{100}Sn in the IT-VSSM calculation using the 2.0/2.0(EM) interaction. In comparison with data, our results slightly overestimate the 2^+ excitation energies. Additionally, we compare our results for ^{100}Sn to those obtained in an equation-of-motion method on top of a CC with singles and doubles solution (EOM-CCSD), which yield a 2^+ excitation energy of 5.51 MeV [Mor+18]. An analog calculation using the recent equation-of-motion method with triples corrections on top of a CC with singles and doubles solution (EOM-CCSD(T)) predicts this 2^+ state at 4.19 MeV. Since the EOM-CCSD and IM-SRG are related regarding their particle-hole content in the model spaces, it is not surprising that our result for the 2^+ excitation energy of ^{100}Sn agrees well with that of the EOM-CCSD method. Since the result from the EOM-CCSD(T) includes corrections of 3p3h excitations, which are not

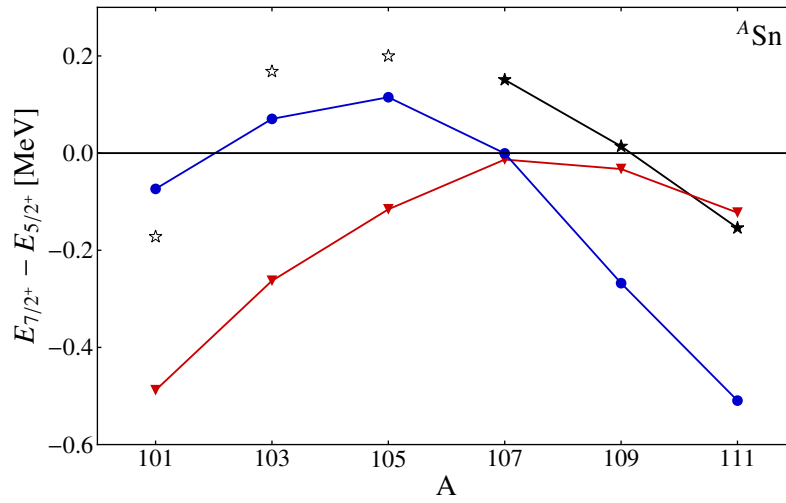


Figure 7.15.: Energy splitting between the lowest $7/2^+$ and $5/2^+$ states in light odd- A tin isotopes obtained in the IT-VSSM for $C_{\min} = 2 \cdot 10^{-4}$ using effective gds valence-space Hamiltonians derived in the IM-SRG from the 1.8/2.0(EM) (●) and 2.0/2.0(EM) (▼) interactions. Experimental data [Dar+10; NNDC] are shown for definite (★) and tentative (☆) spin assignments.

accounted for in the IM-SRG and EOM-CCSD, they provide an estimate for the quality of the truncation of the normal-ordered operators at the two-body level. We expect the inclusion of $3p3h$ excitations in the IM-SRG formalism to slightly reduce the energy of the first 2^+ state, bringing it into agreement with the EOM-CCSD(T) result. The thus calculated 2^+ excitation energy is of a similar magnitude as the experimental excitation energy of 4.04 MeV of the doubly-magic nucleus ^{132}Sn [Bjö+80; Jon+10]. Based on the behavior of the 2^+ excitation energy of ^{100}Sn observed when including $3p3h$ excitations in the CC model space, we expect that such an extension in the IM-SRG will also lower the 2^+ excitation energies of all isotopes and improve agreement with experiment. However, the observed pattern of 2^+ excitation energies alone is no evidence for magicity, and for a definite proof we would need to consider other properties as well, such as changes in pairing strengths.

We can use our results to study the level-ordering in the lowest odd- A tin isotopes, for which controversial data exist. In the naive independent-particle picture, we expect that $^{101,103,105}\text{Sn}$ should have identical ground-state spins determined by the single unpaired neutron in the lowest-energy single-particle orbit on top of the $N = 50$ shell closure, i.e., either the $d_{5/2}$ or $g_{7/2}$ orbit. No experimental data for the known semi-magic isotopic and isotonic chains indicate an exception to this rule, at least in the vicinity of shell closures [Dar+10]. In accordance with this observation, the ground-state spins of $^{101,103,105}\text{Sn}$ have been tentatively assigned to be $5/2^+$ [NNDC]. However, a coincidence measurement of α and γ decays from ^{105}Te to ^{101}Sn indicates that the ^{101}Sn ground state has spin $7/2^+$ and the first excited state $5/2^+$ [Dar+10], in contrast to the previously proposed level ordering [Lid+06]. Figure 7.15 compares the level ordering of the lowest $7/2^+$ and $5/2^+$ states of the

odd- A tin isotopes considered using the most recent experimental data and our theoretical predictions for the energy splitting [Mor+18]. The IT-VSSM results for both interactions used are in agreement with the small energy splittings observed in experiment, but differ in their precise size and sign. Both interactions predict a $7/2^+$ ground state for ^{101}Sn , in accordance with the most recent experiment. Contrary to that, we obtain the ground-state spins $5/2^+$ and $7/2^+$ using the 1.8/2.0(EM) and 2.0/2.0(EM) interaction, respectively, for ^{103}Sn and ^{105}Sn . Also, our calculations do not reproduce the experimentally observed crossing between the $5/2^+$ and $7/2^+$ ground states of ^{109}Sn and ^{111}Sn . Keeping in mind that the uncertainty of the input Hamiltonians alone is larger than the experimental energy splittings of about 200 keV, we conclude that theory is presently not sufficiently precise to make a definite prediction for the ground-state spin of ^{101}Sn and its next neighbors.

8. Applications of IT-NCSM Strength Functions

We use the IT-NCSM in combination with the Lanczos strength-function method for the efficient computation of electric transition strengths and their distributions for nuclei up into the lower sd shell. This provides a unique possibility to compare strength functions from approximate methods, such as the RPA and second-order RPA (SRPA), to *ab initio* results. In section 8.1, we test the validity of these methods and elucidate some of their deficiencies. Then, we study the electric monopole, dipole, and quadrupole response of even-mass oxygen, carbon, and helium isotopes and the systematics throughout the isotopic chains in section 8.2.

8.1. Validation of Strength Functions from RPA-Type Methods

RPA-type methods are based on the definition of operators creating excited states by acting on the ground state, which is typically approximated by the HF ground state. Given these excitation operators, one can derive and solve equations of motion. For the most general excitation operators, the equations of motion are equivalent to the Schrödinger equation. In practice, the definition of the excitation operators always involves some truncation, but extending them allows for systematic improvements of the theory. Both, the Tamm-Dancoff Approximation (TDA) and the RPA, describe excited states as 1p1h excitations on top of the ground state. In the TDA, the excitation operators are linear combinations of particle-hole excitations, while hole-particle excitations are additionally included in the RPA. The SRPA further extends the method to 2p2h (de)excitations with respect to the ground state. An introduction to the TDA and RPA can be found in [RS80], and we refer to [Pro65; Yan87; Dro+90] for details on the SRPA. Practical applications usually rely on the quasi-boson approximation, i.e., one approximates the RPA and SRPA ground states by the HF Slater determinant for the evaluation of certain expressions. Traditionally, effective interactions adjusted at the mean-field level—implicitly accounting for some correlations—are used in RPA calculations, yielding results in good agreement with experimental data for collective excitations. We note that a consistent calculation of ground states in the RPA is possible and includes beyond-mean-field correlations. When using these adjusted interactions in RPA ground-state calculations, some of the correlations are taken into account twice—by the method *per se* and by the interaction—and, thus, result in overbound ground states. The same problem occurs also for the calculation of excited states, when these interactions are used in the SRPA. In this case, the excited states are moved to nonphysically low energies. Recently, a subtraction scheme [Tse07; Tse13] has been introduced which successfully avoids such double counting of correlations in the SRPA for the calculation of excited states [GGE15; Gam+16; GG16; GGV18]. Another path

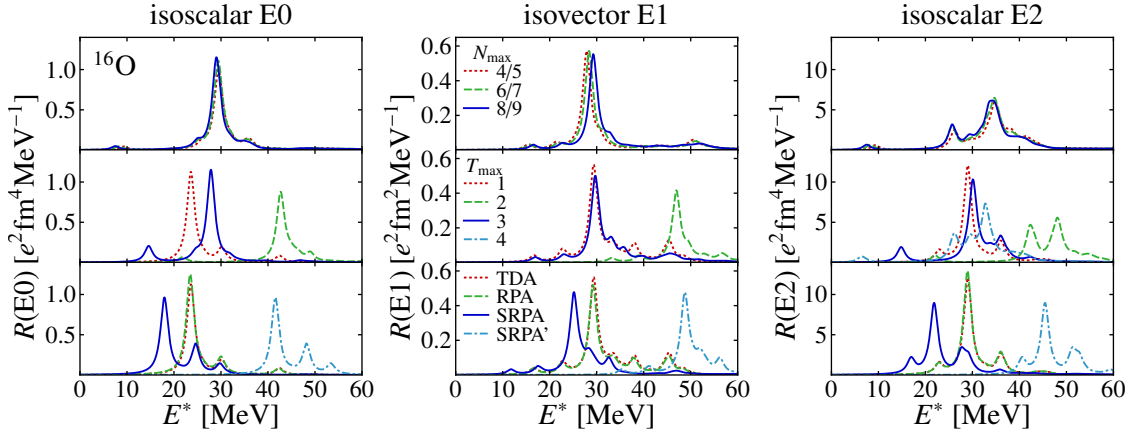


Figure 8.1.: Convergence behavior of isoscalar E0, isovector E1, and isoscalar E2 strength functions of ^{16}O obtained in the IT-NCSM with N_{max} truncation (upper row), IT-NCSM with T_{max} truncation (middle row), and the TDA, RPA, and SRPA (bottom row). SRPA' refers to the SRPA strength shifted by the second-order perturbative energy correction. All calculations use the SRG-evolved EMN400 interaction with $\alpha = 0.08 \text{ fm}^4$ and frequency $\hbar\Omega = 24 \text{ MeV}$. The matrix elements are truncated by $e_{\text{max}} = 12$, $l_{\text{max}} = 10$, and $E_{3\text{max}} = 14$. No Lawson-type Hamiltonian is used here.

of development has been the use of realistic interactions in RPA methods [PR10; Pap14; Tri16], where the same Hamiltonian is employed in the calculation of the HF ground state and in the RPA method. In these applications, the importance of including ground-state correlations in RPA-type methods has been demonstrated.

Figure 8.1 shows isoscalar E0, isovector E1, and isoscalar E2 strength functions obtained in the IT-NCSM with N_{max} truncation, IT-NCSM with T_{max} truncation, and the TDA, RPA, and SRPA [SWR17]. All calculations have been carried out using the EMN400 interaction, SRG-evolved up to $\alpha = 0.08 \text{ fm}^4$, and $\hbar\Omega = 24 \text{ MeV}$. The single-particle basis is truncated at $e_{\text{max}} = 12$ and $l_{\text{max}} = 10$, and we employ an additional cut of $E_{3\text{max}} = 14$ on the 3N matrix elements. In order to allow for a comparison of strength functions from the IT-NCSM with results from the RPA-type methods, we do not use a Lawson-type Hamiltonian here. The top row of figure 8.1 shows the convergence of the strength functions with respect to N_{max} as a reference, see section 6.3 for a detailed discussion.

An interesting alternative to the N_{max} truncation of the many-body basis is the T_{max} truncation, which provides a natural link to traditional RPA-type methods. The middle row of figure 8.1 shows the dependence of the strength distributions on T_{max} . The effects are quite dramatic: Whereas the giant resonances for $T_{\text{max}} = 1$, i.e., in a 1p1h space, appear at reasonable energies, the $T_{\text{max}} = 2$ strength is shifted to higher energies by about 20 MeV. For $T_{\text{max}} = 3$, the resonance energies are shifted back into the neighborhood of their original position. The strength distribution for $T_{\text{max}} = 3$ agrees very well with the converged result for N_{max} -truncated spaces for the E0 and E1 modes. For E2, some fragmentation is still missing. It appears only after including $T_{\text{max}} = 4$ configurations, bringing the strength

functions into agreement with those obtained using the N_{\max} truncation. Note that we show the results for $T_{\max} = 4$ only in case of the isoscalar E2 distribution. The strong impact of $T_{\max} = 3$ configurations was also found in VSSM calculations for the Gamow-Teller strength distribution [Cau+94]. This behavior can be explained quite intuitively: Since we start from an HF basis and by means of Brillouin's theorem, the HF ground state does not couple to 1p1h configurations. Thus, for $T_{\max} = 1$, only the excited states are built from 1p1h excitations. Including 2p2h configurations for $T_{\max} = 2$ into the model space causes a large shift of the ground-state energy by about -25 MeV due to important correlations. In contrast, the excited states are still mainly built of 1p1h excitations and are less affected by the 2p2h configurations in the model space. This is manifested in smaller shifts of about -5 MeV. Therefore, resonances are shifted to unrealistically large excitation energies, which is clearly an artifact of the $T_{\max} = 2$ truncation. At $T_{\max} = 3$, this problem is remedied and both, ground state and 1p1h dominated excitations, acquire the important 2p2h corrections such that excitation energies move back to realistic values. Note that this imbalance of correlation content in ground and excited states does not appear in N_{\max} -truncated model spaces.

In the bottom row of figure 8.1, we present results of conventional RPA and SRPA calculations using the same interaction and single-particle space as in the IT-NCSM calculations. The $T_{\max} = 1$ calculations are formally equivalent to the TDA, and the results are in perfect numerical agreement. Compared to TDA, the strengths obtained from a self-consistent RPA calculation differ only slightly, i.e., the impact of the deexcitations is small. Going from RPA to SRPA, i.e., including 2p2h degrees of freedom into the excitation operator, shifts the strength to lower energies. This shift is a well-known problem of SRPA, which has received quite some attention in the recent literature [PR10; PR09; GGC10; GGC11b; GGC11a; Gam+12; Tse13; Pap14; GGE15; Gam+16; GGV18]. In contrast to the above mentioned issues with double counting of correlations in density-functional based calculations [Tse13; GGE15], the shift we observe is associated with an inconsistency of using the HF ground state when constructing the SRPA equations, which include explicit 2p2h excitations [PR10; Pap14]. Effectively, a standard SRPA calculation yields the energies of the excited modes relative to the HF ground-state energy and not relative to the correlated SRPA ground state. We can mimic the effect of 2p2h ground-state correlations by shifting the SRPA excitation energies by the second-order perturbative correction to the ground-state energy, which is a simple means to quantify the effect of 2p2h admixtures to the ground state. The resulting strength distribution is denoted SRPA' in figure 8.1 and agrees well with the $T_{\max} = 2$ -truncated IT-NCSM result, as expected on the basis of the particle-hole content of the model space. Then, however, SRPA' suffers from the same problem as the $T_{\max} = 2$ -truncated model space that we discussed above. This comparison provides a different perspective on the consistency issues of SRPA and confirms that the use of correlated ground states is essential to improve the results, as already pointed out in [PR10; Pap14]. Recently, the RPA and SRPA have been extended to correlated ground states [Tri16]. One of the approaches of this thesis was the use of IM-SRG-transformed Hamiltonians in RPA-type methods. Such Hamiltonians include correlations in the ground states while decoupling them from excited states. Consequently, the particle-hole content of the model spaces does not affect the reference state, but the excited states only. It has been found that the strength is shifted to higher energies than in SRPA without ground-

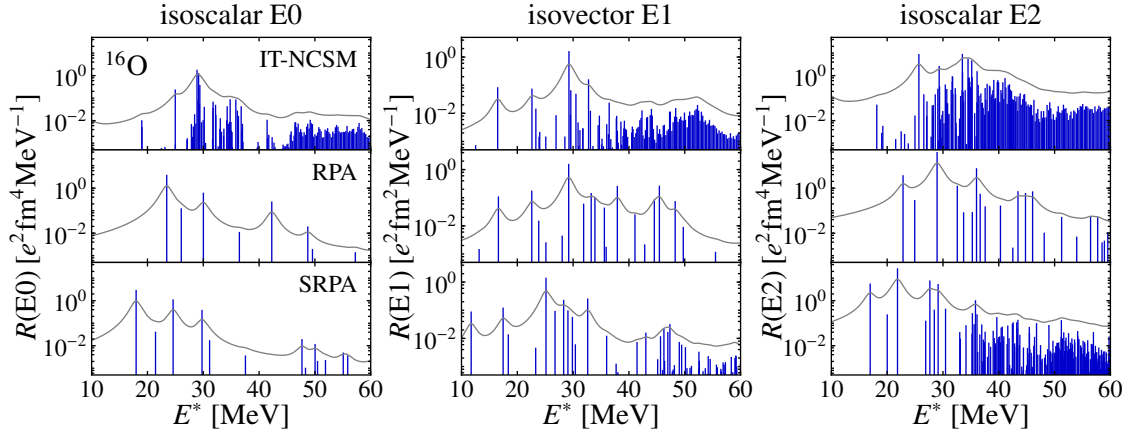


Figure 8.2.: Discrete isoscalar E0, isovector E1, and isoscalar E2 strength distributions for ^{16}O obtained in the IT-NCSM for $N_{\text{max}} = 8/9$, RPA, and SRPA. All calculations use the SRG-evolved EMN400 interaction with $\alpha = 0.08 \text{ fm}^4$ and frequency $\hbar\Omega = 24 \text{ MeV}$. The matrix elements are truncated by $e_{\text{max}} = 12$, $l_{\text{max}} = 10$, and $E_{3\text{max}} = 14$. No Lawson-type Hamiltonian is used here.

state correlations, and that no problematic instabilities occur as in standard SRPA. It is desirable to confirm the validity of the IM-SRPA strength functions in a direct comparison with the IT-NCSM.

One of the main motivations to use SRPA is the description of fragmentation and fine structure of resonances, which is observed in experiment [Lac+00; She+04; She+08; Usm+11; Pol+14; Sav+08; Ton+10]. Here, we do not elaborate on this interesting topic, but rather show that the strength distributions from the IT-NCSM predict substantial fine structure. In figure 8.2, we compare the discrete strength distributions from IT-NCSM, RPA, and SRPA on a logarithmic scale. Evidently, the IT-NCSM strength shows more fragmentation and fine structure than even SRPA, particularly in the energy region of the giant resonance. We note that all methods considered here lack the coupling to the continuum and cannot accommodate for the escape width. The description of the spreading width due to correlations is improved with increasing particle-hole content in the model spaces, demonstrating that the inclusion of complex configurations, mainly of 2p2h and higher-particle rank, are essential for the description of collective modes.

8.2. Electric Strength Functions of Selected Isotopes

In the following, we study electric strength functions of oxygen, carbon, and helium isotopes from the IT-NCSM with HF basis. We use potentials from chiral EFT, SRG-evolved with $\alpha = 0.08 \text{ fm}^4$, in NO2B approximation and the model-space truncations and parameters $e_{\text{max}} = 12$ and $l_{\text{max}} = 10$, $\hbar\Omega = 20 \text{ MeV}$, and $\beta = 0.5$. We use an additional cut of $E_{3\text{max}} = 14$ on the 3N matrix elements. The importance truncation employs the reference threshold $C_{\text{min}} = 2 \cdot 10^{-4}$ and the importance threshold $\kappa_{\text{min}} = 3 \cdot 10^{-5}$. If not

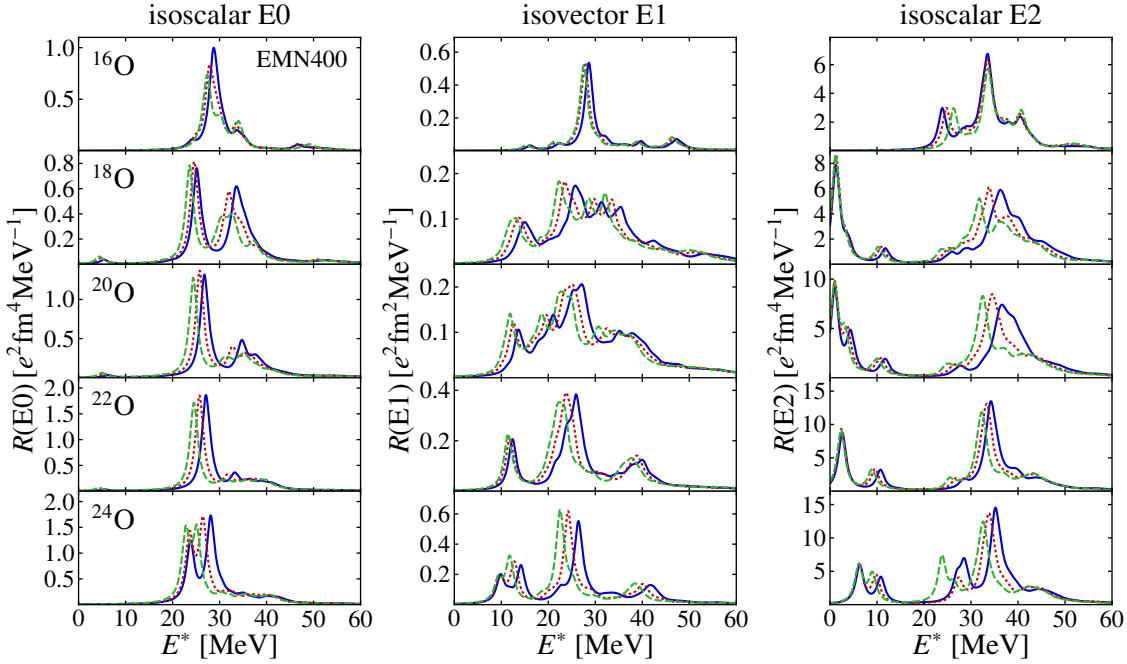


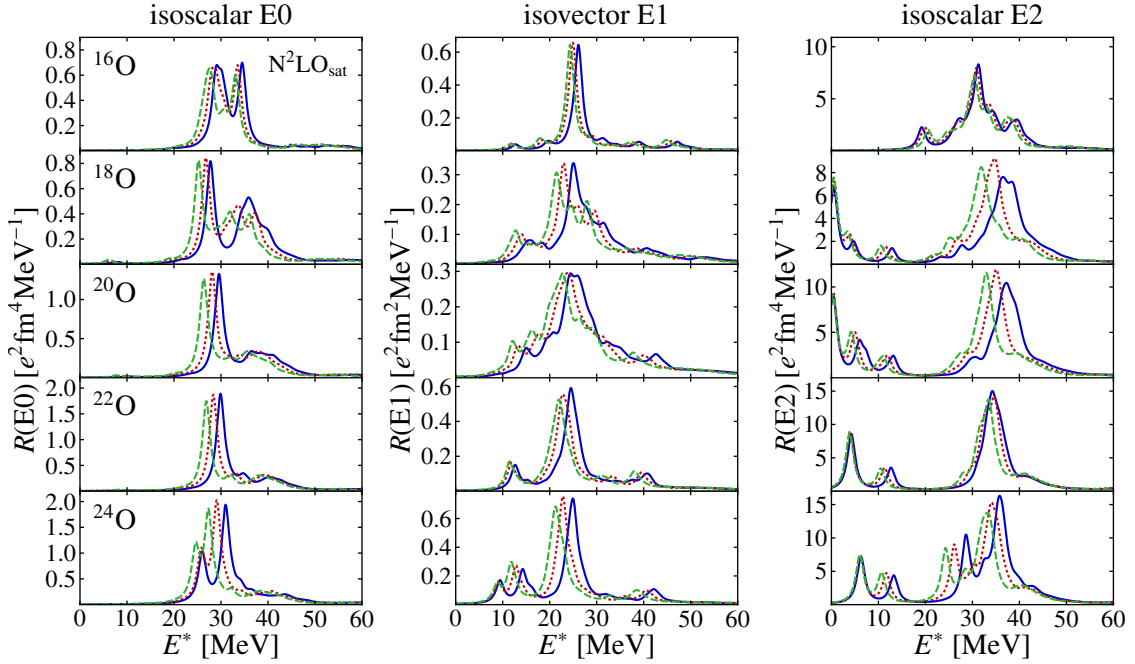
Figure 8.3.: Model-space convergence of the isoscalar E0, isovector E1, and isoscalar E2 strength functions of the even- A oxygen isotopes $^{16-24}\text{O}$ using the EMN400 interaction, SRG-evolved up to $\alpha = 0.08 \text{ fm}^4$. The oscillator frequency is $\hbar\Omega = 20 \text{ MeV}$ and $\beta = 0.5$. The IT-NCSM model spaces are truncated at $N_{\text{max}} = \{4/5(\text{---}), 6/7(\text{---}), 8/9(\text{---})\}$.

stated otherwise, the model space is truncated at $N_{\text{max}} = 8$ and $N_{\text{max}} = 9$ for natural- and unnatural-parity states, respectively.

8.2.1. Oxygen Isotopes

A particularly interesting region for applications of the IT-NCSM to strength distributions is the oxygen isotopic chain. It is easily within the reach of the method and the collective response of the neutron-rich oxygen isotopes has been and continues to be a focus of research [Lei+01; SS99]. Particularly, the neutron-rich isotopes $^{22,24}\text{O}$ will be studied with respect to their low-lying dipole response at GSI (FAIR Phase-0) [Aum17].

The robustness of electric strength distributions with respect to a variation of model-space truncations and parameters was proven in chapter 6. Since the strength functions are most sensitive to the N_{max} truncation, while all other truncations and parameters have only minor effects on the results, we validate the isoscalar E0, isovector E1, and isoscalar E2 strength distributions of $^{16-24}\text{O}$ only regarding their dependence on N_{max} . As shown in figures 8.3 and 8.4, the structure of the strength functions of all oxygen isotopes obtained for the EMN400 and $\text{N}^2\text{LO}_{\text{sat}}$ interactions is evident already for small values of N_{max} . For ^{16}O , we find only a weak dependence of their positions on N_{max} , with more pronounced effects for the neutron-rich isotopes. Particularly for these nuclei, a further improvement


 Figure 8.4.: As figure 8.3 but for the N^2LO_{sat} interaction.

of convergence by increasing N_{max} would be desirable, but is computationally difficult.

In a first step, we study the impact of including initial 3N interactions on the strength distributions. Figure 8.5 compares the strength distributions obtained with the EM and EMN400 interactions, SRG-evolved up to $\alpha = 0.08 \text{ fm}^4$ in three-body space. We note that the former takes into account only NN forces, while the latter includes also initial 3N forces. The shape of the isoscalar E0 and E2 strength distributions remains relatively unchanged whether initial 3N forces are included or not. However, the strength functions are shifted to higher or lower energies, where the direction of the shift depends on the specific isotope. Interestingly, the direction of the shift changes at ^{22}O , which has a sub-shell closure. Therefore, we assume that this change is related to an angular-momentum dependence of the interaction. Furthermore, the picture becomes even more complicated in case of the isovector E1 strength functions. When moving away from the shell closures, e.g., for ^{20}O , also the structure of the strength distributions is affected notably. This underlines the importance of taking into account initial 3N interactions. We include them in all our applications.

In figure 8.6, we present the isoscalar E0, isovector E1, and isoscalar E2 strength functions for the even-mass oxygen isotopes from ^{16}O to ^{24}O for the EMN400 and the N^2LO_{sat} interactions. The corresponding discrete strength distributions, illustrating the fragmentation and fine structure, are shown in figure 8.7. We remind the reader that the difference between the two chiral interactions is that the EMN400 interaction underestimates the ground-state radii of the oxygen isotopes by about 10%, while N^2LO_{sat} is constructed to reproduce the experimental radii well.

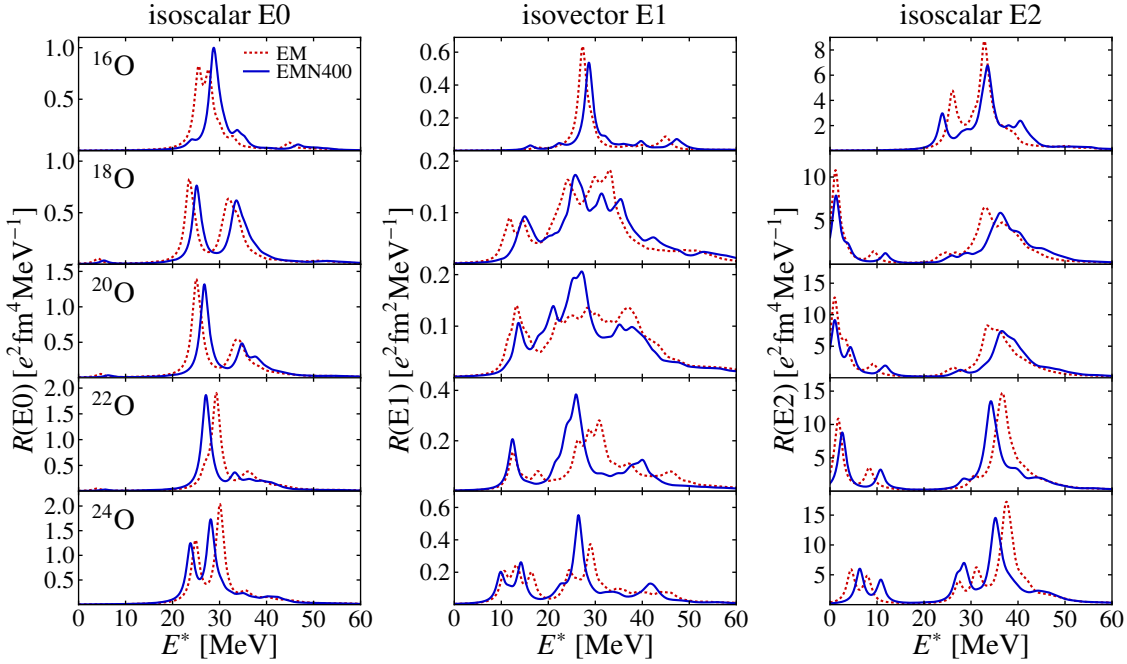


Figure 8.5.: Isoscalar E0, isovector E1, and isoscalar E2 strength functions of the even- A oxygen isotopes $^{16-24}\text{O}$ using the EM (-----) and EMN400 (—) interactions, both SRG-evolved in three-body space up to $\alpha = 0.08 \text{ fm}^4$. The oscillator frequency is $\hbar\Omega = 20 \text{ MeV}$ and $\beta = 0.5$. The IT-NCSM model spaces are truncated at $N_{\text{max}} = 8/9$.

Generally, the structure of the response is very similar for the two interactions. For the isoscalar E0 strength, the main difference is a relative shift of the strength distribution, with the $\text{N}^2\text{LO}_{\text{sat}}$ interaction producing about 4 MeV higher resonance energies. This is surprising since, in a naive mean-field picture, one would expect lower resonance energies for an interaction that produces larger ground-state radii and, thus, produces a wider potential well. The comparison of the $\text{N}^2\text{LO}_{\text{sat}}$ response for ^{16}O to the experimental centroid energy for the isoscalar giant monopole resonance is also surprising. Our predicted monopole resonance appears at too high energies although the interaction is known to predict a nuclear matter incompressibility within the empirical range [Eks+15; SSM14]. This indicates that other aspects of the interaction, e.g., momentum dependence or non-locality, play an important role for the transition strength that is not probed by static properties. The overestimation of the resonance energies compared to experiment is also evident for the E1 and E2 strength distributions. The $\text{N}^2\text{LO}_{\text{sat}}$ interaction tends to predict a lower resonance energy than the EMN400 interaction for these modes, thus improving agreement with experiment here.

The strength distributions exhibit interesting systematics throughout the isotopic chain. The isovector E1 distribution undergoes severe fragmentation and broadens as one moves toward mid-shell at ^{20}O , as observed experimentally [Lei+01]. It narrows again as the

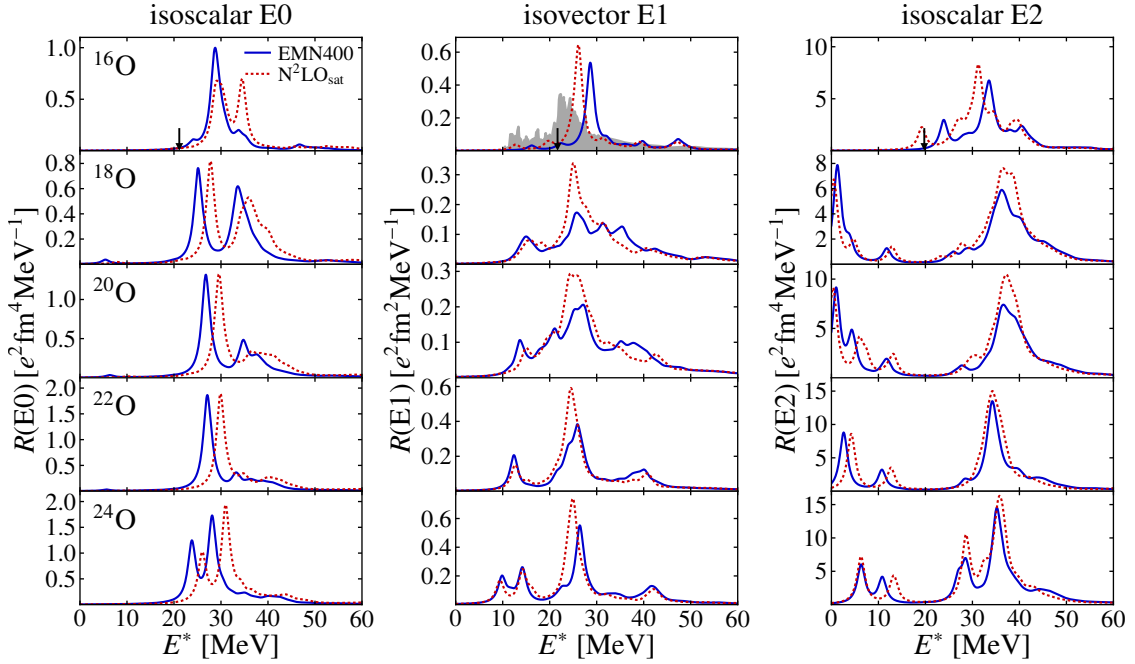


Figure 8.6.: Isoscalar E0, isovector E1, and isoscalar E2 strength functions of the even- A oxygen isotopes $^{16-24}\text{O}$ using the SRG-evolved EMN400 (—) and $\text{N}^2\text{LO}_{\text{sat}}$ (⋯) interactions with $\alpha = 0.08 \text{ fm}^4$. The oscillator frequency is $\hbar\Omega = 20 \text{ MeV}$ and $\beta = 0.5$. The IT-NCSM model spaces are truncated at $N_{\text{max}} = 8/9$. The arrows indicate the experimental centroid energies for ^{16}O from [LCY01], the gray area shows experimental data from [Ahr+75] in arbitrary units.

next closed neutron shell is approached. At the same time, more and more low-energy strength appears, which is compatible with the emergence of pygmy dipole excitations [SAZ13; Cha+94; SIS90]. Our calculations also provide access to a related quantity, the electric dipole polarizability [Pie11; Bac+14; Roc+15; Mio+16], a key ingredient to, e.g., draw conclusions on the neutron-skin thickness of neutron-rich nuclei. In discretized form, it is defined as

$$\alpha_D = \frac{8\pi}{9} \sum_n \frac{|\langle E_n || \mathbf{Q}_{10}^{\text{IV}} || \Psi_0 \rangle|^2}{E_n - E_0}. \quad (8.1)$$

Since the dipole polarizability is proportional to the inverse excitation energy, it is very sensitive to the low-lying dipole strength. Our results for the dipole polarizabilities are listed in table 8.1 and compared to the experimental value available for ^{16}O [Ahr+75]. The uncertainties of the theoretical values are taken as the difference of the dipole polarizabilities obtained for $N_{\text{max}} = 6/7$ and $N_{\text{max}} = 8/9$. We note that our calculations take into account all transitions over the complete energy range. However, experiments provide data only up to a certain energy, typically around 40 MeV, and the dipole polarizability is computed from the transitions up to this maximum energy. Since the calculated strength

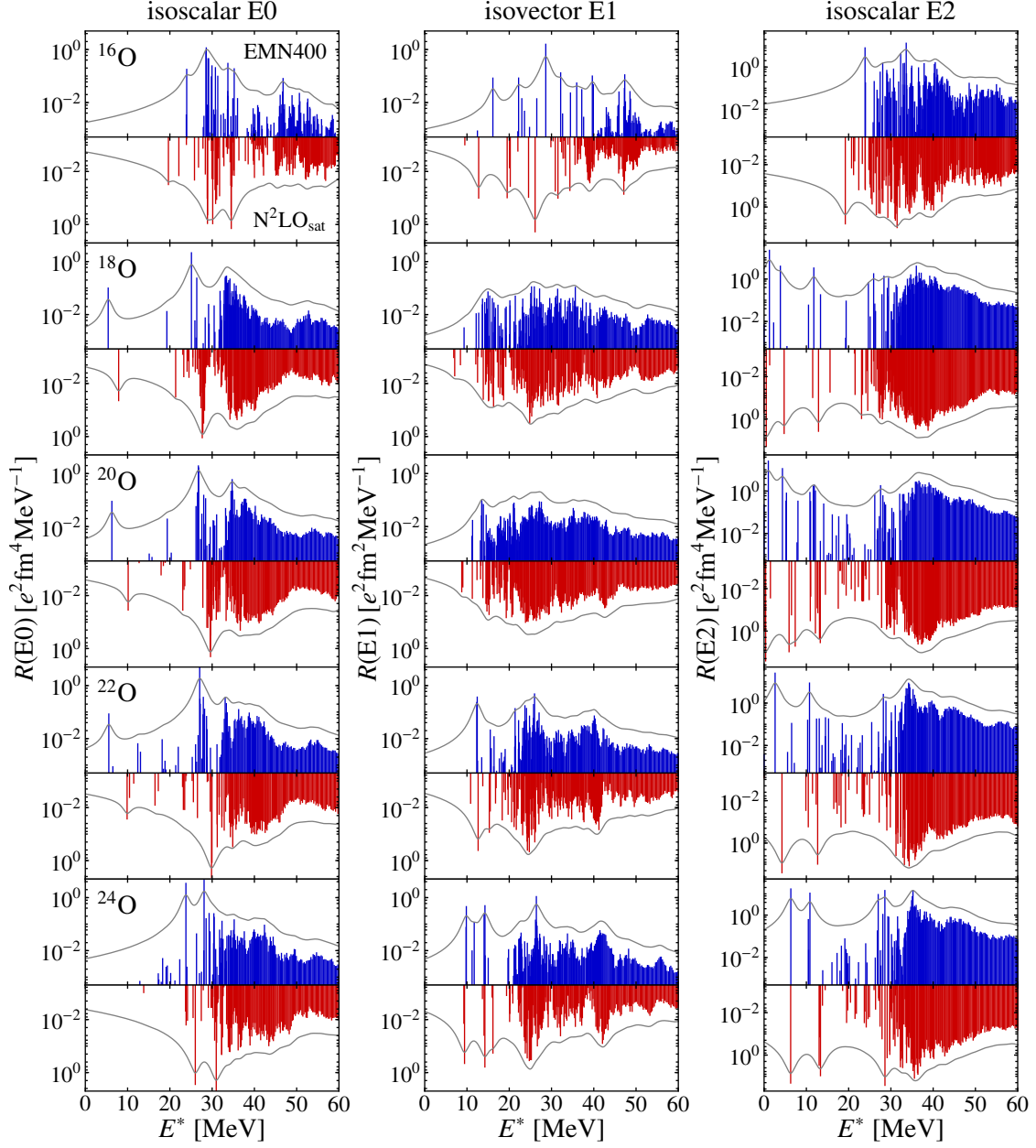


Figure 8.7.: Discrete isoscalar E0, isovector E1, and isoscalar E2 strength functions of the even- A oxygen isotopes $^{16-24}\text{O}$ using the SRG-evolved EMN400 and $\text{N}^2\text{LO}_{\text{sat}}$ interactions with $\alpha = 0.08 \text{ fm}^4$. The oscillator frequency is $\hbar\Omega = 20 \text{ MeV}$ and $\beta = 0.5$. The IT-NCSM model spaces are truncated at $N_{\text{max}} = 8/9$.

Nucleus	EMN400	N ² LO _{sat}	Exp
¹⁶ O	0.372(15)	0.481(31)	0.585(9)
¹⁸ O	0.505(48)	0.576(63)	
²⁰ O	0.612(52)	0.660(69)	
²² O	0.727(52)	0.792(59)	
²⁴ O	0.996(64)	1.087(87)	

Table 8.1.: Electric dipole polarizability for the even- A oxygen isotopes $^{16-24}\text{O}$ obtained for the SRG-evolved EMN400 and N²LO_{sat} interactions with $\alpha = 0.08 \text{ fm}^4$. The experimental value for ^{16}O has been taken from [Ahr+75]. All values are given in units of fm^3 . The theoretical uncertainties are given by the difference of the dipole polarizabilities for $N_{\text{max}} = 6/7$ and $N_{\text{max}} = 8/9$.

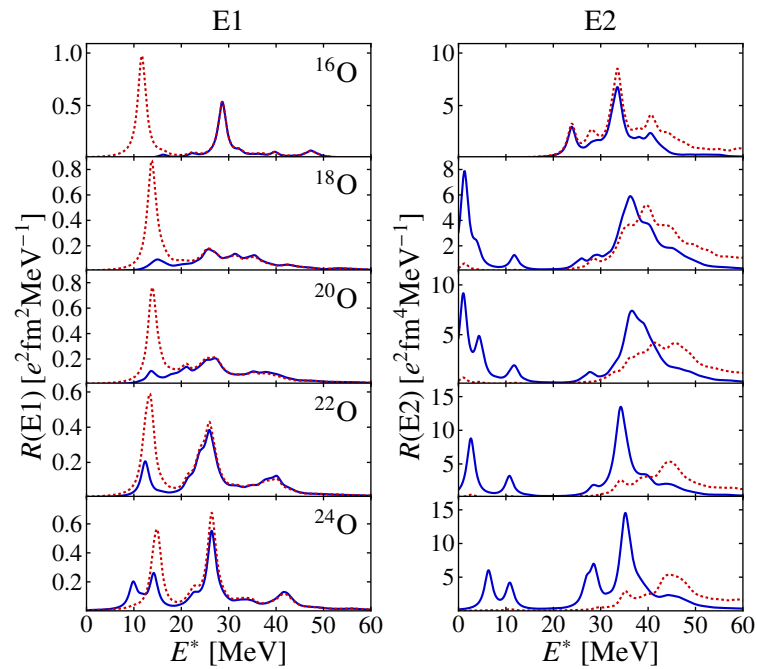


Figure 8.8.: Comparison of the total E1 and E2 responses (.....) of $^{16-24}\text{O}$ with their isovector and isoscalar analog (—), respectively. The strength functions are obtained in the IT-NCSM using the SRG-evolved EMN400 interaction with $\alpha = 0.08 \text{ fm}^4$. The oscillator frequency is $\hbar\Omega = 20 \text{ MeV}$ and $\beta = 0.5$. The IT-NCSM model spaces are truncated at $N_{\text{max}} = 8/9$.

functions are located at too high energies, the dipole polarizabilities are expected to be too small in comparison with experiment, as confirmed for ^{16}O . The $\text{N}^2\text{LO}_{\text{sat}}$ interaction yields larger dipole polarizabilities than the EMN400 interaction throughout the oxygen isotopic chain, in better agreement with experiment. Since the dipole response is located at approximately the same energies for the two interactions, the larger dipole polarizabilities result from the larger transition strengths obtained for the $\text{N}^2\text{LO}_{\text{sat}}$ interaction. With adding more and more neutrons, our predictions for the dipole polarizabilities obtained for the EMN400 and $\text{N}^2\text{LO}_{\text{sat}}$ interactions increase systematically, from 0.372 fm^3 and 0.481 fm^3 for ^{16}O reaching 0.996 fm^3 and 1.087 fm^3 for ^{24}O , respectively.

The isoscalar E2 distribution starting from ^{18}O shows strong contributions from low-lying neutron-dominated 2^+ excitations, which hardly contribute to the total E2 strength without isospin decomposition, see the discussion below. This low-lying quadrupole strength can be interpreted as a pygmy quadrupole resonance, predicted in [TL11] and recently observed in ^{124}Sn [Spi+16].

We study the isospin decomposition of the E1 and E2 strength distributions in more detail for the EMN400 interaction. Figure 8.8 shows the total E1 and E2 as well as the isovector E1 and isoscalar E2 strength functions for the even-mass oxygen isotopes. For ^{16}O , the total and isovector E1 strength distributions are identical except for one pronounced peak, which can be attributed to the excitation of the nucleus' center of mass. This is because the total E1 operator can be decomposed into an intrinsic and center-of-mass part, where the former is identical to the isovector E1 operator for $N = Z$ nuclei. If no effective charges are introduced, the isovector E1 operator differs more and more from the intrinsic E1 operator with increasing or decreasing neutron-proton ratio. This is also manifested in the total and isovector E1 strength distributions. For the E2 transitions, we find that the strong individual transitions found at low energies result from the neutrons only. No comparable peaks are found in the total E2 strength distributions. Furthermore, the isoscalar E2 strength is enhanced in the giant-resonance region compared to the total E2 strength for the heavier oxygen isotopes. These observations indicate the appearance of strong cancellations between proton and neutron contributions in the total E2 strength.

8.2.2. Carbon Isotopes

We turn our attention toward the *ab initio* description of the electric response of the carbon isotopic chain. A first theoretical study of the systematics of the electric dipole strength functions throughout this isotopic chain has been carried out in the VSSM [SSH03], and the photonuclear cross sections for ^{12}C and ^{14}C have been measured [Ahr+75; Pyw+85].

Again, we first benchmark the model-space convergence of the strength distributions with respect to the model-space truncation N_{max} in figures 8.9 and 8.10 for the EMN400 and $\text{N}^2\text{LO}_{\text{sat}}$ interactions. In both cases, the strength functions are remarkably stable for varying N_{max} , with improved convergence compared to the oxygen isotopes for all isotopes and multipoles, except for the isovector E1 distributions of ^{16}C and ^{18}C . Here, the N_{max} dependence is significant, and even more pronounced than for the isovector E1 distributions of ^{18}O and ^{20}O shown in figures 8.3 and 8.4. The strength functions obtained with the EMN400 and $\text{N}^2\text{LO}_{\text{sat}}$ interactions are compared in figure 8.11. They are very similar in their structure, position, and magnitude of the individual transitions.

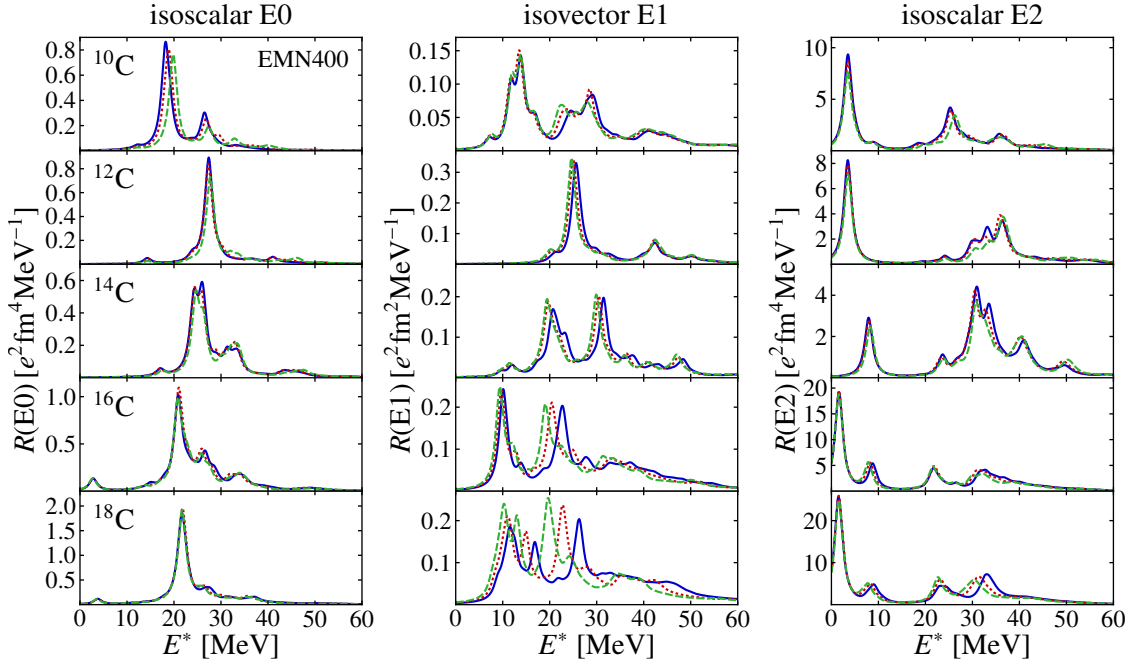


Figure 8.9.: Model-space convergence of the isoscalar E0, isovector E1, and isoscalar E2 strength functions of the even- A carbon isotopes $^{10-18}\text{C}$ using the EMN400 interaction, SRG-evolved up to $\alpha = 0.08 \text{ fm}^4$. The oscillator frequency is $\hbar\Omega = 20 \text{ MeV}$ and $\beta = 0.5$. The IT-NCSM model spaces are truncated at $N_{\text{max}} = \{4/5(\text{---}), 6/7(\text{...}), 8/9(\text{—})\}$.

Only the isovector E1 distributions of ^{16}C and ^{18}C differ notably due to their incomplete convergence. This is expected to be improved by increasing the model-space size. Also here, the E0 distribution calculated with the $\text{N}^2\text{LO}_{\text{sat}}$ interaction is located at slightly higher energies than the one obtained with the EMN400 interaction, contrary to what is expected from an interaction that yields larger nuclear radii.

The E1 distributions reveal an interesting systematics throughout the isotopic chain: For ^{10}C , two resonance regions are observed, with the one at lower energies—between 10 and 20 MeV—exceeding the strength located in the giant-resonance region. We interpret this low-lying strength as the analog of the pygmy dipole resonance driven by the excess protons. Also, the giant resonance is relatively broad compared to the single-peak structure for ^{12}C , which agrees well with experiment. With adding more and more neutrons, the giant resonances broaden again, and a pygmy dipole resonance emerges at lower energies. For ^{14}C , the calculated strength distributions reproduce well the two-resonance structure observed in experiment, however, they are located at too high energies. We also provide the dipole polarizabilities in table 8.2. The theoretical uncertainties correspond to the difference between the values obtained for $N_{\text{max}} = 6/7$ and $N_{\text{max}} = 8/9$. Note that the uncertainties for ^{16}C and ^{18}C are significant due to the incomplete convergence of their E1 responses. The two interactions yield dipole polarizabilities that differ by 10% to

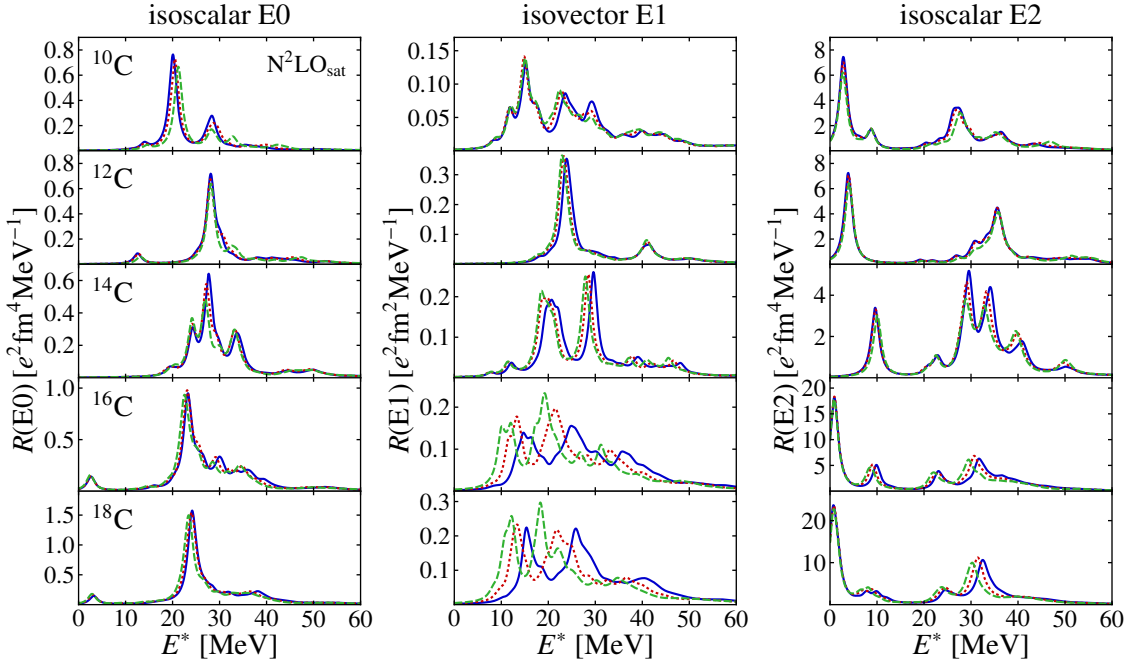


Figure 8.10.: As figure 8.9 but for the $N^2\text{LO}_{\text{sat}}$ interaction.

15%. The value obtained with the $N^2\text{LO}_{\text{sat}}$ interaction is in reasonable agreement with experiment for ^{12}C . Starting from this $N = Z$ nucleus, the dipole polarizabilities increase when neutrons are removed or added successively.

The isoscalar E2 strength functions agree perfectly for the two interactions and consistently exhibit large strength at energies below the giant-resonance region. We note that the large peaks at low energies can be attributed to transitions between the ground state and the first excited 2^+ state.

We compare the isovector E1 and isoscalar E2 responses with the total responses in figure 8.12. The latter has not been considered so far in the analysis. The total E1 response is, in general, similar to the isovector response, but exhibits a pronounced peak around 12 MeV for $^{10,12,14}\text{C}$, which can be attributed to the isoscalar E1 mode and is related to the excitation of the nucleus' center of mass. Thus, it does not affect the isovector E1 distributions. For ^{16}C and ^{18}C , however, this peak moves to energies in the region of the isovector E1 mode and can affect the strength functions.

The total E2 distribution resembles the isoscalar E2 distribution only for ^{10}C and ^{12}C , and the distributions differ more and more with increasing mass number. This underlines that the isoscalar E2 strength is particularly driven by the neutrons.

In order to shed more light on the nature of the different resonance peaks, we investigate the radial transition densities of some discrete levels with prominent isovector E1 and isoscalar E2 strength in the pygmy- and giant-resonance regions for some isotopes. The radial transition density is defined as the function $\rho_{0f}^{m_s, \tau}(r)$ in

$$\rho_{0f}^{m_s, \tau}(\vec{r}) = \rho_{0f}^{m_s, \tau}(r) Y_{JM}(\Omega)$$

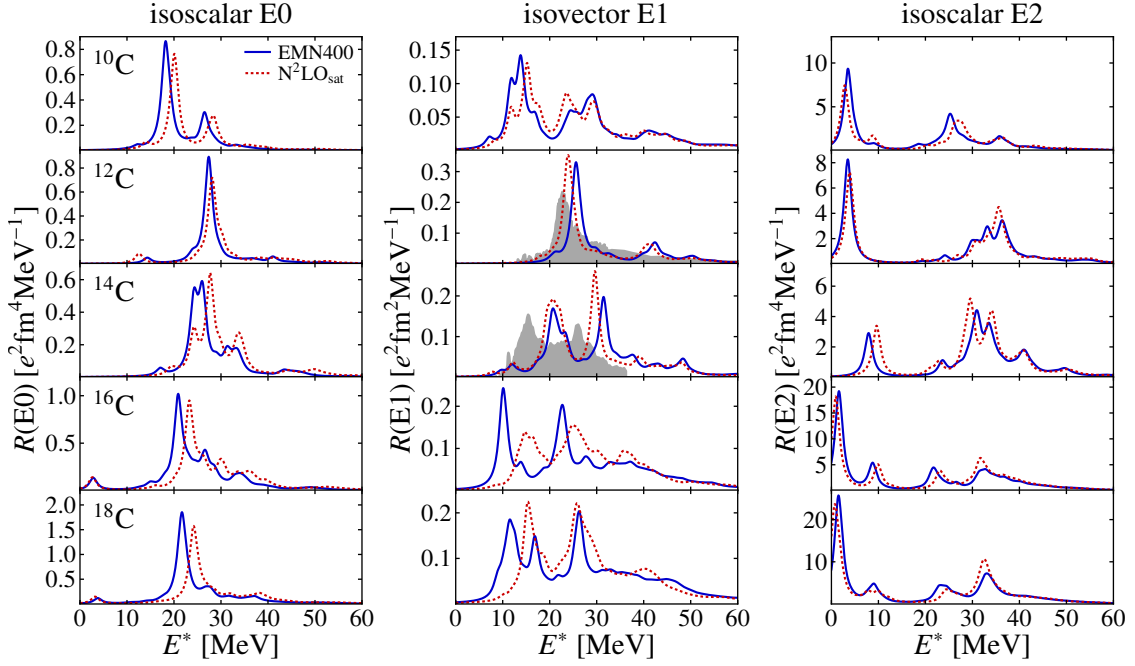


Figure 8.11.: Isoscalar E0, isovector E1, and isoscalar E2 strength functions of the even- A carbon isotopes $^{10-18}\text{C}$ using the SRG-evolved EMN400 (—) and $\text{N}^2\text{LO}_{\text{sat}}$ (⋯) interactions with $\alpha = 0.08 \text{ fm}^4$. The oscillator frequency is $\hbar\Omega = 20 \text{ MeV}$ and $\beta = 0.5$. The IT-NCSM model spaces are truncated at $N_{\text{max}} = 8/9$. The gray areas show experimental data in arbitrary units for ^{12}C and ^{14}C from [Ahr+75] and [Pyw+85], respectively.

Nucleus	EMN400	$\text{N}^2\text{LO}_{\text{sat}}$	Exp
^{10}C	0.412(17)	0.376(14)	
^{12}C	0.281(11)	0.326(12)	0.316(5)
^{14}C	0.393(18)	0.454(25)	
^{16}C	0.695(55)	0.582(100)	
^{18}C	0.755(103)	0.664(133)	

Table 8.2.: Electric dipole polarizability for the even- A carbon isotopes $^{10-18}\text{C}$ obtained for the SRG-evolved EMN400 and $\text{N}^2\text{LO}_{\text{sat}}$ interactions with $\alpha = 0.08 \text{ fm}^4$. The experimental value for ^{16}O has been taken from [Ahr+75]. All values are given in units of fm^3 . The theoretical uncertainties are given by the difference of the dipole polarizabilities for $N_{\text{max}} = 6/7$ and $N_{\text{max}} = 8/9$.

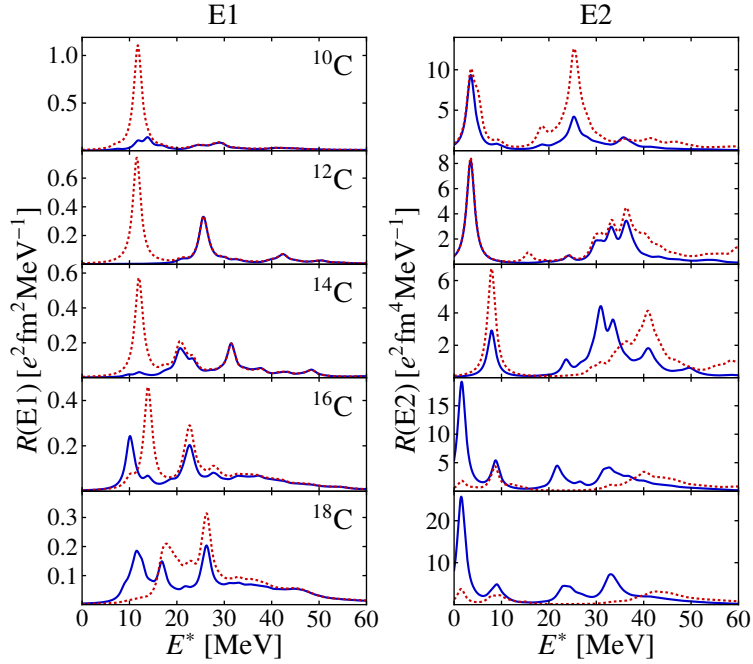


Figure 8.12.: Comparison of the total E1 and E2 responses (.....) of $^{10-18}\text{C}$ with their isovector and isoscalar analog (—). The strength functions are obtained in the IT-NCSM using the SRG-evolved EMN400 interaction. The oscillator frequency is $\hbar\Omega = 20$ MeV and $\beta = 0.5$. The IT-NCSM model spaces are truncated at $N_{\text{max}} = 8/9$.

$$= \langle \Psi_0 | \Psi_{m_s, \tau}^\dagger(\vec{r}) \Psi_{m_s, \tau}(\vec{r}) | \Psi_f \rangle. \quad (8.2)$$

The field operators $\Psi_{m_s, \tau}^\dagger(\vec{r})$ and $\Psi_{m_s, \tau}(\vec{r})$ create and annihilate a nucleon with spin projection m_s and isospin projection τ at position \vec{r} . By projecting onto the spherical coordinate and by summing over m_s , we obtain the radial transition density

$$\rho_{0f}^\tau(r) = \sum_{m_s} \langle \Psi_0 | \int d\Omega Y_{JM}^*(\Omega) \Psi_{m_s, \tau}^\dagger(\vec{r}) \Psi_{m_s, \tau}(\vec{r}) | \Psi_f \rangle, \quad (8.3)$$

where we keep the isospin projection as parameter so that the transition densities for protons and neutrons can be calculated separately. More details and the derivation of the final expressions in a general ls -coupled basis are provided in appendix D. Since the structure of the strength functions is already evident for small N_{max} , we restrict the calculation of the natural-parity and unnatural-parity eigenstates in the IT-NCSM to $N_{\text{max}} = 4$ and 5. Figure 8.13 shows the discrete and folded isovector E1 strength functions of ^{10}C and ^{14}C obtained for the SRG-evolved EMN400 interaction. We consider the eigenstates contributing with prominent peaks to the strength distributions, marked by the red arrows, and draw the corresponding radial transition densities in figures 8.14 and 8.15.

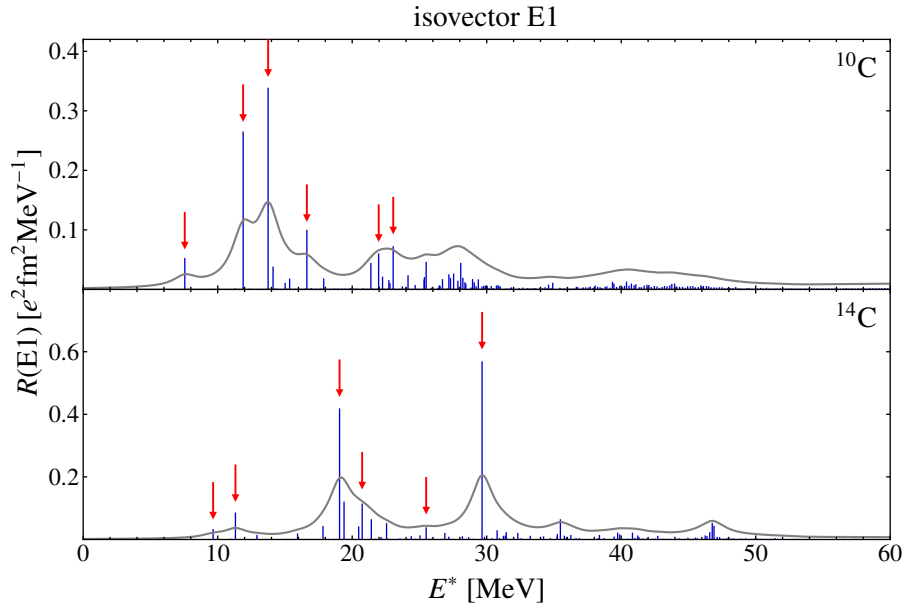


Figure 8.13.: Discrete and folded isovector E1 strength functions of ^{10}C and ^{14}C obtained in the IT-NCSM using the SRG-evolved EMN400 interaction with $\alpha = 0.08 \text{ fm}^4$. The oscillator frequency is $\hbar\Omega = 20 \text{ MeV}$ and $\beta = 0.5$. The IT-NCSM model spaces are truncated at $N_{\text{max}} = 4/5$. The red arrows point at the resonance peaks for which radial transition densities are calculated.

For ^{10}C , all transitions except for the one at 11.89 MeV are represented by bulk protons and neutrons oscillating in phase in the nucleus' interior and out of phase at the nuclear surface. With increasing energies, the isovector oscillation of the protons and neutrons becomes more and more significant, i.e., the isoscalar region in the inner part of the nucleus becomes smaller. The proton excess in this nucleus manifests itself in the prolonged tail in the proton transition density, visible in all transition densities. Only the dipole transition at 11.89 MeV is purely isoscalar, indicating its origin from the motion of the center of mass. This is confirmed by both, a significant expectation value of the center-of-mass Hamiltonian in this state and a sizable dependence of this transition on variations of the center-of-mass control parameter β . We note that the impact of center-of-mass spuriosities might be particularly powered in the model spaces used here, where $N_{\text{max}} = 4/5$ only, and should be reduced for increasing N_{max} . We attribute the first four transitions studied here to the pygmy dipole resonance. The transitions in the region of the giant resonance are typically isovector. This is not found here; however, we have only considered transitions in the low-energy tail of the giant resonance, and the trend observed with increasing excitation energies is consistent with this expectation.

For ^{14}C , the transitions at lower energies are of isoscalar character, while the transitions in the resonance region at intermediate energies are mainly isovector with some isoscalar admixtures in the nucleus' interior. Again, the transition at 11.32 MeV exhibits a simple in-phase oscillation pattern, which in combination with the sizable expectation value of

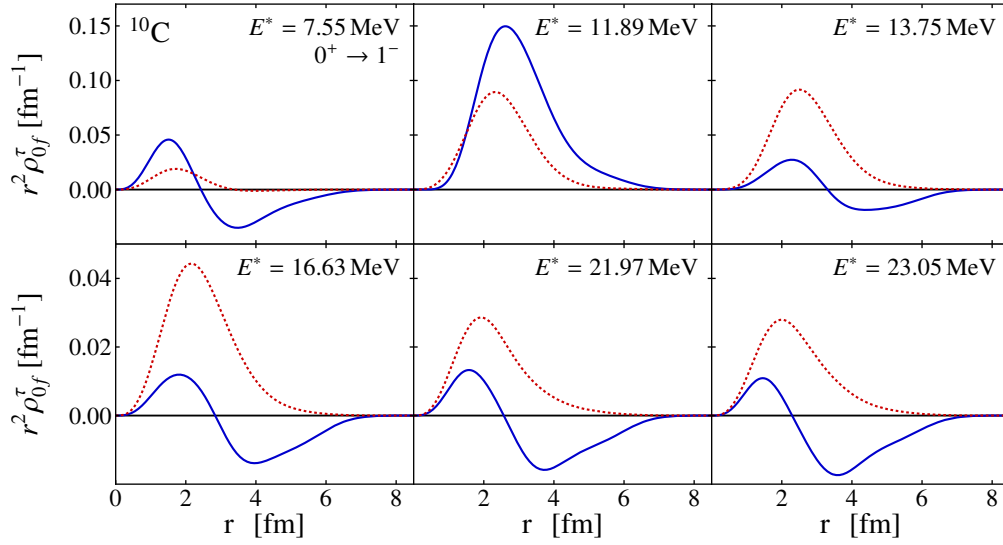


Figure 8.14.: Radial proton (—) and neutron (⋯) transition densities from the 0^+ ground state of ^{10}C to 1^- states with dominant contributions to the isovector E1 response. The transition densities are obtained in the IT-NCSM using the SRG-evolved EMN400 interaction with $\alpha = 0.08 \text{ fm}^4$. The oscillator frequency is $\hbar\Omega = 20 \text{ MeV}$ and $\beta = 0.5$. The IT-NCSM model spaces are truncated at $N_{\text{max}} = 4/5$.

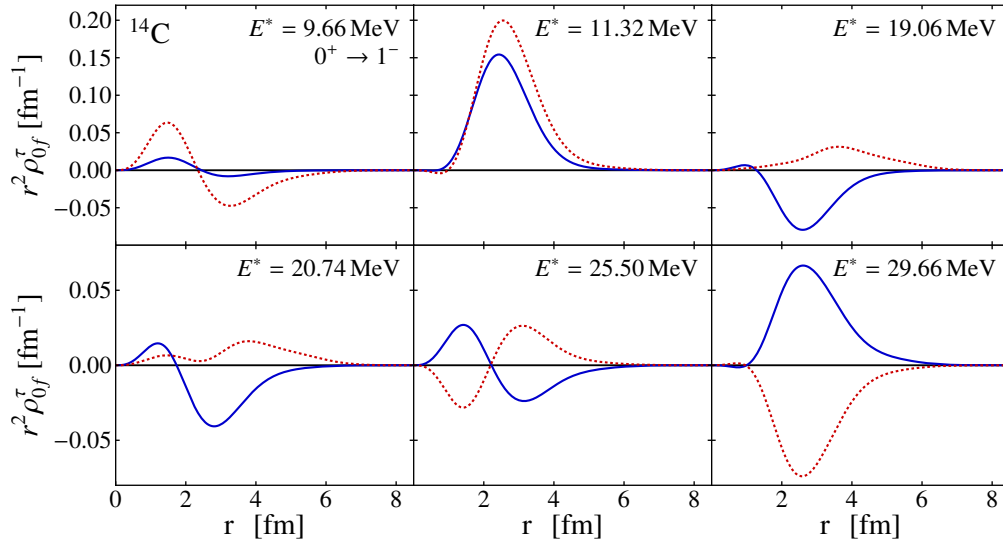


Figure 8.15.: As figure 8.14 but for ^{14}C .

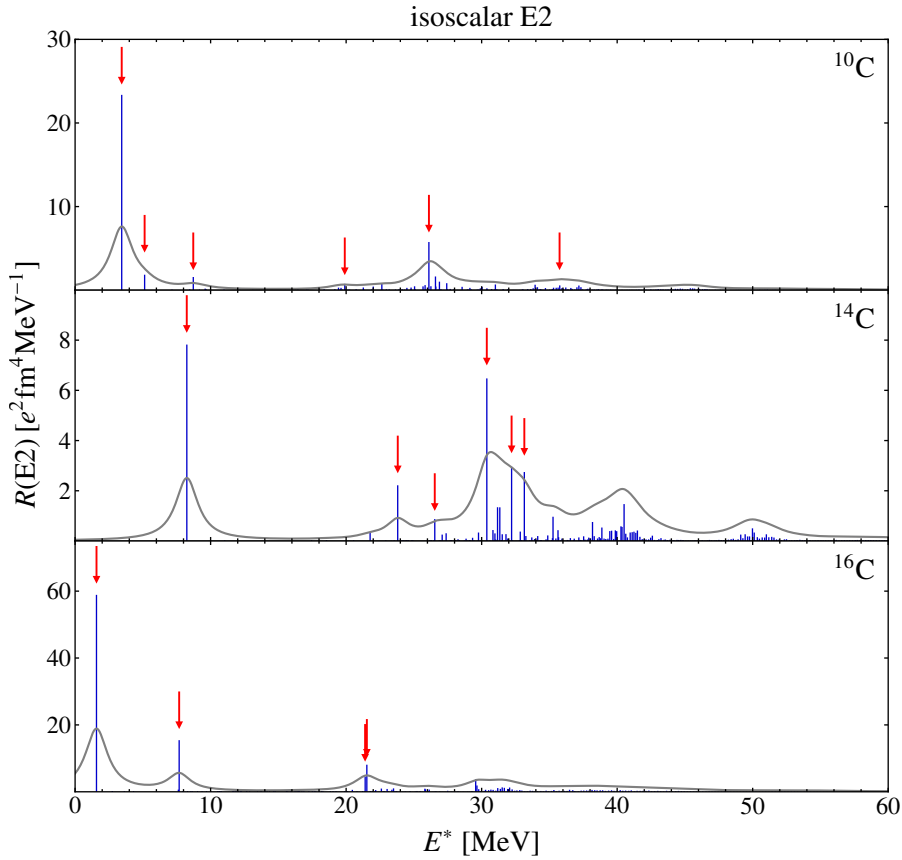


Figure 8.16.: Discrete and folded isoscalar E2 strength functions of $^{10,14,16}\text{C}$ obtained in the IT-NCSM using the SRG-evolved EMN400 interaction with $\alpha = 0.08 \text{ fm}^4$. The oscillator frequency is $\hbar\Omega = 20 \text{ MeV}$ and $\beta = 0.5$. The IT-NCSM model spaces are truncated at $N_{\text{max}} = 4$. The red arrows point at the resonance peaks for which radial transition densities are calculated.

the center-of-mass Hamiltonian in this 1^- state confirms its spurious nature. As expected, the transitions in the giant dipole-resonance region are purely isovector.

We proceed in the same way to analyze the dominant transitions in the isoscalar E2 distributions of $^{10,14,16}\text{C}$. The respective peaks are marked by the red arrows in figure 8.16. Note that for ^{16}C , the calculation of many eigenstates is challenging, and we were able to study only four dominant transitions up into the low-energy tail of the giant resonance. For the interpretation of the transition densities, we need to keep in mind the angular distribution of quadrupole excitations. The radial transition densities are shown in figures 8.17 to 8.19. The two lowest peaks in ^{10}C at $E^* = 3.44 \text{ MeV}$ and 5.13 MeV are close to the experimental proton-separation energy of about 4 MeV and represent the dominant strength for the strength distribution. These and the transition at 8.72 MeV are part of a region of enhanced low-lying quadrupole strength. Their radial transition densities are either of isoscalar or isovector nature, i.e., the bulk protons and neutrons

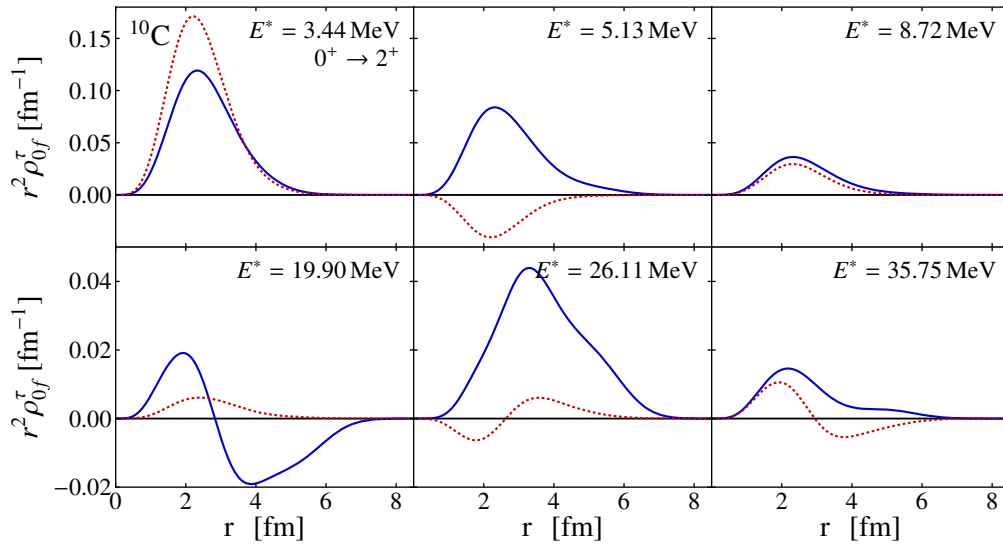


Figure 8.17.: Radial proton (—) and neutron (⋯) transition densities from the 0^+ ground state of ^{10}C to 2^+ states with dominant contributions to the isoscalar E2 response. The transition densities are obtained in the IT-NCSM using the SRG-evolved EMN400 interaction with $\alpha = 0.08 \text{ fm}^4$. The oscillator frequency is $\hbar\Omega = 20 \text{ MeV}$ and $\beta = 0.5$. The IT-NCSM model spaces are truncated at $N_{\text{max}} = 4$.

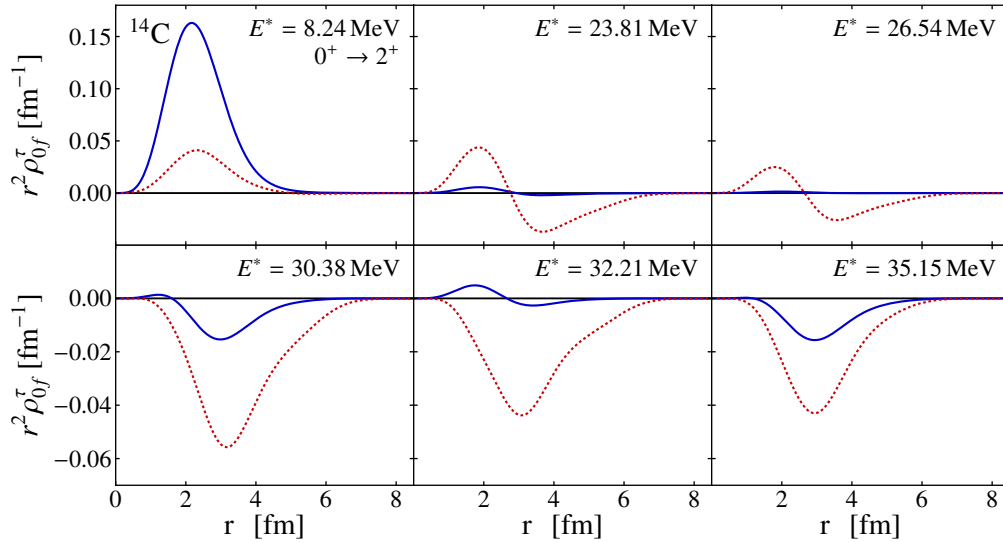
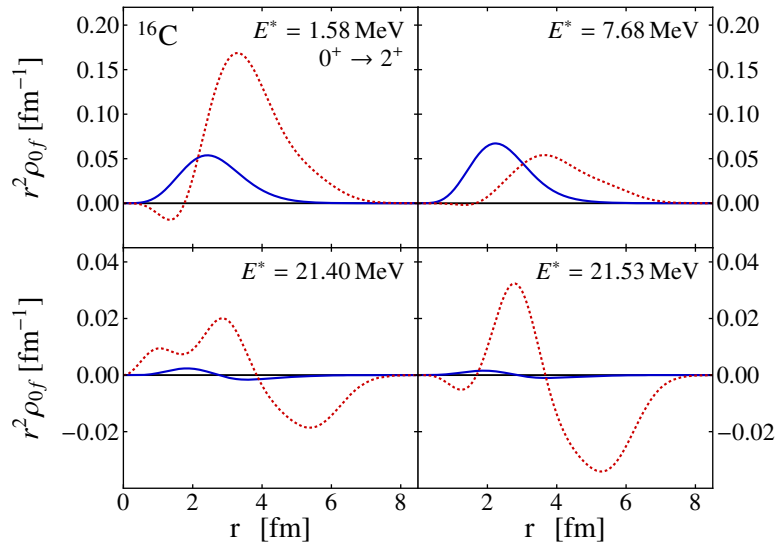


Figure 8.18.: As figure 8.17 but for ^{14}C .


 Figure 8.19.: As figure 8.17 but for ^{16}C .

perform a quadrupole oscillation in or out of phase. Interestingly, the radial densities of transitions at higher energies exhibit more structure and show signatures of both, isoscalar and isovector transitions. For example, the transitions at $E^* = 19.90$ MeV and 35.75 MeV are characterized by protons and neutrons oscillating in phase in a quadrupole pattern in the interior of the nucleus, while they move out of phase at the surface. A reverse situation is found for the transition at $E^* = 26.11$ MeV. Here, the transition is isovector in the inner part of the nucleus and isoscalar at the surface.

The transitions studied for ^{14}C are mainly isoscalar in the complete energy range considered, with small isovector admixtures in the inner part of the nucleus for the transitions at $E^* = 30.38$ MeV and 32.21 MeV. The results are in line with the expected dominant isoscalar character of the transitions in the region of the isoscalar giant-quadrupole resonance.

Figure 8.16 shows that the lowest two peaks found in the isoscalar E2 distribution of ^{16}C , giving rise to the enhanced low-lying quadrupole strength, consist of single transitions, one to the first excited 2^+ state and the other one to a resonance state at about 8 MeV. The transition densities reveal that these transitions are predominantly of isoscalar character, with small isovector contributions in the interior for the first 2^+ state. The transitions in the low-energy tail of the giant quadrupole resonance exhibit more complicated structures, and are dominated by the neutrons. For all transitions considered, the neutron excess of ^{16}C results in a remarkable extension of the neutron transition densities to large distances.

These investigations allow us to provide an illustrative picture on the nature of transitions in the different energy regions of the strength distributions. An analog study of the transition densities of neutron-rich oxygen isotopes, for which we have postulated a pygmy quadrupole resonance, would be particularly interesting.

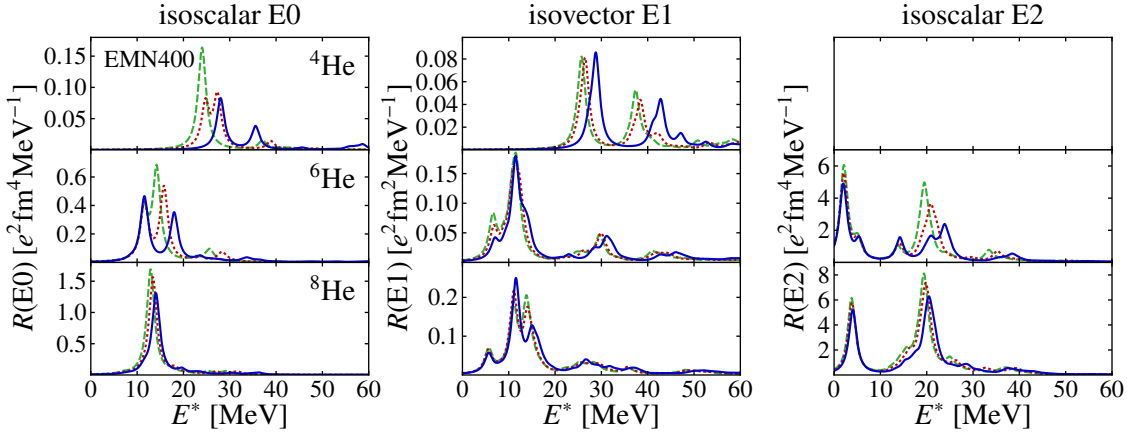


Figure 8.20.: Model-space convergence of the isoscalar E0, isovector E1, and isoscalar E2 strength functions of the helium isotopes ${}^{4,6,8}\text{He}$ using the EMN400 interaction, SRG-evolved up to $\alpha = 0.08 \text{ fm}^4$. The oscillator frequency is $\hbar\Omega = 20 \text{ MeV}$ and $\beta = 0.5$. The IT-NCSM model spaces are truncated at $N_{\text{max}} = \{4/5(\text{---}), 6/7(\text{...}), 8/9(\text{—})\}$.

8.2.3. Helium Isotopes

The helium isotopic chain is perfectly suited for the validation of nuclear theories because it comprises nuclei which probe very different aspects of the nuclear interaction, e.g., the very stable doubly-magic nucleus ${}^4\text{He}$ as well as the two halo nuclei ${}^6\text{He}$ and ${}^8\text{He}$. We note that a wealth of data is available for ${}^4\text{He}$, albeit the photonuclear cross sections are controversial [Shi+05]. For this nucleus, a variety of few- and many-body methods in combination with the LIT has been used to calculate the photonuclear cross section [Bar+01; Gaz+06; QN07; Bac+14], providing a basis for comparisons among these methods. Experiments on the exotic nuclei ${}^6\text{He}$ and ${}^8\text{He}$ have become possible only recently, e.g., the charge radius of ${}^8\text{He}$ has been first measured a decade ago [Mue+07]. In the near future, also the dipole response of ${}^6\text{He}$ will be studied at GSI (FAIR Phase-0) [Aum17].

We provide predictions on the isoscalar E0, isovector E1, and isoscalar E2 distributions of the helium isotopes ${}^{4,6,8}\text{He}$. We compare results obtained with the EMN400, $N^2\text{LO}_{\text{sat}}$, and EMN500 interactions. Note that we do not calculate the E2 distributions for ${}^4\text{He}$ because the lowest 2^+ state lies so high in energy that it is unbound.

Figures 8.20 to 8.22 depict the model-space convergence of the strength functions. The three interactions exhibit a very similar behavior with respect to increasing N_{max} . Some dependence of the strength distributions on N_{max} persists, particularly for ${}^4\text{He}$. Convergence is improved with increasing mass number, and is best for the isovector E1 strength functions.

When comparing the results for $N_{\text{max}} = 8/9$ obtained with the three interactions in figure 8.23, we find excellent agreement of the strength functions for all isotopes and multipoles. For comparison, figure 8.24 shows the discrete strength functions for the EMN500 interaction. For ${}^4\text{He}$, the dominant peaks are governed by single transitions. This

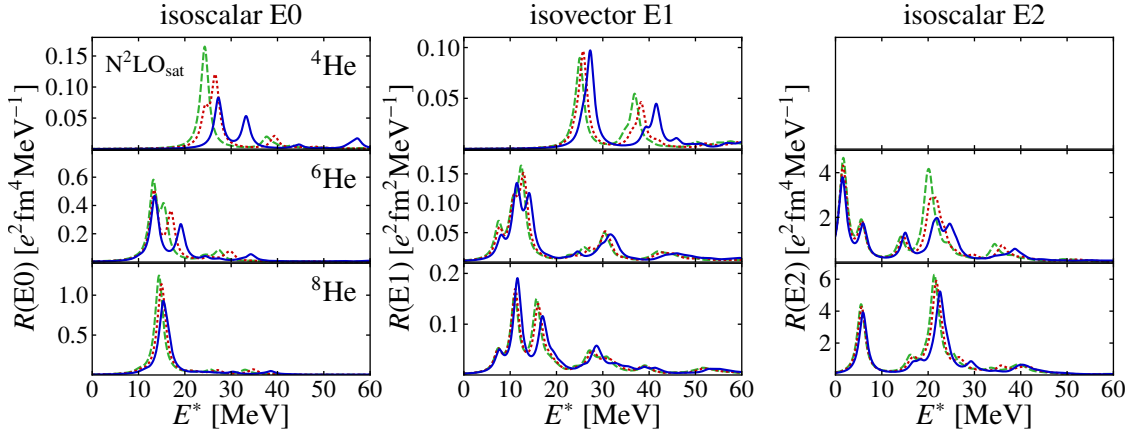
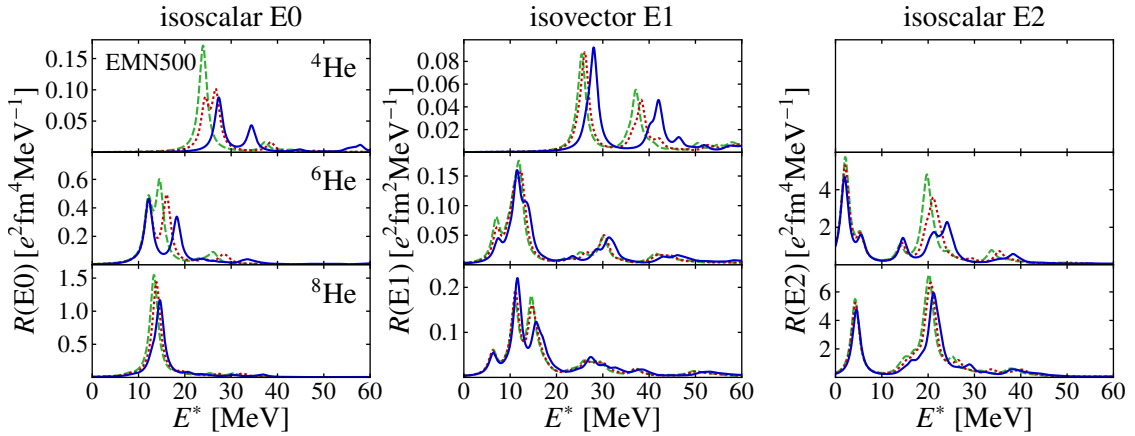

 Figure 8.21.: As figure 8.20 but for the N^2LO_{sat} interaction.


Figure 8.22.: As figure 8.20 but for the EMN500 interaction.

is also found for the lowest peaks in the response of in ${}^6\text{He}$ and ${}^8\text{He}$, however, the regions of the giant monopole, dipole, and quadrupole resonances exhibit more fragmentation.

The systematics of the strength functions throughout the isotopic chain is as follows: The monopole strength at about 24 MeV in ${}^4\text{He}$ is shifted to lower energies when additional neutrons are added. This is consistent with what is expected from nuclei with larger radii based on a naive mean-field picture.

The dipole response of ${}^4\text{He}$ exhibits strength at too high energies compared to data [Ark+80]. The two pronounced peaks in the calculated strength function are not visible in the data. We remark, however, that the data is very controversial, and various experiments yield significant discrepancies, see [Shi+05] for an overview. The availability of precise data is desirable to allow definite conclusions on the quality of theoretical interactions and many-body methods. We note that good agreement with some of the data was found

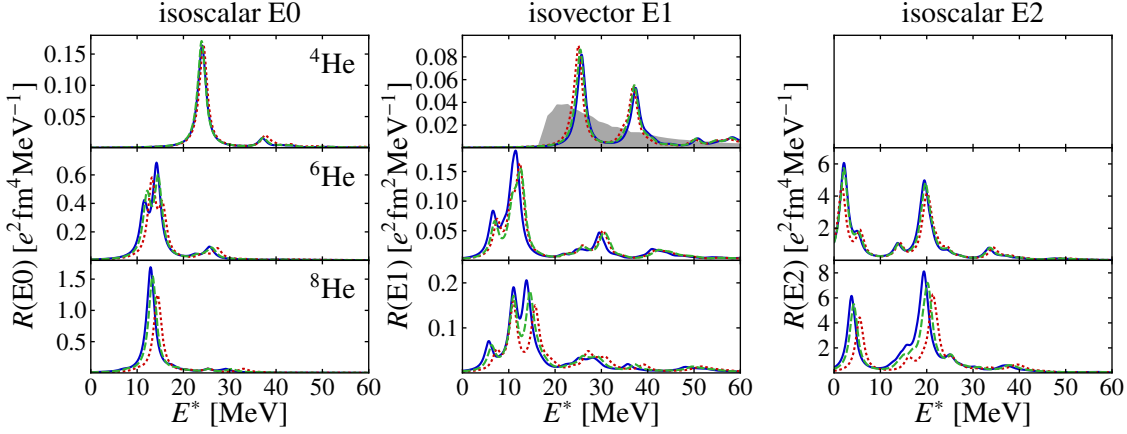


Figure 8.23.: Isoscalar E0, isovector E1, and isoscalar E2 strength functions of ${}^{4,6,8}\text{He}$ using the SRG-evolved EMN400 (—), $\text{N}^2\text{LO}_{\text{sat}}$ (.....), and EMN500 (---) interactions with $\alpha = 0.08 \text{ fm}^4$. The oscillator frequency is $\hbar\Omega = 20 \text{ MeV}$ and $\beta = 0.5$. The IT-NCSM model spaces are truncated at $N_{\text{max}} = 8/9$. The gray areas show experimental data in arbitrary units for ${}^4\text{He}$ from [Ark+80].

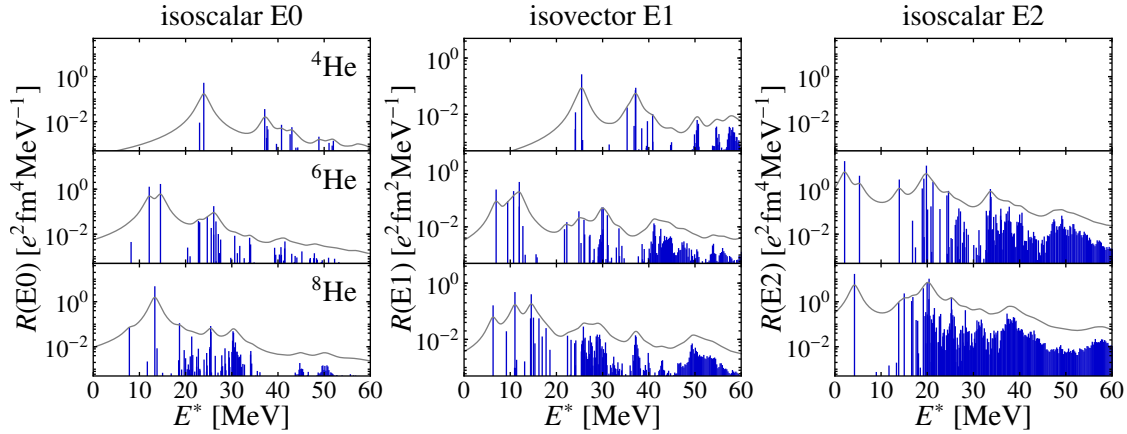


Figure 8.24.: Discrete isoscalar E0, isovector E1, and isoscalar E2 strength functions of ${}^{4,6,8}\text{He}$ using the SRG-evolved EMN500 interaction with $\alpha = 0.08 \text{ fm}^4$. The oscillator frequency is $\hbar\Omega = 20 \text{ MeV}$ and $\beta = 0.5$. The IT-NCSM model spaces are truncated at $N_{\text{max}} = 8/9$.

8. Applications of IT-NCSM Strength Functions

Nucleus	EMN400	N ² LO _{sat}	EMN500	Exp
⁴ He	0.0743(10)	0.0820(3)	0.0782(3)	0.074(9)
⁶ He	0.4710(393)	0.3989(189)	0.4453(285)	
⁸ He	0.5950(1)	0.4454(19)	0.5287(50)	

Table 8.3.: Electric dipole polarizability for ^{4,6,8}He obtained for the SRG-evolved EMN400, N²LO_{sat}, and EMN500 interactions with $\alpha = 0.08 \text{ fm}^4$. The experimental value for ⁴He is taken from [Mio+16]. All values are given in units of fm^3 . The theoretical uncertainties are given by the difference of the dipole polarizabilities for $N_{\text{max}} = 6/7$ and $N_{\text{max}} = 8/9$.

in various few- and many-body methods employing the LIT for the calculation of the cross sections [Bar+01; Gaz+06; QN07; Bac+14]. However, these calculations provide only very gross and smeared-out structures. By increasing the width of the Lorentzian curve employed to fold the discrete transition strengths, we obtain strength functions that resemble these.

When considering ⁶He and ⁸He, the dominant strength is pushed toward lower energies, indicating the emergence of pygmy dipole resonances. We note that—unlike suggested by the name “pygmy”—these resonances are not small at all; they have been found to be significant also in theoretical predictions from the LIT method using three different semirealistic models of the nuclear force for ⁶He [Bac+02; Bac+04]. The dipole polarizabilities are listed in table 8.3. Given the discrepancies between the theoretical and experimental strength functions, the excellent agreement of our theoretical dipole polarizabilities for ⁴He for all interactions with experiment seems to be a lucky coincidence. This underlines that the dipole polarizability cannot be used reliably as a measure for the quality of theoretical models. As expected from the large strength at low energies observed for ⁶He and ⁸He, the dipole polarizabilities are significantly larger than for ⁴He.

The isoscalar E2 distributions for ⁶He and ⁸He exhibit two resonance regions. The one at lower energies corresponds to a pygmy resonance driven by the halo neutrons. Its strength is comparable in magnitude to the strength found in the giant-resonance region.

We study the nature of the enhanced dipole transition strengths by computing the radial transition densities. The respective peaks are marked by the red arrows in figure 8.25. Figure 8.26 shows that all transition strengths considered in ⁴He are of purely isovector character. The dipole transition at $E^* = 26.52 \text{ MeV}$ and 28.04 MeV can be interpreted as a simple out-of-phase oscillation of the bulk protons and neutrons. All the other transition densities exhibit more complex structures, where the bulk and surface nucleons exhibit different out-of-phase oscillation patterns. We note that the respective transitions are located at energies where ⁴He is unbound, i.e., we should not overrate these results. In all cases, the proton and neutron transition densities are almost perfectly symmetric.

The radial transition densities of ⁶He and ⁸He, shown in figures 8.27 and 8.28, share similar features. Most of the transitions are of a mixed character, i.e., they are partly isoscalar and partly isovector. For example, in the lowest transitions considered, i.e., at $E^* = 7.34 \text{ MeV}$ and 6.30 MeV , respectively, the bulk protons and neutrons oscillate

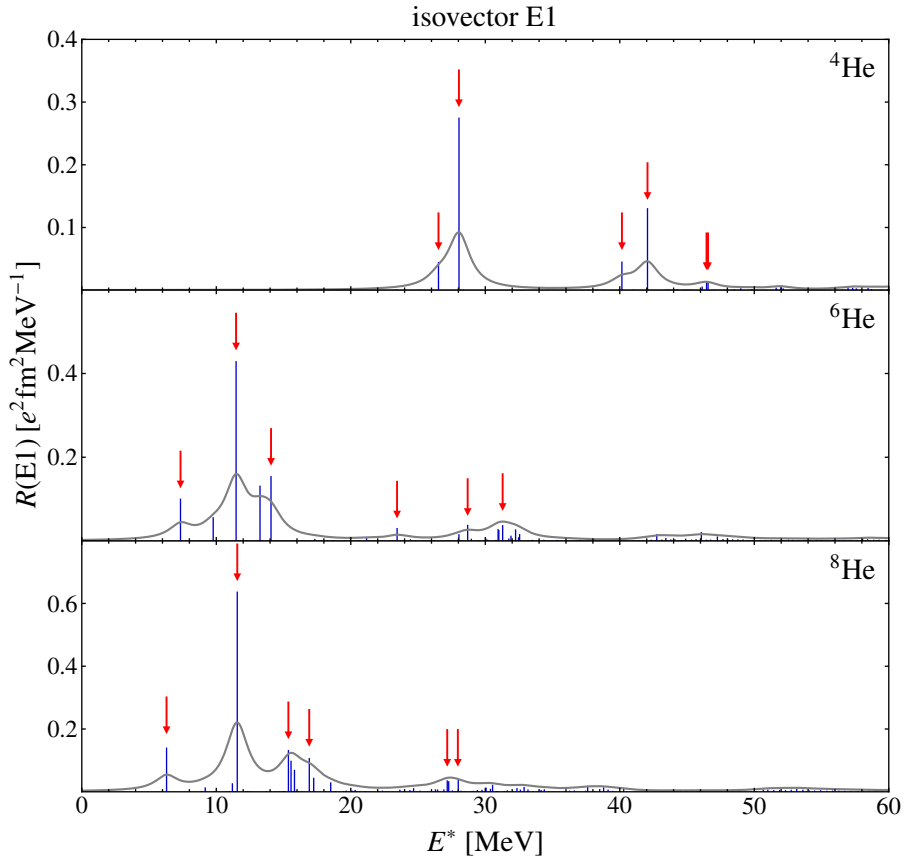


Figure 8.25.: Discrete and folded isovector E1 strength functions of ${}^4,6,8\text{He}$ obtained in the IT-NCSM using the SRG-evolved EMN500 interaction with $\alpha = 0.08 \text{ fm}^4$. The oscillator frequency is $\hbar\Omega = 20 \text{ MeV}$ and $\beta = 0.5$. The IT-NCSM model spaces are truncated at $N_{\text{max}} = 4/5$. The red arrows point at the resonance peaks for which radial transition densities are calculated.

in phase, while they move against each other at the nuclear surface, with the neutrons extending further out. In contrast to that, the most dominant peak in each distribution, at around 11.5 MeV , driving the pygmy dipole response, is purely isoscalar, and is caused by the motion of the center of mass. The transitions in the region of the giant dipole resonance are predominantly of isovector character, as expected.

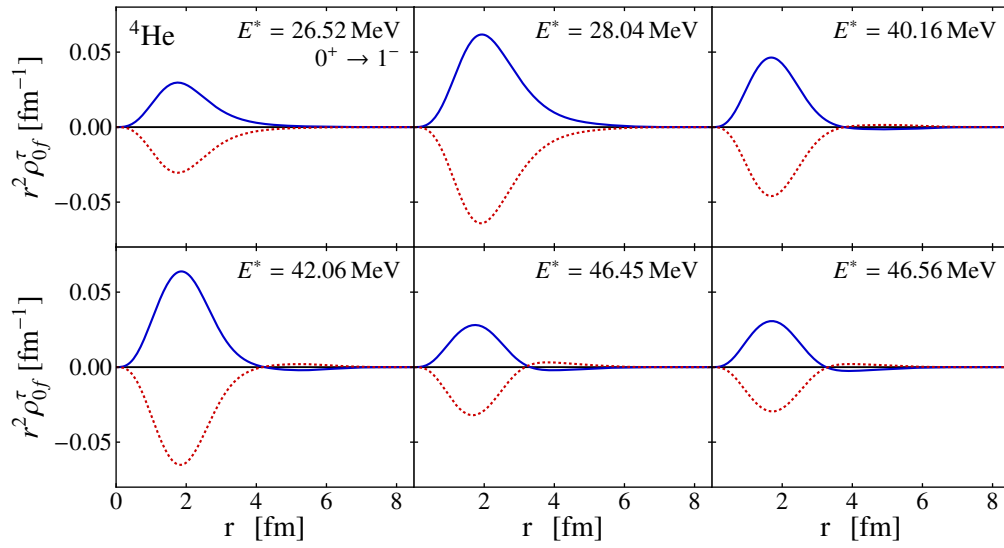


Figure 8.26.: Radial proton (—) and neutron (---) transition densities from the 0^+ ground state of ${}^4\text{He}$ to 1^- states with dominant contributions to the isovector E1 response. The transition densities are obtained in the IT-NCSM using the SRG-evolved EMN500 interaction with $\alpha = 0.08 \text{ fm}^4$. The oscillator frequency is $\hbar\Omega = 20 \text{ MeV}$ and $\beta = 0.5$. The IT-NCSM model spaces are truncated at $N_{\text{max}} = 4/5$.

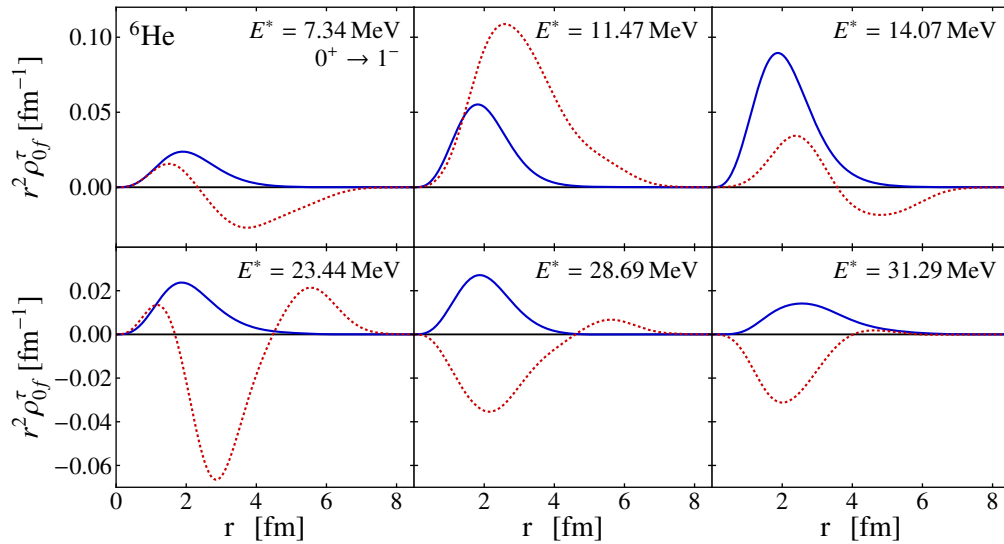


Figure 8.27.: As figure 8.26 but for ${}^6\text{He}$.

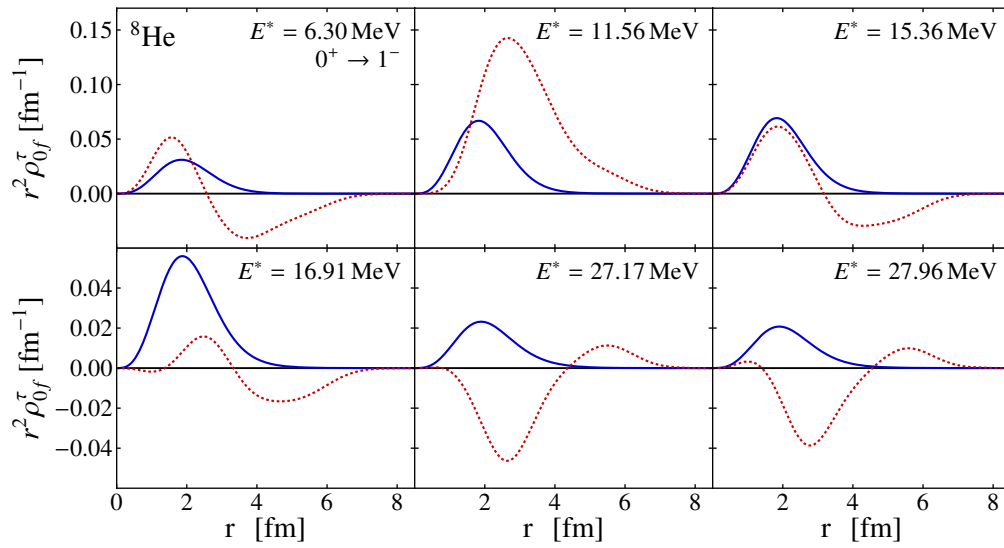


Figure 8.28.: As figure 8.26 but for ${}^8\text{He}$.

9. Conclusions

This work covers two major projects, one in the framework of the VSSM and the other one in the framework of the NCSM. The two projects share the common goal to extend the respective many-body method to new domains of applications.

The first project addresses the well established phenomenological VSSM and comprises several developments that are essential cornerstones toward its implementation as an *ab initio* method. On the one hand, this requires that all truncations are controllable, with the possibility to improve on them in a systematic manner. In the case of the VSSM, this implies an extension of the valence space. On the other hand, we wish to describe nuclei using realistic interactions that are derived in a rigorous theoretical framework rather than interactions that are determined in a phenomenological way by constraining the matrix elements by fits to experimental data of nuclei in the region of interest.

In a first step, we have applied the importance-truncation scheme to the VSSM, thus introducing the IT-VSSM. This approach is based on the definition of an *a priori* importance measure for the basis states, which, by imposing a threshold on this measure, allows for the construction of a model space with significantly smaller dimension than the model space in the conventional VSSM. This importance-truncated model space is tailored specifically to the set of target eigenstates and the Hamiltonian, and reduces the computational cost of the calculation and diagonalization of the Hamilton matrix. We have demonstrated that the IT-VSSM extends the reach of VSSM calculations to large valence spaces, which can comprise more than a single major shell, and to mid-shell nuclei. In addition to the threshold extrapolation, routinely used in the IT-NCSM, we have adopted an extrapolation in terms of the energy variance for the first time in the importance-truncation context. Generally, the threshold extrapolation provides sufficiently accurate energies and electromagnetic observables at no extra computational cost. In specific cases, however, the energy-variance extrapolation provides a better accuracy for energies at significant extra cost, e.g., for states governed by deformation.

Next, we have studied the performance of effective valence-space Hamiltonians derived in the IM-SRG. The IM-SRG is one of several *ab initio* approaches that have become available recently and that provide a consistent framework for the systematic construction of valence-space Hamiltonians and operators starting from realistic interactions, thus providing a connection to the underlying nuclear interaction. By treating all nucleons as active degrees of freedom, the IM-SRG performs a decoupling of the target valence space from the core and excluded space. We have monitored this decoupling procedure in the IM-SRG flow for the *sd*-shell valence space by means of a series of VSSM calculations for ^{18}O and compared it to a series of IT-NCSM calculations using the same IM-SRG-evolved Hamiltonians. The excellent agreement of the results obtained with both methods, which is maintained when the IT-NCSM model space is increased, confirms a successful decoupling of the valence space from the core and excluded space. However, an analog analysis of

the IM-SRG flow for an extended valence space, comprising two major shells, shows that the decoupling fails. The reasons are not yet fully understood, but we assume that this failure is related to the truncation of the IM-SRG at the level of normal-ordered two-body operators as well as the appearance of intruder states. It would be very interesting to see if an extension of the IM-SRG to normal-ordered three-body operators and beyond improves on this and, thus, allows for the construction of effective Hamiltonians for multi-shell valence spaces.

Restricting ourselves to single-shell valence spaces, we apply the IT-VSSM to the study of nuclei that are accessible only within this method. We use effective Hamiltonians derived from realistic interactions that are adjusted exclusively to few-body data. We investigate the ground and first excited states of the neutron-deficient tin isotopes $^{100-114}\text{Sn}$ in the *gds* valence space employing two interactions, 1.8/2.0(EM) and 2.0/2.0(EM), as starting point. These interactions are constructed in a similar way, and there is no *a priori* criterion why one of these interactions should be superior. Although they perform well in the reproduction of the systematic trend of the experimental ground-state energies, the 1.8/2.0(EM) yields results that are impressively close to these data, while the 2.0/2.0(EM) underestimates the ground-state energies. Also, the 2.0/2.0(EM) does not produce a 2^+ first-excited state within the lowest four states calculated, while the 1.8/2.0(EM) interaction yields such a state with an excitation energy of comparable magnitude to the one observed in ^{132}Sn , thus indicating the doubly magic nature of this nucleus. If we conservatively interpret the discrepancies in the energies in terms of uncertainties inherent in the Hamiltonians, these outweigh the uncertainties resulting from the IM-SRG and the importance-threshold extrapolation, and underline the need for a more systematic approach to nuclear interactions. We have also studied the level orderings and energy splittings of the ground and first excited states in the odd-mass tin isotopes considered. We reproduce well the experimentally found near-degeneracy of these states; however, the large uncertainties of the initial Hamiltonians and the uncertainties from the IM-SRG and importance-threshold extrapolation prevent us from making definite spin assignments.

Since other observables are sensitive to other aspects of the nuclear interaction, it would also be interesting to study, e.g, electromagnetic moments and transitions in the framework of the IT-VSSM using consistently evolved operators from the IM-SRG. First steps along these lines have already been done, but indicate the necessity to extend the IM-SRG beyond the truncation of normal-ordered two-body operators [Par+17].

Within the second project, we have formulated an *ab initio* approach for the description of transition strength distributions by combining the IT-NCSM with the Lanczos strength-function method. We have found that the loss of orthogonality in the Lanczos basis—resulting in duplicates in the energy spectrum—does not affect the strength distributions. This allows us to use the simplest possible version of the Lanczos algorithm, rendering the method extremely efficient regarding both, computing time and memory requirements. We have analyzed the sensitivity of the strength distributions on the different model-space parameters and truncations, as well as on the choice of single-particle basis. We have considered the HF, HO, and the newly established natural-orbital basis. Among these, the HF basis performs best for the simultaneous description of all electric multipole transitions considered regarding model-space convergence and frequency dependence. Particularly for the description of the dipole response, the natural-orbital basis has great potential

for forthcoming investigations, as this basis yields frequency-independent results and, additionally, exhibits the best convergence of absolute energies separately for the natural- and unnatural-parity bases. Our approach provides access to the low-energy strength and the giant-resonance region including fragmentation and fine structure. Only the explicit coupling to the continuum, e.g., to describe the escape width above the relevant particle threshold, is not included. In this respect, our method is complementary to the LIT approaches, which formally include continuum physics but cannot address the (sub-)threshold region as well as fragmentation and fine structure.

As a first application, we have compared strength functions from the widely used approximate RPA and SRPA to our *ab initio* results and have focused on the systematics in the model-space convergence. We could demonstrate that a consistent use of model spaces for the calculation of ground and excited states, allowing for the same correlation content, is essential to bring in line the SRPA strength functions with our IT-NCSM strength functions in an analog model space. Furthermore, we have shown that the inclusion of particle-hole excitations up to the four-body level are crucial to capture all the fragmentation necessary for the description of the spreading width, particularly for quadrupole responses.

Then, we have investigated the systematics of electric monopole, dipole, and quadrupole strength functions throughout the oxygen, carbon, and helium isotopic chains using different chiral interactions, with a focus on the emergence and evolution of pygmy and giant resonances. In general, our strength distributions reproduce the expected trends observed in experiments, with a broadening of the resonances when moving away from closed shells; however, the strength is located at too high energies. Particularly surprising is the fact that the N^2LO_{sat} interaction, which is known to predict a nuclear matter incompressibility within the empirical range, produces a monopole resonance at even higher energies than the EMN400 interaction, which is known to predict too small nuclear radii. These findings indicate that other aspects of the nuclear interaction, e.g., momentum dependence and non-locality, play an important role for the description of these dynamic observables and highlight the significance of collective modes for constraining nuclear interactions. Also, we find prominent strength in the isoscalar quadrupole response at low energies, which, in case of the neutron-rich oxygen isotopes, can be interpreted as a pygmy quadrupole resonance. Furthermore, we have provided the dipole polarizabilities for all isotopes and interactions considered. They increase when more and more neutrons are added to an isotope, as expected. Additionally, we can use the eigenstates from IT-NCSM calculations to investigate the nature of the dominant contributions in the strength distributions by means of their transition densities. These provide an illustrative picture on the nuclear dynamics. Our results indicate that pygmy dipole resonances are typically mixtures of both, isoscalar and isovector transitions, while the transitions in the giant-resonance regions are mainly isovector for dipole and mainly isoscalar for quadrupole modes. It would be particularly interesting to investigate the low-lying strength found in the isoscalar E2 distributions of neutron-rich oxygen isotopes, for which we have predicted a pygmy quadrupole resonance, and shed light on their characteristics.

In the future, we aim at an application of the framework also to electroweak transitions, e.g., to the study of Gamow-Teller responses. Furthermore, an interesting path of development could be the use of IM-SRG-evolved Hamiltonians and operators for the calculation

9. Conclusions

of strength distributions. Since these Hamiltonians provide a ground state decoupled from all excitations, the remaining dependence of the strength functions is solely connected to the convergence of the excited states.

A. Derivation of Electromagnetic Quantities

A.1. Relevant Definitions and Notations

In this section, we introduce the quantities and angular-momentum coupling symbols relevant for the derivations in the following sections. We restrict ourselves to the definitions and refer to standard text books for more details and specific properties of the quantities, see, e.g., [Suh07]. We note that several notations may exist in the literature.

Clebsch-Gordan Coefficients and $3j$ Symbols

We consider a system of two angular momenta and its projections, (\vec{j}_1, m_1) and (\vec{j}_2, m_2) . Such a system can be realized by the angular momenta of two different subsystems or two different angular momenta of a single system. A state of such a system in the uncoupled basis is given by $|j_1 m_1, j_2 m_2\rangle$. For many applications, it is convenient to couple the two angular momenta to a total angular momentum (\vec{J}, M) :

$$\begin{aligned} |j_1 j_2 JM\rangle &= \sum_{m_1 m_2} |j_1 m_1, j_2 m_2\rangle \langle j_1 m_1, j_2 m_2 | j_1 j_2 JM\rangle \\ &\equiv \sum_{m_1 m_2} \begin{pmatrix} j_1 & j_2 & J \\ m_1 & m_2 & M \end{pmatrix} |j_1 m_1, j_2 m_2\rangle. \end{aligned} \quad (\text{A.1})$$

The overlap between an uncoupled and a coupled state—denoted by the brackets—represents a so-called Clebsch-Gordan coefficient. Analogously, it is possible to express an uncoupled state in the coupled basis:

$$|j_1 m_1, j_2 m_2\rangle = \sum_{JM} \begin{pmatrix} j_1 & j_2 & J \\ m_1 & m_2 & M \end{pmatrix} |j_1 j_2 JM\rangle. \quad (\text{A.2})$$

We refer to quantum-mechanics text books for the useful properties and symmetry relations of Clebsch-Gordan coefficients.

It is often convenient to resort to $3j$ symbols, which can be obtained from the Clebsch-Gordan coefficients by the following definition:

$$\begin{pmatrix} j_1 & j_2 & j_3 \\ m_1 & m_2 & m_3 \end{pmatrix} \equiv (-1)^{j_1 - j_2 - m_3} \hat{j}_3^{-1} \begin{pmatrix} j_1 & j_2 & j_3 \\ m_1 & m_2 & -m_3 \end{pmatrix}. \quad (\text{A.3})$$

Here, we have introduced the notation

$$\hat{j} \equiv \sqrt{2j+1}. \quad (\text{A.4})$$

We note that the symmetry relations for $3j$ symbols have more symmetric phase factors than the corresponding ones of the Clebsch-Gordan coefficients, see the literature for more details.

6j and 9j Symbols

The angular-momentum coupling machinery can be extended to three or four angular momenta. We note that there are different ways to couple three or four angular momenta, which depend on the order of coupling. The related coupling coefficients are called Wigner nj symbols. If one wants to expand, e.g., a state $|j_1, j_2 j_3(j_{23}); JM\rangle$, where the angular momenta j_2 and j_3 are coupled to j_{23} before coupling j_1 with j_{23} to a total angular momentum J , in the basis $\{|j_1 j_2(j_{12}), j_3; JM\rangle\}$, where j_1 and j_2 are first coupled to j_{12} before coupling the latter with j_3 , this can be accomplished using the following relation:

$$\begin{aligned} |j_1, j_2 j_3(j_{23}); JM\rangle &= \sum_{j_{12}} |j_1 j_2(j_{12}), j_3; JM\rangle \langle j_1 j_2(j_{12}), j_3; JM | j_1, j_2 j_3(j_{23}); JM\rangle \\ &\equiv \sum_{j_{12}} (-1)^{j_1+j_2+j_3+J} \hat{j}_{12} \hat{j}_{23} \begin{Bmatrix} j_1 & j_2 & j_{12} \\ j_3 & J & j_{23} \end{Bmatrix} |j_1 j_2(j_{12}), j_3; JM\rangle. \end{aligned} \quad (\text{A.5})$$

The array with braces is called 6j symbol. There is an explicit expression for the 6j symbol in terms of 3j symbols, which can be particularly useful to summarize sums over products of 3j symbols [VMK88, p. 296 (13)].

Analogously, a 9j symbol can be introduced for the coupling of four angular momentum vectors to a given total angular momentum. The state $|j_1 j_3(j_{13}) j_2 j_4(j_{24}); JM\rangle$ can be expressed in the basis $\{|j_1 j_2(j_{12}) j_3 j_4(j_{34}); JM\rangle\}$ using the relation

$$\begin{aligned} |j_1 j_3(j_{13}) j_2 j_4(j_{24}); JM\rangle &= \sum_{j_{12} j_{34}} |j_1 j_2(j_{12}) j_3 j_4(j_{34}); JM\rangle \times \\ &\quad \langle j_1 j_2(j_{12}) j_3 j_4(j_{34}); JM | j_1 j_3(j_{13}) j_2 j_4(j_{24}); JM\rangle \\ &\equiv \sum_{j_{12} j_{34}} \hat{j}_{12} \hat{j}_{34} \hat{j}_{13} \hat{j}_{24} \begin{Bmatrix} j_1 & j_2 & j_{12} \\ j_3 & j_4 & j_{34} \\ j_{13} & j_{24} & J \end{Bmatrix} |j_1 j_2(j_{12}) j_3 j_4(j_{34}); JM\rangle, \end{aligned} \quad (\text{A.6})$$

where the array with braces denotes the 9j symbol. A 9j symbol can be written in terms of 6j symbols [VMK88, p. 340 (20)], and several special cases exist, where it reduces to simple expressions involving 3j symbols [VMK88, p. 339 (17)].

Spherical Tensor Operators

A spherical tensor operator \mathbf{T}_{JM} with rank J and projection M is defined via its transformation behavior under rotations. In particular, it is required to fulfill the following commutation relations with the z -projection J_z and the ladder operators J_{\pm} of the angular momentum operator \mathbf{J} :

$$[\mathbf{J}_z, \mathbf{T}_{JM}] = M\hbar \mathbf{T}_{JM}, \quad (\text{A.7})$$

$$[\mathbf{J}_{\pm}, \mathbf{T}_{JM}] = \hbar \sqrt{(J \pm M + 1)(J \mp M)} \mathbf{T}_{J, M \pm 1}. \quad (\text{A.8})$$

We note that the angular momentum operator \mathbf{J} itself is a tensor operator of rank 1, and its z -projection J_z and the ladder operators J_{\pm} define its components in the spherical basis.

Wigner-Eckart Theorem

The Wigner-Eckart theorem simplifies the calculation of matrix elements for spherical tensor operators. It allows for the definition of a reduced matrix element that is independent of all projection quantum numbers. All dependencies on the latter are absorbed into a factor:

$$\langle \zeta' j' m' | \mathbf{T}_{JM} | \zeta j m \rangle = (-1)^{j'-m'} \begin{pmatrix} j' & J & j \\ -m' & M & m \end{pmatrix} \langle \zeta' j' || \mathbf{T}_J || \zeta j \rangle \quad (\text{A.9})$$

$$= (-1)^{2J} j^{\hat{J}-1} \begin{pmatrix} j & J & j' \\ m & M & m' \end{pmatrix} \langle \zeta' j' || \mathbf{T}_J || \zeta j \rangle. \quad (\text{A.10})$$

The relevant quantum numbers of a given state are (j, m) , and all other quantum numbers are contained in ζ . In the literature, there are several conventions of the Wigner-Eckart theorem. We use Edmond's convention [Edm64; VMK88].

A.2. Vector Potential and Hamiltonian of the Electromagnetic Field

To derive the vector potential and Hamiltonian of the electromagnetic field, we start from the homogeneous Maxwell equations for a matter- and source-free region:

$$\vec{\nabla} \cdot \vec{\mathbf{E}}(\vec{r}, t) = 0, \quad (\text{A.11a})$$

$$\vec{\nabla} \times \vec{\mathbf{B}}(\vec{r}, t) = \frac{1}{c} \dot{\vec{\mathbf{E}}}(\vec{r}, t), \quad (\text{A.11b})$$

$$\vec{\nabla} \times \vec{\mathbf{E}}(\vec{r}, t) = -\frac{1}{c} \dot{\vec{\mathbf{B}}}(\vec{r}, t), \quad (\text{A.11c})$$

$$\vec{\nabla} \cdot \vec{\mathbf{B}}(\vec{r}, t) = 0. \quad (\text{A.11d})$$

The general procedure to determine the electric and magnetic fields $\vec{\mathbf{E}}(\vec{r}, t)$ and $\vec{\mathbf{B}}(\vec{r}, t)$ is to introduce a scalar potential $\Phi(\vec{r}, t)$ and a vector potential $\vec{\mathbf{A}}(\vec{r}, t)$ that automatically embody the limitations that the Maxwell equations pose on the six field components. The vector potential $\vec{\mathbf{A}}(\vec{r}, t)$ can be defined via

$$\vec{\mathbf{B}}(\vec{r}, t) = \vec{\nabla} \times \vec{\mathbf{A}}(\vec{r}, t) \quad (\text{A.12})$$

and, therefore, the fourth Maxwell equation, (A.11d), is always satisfied. By inserting this relation into (A.11c), the third Maxwell equation reads

$$\vec{\nabla} \times \left(\vec{\mathbf{E}}(\vec{r}, t) + \frac{1}{c} \dot{\vec{\mathbf{A}}}(\vec{r}, t) \right) = 0. \quad (\text{A.13})$$

It is satisfied if the expression in brackets is written as the gradient of a scalar field. We, thus, introduce a scalar potential so that

$$\vec{\mathbf{E}}(\vec{r}, t) = -\vec{\nabla} \Phi(\vec{r}, t) - \frac{1}{c} \dot{\vec{\mathbf{A}}}(\vec{r}, t). \quad (\text{A.14})$$

Substituting expressions (A.12) and (A.14) into (A.11a) and (A.11b) yields the field equations

$$\left(\Delta - \frac{1}{c^2} \frac{\partial^2}{\partial t^2}\right) \Phi(\vec{r}, t) + \frac{1}{c} \frac{\partial}{\partial t} \left(\vec{\nabla} \cdot \vec{\mathbf{A}}(\vec{r}, t) + \frac{1}{c} \frac{\partial}{\partial t} \Phi(\vec{r}, t) \right) = 0, \quad (\text{A.15})$$

$$\left(\Delta - \frac{1}{c^2} \frac{\partial^2}{\partial t^2}\right) \vec{\mathbf{A}}(\vec{r}, t) - \vec{\nabla} \left(\vec{\nabla} \cdot \vec{\mathbf{A}}(\vec{r}, t) + \frac{1}{c} \frac{\partial}{\partial t} \Phi(\vec{r}, t) \right) = 0, \quad (\text{A.16})$$

which are equivalent to the Maxwell equations. The potentials $\Phi(\vec{r}, t)$ and $\vec{\mathbf{A}}(\vec{r}, t)$ behave like the components of a four-vector under Lorentz transformations, where $\Phi(\vec{r}, t)$ corresponds to the time-like component. The field equations (A.15) and (A.16) are invariant under gauge transformations of the form

$$\Phi'(\vec{r}, t) = \Phi(\vec{r}, t) + \frac{1}{c} \frac{\partial}{\partial t} f(\vec{r}, t), \quad (\text{A.17})$$

$$\vec{\mathbf{A}}'(\vec{r}, t) = \vec{\mathbf{A}}(\vec{r}, t) - \vec{\nabla} f(\vec{r}, t). \quad (\text{A.18})$$

One possible choice for the scalar potential $\Phi(\vec{r}, t)$ and the vector potential $\vec{\mathbf{A}}(\vec{r}, t)$ that describe the same given physical situation can be obtained when working in transverse gauge by imposing the conditions

$$\Phi(\vec{r}, t) = 0 \quad \text{and} \quad \vec{\nabla} \cdot \vec{\mathbf{A}}(\vec{r}, t) = 0. \quad (\text{A.19})$$

With this, (A.15) and (A.16) reduce to

$$\Delta \vec{\mathbf{A}}(\vec{r}, t) - \frac{1}{c^2} \frac{\partial^2}{\partial t^2} \vec{\mathbf{A}}(\vec{r}, t) = 0, \quad (\text{A.20})$$

and we obtain for the field Hamiltonian

$$\begin{aligned} \mathbf{H}_{\text{field}} &= \frac{1}{8\pi} \int d^3r \left(\vec{\mathbf{E}}^2(\vec{r}, t) + \vec{\mathbf{B}}^2(\vec{r}, t) \right) \\ &= \frac{1}{8\pi} \int d^3r \left[\left(-\vec{\nabla} \Phi(\vec{r}, t) - \frac{1}{c} \frac{\partial}{\partial t} \vec{\mathbf{A}}(\vec{r}, t) \right)^2 + \left(\vec{\nabla} \times \vec{\mathbf{A}}(\vec{r}, t) \right)^2 \right] \\ &= \frac{1}{8\pi} \int d^3r \left(\frac{1}{c^2} \left(\dot{\vec{\mathbf{A}}}(\vec{r}, t) \right)^2 + \left(\vec{\nabla} \times \vec{\mathbf{A}}(\vec{r}, t) \right)^2 \right). \end{aligned} \quad (\text{A.21})$$

The most general vector potential that fulfills both, field equation (A.20) and the transversality conditions (A.19), is given by

$$\vec{\mathbf{A}}(\vec{r}, t) = \sum_{\alpha} \int d^3k \frac{1}{(2\pi)^{\frac{3}{2}}} \mathbf{N}_{\vec{k}\alpha} \vec{\epsilon}_{\vec{k}\alpha} e^{i(\vec{k}\vec{r} - \omega_k t)}, \quad (\text{A.22})$$

where the sum is over the two independent polarizations. The transversality condition is satisfied when the normalized polarization vectors $\vec{\epsilon}_{\vec{k}\alpha}$ are chosen such that $\vec{\epsilon}_{\vec{k}\alpha} \cdot \vec{k} = 0$. By absorbing the time dependence into a factor via

$$\vec{\mathbf{A}}(\vec{r}, t) = \vec{\mathbf{A}}(\vec{r}) e^{-i\omega_k t}, \quad (\text{A.23})$$

(A.20) can be transformed into the Helmholtz equation

$$(\Delta + k^2)\vec{A}(\vec{r}, t) = 0. \quad (\text{A.24})$$

Since the nuclear Hamiltonian is spherically symmetric, the solutions $\vec{A}(\vec{r}, t)$ are eigenfunctions of the orbital angular-momentum operators \vec{L}^2 and L_3 . This is the case for solutions of the form $j_l(kr)Y_{lm_l}(\Omega)$, where the spherical Bessel functions ensure regularity at the origin. Besides, the photon has spin $s = 1$, and, therefore, the solutions must also be eigenfunctions of the spin operators \vec{S}^2 and S_3 given by \vec{e}_{m_s} . The total angular momentum of the photon is $\vec{\lambda} = \vec{l} + \vec{s}$. The corresponding eigenfunctions of $\vec{L}^2, \vec{S}^2, \vec{\Lambda}^2$ and Λ_3 are the vector spherical harmonics

$$\vec{Y}_{\lambda l \mu} = \sum_{m_s m_l} \begin{pmatrix} l & 1 & \lambda \\ m_l & m_s & \mu \end{pmatrix} Y_{lm_l}(\Omega) \vec{e}_{m_s}. \quad (\text{A.25})$$

For fixed λ , the orbital angular momentum l can be $\lambda - 1, \lambda, \lambda + 1$, which yields, in principle, three independent solutions of (A.24). However, only two independent solutions are found for each combination of λ and μ that satisfy the transversality condition. They can be characterized as electric ($\sigma = E$) and magnetic ($\sigma = M$) radiation:

$$\begin{aligned} \vec{A}_{Mk\lambda\mu}(\vec{r}) &= \mathcal{N} j_\lambda(kr) \vec{Y}_{\lambda\lambda\mu}(\Omega) \\ &= \frac{\mathcal{N}}{\sqrt{\lambda(\lambda+1)}} \frac{1}{i} (\vec{r} \times \vec{\nabla}) (j_\lambda(kr) Y_{\lambda\mu}(\Omega)), \end{aligned} \quad (\text{A.26})$$

$$\begin{aligned} \vec{A}_{Ek\lambda\mu}(\vec{r}) &= \frac{i}{k} (\vec{\nabla} \times \vec{A}_{Mk\lambda\mu}(\vec{r})) \\ &= \frac{-\mathcal{N}}{\sqrt{\lambda(\lambda+1)}} \frac{1}{k} \left[\vec{\nabla} \left(Y_{\lambda\mu}(\Omega) \frac{\partial}{\partial r} (r j_\lambda(kr)) \right) + k^2 \vec{r} j_\lambda(kr) Y_{\lambda\mu}(\Omega) \right]. \end{aligned} \quad (\text{A.27})$$

A detailed derivation of these is given in [EG76, chapter 3.2 and 3.3].

The quantum number k is quantized by imposing the proper boundary conditions at a perfectly conducting sphere with radius R , which is assumed to be much larger than the nuclear radius. The electric field component parallel to the surface of the sphere is required to vanish; the same holds for the magnetic field component perpendicular to the surface of the sphere. This is fulfilled only for a discrete set of k -values, which are determined in the magnetic case by

$$j_\lambda(k_n R) = 0 \quad (\text{A.28})$$

and in the electric case by

$$\frac{\partial}{\partial r} (r j_\lambda(k_n r)) \Big|_{r=R} = 0. \quad (\text{A.29})$$

We use the normalization constant

$$\mathcal{N} = \sqrt{\frac{4\pi\hbar\omega_k}{R}} \quad (\text{A.30})$$

in the limit of large R and for both radiation types σ , so that the orthogonality relation

$$\int_0^R dr r^2 \int_{4\pi} d\Omega \vec{A}_{\sigma'k'\lambda'\mu'}^*(\vec{r}) \cdot \vec{A}_{\sigma k\lambda\mu}(\vec{r}) = \frac{2\pi\hbar c}{k} \delta_{\sigma\sigma'} \delta_{kk'} \delta_{\lambda\lambda'} \delta_{\mu\mu'} \quad (\text{A.31})$$

holds. Thus, we obtain as most general solution for the vector potential

$$\vec{A}(\vec{r}, t) = \sum_{\sigma k\lambda\mu} (\alpha_{\sigma k\lambda\mu}^* \vec{A}_{\sigma k\lambda\mu}(\vec{r}) e^{-i\omega_k t} + c.c.), \quad (\text{A.32})$$

where the coefficients $\alpha_{\sigma k\lambda\mu}$ are independent variables that describe the electromagnetic field.

In our notation, we have indicated all fields, potentials, and the coefficients $\alpha_{\sigma k\lambda\mu}$ as operators. This will be legitimized in the following. Inserting (A.32) into (A.21) yields

$$\mathbf{H}_{\text{field}} = \sum_{\sigma k\lambda\mu} \frac{1}{2} \hbar \omega_k (\alpha_{\sigma k\lambda\mu}^* \alpha_{\sigma k\lambda\mu} + c.c.). \quad (\text{A.33})$$

Since $\mathbf{H}_{\text{field}}$ has the form of a HO Hamiltonian, the variables $\alpha_{\sigma k\lambda\mu}$ are replaced by the creation and annihilation operators for photons of type σ with energy $\hbar\omega_k$. Employing the boson commutation relations for the creation and annihilation operators, we can rewrite the field Hamiltonian as

$$\mathbf{H}_{\text{field}} = \sum_{\sigma k\lambda\mu} \hbar \omega_k \left(\mathbf{a}_{\sigma k\lambda\mu}^\dagger \mathbf{a}_{\sigma k\lambda\mu} + \frac{1}{2} \right). \quad (\text{A.34})$$

Analogously, we obtain for the vector potential

$$\vec{A} = \sum_{\sigma k\lambda\mu} (\vec{A}_{\sigma k\lambda\mu}(\vec{r}) e^{-i\omega_k t} \mathbf{a}_{\sigma k\lambda\mu}^\dagger + \vec{A}_{\sigma k\lambda\mu}^*(\vec{r}) e^{i\omega_k t} \mathbf{a}_{\sigma k\lambda\mu}). \quad (\text{A.35})$$

We remark that the electric and magnetic fields $\vec{E}(\vec{r}, t)$ and $\vec{B}(\vec{r}, t)$ can be determined by substituting (A.35) into (A.12) and (A.14).

A.3. Static Multipole Operators

The static electric multipole operator (3.22) can be derived by inserting the density (3.9) into (3.20):

$$\begin{aligned} \mathcal{Q}_{\lambda\mu} &= \int d^3r \rho(\vec{r}) r^\lambda Y_{\lambda\mu}(\Omega) \\ &= \sum_{i=1}^A \int d^3r e \left(\frac{1}{2} + \mathbf{t}_3^{(i)} \right) \delta(\vec{r} - \vec{r}_i(t)) r^\lambda Y_{\lambda\mu}(\Omega) \\ &= e \sum_{i=1}^A \left(\frac{1}{2} + \mathbf{t}_3^{(i)} \right) \mathbf{r}_i^\lambda Y_{\lambda\mu}(\Omega_i). \end{aligned} \quad (\text{A.36})$$

For the derivation of the static magnetic multipole operator (3.23), we use relation [RS80, (B.20)],

$$\vec{\nabla}(r^\lambda Y_{\lambda\mu}(\Omega)) = \frac{1}{\lambda+1} \vec{\nabla} \times (\vec{\nabla} \times \vec{r}) r^\lambda Y_{\lambda\mu}(\Omega), \quad (\text{A.37})$$

to develop an alternative expression for (3.21):

$$\begin{aligned} \mathbf{M}_{\lambda\mu} &= \int d^3r \vec{\boldsymbol{\mu}}(\vec{r}) \cdot \vec{\nabla}(r^\lambda Y_{\lambda\mu}(\Omega)) \\ &= \frac{1}{\lambda+1} \int d^3r \vec{\boldsymbol{\mu}}(\vec{r}) \cdot \vec{\nabla} \times (\vec{\nabla} \times \vec{r}) r^\lambda Y_{\lambda\mu}(\Omega) \\ &= \frac{1}{\lambda+1} \int d^3r \boldsymbol{\mu}_i(\vec{r}) \vec{e}_i \cdot \epsilon_{lmn} \epsilon_{jkm} \partial_l \partial_j r_k \vec{e}_n r^\lambda Y_{\lambda\mu}(\Omega) \\ &= \frac{1}{\lambda+1} \int d^3r \boldsymbol{\mu}_i(\vec{r}) \epsilon_{lmi} \epsilon_{jkm} \partial_l \partial_j r_k r^\lambda Y_{\lambda\mu}(\Omega). \end{aligned} \quad (\text{A.38})$$

We carry out the second derivative and then perform an integration by parts. Since the nuclear spin density is located in the nucleus, the surface term vanishes:

$$\begin{aligned} \mathbf{M}_{\lambda\mu} &= \frac{1}{\lambda+1} \int d^3r \boldsymbol{\mu}_i(\vec{r}) \epsilon_{lmi} \epsilon_{jkm} \partial_l (\delta_{jk} r^\lambda Y_{\lambda\mu}(\Omega) + r_k \partial_j r^\lambda Y_{\lambda\mu}(\Omega)) \\ &= \frac{1}{\lambda+1} \int d^3r \boldsymbol{\mu}_i(\vec{r}) \epsilon_{lmi} \epsilon_{jkm} \partial_l r_k \partial_j r^\lambda Y_{\lambda\mu}(\Omega) \\ &= -\frac{1}{\lambda+1} \int d^3r \partial_l (\boldsymbol{\mu}_i(\vec{r})) \epsilon_{lmi} \epsilon_{jkm} r_k \partial_j r^\lambda Y_{\lambda\mu}(\Omega) \\ &= \frac{1}{\lambda+1} \int d^3r r_k \epsilon_{kmj} \epsilon_{lim} \partial_l (\boldsymbol{\mu}_i(\vec{r})) \partial_j r^\lambda Y_{\lambda\mu}(\Omega) \\ &= \frac{1}{\lambda+1} \int d^3r r_k \epsilon_{kmj} (\vec{\nabla} \times \vec{\boldsymbol{\mu}}(\vec{r}))_m \partial_j r^\lambda Y_{\lambda\mu}(\Omega) \\ &= \frac{1}{\lambda+1} \int d^3r (\vec{r} \times (\vec{\nabla} \times \vec{\boldsymbol{\mu}}(\vec{r})))_j \partial_j r^\lambda Y_{\lambda\mu}(\Omega) \\ &= \frac{1}{\lambda+1} \int d^3r [\vec{r} \times (\vec{\nabla} \times \vec{\boldsymbol{\mu}}(\vec{r}))] \cdot \vec{\nabla}(r^\lambda Y_{\lambda\mu}(\Omega)) \\ &= \frac{1}{c(\lambda+1)} \int d^3r (\vec{r} \times \vec{\mathbf{j}}(\vec{r})) \cdot \vec{\nabla}(r^\lambda Y_{\lambda\mu}(\Omega)). \end{aligned} \quad (\text{A.39})$$

We split the magnetic multipole operator into spin and orbit part, and use the most suitable start expression for each:

$$\begin{aligned} \mathbf{M}_{\lambda\mu} &= \frac{1}{c(\lambda+1)} \int d^3r (\vec{r} \times \vec{\mathbf{j}}(\vec{r})) \cdot \vec{\nabla}(r^\lambda Y_{\lambda\mu}(\Omega)) \\ &= \frac{1}{c(\lambda+1)} \int d^3r (\vec{r} \times \vec{\mathbf{j}}^o(\vec{r})) \cdot \vec{\nabla}(r^\lambda Y_{\lambda\mu}(\Omega)) \\ &\quad + \frac{1}{c(\lambda+1)} \int d^3r (\vec{r} \times \vec{\mathbf{j}}^s(\vec{r})) \cdot \vec{\nabla}(r^\lambda Y_{\lambda\mu}(\Omega)) \end{aligned}$$

$$\begin{aligned}
&= \frac{1}{c(\lambda+1)} \int d^3r (\vec{r} \times \vec{j}^o(\vec{r})) \cdot \vec{\nabla}(r^\lambda Y_{\lambda\mu}(\Omega)) \\
&\quad + \int d^3r \vec{\mu}^s(\vec{r}) \cdot \vec{\nabla}(r^\lambda Y_{\lambda\mu}(\Omega)).
\end{aligned} \tag{A.40}$$

We insert the orbit current density (3.10) into the first term and use an approximation for velocity-independent potentials, where $\vec{v}_i = \vec{p}_i/m$. In this way, we obtain

$$\begin{aligned}
&\frac{1}{c(\lambda+1)} \int d^3r (\vec{r} \times \vec{j}^o(\vec{r})) \cdot \vec{\nabla}(r^\lambda Y_{\lambda\mu}(\Omega)) \\
&= \frac{1}{c(\lambda+1)} e \sum_{i=1}^A \int d^3r \left[\vec{r} \times \left(\frac{1}{2} + \mathbf{t}_3^{(i)} \right) \frac{\vec{p}_i}{m} \delta(\vec{r} - \vec{r}_i) \right] \cdot \vec{\nabla}(r^\lambda Y_{\lambda\mu}(\Omega)) \\
&= \frac{2\mu_N}{\lambda+1} \sum_{i=1}^A g_l^{(i)} \vec{l}_i \cdot \vec{\nabla}_i(r^\lambda Y_{\lambda\mu}(\Omega_i))
\end{aligned} \tag{A.41}$$

with the orbit g factors $g_l^{(i)} = 1$ for protons and $g_l^{(i)} = 0$ for neutrons.

The second term yields

$$\begin{aligned}
&\int d^3r \vec{\mu}^s(\vec{r}) \cdot \vec{\nabla}(r^\lambda Y_{\lambda\mu}(\Omega)) \\
&= \mu_N \sum_{i=1}^A \int d^3r \delta(\vec{r} - \vec{r}_i(t)) \left[\left(\frac{1}{2} + \mathbf{t}_3^{(i)} \right) g_p + \left(\frac{1}{2} - \mathbf{t}_3^{(i)} \right) g_n \right] \vec{s}_i \cdot \vec{\nabla}(r^\lambda Y_{\lambda\mu}(\Omega)) \\
&= \mu_N \sum_{i=1}^A g_s^{(i)} \vec{s}_i \cdot \vec{\nabla}_i(r^\lambda Y_{\lambda\mu}(\Omega_i))
\end{aligned} \tag{A.42}$$

with the current spin density (3.12). Here, we have introduced the definitions $g_s^{(i)} = g_p$ for protons and $g_s^{(i)} = g_n$ for neutrons.

The sum of (A.41) and (A.42) yields expression (3.23) for the static magnetic multipole operator

$$\mathbf{M}_{\lambda\mu} = \mu_N \sum_{i=1}^A \left[g_s^{(i)} \vec{s}_i + \frac{2}{\lambda+1} g_l^{(i)} \vec{l}_i \right] \cdot (\vec{\nabla}_i r^\lambda Y_{\lambda\mu}(\Omega_i)). \tag{A.43}$$

A.4. Electromagnetic Multipole Transition Operators

In order to derive the electromagnetic multipole transition operators, we start from Fermi's golden rule (3.30) and use an expression for the density of final states from the continuity conditions of an electromagnetic field at the surface of a perfectly conducting sphere. In the limit of large R , this yields

$$g(E_f) = \frac{1}{\hbar c} \frac{R}{\pi}. \tag{A.44}$$

We first derive expression (3.31) for the electric multipole transition operator (3.32). We insert the electric component of \mathbf{H}_{int} in transverse gauge (3.13) and exploit that we are considering one-photon absorption processes:

$$\begin{aligned}
 T_{fi}(E, k\lambda\mu) &= \frac{2\pi}{\hbar} |\langle f | \mathbf{H}_{\text{int}} | i \rangle|^2 g(E_f) \\
 &= \frac{2\pi}{\hbar} \frac{1}{\hbar c} \frac{R}{\pi} \left| \langle \Psi_f | -\frac{1}{c} \int d^3r \vec{\mathbf{j}}(\vec{r}, t) \cdot \vec{A}_{Ek\lambda\mu}(\vec{r}) e^{i\omega_k t} | \Psi_i \rangle \right|^2 \\
 &= \frac{2\pi}{\hbar} \frac{1}{\hbar c} \frac{R}{\pi} \frac{4\pi\hbar ck}{R} \left| \langle \Psi_f | \frac{1}{c} \frac{i}{k} \int d^3r \vec{\mathbf{j}}(\vec{r}, t) \cdot \vec{\nabla} \times j_\lambda(kr) \vec{Y}_{\lambda\lambda\mu}(\Omega) | \Psi_i \rangle \right|^2 \\
 &= \frac{8\pi k}{\hbar} \left| \langle \Psi_f | \frac{1}{ck} \int d^3r \vec{\mathbf{j}}(\vec{r}, t) \cdot \vec{\nabla} \times j_\lambda(kr) \vec{Y}_{\lambda\lambda\mu}(\Omega) | \Psi_i \rangle \right|^2. \tag{A.45}
 \end{aligned}$$

We use relation [Edm64, (5.9.14)] to rewrite the vector spherical harmonics and exploit that the spherical Bessel function commutes with $\vec{r} \times \vec{\nabla}$:

$$\begin{aligned}
 T_{fi}(E, k\lambda\mu) &= \frac{8\pi k}{\hbar} \left| \langle \Psi_f | \frac{1}{ck} \int d^3r \vec{\mathbf{j}}(\vec{r}, t) \cdot \vec{\nabla} \times j_\lambda(kr) \frac{1}{i\sqrt{\lambda(\lambda+1)}} (\vec{r} \times \vec{\nabla}) Y_{\lambda\mu}(\Omega) | \Psi_i \rangle \right|^2 \\
 &= \frac{8\pi k}{\hbar} \frac{1}{(ck)^2} \frac{1}{\lambda(\lambda+1)} \\
 &\quad \times \left| \langle \Psi_f | i \int d^3r \vec{\mathbf{j}}(\vec{r}, t) \cdot \vec{\nabla} \times (\vec{\nabla} \times \vec{r}) (j_\lambda(kr) Y_{\lambda\mu}(\Omega)) | \Psi_i \rangle \right|^2. \tag{A.46}
 \end{aligned}$$

The expression within the absolute value bars, including some additional factors, can be defined as the electric multipole transition operator $\mathbf{O}(E, k\lambda\mu)$. We further substitute $E_k = \hbar kc$ and obtain

$$T_{fi}(E, k\lambda\mu) = \frac{8\pi}{\hbar} \frac{\lambda+1}{\lambda[(2\lambda+1)!!]^2} \left(\frac{E_k}{\hbar c} \right)^{2\lambda+1} \left| \langle \Psi_f | \mathbf{O}(E, k\lambda\mu) | \Psi_i \rangle \right|^2 \tag{A.47}$$

with

$$\mathbf{O}(E, k\lambda\mu) = \frac{i(2\lambda+1)!!}{ck^{\lambda+1}(\lambda+1)} \int d^3r \vec{\mathbf{j}}(\vec{r}, t) \cdot \vec{\nabla} \times (\vec{\nabla} \times \vec{r}) (j_\lambda(kr) Y_{\lambda\mu}(\Omega)). \tag{A.48}$$

Equation (A.47) corresponds to (3.31) in the electric case, which we wanted to derive.

The electric multipole transition operator (A.48) can be written in a more convenient way. To this aim, we partly rewrite the integrand:

$$\begin{aligned}
 \vec{\nabla} \times (\vec{\nabla} \times \vec{r}) (j_\lambda(kr) Y_{\lambda\mu}(\Omega)) &= \vec{\nabla} (\vec{\nabla} \cdot r \vec{e}_r j_\lambda(kr) Y_{\lambda\mu}(\Omega)) - \vec{r} \Delta (j_\lambda(kr) Y_{\lambda\mu}(\Omega)) \\
 &= \vec{\nabla} (Y_{\lambda\mu}(\Omega) \frac{\partial}{\partial r} (r j_\lambda(kr))) + k^2 \vec{r} j_\lambda(kr) Y_{\lambda\mu}(\Omega). \tag{A.49}
 \end{aligned}$$

Here, we have exploited that the divergence in the first term contributes only in \vec{e}_r direction, and we have applied the Helmholtz equation to the second term. We substitute (A.49) into (A.48) and obtain (3.32),

$$\begin{aligned}
 \mathbf{O}(E, k\lambda\mu) &= \frac{(2\lambda+1)!!}{k^\lambda(\lambda+1)} \int d^3r \left(\boldsymbol{\rho}(\vec{r}, t) Y_{\lambda\mu}(\Omega) \frac{\partial}{\partial r} r j_\lambda(kr) \right. \\
 &\quad \left. + i \frac{k}{c} \vec{\mathbf{j}}(\vec{r}, t) \cdot \vec{r} Y_{\lambda\mu}(\Omega) j_\lambda(kr) \right), \tag{A.50}
 \end{aligned}$$

after integrating the first term by parts and exploiting the continuity equation

$$\vec{\nabla} \cdot \vec{j}(\vec{r}, t) = -\frac{\partial}{\partial t} \rho(\vec{r}, t) = i\omega_k \rho(\vec{r}, t). \quad (\text{A.51})$$

In the magnetic case, we proceed analogously starting from Fermi's golden rule and inserting the magnetic component of \mathbf{H}_{int} in transverse gauge (3.13):

$$\begin{aligned} T_{fi}(M, k\lambda\mu) &= \frac{2\pi}{\hbar} |\langle f | \mathbf{H}_{\text{int}} | i \rangle|^2 g(E_f) \\ &= \frac{2\pi}{\hbar} \frac{1}{\hbar c} \frac{R}{\pi} \frac{4\pi\hbar ck}{R} \left| \langle \Psi_f | -\frac{1}{c} \int d^3r \vec{j}(\vec{r}, t) \cdot j_\lambda(kr) \vec{Y}_{\lambda\lambda\mu}(\Omega) | \Psi_i \rangle \right|^2. \end{aligned} \quad (\text{A.52})$$

Again, we substitute the vector spherical harmonics using [Edm64, (5.9.14)] and commute the spherical Bessel function with the orbital angular-momentum operator. We absorb the expression within the absolute value bars into the magnetic multipole operator, where we introduce some additional factors. In this way, we obtain the transition probability in the magnetic case (3.31),

$$\begin{aligned} T_{fi}(M, k\lambda\mu) &= \frac{8\pi k}{\hbar} \frac{1}{\lambda(\lambda+1)} \left| \langle \Psi_f | \frac{1}{c} \int d^3r \vec{j}(\vec{r}, t) \cdot i(\vec{r} \times \vec{\nabla}) Y_{\lambda\mu}(\Omega) | \Psi_i \rangle \right|^2 \\ &= \frac{8\pi}{\hbar} \frac{\lambda+1}{\lambda[(2\lambda+1)!!]^2} \left(\frac{E_k}{\hbar c} \right)^{2\lambda+1} \left| \langle \Psi_f | \mathbf{O}(M, k\lambda\mu) | \Psi_i \rangle \right|^2, \end{aligned} \quad (\text{A.53})$$

with the magnetic multipole operator (3.33)

$$\mathbf{O}(M, k\lambda\mu) = \frac{-(2\lambda+1)!!}{ck^\lambda(\lambda+1)} \int d^3r \vec{j}(\vec{r}, t) \cdot (\vec{r} \times \vec{\nabla}) (j_\lambda(kr) Y_{\lambda\mu}(\Omega)). \quad (\text{A.54})$$

A.5. Single-Particle Matrix Elements of the Reduced Electric Multipole Operator

We use single-particle states obtained from the HO potential and derive (3.43) for the reduced single-particle matrix elements of the electric multipole operator

$$\langle \psi_f | \mathbf{Q}_\lambda | \psi_i \rangle = \langle n' s' l' j' | e r^\lambda Y_\lambda(\Omega) | n s l j \rangle. \quad (\text{A.55})$$

We note that the application in a many-body calculation using a different reference basis, e.g., the HF basis, requires the transformation of the radial component in the final expression into the reference basis.

In order to decouple the spin and spatial part of the operator and the states, we employ the reduced version of [VMK88, p. 479 (28)]. The spin part of the operator is given by the unit operator:

$$\begin{aligned} \langle \psi_f | \mathbf{Q}_\lambda | \psi_i \rangle &= e \hat{\lambda} \hat{j} \hat{j}' \begin{Bmatrix} 0 & \lambda & \lambda \\ s' & l' & j' \\ s & l & j \end{Bmatrix} \langle s' | \mathbf{1} | s \rangle \langle n' l' | r^\lambda Y_\lambda(\Omega) | n l \rangle \\ &= e \hat{\lambda} \hat{j} \hat{j}' \begin{Bmatrix} 0 & \lambda & \lambda \\ s' & l' & j' \\ s & l & j \end{Bmatrix} \delta_{s's} \hat{s} \langle n' l' | r^\lambda Y_\lambda(\Omega) | n l \rangle. \end{aligned} \quad (\text{A.56})$$

In the following, we exploit that we consider fermions with $s = s' = 1/2$, and we, therefore, omit the factor $\delta_{s's}$. We unreduce the matrix element in (A.56) and insert an identity in position space to evaluate the eigenvalue relations for $r^\lambda Y_\lambda(\mathbf{\Omega})$. In this way, we obtain

$$\begin{aligned}
& \langle n'l' || r^\lambda Y_\lambda(\mathbf{\Omega}) || nl \rangle \\
&= (-1)^{l'-m'_l} \begin{pmatrix} l' & \lambda & l \\ -m'_l & \mu & m_l \end{pmatrix}^{-1} \langle n'l'm'_l | r^\lambda Y_\lambda(\mathbf{\Omega}) | nlm_l \rangle \\
&= (-1)^{l'-m'_l} \begin{pmatrix} l' & \lambda & l \\ -m'_l & \mu & m_l \end{pmatrix}^{-1} \int d\mathbf{r} r^2 \int d\Omega \langle n'l'm'_l | r\Omega \rangle r^\lambda Y_{\lambda\mu}(\Omega) \langle r\Omega | nlm_l \rangle \\
&= (-1)^{l'-m'_l} \begin{pmatrix} l' & \lambda & l \\ -m'_l & \mu & m_l \end{pmatrix}^{-1} \int d\mathbf{r} r^2 R_{n'l'}(r) r^\lambda R_{nl}(r) \\
&\quad \times \int d\Omega (-1)^{-m'_l} Y_{l'-m'_l}(\Omega) Y_{\lambda\mu}(\Omega) Y_{lm_l}(\Omega). \tag{A.57}
\end{aligned}$$

We use the definition of the radial integrals (3.47) and exploit relation [VMK88, p. 148 (5)]

$$\begin{aligned}
& \langle n'l' || r^\lambda Y_\lambda(\mathbf{\Omega}) || nl \rangle \\
&= (-1)^{l'} \begin{pmatrix} l' & \lambda & l \\ -m'_l & \mu & m_l \end{pmatrix}^{-1} \langle n'l' | r^\lambda | nl \rangle \frac{\hat{l}' \hat{\lambda} \hat{l}}{\sqrt{4\pi}} \begin{pmatrix} l' & \lambda & l \\ 0 & 0 & 0 \end{pmatrix} \begin{pmatrix} l' & \lambda & l \\ -m'_l & \mu & m_l \end{pmatrix} \\
&= (-1)^{l'} \langle n'l' | r^\lambda | nl \rangle \frac{\hat{l}' \hat{\lambda} \hat{l}}{\sqrt{4\pi}} \begin{pmatrix} l' & \lambda & l \\ 0 & 0 & 0 \end{pmatrix}. \tag{A.58}
\end{aligned}$$

By employing the explicit form of the $9j$ symbol given in [VMK88, p. 357 (2)], (A.56) yields

$$\begin{aligned}
& \langle \psi_f || \mathbf{Q}_\lambda || \psi_i \rangle \\
&= e^{\hat{\lambda} \hat{j} \hat{j}'} (-1)^{j'+l+\lambda+s} \hat{\lambda}^{-1} \hat{s}^{-1} \left\{ \begin{matrix} j & j' & \lambda \\ l' & l & s \end{matrix} \right\} \hat{s} (-1)^{l'} \langle n'l' | r^\lambda | nl \rangle \frac{\hat{l}' \hat{\lambda} \hat{l}}{\sqrt{4\pi}} \begin{pmatrix} l' & \lambda & l \\ 0 & 0 & 0 \end{pmatrix} \\
&= e^{\frac{\hat{j} \hat{j}' \hat{l}' \hat{\lambda} \hat{l}}{\sqrt{4\pi}}} (-1)^{j'+l+\lambda+s+l'} \left\{ \begin{matrix} j & j' & \lambda \\ l' & l & s \end{matrix} \right\} \langle n'l' | r^\lambda | nl \rangle \begin{pmatrix} l' & \lambda & l \\ 0 & 0 & 0 \end{pmatrix} \\
&= e^{\frac{\hat{j} \hat{j}' \hat{l}' \hat{\lambda} \hat{l}}{\sqrt{4\pi}}} (-1)^{j'+l+\lambda+s+l'} \left\{ \begin{matrix} l' & \lambda & l \\ j & s & j' \end{matrix} \right\} \langle n'l' | r^\lambda | nl \rangle \begin{pmatrix} l' & \lambda & l \\ 0 & 0 & 0 \end{pmatrix}. \tag{A.59}
\end{aligned}$$

In the last step, we have used symmetry relations of the $6j$ symbols, so that [VMK88, p. 454 (6)] can be employed to further evaluate the $6j$ and $3j$ symbols in (A.59). We also exploit symmetry relations of the $3j$ symbols or convert them into Clebsch-Gordan coefficients to obtain a convenient form for (A.59) and summarize or cancel the phase factors whenever possible. For this purpose, we require integer values for λ, l, l' and half-integer values for s, j, j' :

$$\begin{aligned}
& \langle \psi_f || \mathbf{Q}_\lambda || \psi_i \rangle \\
&= e^{\frac{\hat{j} \hat{j}' \hat{l}' \hat{\lambda} \hat{l}}{\sqrt{4\pi}}} (-1)^{j'+l+\lambda+s+l'} \langle n'l' | r^\lambda | nl \rangle \sum_{\zeta} (-1)^{s-3\zeta+j'+j} \begin{pmatrix} s & l' & j' \\ \zeta & 0 & -\zeta \end{pmatrix} \begin{pmatrix} j' & \lambda & j \\ \zeta & 0 & -\zeta \end{pmatrix} \begin{pmatrix} j & l & s \\ \zeta & 0 & -\zeta \end{pmatrix}
\end{aligned}$$

$$\begin{aligned}
&= e \frac{\hat{j}\hat{j}'\hat{l}'\hat{\lambda}\hat{l}}{\sqrt{4\pi}} (-1)^{2j'+l+\lambda+2s+l'+j} \langle n'l'|r^\lambda|nl\rangle \\
&\quad \times \sum_{\zeta} (-1)^{-3\zeta} (-1)^{s+l'+j'} \begin{pmatrix} l' & s & j' \\ 0 & \zeta & -\zeta \end{pmatrix} \begin{pmatrix} j' & \lambda & j \\ \zeta & 0 & -\zeta \end{pmatrix} (-1)^{j+l+s} \begin{pmatrix} j & s & l \\ \zeta & -\zeta & 0 \end{pmatrix} \\
&= e \frac{\hat{j}\hat{j}'\hat{l}'\hat{\lambda}\hat{l}}{\sqrt{4\pi}} (-1)^{3j'+2l+\lambda+2l'+2j} \langle n'l'|r^\lambda|nl\rangle \\
&\quad \times \sum_{\zeta} (-1)^{-3\zeta} \begin{pmatrix} l' & s & j' \\ 0 & \zeta & -\zeta \end{pmatrix} \begin{pmatrix} j' & \lambda & j \\ \zeta & 0 & -\zeta \end{pmatrix} \begin{pmatrix} j & s & l \\ \zeta & -\zeta & 0 \end{pmatrix} \\
&= e \frac{\hat{j}\hat{j}'\hat{l}'\hat{\lambda}\hat{l}}{\sqrt{4\pi}} (-1)^{3j'+2l+\lambda+2l'+2j} \langle n'l'|r^\lambda|nl\rangle \\
&\quad \times \sum_{\zeta} (-1)^{-3\zeta} (-1)^{l'-s+\zeta} \hat{j}^{\zeta-1} \begin{pmatrix} l' & s & j' \\ 0 & \zeta & \zeta \end{pmatrix} (-1)^{j'+\lambda+j} \begin{pmatrix} j' & \lambda & j \\ -\zeta & 0 & \zeta \end{pmatrix} (-1)^{j-s} \hat{l}^{-1} \begin{pmatrix} j & s & l \\ \zeta & -\zeta & 0 \end{pmatrix} \\
&= e \frac{\hat{j}\hat{j}'\hat{\lambda}}{\sqrt{4\pi}} (-1)^{l'} \langle n'l'|r^\lambda|nl\rangle \sum_{\zeta} (-1)^{-2(s+\zeta)} \begin{pmatrix} l' & s & j' \\ 0 & \zeta & \zeta \end{pmatrix} \begin{pmatrix} j' & \lambda & j \\ -\zeta & 0 & \zeta \end{pmatrix} \begin{pmatrix} j & s & l \\ \zeta & -\zeta & 0 \end{pmatrix}. \tag{A.60}
\end{aligned}$$

At this point, we set $\zeta = \pm 1/2$ as it represents the spin projection of $s = 1/2$:

$$\begin{aligned}
&\langle \psi_f || \mathbf{Q}_\lambda || \psi_i \rangle \\
&= e \frac{\hat{j}\hat{l}'\hat{\lambda}}{\sqrt{4\pi}} (-1)^{l'} \langle n'l'|r^\lambda|nl\rangle \begin{pmatrix} j' & \lambda & j \\ -\frac{1}{2} & 0 & \frac{1}{2} \end{pmatrix} \\
&\quad \times \left[\begin{pmatrix} l' & \frac{1}{2} & j' \\ 0 & \frac{1}{2} & \frac{1}{2} \end{pmatrix} \begin{pmatrix} j & \frac{1}{2} & l \\ \frac{1}{2} & -\frac{1}{2} & 0 \end{pmatrix} + (-1)^{j'+\lambda+j} \begin{pmatrix} l' & \frac{1}{2} & j' \\ 0 & -\frac{1}{2} & -\frac{1}{2} \end{pmatrix} \begin{pmatrix} j & \frac{1}{2} & l \\ -\frac{1}{2} & \frac{1}{2} & 0 \end{pmatrix} \right]. \tag{A.61}
\end{aligned}$$

We evaluate the expression in the brackets by inserting algebraic formulas for the Clebsch-Gordan coefficients, e.g., provided in [VMK88, p. 271], and by considering the four possible combinations for $j' = l' \pm 1/2$ and $j = l \pm 1/2$. All combinations yield the same result.

For illustration purposes, we explicitly show the evaluation for $j' = l' + 1/2$ and $j = l + 1/2$:

$$\begin{aligned}
&(-1)^{l'} \left[\begin{pmatrix} l' & \frac{1}{2} & j' \\ 0 & \frac{1}{2} & \frac{1}{2} \end{pmatrix} \begin{pmatrix} j & \frac{1}{2} & l \\ \frac{1}{2} & -\frac{1}{2} & 0 \end{pmatrix} + (-1)^{j'+\lambda+j} \begin{pmatrix} l' & \frac{1}{2} & j' \\ 0 & -\frac{1}{2} & -\frac{1}{2} \end{pmatrix} \begin{pmatrix} j & \frac{1}{2} & l \\ -\frac{1}{2} & \frac{1}{2} & 0 \end{pmatrix} \right] \\
&= (-1)^{j'-\frac{1}{2}} \left[\sqrt{\frac{j'+\frac{1}{2}}{2j'}} \sqrt{\frac{j+\frac{1}{2}}{2(j+\frac{1}{2})}} + (-1)^{j'+\lambda+j} \sqrt{\frac{j'+\frac{1}{2}}{2(l'+\frac{1}{2})}} (-1) \sqrt{\frac{j+\frac{1}{2}}{2(j+\frac{1}{2})}} \right] \\
&= (-1)^{j'-\frac{1}{2}} \frac{1}{2} \hat{j}^{\zeta} \hat{l}'^{-1} (1 - (-1)^{j'+\lambda+j}) \\
&= (-1)^{j'-\frac{1}{2}} \frac{1}{2} \hat{j}^{\zeta} \hat{l}'^{-1} (1 + (-1)^{l'+\lambda+l}). \tag{A.62}
\end{aligned}$$

With this, we can summarize the expression for the reduced single-particle matrix

elements of the electric multipole operators:

$$\begin{aligned}\langle \psi_f \| \mathbf{Q}_\lambda \| \psi_i \rangle &= e \frac{\hat{j}^{\lambda'} \hat{\lambda}}{\sqrt{4\pi}} \langle n'l' | r^\lambda | nl \rangle \begin{pmatrix} j' & \lambda & j \\ -\frac{1}{2} & 0 & \frac{1}{2} \end{pmatrix} (-1)^{j'-\frac{1}{2}} \frac{1}{2} \hat{j}^{\lambda'} \hat{l}^{\lambda-1} (1 + (-1)^{l'+\lambda+l}) \\ &= e \frac{1 + (-1)^{l'+\lambda+l}}{2} \langle n'l' | r^\lambda | nl \rangle \frac{\hat{j}^{\lambda'} \hat{j}}{\sqrt{4\pi}} (-1)^{j'-\frac{1}{2}} \begin{pmatrix} j' & \lambda & j \\ -\frac{1}{2} & 0 & \frac{1}{2} \end{pmatrix}.\end{aligned}\quad (\text{A.63})$$

A.6. Translational Invariance of Electric Multipole Operators

Translationally Invariant Form of the Electric Monopole Operator

We derive the translationally invariant form of the electric monopole operator (3.57) by inserting the intrinsic coordinate $\vec{r} - \vec{R}_{\text{cm}}$ into (3.22) and exploiting the definition of the center-of-mass coordinate $\vec{R}_{\text{cm}} = \sum_i \vec{r}_i / A$:

$$\begin{aligned}\mathbf{Q}_{00} &= e \sum_{i=1}^A \Pi_i^\pi (\vec{r}_i - \vec{R}_{\text{cm}})^2 Y_{00}(\bar{\omega}_i) \\ &= \frac{1}{\sqrt{4\pi}} e \left(\sum_{i=1}^A \Pi_i^\pi \vec{r}_i^2 - \frac{2}{A} \sum_{i,j=1}^A \Pi_i^\pi \vec{r}_i \cdot \vec{r}_j + \frac{1}{A^2} \sum_{i=1}^A \Pi_i^\pi \sum_{j,k=1}^A \vec{r}_j \cdot \vec{r}_k \right).\end{aligned}\quad (\text{A.64})$$

Note that the angle $\bar{\omega}_i$ is defined in the reference frame of the nucleus' center of mass. We use $\vec{r}_i \cdot \vec{r}_j = (\vec{r}_i^2 + \vec{r}_j^2 - \vec{r}_{ij}^2)/2$ with $\vec{r}_{ij}^2 = (\vec{r}_i - \vec{r}_j)^2$. Whenever possible, we rename the indices for convenience. In this way, we obtain a translationally invariant form of \mathbf{Q}_{00} :

$$\begin{aligned}\mathbf{Q}_{00} &= \frac{1}{\sqrt{4\pi}} e \left(\sum_{i=1}^A \Pi_i^\pi \vec{r}_i^2 - \frac{1}{A} \sum_{i,j=1}^A \Pi_i^\pi (\vec{r}_i^2 + \vec{r}_j^2 - \vec{r}_{ij}^2) + \frac{Z}{2A^2} \sum_{i,j=1}^A (\vec{r}_i^2 + \vec{r}_j^2 - \vec{r}_{ij}^2) \right) \\ &= \frac{1}{\sqrt{4\pi}} e \left(\sum_{i=1}^A \Pi_i^\pi \vec{r}_i^2 - \sum_{i=1}^A \Pi_i^\pi \vec{r}_i^2 - \frac{Z}{A} \sum_{i=1}^A \vec{r}_i^2 + \frac{1}{A} \sum_{i,j=1}^A \Pi_i^\pi \vec{r}_{ij}^2 \right. \\ &\quad \left. + \frac{Z}{2A} \sum_{i=1}^A \vec{r}_i^2 + \frac{Z}{2A} \sum_{i=1}^A \vec{r}_i^2 - \frac{Z}{2A^2} \sum_{i,j=1}^A \vec{r}_{ij}^2 \right) \\ &= \frac{1}{\sqrt{4\pi}} e \frac{1}{A} \sum_{i,j=1}^A \left(\Pi_i^\pi - \frac{Z}{2A} \right) \vec{r}_{ij}^2 \\ &= \frac{1}{\sqrt{4\pi}} e \frac{2}{A} \sum_{i>j=1}^A \left(\Pi_i^\pi - \frac{Z}{2A} \right) \vec{r}_{ij}^2.\end{aligned}\quad (\text{A.65})$$

Index symmetrization yields (3.57):

$$\mathbf{Q}_{00} = \frac{1}{\sqrt{4\pi}} e \frac{1}{A} \sum_{i>j=1}^A \left(\Pi_i^\pi + \Pi_j^\pi - \frac{Z}{A} \right) \vec{r}_{ij}^2.\quad (\text{A.66})$$

Translationally Invariant Form of the Electric Dipole Operator

In order to derive the translationally invariant form of the electric dipole operator (3.59), we resort to the cartesian representation of the spherical harmonics:

$$\begin{aligned}
 \mathbf{Q}_{10} &= e \sum_{i=1}^A \Pi_i^\pi |\vec{\mathbf{r}}_i - \vec{\mathbf{R}}_{\text{cm}}| Y_{10}(\vec{\omega}_i) \\
 &= e \sum_{i=1}^A \Pi_i^\pi |\vec{\mathbf{r}}_i - \vec{\mathbf{R}}_{\text{cm}}| \sqrt{\frac{3}{4\pi}} \frac{(\mathbf{z}_i - \mathbf{Z}_{\text{cm}})}{|\vec{\mathbf{r}}_i - \vec{\mathbf{R}}_{\text{cm}}|} \\
 &= \sqrt{\frac{3}{4\pi}} e \sum_{i=1}^A \Pi_i^\pi (\mathbf{z}_i - \mathbf{Z}_{\text{cm}}). \tag{A.67}
 \end{aligned}$$

We exploit $Z_{\text{cm}} = \sum_i z_i / A$ and $\Pi_i^\pi + \Pi_i^\nu = 1$ to express the dipole operator in two-body form:

$$\begin{aligned}
 \mathbf{Q}_{10} &= \sqrt{\frac{3}{4\pi}} e \left(\frac{1}{A} \sum_{i,j=1}^A \Pi_i^\pi (\Pi_j^\pi + \Pi_j^\nu) \mathbf{z}_i - \frac{1}{A} \sum_{i,j=1}^A \Pi_i^\nu (\Pi_j^\pi + \Pi_j^\nu) \mathbf{z}_j \right) \\
 &= \sqrt{\frac{3}{4\pi}} e \frac{1}{A} \sum_{i,j=1}^A \left(\Pi_i^\pi \Pi_j^\pi + \Pi_i^\pi \Pi_j^\nu \right) \mathbf{z}_{ij}. \tag{A.68}
 \end{aligned}$$

Here, we have introduced the relative z-component z_{ij} of $\vec{\mathbf{r}}_{ij}$. The final expression (3.59) is obtained by reinserting the spherical harmonics:

$$\mathbf{Q}_{10} = e \frac{2}{A} \sum_{i>j=1}^A \left(\Pi_i^\pi \Pi_j^\pi + \Pi_i^\pi \Pi_j^\nu \right) |\vec{\mathbf{r}}_{ij}| Y_{10}(\vec{\omega}_{ij}). \tag{A.69}$$

We remark that we can make use of (3.43) for the calculation of the reduced matrix elements if we work in a relative HO basis. The corresponding two-body matrix elements can be obtained by applying the Talmi-Moshinsky transformation [Tal52; Mos59], which separates HO matrix elements into relative and center-of-mass components and vice versa.

Translationally Invariant Form of the Electric Quadrupole Operator

The translationally invariant form of the electric quadrupole operator (3.61) can be derived in cartesian coordinates:

$$\begin{aligned}
 \mathbf{Q}_{20} &= e \sum_{i=1}^A \Pi_i^\pi (\vec{\mathbf{r}}_i - \vec{\mathbf{R}}_{\text{cm}})^2 Y_{20}(\vec{\omega}_i) \\
 &= e \sum_{i=1}^A \Pi_i^\pi (\vec{\mathbf{r}}_i - \vec{\mathbf{R}}_{\text{cm}})^2 \sqrt{\frac{5}{16\pi}} \frac{2(\mathbf{z}_i - \mathbf{Z}_{\text{cm}})^2 - (\mathbf{x}_i - \mathbf{X}_{\text{cm}})^2 - (\mathbf{y}_i - \mathbf{Y}_{\text{cm}})^2}{(\vec{\mathbf{r}}_i - \vec{\mathbf{R}}_{\text{cm}})^2} \\
 &= \sqrt{\frac{5}{16\pi}} e \sum_{i=1}^A \Pi_i^\pi \left(2(\mathbf{z}_i - \mathbf{Z}_{\text{cm}})^2 - (\mathbf{x}_i - \mathbf{X}_{\text{cm}})^2 - (\mathbf{y}_i - \mathbf{Y}_{\text{cm}})^2 \right). \tag{A.70}
 \end{aligned}$$

Each term can be rewritten in the following way:

$$\begin{aligned}
\sum_{i=1}^A \Pi_i^\pi (\mathbf{z}_i - \mathbf{Z}_{\text{cm}})^2 &= \sum_{i=1}^A \Pi_i^\pi \mathbf{z}_i^2 - \frac{2}{A} \sum_{i,j=1}^A \Pi_i^\pi \mathbf{z}_i \mathbf{z}_j + \frac{1}{A^2} \sum_{i=1}^A \Pi_i^\pi \sum_{j,k=1}^A \mathbf{z}_j \mathbf{z}_k \\
&= \sum_{i=1}^A \Pi_i^\pi \mathbf{z}_i^2 - \frac{1}{A} \sum_{i,j=1}^A \Pi_i^\pi (\mathbf{z}_i^2 + \mathbf{z}_j^2 - \mathbf{z}_{ij}^2) + \frac{Z}{2A^2} \sum_{i,j=1}^A (\mathbf{z}_i^2 + \mathbf{z}_j^2 - \mathbf{z}_{ij}^2) \\
&= \frac{1}{A} \sum_{i,j=1}^A \left(\Pi_i^\pi - \frac{Z}{2A} \right) \mathbf{z}_{ij}^2.
\end{aligned} \tag{A.71}$$

Index symmetrization yields

$$\sum_{i=1}^A \Pi_i^\pi (\mathbf{z}_i - \mathbf{Z}_{\text{cm}})^2 = \frac{1}{A} \sum_{i>j=1}^A \left(\Pi_i^\pi + \Pi_j^\pi - \frac{Z}{A} \right) \mathbf{z}_{ij}^2. \tag{A.72}$$

By inserting this into (A.70) and combining the three terms to a spherical harmonics, we obtain

$$\begin{aligned}
\mathcal{Q}_{20} &= \sqrt{\frac{5}{16\pi}} e \frac{1}{A} \sum_{i>j=1}^A \left(\Pi_i^\pi + \Pi_j^\pi - \frac{Z}{A} \right) (2\mathbf{z}_{ij}^2 - \mathbf{x}_{ij}^2 - \mathbf{y}_{ij}^2) \\
&= e \frac{1}{A} \sum_{i>j=1}^A \left(\Pi_i^\pi + \Pi_j^\pi - \frac{Z}{A} \right) \bar{r}_{ij}^2 Y_{20}(\bar{\omega}_{ij}).
\end{aligned} \tag{A.73}$$

As for the translationally invariant electric dipole operator, we can calculate the reduced matrix elements in a relative HO basis using (3.43) and transform them into a two-body HO basis via Talmi-Moshinsky transformation [Tal52; Mos59] afterward.

One-Body Electric Dipole and Quadrupole Operators in the NCSM

The translationally invariant form of the electric isovector dipole operator can be rewritten using [VMK88, p. 167 (35)] as

$$\begin{aligned}
\mathcal{Q}_{10}^{\text{IV}} &= e \sum_{i=1}^A \boldsymbol{\tau}_i |\bar{\mathbf{r}}_i - \bar{\mathbf{R}}_{\text{cm}}| Y_{10}(\bar{\omega}_i) \\
&= e \sum_{i=1}^A \boldsymbol{\tau}_i \sqrt{4\pi} 3! \left[\frac{\mathbf{r}_i}{3!} \{ Y_1(\boldsymbol{\Omega}_i) \otimes Y_0(\boldsymbol{\Omega}_{\text{cm}}) \}_{10} - \frac{\mathbf{R}_{\text{cm}}}{3!} \{ Y_0(\boldsymbol{\Omega}_i) \otimes Y_1(\boldsymbol{\Omega}_{\text{cm}}) \}_{10} \right] \\
&= e \sum_{i=1}^A \boldsymbol{\tau}_i [\mathbf{r}_i Y_{10}(\boldsymbol{\Omega}_i) - \mathbf{R}_{\text{cm}} Y_{10}(\boldsymbol{\Omega}_{\text{cm}})] \\
&= e \sum_{i=1}^A \boldsymbol{\tau}_i \mathbf{r}_i Y_{10}(\boldsymbol{\Omega}_i) - e \frac{Z-N}{2} \mathbf{R}_{\text{cm}} Y_{10}(\boldsymbol{\Omega}_{\text{cm}}),
\end{aligned} \tag{A.74}$$

where we have used [VMK88, p. 160 (1)] and the explicit form of the spherical harmonics $Y_{00}(\boldsymbol{\Omega})$.

In order to reformulate the expression for the translationally invariant electric isoscalar quadrupole operator, we artificially write the one-body operator in a two-body form. For shortness, we introduce $O(\vec{r}_i) = r_i^2 Y_{20}(\mathbf{\Omega}_i)$ and obtain

$$\begin{aligned} \mathcal{Q}_{20}^{\text{IS}} &= \frac{e}{2} \sum_{i=1}^A O(\vec{r}_i) \\ &= \frac{e}{2(A-1)} \sum_{i>j=1}^A [O(\vec{r}_i) + O(\vec{r}_j)]. \end{aligned} \quad (\text{A.75})$$

To further utilize the expression in brackets, we exploit [VMK88, p. 167 (35)] for spherical waves with $r = |\vec{r}_1 - \vec{r}_2|$ and $R = |\vec{r}_1 + \vec{r}_2|$ and rewrite $O(\vec{r}_{ij}) = O(\vec{r}_i - \vec{r}_j)$ and $O(\vec{R}_{ij,\text{cm}}) = O(\vec{r}_i + \vec{r}_j)/4$ as

$$\begin{aligned} O(\vec{r}_{ij}) &= \sqrt{4\pi 5!} \left[\frac{r_j^2}{\sqrt{5!}} \{Y_0(\mathbf{\Omega}_i) \otimes Y_2(\mathbf{\Omega}_j)\}_{20} + \frac{r_i^2}{\sqrt{5!}} \{Y_2(\mathbf{\Omega}_i) \otimes Y_0(\mathbf{\Omega}_j)\}_{20} \right. \\ &\quad \left. - \frac{\mathbf{r}_i \mathbf{r}_j}{3!} \{Y_1(\mathbf{\Omega}_i) \otimes Y_1(\mathbf{\Omega}_j)\}_{20} \right] \end{aligned} \quad (\text{A.76})$$

$$= O(\vec{r}_i) + O(\vec{r}_j) - \frac{\sqrt{4\pi 5!}}{3!} \mathbf{r}_i \mathbf{r}_j \{Y_1(\mathbf{\Omega}_i) \otimes Y_1(\mathbf{\Omega}_j)\}_{20}, \quad (\text{A.77})$$

$$\begin{aligned} O(\vec{R}_{ij,\text{cm}}) &= \frac{1}{4} \sqrt{4\pi 5!} \left[\frac{r_j^2}{\sqrt{5!}} \{Y_0(\mathbf{\Omega}_i) \otimes Y_2(\mathbf{\Omega}_j)\}_{20} + \frac{r_i^2}{\sqrt{5!}} \{Y_2(\mathbf{\Omega}_i) \otimes Y_0(\mathbf{\Omega}_j)\}_{20} \right. \\ &\quad \left. + \frac{\mathbf{r}_i \mathbf{r}_j}{3!} \{Y_1(\mathbf{\Omega}_i) \otimes Y_1(\mathbf{\Omega}_j)\}_{20} \right] \end{aligned} \quad (\text{A.78})$$

$$= \frac{1}{4} \left[O(\vec{r}_i) + O(\vec{r}_j) + \frac{\sqrt{4\pi 5!}}{3!} \mathbf{r}_i \mathbf{r}_j \{Y_1(\mathbf{\Omega}_i) \otimes Y_1(\mathbf{\Omega}_j)\}_{20} \right], \quad (\text{A.79})$$

where we have evaluated the first two terms in (A.76) and (A.78) using [VMK88, p. 160 (1)] and the explicit form of the spherical harmonics $Y_{00}(\Omega)$. A combination of (A.77) and (A.79) yields

$$O(\vec{r}_i) + O(\vec{r}_j) = \frac{1}{2} O(\vec{r}_{ij}) + 2O(\vec{R}_{ij,\text{cm}}). \quad (\text{A.80})$$

The translationally invariant analog of (A.75) is given by

$$\begin{aligned} \mathcal{Q}_{20}^{\text{IS}} &= \frac{e}{2} \sum_{i=1}^A O(\vec{r}_i - \vec{R}_{\text{cm}}) \\ &= \frac{e}{2(A-1)} \sum_{i>j=1}^A [O(\vec{r}_i - \vec{R}_{\text{cm}}) + O(\vec{r}_j - \vec{R}_{\text{cm}})], \end{aligned} \quad (\text{A.81})$$

which we can reformulate using (A.80):

$$\mathbf{Q}_{20}^{\text{IS}} = \frac{e}{2(A-1)} \sum_{i>j=1}^A \left[\frac{1}{2} O(\vec{\mathbf{r}}_{ij}) + 2O(\vec{\mathbf{R}}_{ij,\text{cm}} - \vec{\mathbf{R}}_{\text{cm}}) \right]. \quad (\text{A.82})$$

With [VMK88, p. 167 (35)], we can rewrite the last term and obtain

$$\begin{aligned} \mathbf{Q}_{20}^{\text{IS}} = \frac{e}{4(A-1)} \sum_{i \neq j}^A & \left[\frac{1}{2} O(\vec{\mathbf{r}}_{ij}) + 2O(\vec{\mathbf{R}}_{\text{cm}}) + 2O(\vec{\mathbf{R}}_{ij,\text{cm}}) \right. \\ & \left. - \frac{\sqrt{4\pi} 5!}{3} \mathbf{R}_{ij,\text{cm}} \mathbf{R}_{\text{cm}} \{ Y_1(\mathbf{\Omega}_{ij,\text{cm}}) \otimes Y_1(\mathbf{\Omega}_{\text{cm}}) \}_{20} \right]. \end{aligned} \quad (\text{A.83})$$

The first and third term of (A.83) can be combined using (A.80):

$$\begin{aligned} \sum_{i \neq j}^A \left[\frac{1}{2} O(\vec{\mathbf{r}}_{ij}) + 2O(\vec{\mathbf{R}}_{ij,\text{cm}}) \right] &= \sum_{i \neq j}^A [O(\vec{\mathbf{r}}_i) + O(\vec{\mathbf{r}}_j)] \\ &= 2(A-1) \sum_{i=1}^A O(\vec{\mathbf{r}}_i). \end{aligned} \quad (\text{A.84})$$

Regarding the second term of (A.83), we only need to carry out the sums:

$$\sum_{i \neq j}^A 2O(\vec{\mathbf{R}}_{\text{cm}}) = 2A(A-1)O(\vec{\mathbf{R}}_{\text{cm}}). \quad (\text{A.85})$$

In order to rewrite the last term of (A.83), we exploit the bilinearity of the bipolar spherical harmonics and use the definition of the center-of-mass coordinate. In this way, we obtain

$$\begin{aligned} & \sum_{i \neq j}^A \mathbf{R}_{ij,\text{cm}} \mathbf{R}_{\text{cm}} \{ Y_1(\mathbf{\Omega}_{ij,\text{cm}}) \otimes Y_1(\mathbf{\Omega}_{\text{cm}}) \}_{20} \\ &= \mathbf{R}_{\text{cm}} \sum_{i \neq j}^A \{ \mathbf{R}_{ij,\text{cm}} Y_1(\mathbf{\Omega}_{ij,\text{cm}}) \otimes Y_1(\mathbf{\Omega}_{\text{cm}}) \}_{20} \\ &= \mathbf{R}_{\text{cm}} \sum_{i \neq j}^A \{ \vec{\mathbf{R}}_{ij,\text{cm}} \otimes Y_1(\mathbf{\Omega}_{\text{cm}}) \}_{20} \\ &= \frac{\mathbf{R}_{\text{cm}}}{2} \sum_{i \neq j}^A \{ (\vec{\mathbf{r}}_i + \vec{\mathbf{r}}_j) \otimes Y_1(\mathbf{\Omega}_{\text{cm}}) \}_{20} \\ &= \frac{\mathbf{R}_{\text{cm}}}{2} (A-1) \left[\sum_{i=1}^A \{ \vec{\mathbf{r}}_i \otimes Y_1(\mathbf{\Omega}_{\text{cm}}) \}_{20} + \sum_{j=1}^A \{ \vec{\mathbf{r}}_j \otimes Y_1(\mathbf{\Omega}_{\text{cm}}) \}_{20} \right] \\ &= \mathbf{R}_{\text{cm}}^2 A(A-1) \{ Y_1(\mathbf{\Omega}_{\text{cm}}) \otimes Y_1(\mathbf{\Omega}_{\text{cm}}) \}_{20}. \end{aligned} \quad (\text{A.86})$$

Finally, we can write the translationally invariant electric isoscalar quadrupole operator as

$$\mathbf{Q}_{20}^{\text{IS}} = \frac{e}{2} \left[\sum_{i=1}^A O(\vec{r}_i) + AO(\vec{\mathbf{R}}_{\text{cm}}) - \frac{\sqrt{4\pi} 5!}{3} \frac{A}{2} \mathbf{R}_{\text{cm}}^2 \{ Y_1(\mathbf{\Omega}_{\text{cm}}) \otimes Y_1(\mathbf{\Omega}_{\text{cm}}) \}_{20} \right]. \quad (\text{A.87})$$

The eigenstates obtained in the NCSM with HO basis and N_{max} truncation factorize exactly into a component depending only on relative coordinates and a component depending only on center-of-mass coordinates, $|\Psi\rangle = |\psi_{\text{int}}\rangle \otimes |\psi_{\text{cm}}\rangle$. Since we usually employ a modified Hamiltonian, $\mathbf{H}_{\text{int}} + \beta\mathbf{H}_{\text{cm}}$ with finite β , for the solution of the eigenvalue problem, the center-of-mass component of the eigenstates is always in its $0\hbar\Omega$ ground state with $L = 0$, cf. chapter 4.

The translationally invariant form of both, the electric isovector dipole and isoscalar quadrupole operator, depend on the respective one-body operator and additional terms with spherical harmonics of multipolarity $\lambda = 1$ or $\lambda = 2$ that act exclusively on the center-of-mass component. Since transitions with initial $L_i = 0$ and final $L_f = 0$ cannot be mediated via operators with $\lambda > 0$, the center-of-mass parts of (A.74) and (A.87) cannot contribute, and, thus, the use of the one-body electric isovector dipole and isoscalar quadrupole operators does not induce spuriousities in the results.

B. Hartree-Fock Method

The HF method is an approximate method for the solution of the nuclear A -body eigenvalue problem derived from the variational principle. It is motivated by the success of the naive shell model where the nucleus is considered as a system of nucleons moving independently in an average potential generated by all of them. Starting point of a HF calculation is a nuclear Hamiltonian \mathbf{H}_{nucl} comprising, in general, a zero-, one-, two-, and three-body part. From this Hamiltonian, we construct a self-consistent one-body Hamiltonian in such a way that the Slater determinant constructed from its A energetically lowest single-particle states represents the best approximation to the ground state possible if the only degrees of freedom for variation are the single-particle states. The purpose of the HF method in this work is the construction of a single-particle potential that incorporates a part of the physics relevant for the description of the nucleus under consideration. Its single-particle states and energies are then used as reference basis in a subsequent CI calculation, which hopefully exhibits improved convergence properties compared to calculations using generic single-particle potentials as, e.g., the HO potential.

We aim at the determination of a single-particle basis $\{|\alpha_i\rangle\}$ with $|\alpha_i\rangle = \mathbf{a}_i^\dagger |0\rangle$ so that the Slater determinant

$$|\Phi\rangle = \mathbf{a}_1^\dagger \mathbf{a}_2^\dagger \dots \mathbf{a}_A^\dagger |0\rangle \quad (\text{B.1})$$

minimizes the energy functional $E[\Phi] = \langle \Phi | \mathbf{H}_{\text{nucl}} | \Phi \rangle$. A convenient working basis is the HO basis with ls -coupled single-particle states

$$|\gamma_i\rangle = |n_i l_i j_i m_i \tau_i\rangle = \mathbf{c}_i^\dagger |0\rangle. \quad (\text{B.2})$$

We apply the procedure outlined below to determine the coefficients $D_k^{(i)}$ of the basis expansion of the HF single-particle states in the HO basis, i.e.,

$$|\alpha_i\rangle = \sum_k D_k^{(i)} |\gamma_k\rangle, \quad \text{or equivalently,} \quad \mathbf{a}_i^\dagger = \sum_k D_k^{(i)} \mathbf{c}_k^\dagger. \quad (\text{B.3})$$

The HO single-particle basis is truncated and includes only states up to a maximum quantum number $e_{\text{max}} = (2n + l)_{\text{max}}$. An additional truncation is possible by imposing a maximum angular momentum l_{max} . Since Slater determinants are, besides an irrelevant phase factor, invariant under unitary transformations within the occupied single-particle states, the minimization of the energy functional $E[\Phi]$ does not yield unique coefficients

$D_k^{(i)}$. Therefore, it is convenient to resort to single-particle densities

$$\begin{aligned}
 \rho_{kk'} &= \langle \Phi | \mathbf{c}_k^\dagger \mathbf{c}_k | \Phi \rangle \\
 &= \sum_{i,i'} D_{k'}^{(i')*} D_k^{(i)} \langle \Phi | \mathbf{a}_i^\dagger \mathbf{a}_i | \Phi \rangle \\
 &= \sum_i^{\text{occ.}} D_{k'}^{(i)*} D_k^{(i)}
 \end{aligned} \tag{B.4}$$

for the variation of the energy functional, which provide a one-to-one correspondence to Slater determinants [RS80, App. D.2]. Instead of varying the single-particle states of $|\Phi\rangle$, we vary the matrix elements $\rho_{kk'}$ of the density operator. The hermiticity and idempotence of the density operator enters the variation as a constraint.

We start by constructing the energy functional of a Hamiltonian with up to three-body terms. The Hamiltonian in second quantization reads

$$\begin{aligned}
 \mathbf{H}_{\text{nucl}} &= \mathbf{H}_{0\text{B}} + \mathbf{H}_{1\text{B}} + \mathbf{H}_{2\text{B}} + \mathbf{H}_{3\text{B}} \\
 &= E_0 + \sum_{i,i'} h_{i,i'}^{(1\text{B})} \mathbf{c}_i^\dagger \mathbf{c}_{i'} + \frac{1}{4} \sum_{ij,i'j'} h_{ij,i'j'}^{(2\text{B})} \mathbf{c}_i^\dagger \mathbf{c}_j^\dagger \mathbf{c}_{j'} \mathbf{c}_{i'} \\
 &\quad + \frac{1}{36} \sum_{ijk,i'j'k'} h_{ijk,i'j'k'}^{(3\text{B})} \mathbf{c}_i^\dagger \mathbf{c}_j^\dagger \mathbf{c}_k^\dagger \mathbf{c}_{k'} \mathbf{c}_{j'} \mathbf{c}_{i'}.
 \end{aligned} \tag{B.5}$$

The summation indices run over the single-particle basis and E_0 , $h_{i,i'}^{(1\text{B})}$, $h_{ij,i'j'}^{(2\text{B})}$ and $h_{ijk,i'j'k'}^{(3\text{B})}$ denote the antisymmetrized matrix elements of the individual parts of the Hamiltonian. The expectation value of the Hamilton operator

$$\begin{aligned}
 E[\Phi] &= \langle \Phi | \mathbf{H}_{\text{nucl}} | \Phi \rangle \\
 &= E_0 + \sum_{i,i'} h_{i,i'}^{(1\text{B})} \langle \Phi | \mathbf{c}_i^\dagger \mathbf{c}_{i'} | \Phi \rangle + \frac{1}{4} \sum_{ij,i'j'} h_{ij,i'j'}^{(2\text{B})} \langle \Phi | \mathbf{c}_i^\dagger \mathbf{c}_j^\dagger \mathbf{c}_{j'} \mathbf{c}_{i'} | \Phi \rangle \\
 &\quad + \frac{1}{36} \sum_{ijk,i'j'k'} h_{ijk,i'j'k'}^{(3\text{B})} \langle \Phi | \mathbf{c}_i^\dagger \mathbf{c}_j^\dagger \mathbf{c}_k^\dagger \mathbf{c}_{k'} \mathbf{c}_{j'} \mathbf{c}_{i'} | \Phi \rangle
 \end{aligned} \tag{B.6}$$

can be expressed via density matrices. We can further apply Slater-Condon rules [Sla29; Con30; SO96] or Wick's theorem (see (A.10)) to write the two- and three-body density matrices as products of one-body densities:

$$E[\rho] = E_0 + \sum_{i,i'} h_{i,i'}^{(1\text{B})} \rho_{i',i} + \frac{1}{2} \sum_{ij,i'j'} h_{ij,i'j'}^{(2\text{B})} \rho_{j',j} \rho_{i',i} + \frac{1}{6} \sum_{ijk,i'j'k'} h_{ijk,i'j'k'}^{(3\text{B})} \rho_{k',k} \rho_{j',j} \rho_{i',i}. \tag{B.7}$$

The variation of the energy with respect to the one-body density yields

$$\begin{aligned}
 \delta E[\rho] &= E[\rho + \delta\rho] - E[\rho] \\
 &= \sum_{i,i'} h_{i,i'}^{(1\text{B})} \delta\rho_{i',i} + \sum_{ij,i'j'} h_{ij,i'j'}^{(2\text{B})} \delta\rho_{j',j} \rho_{i',i} + \frac{1}{2} \sum_{ijk,i'j'k'} h_{ijk,i'j'k'}^{(3\text{B})} \delta\rho_{k',k} \rho_{j',j} \rho_{i',i},
 \end{aligned} \tag{B.8}$$

where we have included variations of ρ only up to linear order. By renaming the indices, we can rewrite (B.8) as

$$\delta E[\rho] = \sum_{i,i'} h_{i,i'}[\rho] \delta \rho_{i',i} \quad (\text{B.9})$$

with the matrix elements of the density-dependent Hamiltonian

$$h_{i,i'}[\rho] = h_{i,i'}^{(1B)} + \sum_{j,j'} h_{ij,i'j'}^{(2B)} \rho_{j',j} + \frac{1}{2} \sum_{jk,j'k'} h_{ijk,i'j'k'}^{(3B)} \rho_{k',k} \rho_{j',j}. \quad (\text{B.10})$$

Since the density matrix is constrained to the space of Slater determinants, its variation $\delta\rho$ is limited. In the HF basis, the density matrix ρ is required to be diagonal with entries 1 for the A occupied single-particle states and entries 0 for the unoccupied single-particle states. In order to guarantee idempotence by requiring $(\rho + \delta\rho)^2 = \rho + \delta\rho$, the variation $\delta\rho$ is only allowed to connect occupied with unoccupied states, i.e., hole with particle states. Consequently, the density matrix may only have non-vanishing entries in the off-diagonal blocks of the matrix that neither belong to hole-hole nor particle-particle states, and the variation is only between occupied and unoccupied states. Additionally, if the one-body Hamilton matrix $h[\rho]$ in HF basis had block-diagonal structure, the stationary condition for (B.9) would be guaranteed for arbitrary $\delta\rho$. A block-diagonal structure of $h[\rho]$ and an off-diagonal structure of $\delta\rho$, however, imply that the commutator of the two quantities vanishes:

$$[h[\rho], \rho] = 0. \quad (\text{B.11})$$

We transfer this reasoning to operators and conclude that the density operator ρ and the one-body Hamilton operator $\mathbf{h}[\rho]$ have a simultaneous eigenbasis, i.e., the eigenstates of $\mathbf{h}[\rho]$ define a single-particle basis $\{|\alpha_i\rangle\}$ in which the density operator is diagonal—the stationary condition is fulfilled and the single-particle states that minimize the energy are uniquely determined. Therefore, the HF method consists of the solution of the eigenvalue problem

$$\mathbf{h}[\rho] |\alpha_i\rangle = \epsilon_i |\alpha_i\rangle \quad (\text{B.12})$$

of the mean-field Hamiltonian $\mathbf{h}[\rho]$. The eigenvalue problem (B.12) is non-linear because the Hamiltonian depends on the density, which, in turn, depends on the solution of (B.12). In practice, we employ an iterative procedure to determine the self-consistent solution: We expand the eigenstates in the basis $\{|\gamma_i\rangle\}$ and diagonalize the resulting Hamilton matrix. In this way, we obtain the coefficients $D_k^{(i)}$. From these, we calculate the new density matrix and solve the eigenvalue problem again. The previous steps are repeated until convergence is obtained.

The mean-field Hamilton matrix in HF basis reduces to

$$h_{i,i'}[\rho] = h_{i,i'}^{(1B)} + \sum_j^{\text{occ}} h_{ij,i'j}^{(2B)} + \frac{1}{2} \sum_{jk}^{\text{occ}} h_{ijk,i'j'k'}^{(3B)} \quad (\text{B.13})$$

where the sum runs over occupied (occ.) states only, and its eigenenergies are given by

$$\epsilon_i = h_{i,i}^{(1B)} + \sum_j^{\text{occ.}} h_{ij,ij}^{(2B)} + \frac{1}{2} \sum_{jk}^{\text{occ.}} h_{ijk,ijk}^{(3B)}. \quad (\text{B.14})$$

The Slater determinant constructed from the A single-particle states with lowest ϵ_i is the HF Slater determinant $|\Phi\rangle$ with ground-state energy

$$\begin{aligned} E[\Phi] &= \langle \Phi | \mathbf{H}_{\text{nucl}} | \Phi \rangle \\ &= \sum_i^{\text{occ.}} h_{i,i}^{(1B)} + \frac{1}{2} \sum_{ij}^{\text{occ.}} h_{ij,ij}^{(2B)} + \frac{1}{6} \sum_{ijk}^{\text{occ.}} h_{ijk,ijk}^{(3B)} \\ &= \sum_i^{\text{occ.}} \epsilon_i - \frac{1}{2} \sum_{ij}^{\text{occ.}} h_{ij,ij}^{(2B)} - \frac{1}{3} \sum_{ijk}^{\text{occ.}} h_{ijk,ijk}^{(3B)}. \end{aligned} \quad (\text{B.15})$$

Note that the ground-state energy is different from the sum of the single-particle energies of the ground state.

The HF method as described above can only be applied to closed-shell nuclei. For all other nuclei, we use the equal-filling approximation [PR08], where we assume that occupation numbers on the diagonal of the density matrix ρ are fractional. If we want to calculate the ground-state energy of an open-shell nucleus using the HF method, we assume that the entries of the density matrix of a given single-particle state are $x/(2j+1)$, where x is the number of particles in the (partially) occupied orbit and j its total angular momentum quantum number.

C. Multiconfigurational Perturbation Theory

We aim at finding an approximate solution of the nuclear eigenvalue problem in a given full model space $\mathcal{M}_{\text{full}}$ spanned by a set of many-body basis states $\{|\Phi_j\rangle\}$, e.g., Slater determinants constructed from the HO or an HF single-particle basis, with some model-space truncation. We start from a reference state $|\Psi_{\text{ref}}\rangle$, representing a zeroth-order approximation for a target eigenstate. In general, the reference state can be an arbitrary superposition of basis states from a subspace \mathcal{M}_{ref} of the full model space,

$$|\Psi_{\text{ref}}\rangle = \sum_{j \in \mathcal{M}_{\text{ref}}} c_{j,\text{ref}} |\Phi_j\rangle, \quad (\text{C.1})$$

and is typically chosen to be an eigenstate of the Hamiltonian \mathbf{H} in a manageable reference space. We employ low-order MCPT to estimate the leading corrections to $|\Psi_{\text{ref}}\rangle$ resulting from basis states outside the reference space.

We split the Hamiltonian \mathbf{H} into an unperturbed part \mathbf{H}_0 and a perturbation \mathbf{W} :

$$\mathbf{H} = \mathbf{H}_0 + \mathbf{W}. \quad (\text{C.2})$$

The eigenvalue problem of the unperturbed Hamiltonian is

$$\mathbf{H}_0 |\Psi_{\text{ref}}\rangle = \epsilon_{\text{ref}} |\Psi_{\text{ref}}\rangle, \quad (\text{C.3a})$$

$$\epsilon_{\text{ref}} = \langle \Psi_{\text{ref}} | \mathbf{H} | \Psi_{\text{ref}} \rangle, \quad (\text{C.3b})$$

where the eigenvalue is given by the expectation value of the full Hamiltonian with respect to the reference state. Formally, we can define the unperturbed Hamiltonian as

$$\mathbf{H}_0 = \epsilon_{\text{ref}} |\Psi_{\text{ref}}\rangle \langle \Psi_{\text{ref}}| + \sum_{j \notin \mathcal{M}_{\text{ref}}} \epsilon_j |\Phi_j\rangle \langle \Phi_j|, \quad (\text{C.4})$$

so that it fulfills the eigenvalue relation (C.3). It can be shown that eigenstates of \mathbf{H}_0 within \mathcal{M}_{ref} which are orthogonal to $|\Psi_{\text{ref}}\rangle$ do not contribute to the perturbative energy and state corrections [Stu13] and can be omitted for simplicity. Since the partitioning of the Hamiltonian is arbitrary, there are different choices for the unperturbed energies ϵ_j of the basis states outside \mathcal{M}_{ref} . A computationally efficient possibility is to use the simple Møller-Plesset-type formulation of MCPT [Sur+04], where these unperturbed energies are defined relative to the reference state:

$$\epsilon_j = \epsilon_{\text{ref}} + \Delta\epsilon_j. \quad (\text{C.5})$$

The excitation energy $\Delta\epsilon_j$ is computed from the single-particle energies of the underlying basis. If we use, e.g., the HO single-particle basis, the single-particle energies are given by $e = (2n + l + 3/2)$. When using an HF basis, they are the HF single-particle energies, and

in the VSSM, they are the effective single-particle energies. The choice of the unperturbed Hamiltonian defines the perturbation

$$\mathbf{W} = \mathbf{H} - \mathbf{H}_0. \quad (\text{C.6})$$

In the following, we derive the lowest-order corrections to the unperturbed eigenvalue ϵ_{ref} and eigenstate $|\Psi_{\text{ref}}\rangle$. In order to set up the perturbation series, we introduce a parameter λ to control the perturbation \mathbf{W} :

$$\mathbf{H} = \mathbf{H}_0 + \lambda \mathbf{W}. \quad (\text{C.7})$$

We further expand the target eigenvalue E and eigenstate $|\Psi\rangle$ in terms of a power series in this parameter:

$$E = \epsilon_{\text{ref}} + \lambda E^{(1)} + \lambda^2 E^{(2)} + \dots, \quad (\text{C.8a})$$

$$|\Psi\rangle = |\Psi_{\text{ref}}\rangle + \lambda |\Psi^{(1)}\rangle + \lambda^2 |\Psi^{(2)}\rangle + \dots. \quad (\text{C.8b})$$

By inserting the Equations (C.7) and (C.8) into the full eigenvalue problem, we obtain

$$\begin{aligned} & (\mathbf{H}_0 + \lambda \mathbf{W}) \left(|\Psi_{\text{ref}}\rangle + \lambda |\Psi^{(1)}\rangle + \lambda^2 |\Psi^{(2)}\rangle + \dots \right) \\ &= \left(\epsilon_{\text{ref}} + \lambda E^{(1)} + \lambda^2 E^{(2)} + \dots \right) \left(|\Psi_{\text{ref}}\rangle + \lambda |\Psi^{(1)}\rangle + \lambda^2 |\Psi^{(2)}\rangle + \dots \right), \end{aligned} \quad (\text{C.9})$$

which yields the unperturbed eigenvalue problem in the limit of vanishing λ and the exact one if evaluated at $\lambda = 1$. We expand (C.9) and arrange the terms according to the power of λ . The zeroth order of the expansion reproduces the unperturbed eigenvalue problem (C.3). The first-order terms yield

$$\mathbf{H}_0 |\Psi^{(1)}\rangle + \mathbf{W} |\Psi_{\text{ref}}\rangle = \epsilon_{\text{ref}} |\Psi^{(1)}\rangle + E^{(1)} |\Psi_{\text{ref}}\rangle. \quad (\text{C.10})$$

We derive the first-order energy correction by multiplying (C.10) by $\langle \Psi_{\text{ref}} |$:

$$\langle \Psi_{\text{ref}} | \mathbf{H}_0 | \Psi^{(1)} \rangle + \langle \Psi_{\text{ref}} | \mathbf{W} | \Psi_{\text{ref}} \rangle = \epsilon_{\text{ref}} \langle \Psi_{\text{ref}} | \Psi^{(1)} \rangle + E^{(1)} \langle \Psi_{\text{ref}} | \Psi_{\text{ref}} \rangle. \quad (\text{C.11})$$

It is convenient to use the intermediate normalization

$$\langle \Psi_{\text{ref}} | \Psi \rangle = 1, \quad (\text{C.12})$$

from which follows

$$\langle \Psi_{\text{ref}} | \Psi^{(p>0)} \rangle = 0. \quad (\text{C.13})$$

The order of the perturbative correction is denoted by p . On the left-hand side of (C.11), we can exploit the eigenvalue relation for the unperturbed Hamiltonian. Then, the first term on each side of the equation vanishes because of the intermediate normalization (C.12). The first-order correction to the energy is then given by

$$E^{(1)} = \langle \Psi_{\text{ref}} | \mathbf{W} | \Psi_{\text{ref}} \rangle = 0 \quad (\text{C.14})$$

and vanishes due to the specific choice of the unperturbed Hamiltonian. We note that

$$\begin{aligned}
\langle \Phi_j | \mathbf{W} | \Psi_{\text{ref}} \rangle &= \langle \Phi_j | \mathbf{H} | \Psi_{\text{ref}} \rangle - \langle \Phi_j | \mathbf{H}_0 | \Psi_{\text{ref}} \rangle \\
&= \epsilon_{\text{ref}} \langle \Phi_j | \Psi_{\text{ref}} \rangle - \epsilon_{\text{ref}} \langle \Phi_j | \Psi_{\text{ref}} \rangle \\
&= 0
\end{aligned} \tag{C.15}$$

holds for all $|\Phi_j\rangle \in \mathcal{M}_{\text{ref}}$. Here, we have used that matrix elements of \mathbf{H} between arbitrary states of \mathcal{M}_{ref} are identical to the corresponding matrix elements of the unperturbed Hamiltonian \mathbf{H}_0 . By taking into account the coefficients of second order in λ of (C.9) and proceeding analogously, we obtain the second-order energy correction

$$E^{(2)} = \langle \Psi_{\text{ref}} | \mathbf{W} | \Psi^{(1)} \rangle. \tag{C.16}$$

For the computation of $E^{(2)}$, we need to know the first-order correction $|\Psi^{(1)}\rangle$ for the eigenstate. We can expand $|\Psi^{(1)}\rangle$ in terms of the basis states of the full model space:

$$|\Psi^{(1)}\rangle = \sum_{j \in \mathcal{M}_{\text{full}}} |\Phi_j\rangle \langle \Phi_j | \Psi^{(1)} \rangle. \tag{C.17}$$

The coefficient $\langle \Phi_j | \Psi^{(1)} \rangle$ can be determined by multiplying (C.10) by $\langle \Phi_j |$:

$$\langle \Phi_j | \mathbf{H}_0 | \Psi^{(1)} \rangle + \langle \Phi_j | \mathbf{W} | \Psi_{\text{ref}} \rangle = \epsilon_{\text{ref}} \langle \Phi_j | \Psi^{(1)} \rangle. \tag{C.18}$$

In the following, we consider basis states $|\Phi_j\rangle$ inside and outside the reference space separately:

- $|\Phi_j\rangle \in \mathcal{M}_{\text{ref}}$:

We show that the first term of (C.18) vanishes by inserting the explicit form of the unperturbed Hamiltonian (C.4):

$$\langle \Phi_j | \mathbf{H}_0 | \Psi^{(1)} \rangle = \epsilon_{\text{ref}} \langle \Phi_j | \Psi_{\text{ref}} \rangle \langle \Psi_{\text{ref}} | \Psi^{(1)} \rangle + \sum_{i \notin \mathcal{M}_{\text{ref}}} \epsilon_i \langle \Phi_j | \Phi_i \rangle \langle \Phi_i | \Psi^{(1)} \rangle = 0. \tag{C.19}$$

We have used the intermediate normalization (C.12) and the fact that basis states of orthogonal spaces do not overlap. The second term of (C.18) also vanishes because of (C.15), and, therefore, we find

$$\langle \Phi_j | \Psi^{(1)} \rangle = 0 \quad \forall |\Phi_j\rangle \in \mathcal{M}_{\text{ref}}. \tag{C.20}$$

Hence, basis states of the reference space do not contribute to the basis expansion of the first-order correction to the eigenstate.

- $|\Phi_j\rangle \notin \mathcal{M}_{\text{ref}}$:

The first term of (C.18) yields

$$\begin{aligned}
\langle \Phi_j | \mathbf{H}_0 | \Psi^{(1)} \rangle &= \epsilon_{\text{ref}} \langle \Phi_j | \Psi_{\text{ref}} \rangle \langle \Psi_{\text{ref}} | \Psi^{(1)} \rangle + \sum_{i \notin \mathcal{M}_{\text{ref}}} \epsilon_i \langle \Phi_j | \Phi_i \rangle \langle \Phi_i | \Psi^{(1)} \rangle \\
&= \sum_{i \notin \mathcal{M}_{\text{ref}}} \epsilon_i \langle \Phi_j | \Phi_i \rangle \langle \Phi_i | \Psi^{(1)} \rangle \\
&= \epsilon_j \langle \Phi_j | \Psi^{(1)} \rangle,
\end{aligned} \tag{C.21}$$

and, thus, (C.18) reduces to

$$\epsilon_j \langle \Phi_j | \Psi^{(1)} \rangle + \langle \Phi_j | \mathbf{W} | \Psi_{\text{ref}} \rangle = \epsilon_{\text{ref}} \langle \Phi_j | \Psi^{(1)} \rangle. \quad (\text{C.22})$$

We rewrite this relation and obtain the coefficient $\langle \Phi_j | \Psi^{(1)} \rangle$ for basis states $|\Phi_j\rangle$ outside the reference space:

$$\langle \Phi_j | \Psi^{(1)} \rangle = -\frac{\langle \Phi_j | \mathbf{W} | \Psi_{\text{ref}} \rangle}{\epsilon_j - \epsilon_{\text{ref}}} \quad \forall |\Phi_j\rangle \notin \mathcal{M}_{\text{ref}}. \quad (\text{C.23})$$

In summary, the first-order correction to the state is then given by

$$\begin{aligned} |\Psi^{(1)}\rangle &= \sum_{j \notin \mathcal{M}_{\text{ref}}} -\frac{\langle \Phi_j | \mathbf{W} | \Psi_{\text{ref}} \rangle}{\epsilon_j - \epsilon_{\text{ref}}} |\Phi_j\rangle \\ &= \sum_{j \notin \mathcal{M}_{\text{ref}}} -\frac{\langle \Phi_j | \mathbf{H} | \Psi_{\text{ref}} \rangle}{\epsilon_j - \epsilon_{\text{ref}}} |\Phi_j\rangle, \end{aligned} \quad (\text{C.24})$$

where we have exploited that matrix elements of the unperturbed Hamiltonian between $|\Psi_{\text{ref}}\rangle$ and basis states outside the reference space vanish by construction. Inserting the basis expansion of $|\Psi^{(1)}\rangle$ into (C.16), we obtain

$$\begin{aligned} E^{(2)} &= -\sum_{j \notin \mathcal{M}_{\text{ref}}} \frac{|\langle \Phi_j | \mathbf{W} | \Psi_{\text{ref}} \rangle|^2}{\epsilon_j - \epsilon_{\text{ref}}} \\ &= -\sum_{j \notin \mathcal{M}_{\text{ref}}} \frac{|\langle \Phi_j | \mathbf{H} | \Psi_{\text{ref}} \rangle|^2}{\epsilon_j - \epsilon_{\text{ref}}}. \end{aligned} \quad (\text{C.25})$$

D. Transition Density

Transition densities $\langle \Psi_0 | \mathbf{a}_{\xi}^{\dagger} \mathbf{a}_{\xi'} | \Psi_f \rangle$ characterize the relationship between two nuclear eigenstates $|\Psi_0\rangle$ and $|\Psi_f\rangle$. Here, ξ and ξ' denote the quantum numbers of a single-particle state of a given reference basis, e.g., the ls -coupled HO or HF basis. Their calculation is straightforward; however, their interpretation requires to go to a representation in coordinate space.

We restrict the following discussion to cases where the state $|\Psi_0\rangle$ has quantum numbers $J_i = 0, M_i = 0$, and we typically choose this state to be the ground state of the system. The radial transition density is the function $\rho_{0f}^{m_s, \tau}(r)$ defined by

$$\begin{aligned} \rho_{0f}^{m_s, \tau}(\vec{r}) &= \rho_{0f}^{m_s, \tau}(r) Y_{JM}(\Omega) \\ &= \langle \Psi_0 | \mathbf{\Psi}_{m_s, \tau}^{\dagger}(\vec{r}) \mathbf{\Psi}_{m_s, \tau}(\vec{r}) | \Psi_f \rangle. \end{aligned} \quad (\text{D.1})$$

Note that the constraint regarding the quantum numbers of the initial state implies that the spherical harmonics have rank $J = J_f$ and projection $M = M_f$ according to the quantum numbers of the final state. The operator $\mathbf{\Psi}_{m_s, \tau}^{\dagger}(\vec{r}) \mathbf{\Psi}_{m_s, \tau}(\vec{r})$ is the nucleon density operator for spin $s = 1/2$ with projection m_s and isospin $t = 1/2$ with projection τ evaluated at the point \vec{r} . Since nucleons always carry the quantum numbers $s = 1/2$ and $t = 1/2$, we neglect them in our notation for brevity. Furthermore, we do not discriminate between the two spin projections, i.e., we sum over m_s , but we keep the isospin projection as degree of freedom. In this way, we can calculate proton and neutron transition densities separately.

To derive an expression for the radial transition density, we project (D.1) onto the spherical component:

$$\rho_{0f}^{\tau}(r) = \sum_{m_s} \langle \Psi_0 | \int d\Omega Y_{JM}^*(\Omega) \mathbf{\Psi}_{m_s, \tau}^{\dagger}(\vec{r}) \mathbf{\Psi}_{m_s, \tau}(\vec{r}) | \Psi_f \rangle. \quad (\text{D.2})$$

In a next step, we write the field operators $\mathbf{\Psi}_{m_s, \tau}^{\dagger}(\vec{r})$ and $\mathbf{\Psi}_{m_s, \tau}(\vec{r})$ in terms of creators and annihilators of a general ls -coupled basis:

$$\mathbf{\Psi}_{m_s, \tau}^{\dagger}(\vec{r}) = \sum_{nlm_l j m} R_{nl}(r) Y_{lm_l}^*(\Omega) \begin{pmatrix} l & \frac{1}{2} & j \\ m_l & m_s & m \end{pmatrix} \mathbf{a}_{nljm\tau}^{\dagger} \quad (\text{D.3a})$$

$$\mathbf{\Psi}_{m_s, \tau}(\vec{r}) = \sum_{nlm_l j m} R_{nl}(r) Y_{lm_l}(\Omega) \begin{pmatrix} l & \frac{1}{2} & j \\ m_l & m_s & m \end{pmatrix} \mathbf{a}_{nljm\tau}. \quad (\text{D.3b})$$

Here, we have used that the radial functions $R_{nl}(r)$ are real.

D. Transition Density

We insert the field operators into (D.2) and rewrite the complex conjugate of the spherical harmonics using $Y_{lm}^*(\Omega) = (-1)^m Y_{l-m}(\Omega)$:

$$\begin{aligned}
\rho_{0f}^\tau(r) &= \sum_{m_s} \sum_{nlm_j m} \sum_{n'l'm'_j m'} \int d\Omega Y_{JM}^*(\Omega) R_{nl}(r) Y_{lm_l}^*(\Omega) \begin{pmatrix} l & \frac{1}{2} & j \\ m_l & m_s & m \end{pmatrix} \\
&\quad \times R_{n'l'}(r) Y_{l'm'_l}(\Omega) \begin{pmatrix} l' & \frac{1}{2} & j' \\ m'_l & m_s & m' \end{pmatrix} \langle \Psi_0 | \mathbf{a}_{nljm\tau}^\dagger \mathbf{a}_{n'l'j'm'\tau} | \Psi_f \rangle \\
&= \sum_{m_s} \sum_{nlm_j m} \sum_{n'l'm'_j m'} \int d\Omega (-1)^{M+m_l} Y_{J-M}(\Omega) Y_{l-m_l}(\Omega) Y_{l'm'_l}(\Omega) \\
&\quad \times R_{nl}(r) R_{n'l'}(r) \begin{pmatrix} l & \frac{1}{2} & j \\ m_l & m_s & m \end{pmatrix} \begin{pmatrix} l' & \frac{1}{2} & j' \\ m'_l & m_s & m' \end{pmatrix} \langle \Psi_0 | \mathbf{a}_{nljm\tau}^\dagger \mathbf{a}_{n'l'j'm'\tau} | \Psi_f \rangle. \tag{D.4}
\end{aligned}$$

We carry out the integration over the full solid angle and obtain:

$$\begin{aligned}
\rho_{0f}^\tau(r) &= \frac{\hat{j}\hat{l}'}{\sqrt{4\pi}} \sum_{m_s} \sum_{nlm_j m} \sum_{n'l'm'_j m'} (-1)^{M+m_l} \begin{pmatrix} J & l & l' \\ 0 & 0 & 0 \end{pmatrix} \begin{pmatrix} J & l & l' \\ -M & -m_l & m'_l \end{pmatrix} \\
&\quad \times R_{nl}(r) R_{n'l'}(r) \begin{pmatrix} l & \frac{1}{2} & j \\ m_l & m_s & m \end{pmatrix} \begin{pmatrix} l' & \frac{1}{2} & j' \\ m'_l & m_s & m' \end{pmatrix} \langle \Psi_0 | \mathbf{a}_{nljm\tau}^\dagger \mathbf{a}_{n'l'j'm'\tau} | \Psi_f \rangle. \tag{D.5}
\end{aligned}$$

This expression can be evaluated using the radial wave functions and the transition-density matrix elements in the underlying single-particle basis.

The quantity $\rho_{0f}^\tau(r)$ can be used to decide whether a transition is of mainly isoscalar or isovector character. In an ideal case of a purely isoscalar transition, we expect that both, the proton and neutron transition densities, scale in the same way and have the same sign. Contrary, a purely isovector transition is expected to give proton and neutron transition densities that scale with the number of protons and neutrons, respectively, and have opposite sign [Roc+12]. Since isospin is only an approximate symmetry, transition densities between two eigenstates typically exhibit a mixture of isoscalarity and isovectoriality.

Analogously to the definition of isospin-decomposed electromagnetic transition operators, we define isoscalar and isovector transition densities via:

$$\rho_{0f}^{\text{IS}}(r) = \frac{1}{2} \left(\rho_{0f}^\pi(r) + \rho_{0f}^\nu(r) \right), \tag{D.6a}$$

$$\rho_{0f}^{\text{IV}}(r) = \frac{1}{2} \left(\rho_{0f}^\pi(r) - \rho_{0f}^\nu(r) \right). \tag{D.6b}$$

We note that a direct connection exists between the transition densities and the transition matrix elements. For example, for electric multipole transitions, the following relation holds:

$$\langle \Psi_0 | \mathcal{Q}_{\lambda\mu} | \Psi_f \rangle = \sum_\tau \int dr r^2 r^\lambda \rho_{0f}^\tau(r). \tag{D.7}$$

We recall that for the monopole transition, the exponent of the radial coordinate is chosen $\lambda = 2$.

Bibliography

- [Ahr+75] J. Ahrens et al. "Total nuclear photon absorption cross sections for some light elements". In: *Nucl. Phys. A* 251 (1975), p. 479. DOI: 10.1016/0375-9474(75)90543-6.
- [And+08] E. Anderson et al. "Block diagonalization using similarity renormalization group flow equations". In: *Phys. Rev. C* 77 (2008), p. 037001. DOI: 10.1103/PhysRevC.77.037001.
- [Ark+80] Y. M. Arkatov et al. "Experimental test of the sum rules for 4He photodisintegration." In: *Sov. J. Nucl. Phys.* 31 (1980), p. 726.
- [Aum17] T. Aumann. private communication. 2017.
- [Bac+02] S. Bacca et al. "Microscopic Calculation of Six-Body Inelastic Reactions with Complete Final State Interaction: Photoabsorption of 6He and 6Li". In: *Phys. Rev. Lett.* 89 (2002), p. 052502. DOI: 10.1103/PhysRevLett.89.052502.
- [Bac+04] S. Bacca et al. "Effect of P-wave interaction in 6He and 6Li photoabsorption". In: *Phys. Rev. C* 69 (2004), p. 057001. DOI: 10.1103/PhysRevC.69.057001.
- [Bac+13] S. Bacca et al. "First Principles Description of the Giant Dipole Resonance in 16O". In: *Phys. Rev. Lett.* 111 (2013), p. 122502. DOI: 10.1103/PhysRevLett.111.122502.
- [Bac+14] S. Bacca et al. "Giant and pigmy dipole resonances in 4He, 16,22O, and 40Ca from chiral nucleon-nucleon interactions". In: *Phys. Rev. C* 90 (2014), p. 064619. DOI: 10.1103/PhysRevC.90.064619.
- [Bar+01] N. Barnea et al. "Total 4He photoabsorption cross section reexamined: Correlated versus effective interaction hyperspherical harmonics". In: *Phys. Rev. C* 63 (2001), p. 057002. DOI: 10.1103/PhysRevC.63.057002.
- [Bar+16] A. Baroni et al. "Nuclear axial currents in chiral effective field theory". In: *Phys. Rev. C* 93 (2016), p. 015501. DOI: 10.1103/PhysRevC.93.015501.
- [Bea+13] S. R. Beane et al. "Light nuclei and hypernuclei from quantum chromodynamics in the limit of SU(3) flavor symmetry". In: *Phys. Rev. D* 87 (2013), p. 034506. DOI: 10.1103/PhysRevD.87.034506.
- [Bea+14] S. R. Beane et al. "Magnetic Moments of Light Nuclei from Lattice Quantum Chromodynamics". In: *Phys. Rev. Lett.* 113 (2014), p. 252001. DOI: 10.1103/PhysRevLett.113.252001.
- [Ber+08] V. Bernard et al. "Subleading contributions to the chiral three-nucleon force: Long-range terms". In: *Phys. Rev. C* 77 (2008), p. 064004. DOI: 10.1103/PhysRevC.77.064004.

- [Ber+11] V. Bernard et al. “Subleading contributions to the chiral three-nucleon force. II. Short-range terms and relativistic corrections”. In: *Phys. Rev. C* 84 (2011), p. 054001. DOI: 10.1103/PhysRevC.84.054001.
- [Ber68] T. Berggren. “On the use of resonant states in eigenfunction expansions of scattering and reaction amplitudes”. In: *Nucl. Phys. A* 109 (1968), p. 265. DOI: 10.1016/0375-9474(68)90593-9.
- [BFP07] S. K. Bogner, R. J. Furnstahl, and R. J. Perry. “Similarity renormalization group for nucleon-nucleon interactions”. In: *Phys. Rev. C* 75 (2007), p. 061001. DOI: 10.1103/PhysRevC.75.061001.
- [BFS10] S. Bogner, R. Furnstahl, and A. Schwenk. “From low-momentum interactions to nuclear structure”. In: *Prog. Part. Nucl. Phys.* 65 (2010), p. 94. DOI: 10.1016/j.pnpnp.2010.03.001.
- [Bin+16] S. Binder et al. “Few-nucleon systems with state-of-the-art chiral nucleon-nucleon forces”. In: *Phys. Rev. C* 93 (2016), p. 044002. DOI: 10.1103/PhysRevC.93.044002.
- [Bin+18] S. Binder et al. *Few- and many-nucleon systems with semilocal coordinate-space regularized chiral nucleon-nucleon forces*. 2018. arXiv: 1802.08584.
- [Bir+17] J. Birkhan et al. “Electric Dipole Polarizability of ^{48}Ca and Implications for the Neutron Skin”. In: *Phys. Rev. Lett.* 118 (2017), p. 252501. DOI: 10.1103/PhysRevLett.118.252501.
- [Bjö+80] T. Björnstad et al. “Structure of the levels in the doubly magic nucleus ^{132}Sn ”. In: *Phys. Lett. B* 91 (1980), p. 35. DOI: 10.1016/0370-2693(80)90656-5.
- [BNQ13] S. Baroni, P. Navrátil, and S. Quaglioni. “Unified ab initio approach to bound and unbound states: No-core shell model with continuum and its application to ^7He ”. In: *Phys. Rev. C* 87 (2013), p. 034326. DOI: 10.1103/PhysRevC.87.034326.
- [BNV13] B. R. Barrett, P. Navrátil, and J. P. Vary. “Ab initio no core shell model”. In: *Prog. Part. Nucl. Phys.* 69 (2013), p. 131. DOI: 10.1016/j.pnpnp.2012.10.003.
- [Bog+14] S. K. Bogner et al. “Nonperturbative Shell-Model Interactions from the In-Medium Similarity Renormalization Group”. In: *Phys. Rev. Lett.* 113 (2014), p. 142501. DOI: 10.1103/PhysRevLett.113.142501.
- [Cal+16] A. Calci et al. “Can Ab Initio Theory Explain the Phenomenon of Parity Inversion in ^{11}Be ?” In: *Phys. Rev. Lett.* 117 (2016), p. 242501. DOI: 10.1103/PhysRevLett.117.242501.
- [Car+16] B. D. Carlsson et al. “Uncertainty Analysis and Order-by-Order Optimization of Chiral Nuclear Interactions”. In: *Phys. Rev. X* 6 (2016), p. 011019. DOI: 10.1103/PhysRevX.6.011019.
- [Cau+05] E. Caurier et al. “The shell model as a unified view of nuclear structure”. In: *Rev. Mod. Phys.* 77 (2005), p. 427. DOI: 10.1103/RevModPhys.77.427.
- [Cau+94] E. Caurier et al. “Full pf shell model study of $A=48$ nuclei”. In: *Phys. Rev. C* 50 (1994), p. 225. DOI: 10.1103/PhysRevC.50.225.

- [Cau04] E. Caurier. *Shell-model code ANTOINE*. IRES, Strasbourg. 1989-2004.
- [Cha+94] J. Chambers et al. “Pygmy dipole resonances in the calcium isotopes”. In: *Phys. Rev. C* 50 (1994), p. 2671. DOI: 10.1103/PhysRevC.50.R2671.
- [Cha32] J. Chadwick. “The Existence of a Neutron”. In: *Proc. Roy. Soc. A* 136 (1932), p. 692. DOI: 10.1098/rspa.1932.0112.
- [CN99] E. Caurier and F. Nowacki. “Present status of shell model techniques”. In: *Acta Phys. Pol. B* 30 (1999), p. 705. ISSN: 05874254.
- [Con+17] C. Constantinou et al. “Natural orbital description of the halo nucleus 6He ”. In: *Nucl. Sci. Tech.* 28 (2017), p. 179. DOI: 10.1007/s41365-017-0332-6.
- [Con30] E. U. Condon. “The Theory of Complex Spectra”. In: *Phys. Rev.* 36 (1930), p. 1121. DOI: 10.1103/PhysRev.36.1121.
- [Coo+12] S. A. Coon et al. “Convergence properties of ab initio calculations of light nuclei in a harmonic oscillator basis”. In: *Phys. Rev. C* 86 (2012), p. 054002. DOI: 10.1103/PhysRevC.86.054002.
- [Cor+09] L. Coraggio et al. “Shell-model calculations and realistic effective interactions”. In: *Prog. Part. Nucl. Phys.* 62 (2009), p. 135. DOI: 10.1016/j.ppnp.2008.06.001.
- [Cor+14] L. Coraggio et al. “From Kuo–Brown to today’s realistic shell-model calculations”. In: *Nucl. Phys. A* 928 (2014), p. 43. DOI: 10.1016/j.nuclphysa.2014.03.018.
- [CPZ90] E. Caurier, A. Poves, and A. Zuker. “A full description of the $2\nu\beta\beta$ decay of 48Ca ”. In: *Phys. Lett. B* 252 (1990), p. 13. DOI: 10.1016/0370-2693(90)91071-I.
- [CPZ95] E. Caurier, A. Poves, and A. P. Zuker. “Missing and Quenched Gamow-Teller Strength”. In: *Phys. Rev. Lett.* 74 (1995), p. 1517. DOI: 10.1103/PhysRevLett.74.1517.
- [CW81] J. Cullum and R. A. Willoughby. “Computing eigenvalues of very large symmetric matrices—An implementation of a Lanczos algorithm with no reorthogonalization”. In: *J. Comput. Phys.* 44 (1981), p. 329. DOI: 10.1016/0021-9991(81)90056-5.
- [Dar+10] I. G. Darby et al. “Orbital Dependent Nucleonic Pairing in the Lightest Known Isotopes of Tin”. In: *Phys. Rev. Lett.* 105 (2010), p. 162502. DOI: 10.1103/PhysRevLett.105.162502.
- [Dik+15] E. Dikmen et al. “Ab initio effective interactions for sd-shell valence nucleons”. In: *Phys. Rev. C* 91 (2015), p. 064301. DOI: 10.1103/PhysRevC.91.064301.
- [DON14] N. M. Dicaire, C. Omand, and P. Navrátil. “Alternative similarity renormalization group generators in nuclear structure calculations”. In: *Phys. Rev. C* 90 (2014), p. 034302. DOI: 10.1103/PhysRevC.90.034302.
- [Dro+90] S. Drożdż et al. “The nuclear response within extended RPA theories”. In: *Phys. Rep.* 197 (1990), p. 1. DOI: 10.1016/0370-1573(90)90084-F.

- [Edm64] A. R. Edmonds. *Drehimpulse in der Quantenmechanik*. Princeton University Press, 1964.
- [EG76] J. M. Eisenberg and W. Greiner. *Nuclear Theory 2: Excitation Mechanisms of the Nucleus*. North-Holland Publishing Company, 1976.
- [EHM09] E. Epelbaum, H.-W. Hammer, and U.-G. Meißner. “Modern theory of nuclear forces”. In: *Rev. Mod. Phys.* 81 (2009), p. 1773. DOI: 10.1103/RevModPhys.81.1773.
- [EHV92] J. Engel, W. C. Haxton, and P. Vogel. “Effective summation over intermediate states in double-beta decay”. In: *Phys. Rev. C* 46 (1992), p. 2153. DOI: 10.1103/PhysRevC.46.R2153.
- [EKM15a] E. Epelbaum, H. Krebs, and U. G. Meißner. “Improved chiral nucleon-nucleon potential up to next-to-next-to-next-to-leading order”. In: *Eur. Phys. J. A* 51 (2015), p. 53. DOI: 10.1140/epja/i2015-15053-8.
- [EKM15b] E. Epelbaum, H. Krebs, and U.-G. Meißner. “Precision Nucleon-Nucleon Potential at Fifth Order in the Chiral Expansion”. In: *Phys. Rev. Lett.* 115 (2015), p. 122301. DOI: 10.1103/PhysRevLett.115.122301.
- [Eks+15] A. Ekström et al. “Accurate nuclear radii and binding energies from a chiral interaction”. In: *Phys. Rev. C* 91 (2015), p. 051301. DOI: 10.1103/PhysRevC.91.051301.
- [EM03] D. R. Entem and R. Machleidt. “Accurate charge-dependent nucleon-nucleon potential at fourth order of chiral perturbation theory”. In: *Phys. Rev. C* 68 (2003), p. 041001. DOI: 10.1103/PhysRevC.68.041001.
- [EMN10] G. Ecker, P. Masjuan, and H. Neufeld. “Chiral extrapolation and determination of low-energy constants from lattice data”. In: *Phys. Lett. B* 692 (2010), p. 184. DOI: 10.1016/j.physletb.2010.07.037.
- [EMN17] D. R. Entem, R. Machleidt, and Y. Nosyk. “High-quality two-nucleon potentials up to fifth order of the chiral expansion”. In: *Phys. Rev. C* 96 (2017), p. 024004. DOI: 10.1103/PhysRevC.96.024004.
- [Epe+02] E. Epelbaum et al. “Three-nucleon forces from chiral effective field theory”. In: *Phys. Rev. C* 66 (2002), p. 064001. DOI: 10.1103/PhysRevC.66.064001.
- [Epe07] E. Epelbaum. “Four-nucleon force using the method of unitary transformation”. In: *Eur. Phys. J. A* 34 (2007), p. 197. DOI: 10.1140/epja/i2007-10496-0.
- [Fer50] E. Fermi. *Nuclear physics*. University of Chicago Press, 1950.
- [FGG13] T. Faestermann, M. Górska, and H. Grawe. “The structure of ^{100}Sn and neighbouring nuclei”. In: *Prog. Part. Nucl. Phys.* 69 (2013), p. 85. DOI: 10.1016/j.pnpnp.2012.10.002.
- [FHP12] R. J. Furnstahl, G. Hagen, and T. Papenbrock. “Corrections to nuclear energies and radii in finite oscillator spaces”. In: *Phys. Rev. C* 86 (2012), p. 031301. DOI: 10.1103/PhysRevC.86.031301.

- [Gam+12] D. Gambacurta et al. "Second random-phase approximation with the Gogny force: First applications". In: *Phys. Rev. C* 86 (2012), p. 021304. DOI: 10.1103/PhysRevC.86.021304.
- [Gam+16] D. Gambacurta et al. "Nuclear excitations as coupled one and two random-phase-approximation modes". In: *Phys. Rev. C* 93 (2016), p. 024309. DOI: 10.1103/PhysRevC.93.024309.
- [Gar+16] R. F. Garcia Ruiz et al. *Laser Spectroscopy of neutron-deficient Sn isotopes*. CERN-INTC-2016-006; INTC-P-458. 2016.
- [Gaz+06] D. Gazit et al. "Photoabsorption on 4He with a Realistic Nuclear Force". In: *Phys. Rev. Lett.* 96 (2006), p. 112301. DOI: 10.1103/PhysRevLett.96.112301.
- [GCR16] E. Gebrerufael, A. Calci, and R. Roth. "Open-shell nuclei and excited states from multireference normal-ordered Hamiltonians". In: *Phys. Rev. C* 93 (2016), p. 031301. DOI: 10.1103/PhysRevC.93.031301.
- [GDJ00] V. G. Gueorguiev, J. P. Draayer, and C. W. Johnson. "SU(3) symmetry breaking in lower fp-shell nuclei". In: *Phys. Rev. C* 63 (2000), p. 014318. DOI: 10.1103/PhysRevC.63.014318.
- [Geb+17] E. Gebrerufael et al. "Ab Initio Description of Open-Shell Nuclei: Merging No-Core Shell Model and In-Medium Similarity Renormalization Group". In: *Phys. Rev. Lett.* 118 (2017), p. 152503. DOI: 10.1103/PhysRevLett.118.152503.
- [Geb17] E. Gebrerufael. "In-Medium No-Core Shell Model for Ab Initio Nuclear Structure Calculations". PhD thesis. Technische Universität Darmstadt, 2017.
- [GG16] D. Gambacurta and M. Grasso. "Second RPA calculations with the Skyrme and Gogny interactions". In: *Eur. Phys. J. A* 52 (2016), p. 198. DOI: 10.1140/epja/i2016-16198-6.
- [GGC10] D. Gambacurta, M. Grasso, and F. Catara. "Collective nuclear excitations with Skyrme-second random-phase approximation". In: *Phys. Rev. C* 81 (2010), p. 054312. DOI: 10.1103/PhysRevC.81.054312.
- [GGC11a] D. Gambacurta, M. Grasso, and F. Catara. "Low-lying dipole response in the stable $40,48\text{Ca}$ nuclei with the second random-phase approximation". In: *Phys. Rev. C* 84 (2011), p. 034301. DOI: 10.1103/PhysRevC.84.034301.
- [GGC11b] D. Gambacurta, M. Grasso, and F. Catara. "Residual interaction in second random-phase approximation with density-dependent forces: rearrangement terms". In: *J. Phys. G* 38 (2011), p. 035103. DOI: 10.1088/0954-3899/38/3/035103.
- [GGE15] D. Gambacurta, M. Grasso, and J. Engel. "Subtraction method in the second random-phase approximation: First applications with a Skyrme energy functional". In: *Phys. Rev. C* 92 (2015), p. 034303. DOI: 10.1103/PhysRevC.92.034303.

- [GGV18] D. Gambacurta, M. Grasso, and O. Vasseur. “Electric dipole strength and dipole polarizability in ^{48}Ca within a fully self-consistent second random-phase approximation”. In: *Phys. Lett. B* 777 (2018), p. 163. DOI: 10.1016/j.physletb.2017.12.026.
- [GL74] D. Gloeckner and R. Lawson. “Spurious center-of-mass motion”. In: *Phys. Lett. B* 53 (1974), p. 313. DOI: 10.1016/0370-2693(74)90390-6.
- [GQN09] D. Gazit, S. Quaglioni, and P. Navrátil. “Three-Nucleon Low-Energy Constants from the Consistency of Interactions and Currents in Chiral Effective Field Theory”. In: *Phys. Rev. Lett.* 103 (2009), p. 102502. DOI: 10.1103/PhysRevLett.103.102502.
- [Hag+16] G. Hagen et al. “Neutron and weak-charge distributions of the ^{48}Ca nucleus”. In: *Nat. Phys.* 12 (2016), p. 186. DOI: 10.1038/nphys3529.
- [HBZ03] M. Horoi, B. A. Brown, and V. Zelevinsky. “Exponential convergence method: Nonyrast states, occupation numbers, and a shell-model description of the superdeformed band in ^{56}Ni ”. In: *Phys. Rev. C* 67 (2003), p. 034303. DOI: 10.1103/PhysRevC.67.034303.
- [Heb+11] K. Hebeler et al. “Improved nuclear matter calculations from chiral low-momentum interactions”. In: *Phys. Rev. C* 83 (2011), p. 031301. DOI: 10.1103/PhysRevC.83.031301.
- [Her+13] H. Hergert et al. “In-medium similarity renormalization group with chiral two- plus three-nucleon interactions”. In: *Phys. Rev. C* 87 (2013), p. 034307. DOI: 10.1103/PhysRevC.87.034307.
- [Her+14] H. Hergert et al. “Ab initio multireference in-medium similarity renormalization group calculations of even calcium and nickel isotopes”. In: *Phys. Rev. C* 90 (2014), p. 041302. DOI: 10.1103/PhysRevC.90.041302.
- [Her+16] H. Hergert et al. “The In-Medium Similarity Renormalization Group: A novel ab initio method for nuclei”. In: *Phys. Rep.* 621 (2016), p. 165. DOI: 10.1016/j.physrep.2015.12.007.
- [Her17] H. Hergert. “In-medium similarity renormalization group for closed and open-shell nuclei”. In: *Phys. Scr.* 92 (2017), p. 023002. DOI: 10.1088/1402-4896/92/2/023002.
- [Hin+12] C. B. Hinke et al. “Superallowed Gamow–Teller decay of the doubly magic nucleus ^{100}Sn ”. In: *Nature* 486 (2012), p. 341. DOI: 10.1038/nature11116.
- [HJP16] G. Hagen, G. R. Jansen, and T. Papenbrock. “Structure of ^{78}Ni from First-Principles Computations”. In: *Phys. Rev. Lett.* 117 (2016), p. 172501. DOI: 10.1103/PhysRevLett.117.172501.
- [HJS49] O. Haxel, J. H. D. Jensen, and H. E. Suess. “On the “Magic Numbers” in Nuclear Structure”. In: *Phys. Rev.* 75 (1949), p. 1766. DOI: 10.1103/PhysRev.75.1766.2.

- [HKO95] M. Hjorth-Jensen, T. T. Kuo, and E. Osnes. “Realistic effective interactions for nuclear systems”. In: *Phys. Rep.* 261 (1995), p. 125. DOI: 10.1016/0370-1573(95)00012-6.
- [HNZ05] W. C. Haxton, K. M. Nollett, and K. M. Zurek. “Piecewise moments method: Generalized Lanczos technique for nuclear response surfaces”. In: *Phys. Rev. C* 72 (2005), p. 065501. DOI: 10.1103/PhysRevC.72.065501.
- [Hon+] M. Honma et al. unpublished.
- [Hon+05] M. Honma et al. “Shell-model description of neutron-rich pf-shell nuclei with a new effective interaction GXPF 1”. In: *Eur. Phys. J. A* 25 (2005), p. 499. DOI: 10.1140/epjad/i2005-06-032-2.
- [Hor+06] M. Horoi et al. “Shell model analysis of the ^{56}Ni spectrum in the full pf model space”. In: *Phys. Rev. C* 73 (2006), p. 061305. DOI: 10.1103/PhysRevC.73.061305.
- [HR07] H. Hergert and R. Roth. “Unitary correlation operator method from a similarity renormalization group perspective”. In: *Phys. Rev. C* 75 (2007), p. 051001. DOI: 10.1103/PhysRevC.75.051001.
- [HU30] E. A. Hylleraas and B. Undheim. “Numerische Berechnung der 2S-Terme von Ortho- und Par-Helium”. In: *Z. Phys.* 65 (1930), p. 759. DOI: 10.1007/BF01397263.
- [HW01] M. N. Harakeh and A. van der Woude. “Giant Resonances: Fundamental High-Frequency Modes of Nuclear Excitation”. In: *Oxford Univ. Press* (2001).
- [Jan+14] G. R. Jansen et al. “Ab Initio Coupled-Cluster Effective Interactions for the Shell Model: Application to Neutron-Rich Oxygen and Carbon Isotopes”. In: *Phys. Rev. Lett.* 113 (2014), p. 142502. DOI: 10.1103/PhysRevLett.113.142502.
- [Jan+16] G. R. Jansen et al. “Open sd-shell nuclei from first principles”. In: *Phys. Rev. C* 94 (2016), p. 011301. DOI: 10.1103/PhysRevC.94.011301.
- [JOK13] C. W. Johnson, W. E. Ormand, and P. G. Krastev. “Factorization in large-scale many-body calculations”. In: *Comp. Phys. Comm.* 184 (2013), p. 2761. DOI: 10.1016/j.cpc.2013.07.022.
- [Jon+10] K. L. Jones et al. “The magic nature of ^{132}Sn explored through the single-particle states of ^{133}Sn ”. In: *Nature* 465 (2010), p. 454. DOI: 10.1038/nature09048.
- [KB66] T. Kuo and G. Brown. “Structure of finite nuclei and the free nucleon-nucleon interaction”. In: *Nucl. Phys.* 85 (1966), p. 40. DOI: 10.1016/0029-5582(66)90131-3.
- [KEM17] H. Krebs, E. Epelbaum, and U.-G. Meißner. “Nuclear axial current operators to fourth order in chiral effective field theory”. In: *Ann. Phys. (NY)* 378 (2017), p. 317. DOI: 10.1016/j.aop.2017.01.021.
- [Krü+13] T. Krüger et al. “Neutron matter from chiral effective field theory interactions”. In: *Phys. Rev. C* 88 (2013), p. 025802. DOI: 10.1103/PhysRevC.88.025802.

- [Lac+00] D. Lacroix et al. "Multiple scales in the fine structure of the isoscalar giant quadrupole resonance in ^{208}Pb ". In: *Phys. Lett. B* 479 (2000), p. 15. DOI: 10.1016/S0370-2693(00)00301-4.
- [Lan50] C. Lanczos. "An iteration method for the solution of the eigenvalue problem of linear differential and integral operators". In: *J. Res. Natl. Bur. Stand.* 45 (1950), p. 255. DOI: 10.6028/jres.045.026.
- [LCY01] Y.-W. Lui, H. L. Clark, and D. H. Youngblood. "Giant resonances in ^{16}O ". In: *Phys. Rev. C* 64 (2001), p. 064308. DOI: 10.1103/PhysRevC.64.064308.
- [Leg+15] Ö. Legeza et al. "Advanced density matrix renormalization group method for nuclear structure calculations". In: *Phys. Rev. C* 92 (2015), p. 051303. DOI: 10.1103/PhysRevC.92.051303.
- [Lei+01] A. Leistenschneider et al. "Photoneutron Cross Sections for Unstable Neutron-Rich Oxygen Isotopes". In: *Phys. Rev. Lett.* 86 (2001), p. 5442. DOI: 10.1103/PhysRevLett.86.5442.
- [Len+10] S. M. Lenzi et al. "Island of inversion around ^{64}Cr ". In: *Phys. Rev. C* 82 (2010), p. 054301. DOI: 10.1103/PhysRevC.82.054301.
- [Lew+94] M. Lewitowicz et al. "Identification of the doubly-magic nucleus ^{100}Sn in the reaction $^{112}\text{Sn}+\text{natNi}$ at 63 MeV/nucleon". In: *Phys. Lett. B* 332 (1994), p. 20. DOI: 10.1016/0370-2693(94)90852-4.
- [Lid+06] S. N. Liddick et al. "Discovery of ^{109}Xe and ^{105}Te Superallowed alpha Decay near Doubly Magic ^{100}Sn ". In: *Phys. Rev. Lett.* 97 (2006), p. 082501. DOI: 10.1103/PhysRevLett.97.082501.
- [Loe+12] H. P. Loens et al. "M1 strength functions from large-scale shell-model calculations and their effect on astrophysical neutron capture cross-sections". In: *Eur. Phys. J. A* 48 (2012), p. 34. DOI: 10.1140/epja/i2012-12034-5.
- [LSY98] R. B. Lehoucq, D. C. Sorensen, and C. Yang. *ARPACK Users' Guide*. Society for Industrial and Applied Mathematics, 1998. ISBN: 978-0-89871-407-4. DOI: 10.1137/1.9780898719628.
- [Mac89] R. Machleidt. "The Meson Theory of Nuclear Forces and Nuclear Structure". In: *Adv. Nucl. Phys.* 19 (1989), p. 189. DOI: 10.1007/978-1-4613-9907-0_2.
- [Mar+14] P. Maris et al. " ^{12}C properties with evolved chiral three-nucleon interactions". In: *Phys. Rev. C* 90 (2014), p. 014314. DOI: 10.1103/PhysRevC.90.014314.
- [May49] M. G. Mayer. "On Closed Shells in Nuclei. II". In: *Phys. Rev.* 75 (1949), p. 1969. DOI: 10.1103/PhysRev.75.1969.
- [ME11] R. Machleidt and D. Entem. "Chiral effective field theory and nuclear forces". In: *Phys. Rep.* 503 (2011), p. 1. DOI: 10.1016/j.physrep.2011.02.001.
- [Meu06] G. Meurant. *The Lanczos and Conjugate Gradient Algorithms*. Society for Industrial and Applied Mathematics, 2006. ISBN: 978-0-89871-616-0. DOI: 10.1137/1.9780898718140.

- [MI03] T. Mizusaki and M. Imada. “Precise estimation of shell model energy by second-order extrapolation method”. In: *Phys. Rev. C* 67 (2003), p. 041301. DOI: 10.1103/PhysRevC.67.041301.
- [Mio+16] M. Miorelli et al. “Electric dipole polarizability from first principles calculations”. In: *Phys. Rev. C* 94 (2016), p. 034317. DOI: 10.1103/PhysRevC.94.034317.
- [Miz04] T. Mizusaki. “Extrapolation method in shell model calculations with a deformed basis”. In: *Phys. Rev. C* 70 (2004), p. 044316. DOI: 10.1103/PhysRevC.70.044316.
- [Mor+13] S. N. More et al. “Universal properties of infrared oscillator basis extrapolations”. In: *Phys. Rev. C* 87 (2013), p. 044326. DOI: 10.1103/PhysRevC.87.044326.
- [Mor+18] T. D. Morris et al. “Structure of the Lightest Tin Isotopes”. In: *Phys. Rev. Lett.* 120 (2018), p. 152503. DOI: 10.1103/PhysRevLett.120.152503.
- [Mos59] M. Moshinsky. “Transformation brackets for harmonic oscillator functions”. In: *Nucl. Phys.* 13 (1959), p. 104. DOI: 10.1016/0029-5582(59)90143-9.
- [Mue+07] P. Mueller et al. “Nuclear Charge Radius of ^8He ”. In: *Phys. Rev. Lett.* 99 (2007), p. 252501. DOI: 10.1103/PhysRevLett.99.252501.
- [Nav+09] P. Navrátil et al. “Recent developments in no-core shell-model calculations”. In: *J. Phys. G* 36 (2009), p. 083101. DOI: 10.1088/0954-3899/36/8/083101.
- [Nav07] P. Navrátil. “Local three-nucleon interaction from chiral effective field theory”. In: *Few-Body Syst.* 41 (2007), p. 117. DOI: 10.1007/s00601-007-0193-3.
- [NBS04] A. Nogga, S. K. Bogner, and A. Schwenk. “Low-momentum interaction in few-nucleon systems”. In: *Phys. Rev. C* 70 (2004), p. 061002. DOI: 10.1103/PhysRevC.70.061002.
- [NKB00] P. Navrátil, G. P. Kamuntavičius, and B. R. Barrett. “Few-nucleon systems in a translationally invariant harmonic oscillator basis”. In: *Phys. Rev. C* 61 (2000), p. 044001. DOI: 10.1103/PhysRevC.61.044001.
- [NNDC] National Nuclear Data Center. Information extracted from the Chart of Nuclides database. URL: <http://www.nndc.bnl.gov/chart/>.
- [NO02] P. Navrátil and W. E. Ormand. “Ab Initio Shell Model Calculations with Three-Body Effective Interactions for p-Shell Nuclei”. In: *Phys. Rev. Lett.* 88 (2002), p. 152502. DOI: 10.1103/PhysRevLett.88.152502.
- [NO03] P. Navrátil and W. E. Ormand. “Ab initio shell model with a genuine three-nucleon force for the p-shell nuclei”. In: *Phys. Rev. C* 68 (2003), p. 034305. DOI: 10.1103/PhysRevC.68.034305.
- [Nog+10] A. Nogga et al. “Four-nucleon force contribution to the binding energy of ^4He ”. In: *EPJ Web Conf.* 3 (2010), p. 05006. DOI: 10.1051/epjconf/20100305006.

- [Now02] F. Nowacki. "Shell model description of correlations in ^{56}Ni and ^{100}Sn ". In: *Nucl. Phys. A* 704 (2002), p. 223. DOI: 10.1016/S0375-9474(02)00782-0.
- [NVB00a] P. Navrátil, J. P. Vary, and B. R. Barrett. "Large-basis ab initio no-core shell model and its application to ^{12}C ". In: *Phys. Rev. C* 62 (2000), p. 054311. DOI: 10.1103/PhysRevC.62.054311.
- [NVB00b] P. Navrátil, J. P. Vary, and B. R. Barrett. "Properties of ^{12}C in the Ab Initio Nuclear Shell Model". In: *Phys. Rev. Lett.* 84 (2000), p. 5728. DOI: 10.1103/PhysRevLett.84.5728.
- [Ots] T. Otsuka. private communication.
- [Ots+01] T. Otsuka et al. "Monte Carlo shell model for atomic nuclei". In: *Prog. Part. Nucl. Phys.* 47 (2001), p. 319. DOI: 10.1016/S0146-6410(01)00157-0.
- [Pai71] C. Paige. "The computation of eigenvalues and eigenvectors of very large sparse matrices." PhD thesis. 1971.
- [Pap+13] G. Papadimitriou et al. "Ab initio no-core Gamow shell model calculations with realistic interactions". In: *Phys. Rev. C* 88 (2013), p. 044318. DOI: 10.1103/PhysRevC.88.044318.
- [Pap14] P. Papakonstantinou. "Second random-phase approximation, Thouless' theorem, and the stability condition reexamined and clarified". In: *Phys. Rev. C* 90 (2014), p. 024305. DOI: 10.1103/PhysRevC.90.024305.
- [Par+17] N. M. Parzuchowski et al. "Ab initio electromagnetic observables with the in-medium similarity renormalization group". In: *Phys. Rev. C* 96 (2017), p. 034324. DOI: 10.1103/PhysRevC.96.034324.
- [Par98] B. N. Parlett. *The Symmetric Eigenvalue Problem*. Society for Industrial and Applied Mathematics, 1998. ISBN: 978-0-89871-402-9. DOI: 10.1137/1.9781611971163.
- [Pas+13] S. Pastore et al. "Quantum Monte Carlo calculations of electromagnetic moments and transitions in $A \leq 9$ nuclei with meson-exchange currents derived from chiral effective field theory". In: *Phys. Rev. C* 87 (2013), p. 035503. DOI: 10.1103/PhysRevC.87.035503.
- [Pie11] J. Piekarewicz. "Pygmy resonances and neutron skins". In: *Phys. Rev. C* 83 (2011), p. 034319. DOI: 10.1103/PhysRevC.83.034319.
- [Pol+14] I. Poltoratska et al. "Fine structure of the isovector giant dipole resonance in ^{208}Pb : Characteristic scales and level densities". In: *Phys. Rev. C* 89 (2014), p. 054322. DOI: 10.1103/PhysRevC.89.054322.
- [PR08] S. Perez-Martin and L. M. Robledo. "Microscopic justification of the equal filling approximation". In: *Phys. Rev. C* 78 (2008), p. 014304. DOI: 10.1103/PhysRevC.78.014304.
- [PR09] P. Papakonstantinou and R. Roth. "Second random phase approximation and renormalized realistic interactions". In: *Phys. Lett. B* 671 (2009), p. 356. DOI: 10.1016/j.physletb.2008.12.037.

- [PR10] P. Papakonstantinou and R. Roth. "Large-scale second random-phase approximation calculations with finite-range interactions". In: *Phys. Rev. C* 81 (2010), p. 024317. DOI: 10.1103/PhysRevC.81.024317.
- [Pro65] J. Da Providência. "Variational approach to the many-body problem". In: *Nucl. Phys.* 61 (1965), p. 87. DOI: 10.1016/0029-5582(65)90937-5.
- [PS79] B. N. Parlett and D. S. Scott. "The Lanczos algorithm with selective orthogonalization". In: *Math. Comput.* 33 (1979), p. 217. DOI: 10.1090/S0025-5718-1979-0514820-3.
- [Pyw+85] R. E. Pywell et al. "Photoneutron cross sections for ^{14}C ". In: *Phys. Rev. C* 32 (1985), p. 384. DOI: 10.1103/PhysRevC.32.384.
- [QN07] S. Quaglioni and P. Navrátil. "The ^4He total photo-absorption cross section with two- plus three-nucleon interactions from chiral effective field theory". In: *Phys. Lett. B* 652 (2007), p. 370. DOI: 10.1016/j.physletb.2007.06.082.
- [Rit09] W. Ritz. "Über eine neue Methode zur Lösung gewisser Variationsprobleme der mathematischen Physik." In: *J. für die reine und Angew. Math.* 135 (1909), p. 1. DOI: 10.1515/crll.1909.135.1.
- [RN07] R. Roth and P. Navrátil. "Ab Initio Study of ^{40}Ca with an Importance-Truncated No-Core Shell Model". In: *Phys. Rev. Lett.* 99 (2007), p. 092501. DOI: 10.1103/PhysRevLett.99.092501.
- [RNF10] R. Roth, T. Neff, and H. Feldmeier. "Nuclear structure in the framework of the Unitary Correlation Operator Method". In: *Prog. Part. Nucl. Phys.* 65 (2010), p. 50. DOI: 10.1016/j.ppnp.2010.02.003.
- [Roc+12] X. Roca-Maza et al. "Low-lying dipole response: Isospin character and collectivity in ^{68}Ni , ^{132}Sn , and ^{208}Pb ". In: *Phys. Rev. C* 85 (2012), p. 024601. DOI: 10.1103/PhysRevC.85.024601.
- [Roc+15] X. Roca-Maza et al. "Neutron skin thickness from the measured electric dipole polarizability in ^{68}Ni , ^{120}Sn , and ^{208}Pb ". In: *Phys. Rev. C* 92 (2015), p. 064304. DOI: 10.1103/PhysRevC.92.064304.
- [Rot+12] R. Roth et al. "Medium-Mass Nuclei with Normal-Ordered Chiral NN+3N Interactions". In: *Phys. Rev. Lett.* 109 (2012), p. 052501. DOI: 10.1103/PhysRevLett.109.052501.
- [Rot+14] R. Roth et al. "Evolved chiral NN+3N Hamiltonians for ab initio nuclear structure calculations". In: *Phys. Rev. C* 90 (2014), p. 024325. DOI: 10.1103/PhysRevC.90.024325.
- [Rot09] R. Roth. "Importance truncation for large-scale configuration interaction approaches". In: *Phys. Rev. C* 79 (2009), p. 064324. DOI: 10.1103/PhysRevC.79.064324.
- [Row10] D. J. Rowe. *Nuclear collective motion: models and theory*. World Scientific, 2010.
- [RS80] P. Ring and P. Schuck. *The nuclear many-body problem*. Springer-Verlag Berlin Heidelberg, 1980.

- [Saa11] Y. Saad. *Numerical Methods for Large Eigenvalue Problems*. Society for Industrial and Applied Mathematics, 2011. ISBN: 978-1-61197-072-2. DOI: 10.1137/1.9781611970739.
- [Sav+08] D. Savran et al. "Fine Structure of the Pygmy Dipole Resonance in ^{136}Xe ". In: *Phys. Rev. Lett.* 100 (2008), p. 232501. DOI: 10.1103/PhysRevLett.100.232501.
- [SAZ13] D. Savran, T. Aumann, and A. Zilges. "Experimental studies of the Pygmy Dipole Resonance". In: *Prog. Part. Nucl. Phys.* 70 (2013), p. 210. DOI: 10.1016/j.pnpnp.2013.02.003.
- [SBR16] C. Stumpf, J. Braun, and R. Roth. "Importance-truncated large-scale shell model". In: *Phys. Rev. C* 93 (2016), p. 021301. DOI: 10.1103/PhysRevC.93.021301.
- [Sch+14] M. D. Schuster et al. "Operator evolution for ab initio theory of light nuclei". In: *Phys. Rev. C* 90 (2014), p. 011301. DOI: 10.1103/PhysRevC.90.011301.
- [Sch+15] M. D. Schuster et al. "Operator evolution for ab initio electric dipole transitions of ^4He ". In: *Phys. Rev. C* 92 (2015), p. 014320. DOI: 10.1103/PhysRevC.92.014320.
- [Sch18] S. Schulz. "Four-Nucleon Forces in Ab Initio Nuclear Structure". PhD thesis. Technische Universität Darmstadt, 2018.
- [She+04] A. Shevchenko et al. "Fine Structure in the Energy Region of the Isoscalar Giant Quadrupole Resonance: Characteristic Scales from a Wavelet Analysis". In: *Phys. Rev. Lett.* 93 (2004), p. 122501. DOI: 10.1103/PhysRevLett.93.122501.
- [She+08] A. Shevchenko et al. "Analysis of fine structure in the nuclear continuum". In: *Phys. Rev. C* 77 (2008), p. 024302. DOI: 10.1103/PhysRevC.77.024302.
- [Shi+05] T. Shima et al. "Simultaneous measurement of the photodisintegration of ^4He in the giant dipole resonance region". In: *Phys. Rev. C* 72 (2005), p. 044004. DOI: 10.1103/PhysRevC.72.044004.
- [Shi+10] N. Shimizu et al. "Novel extrapolation method in the Monte Carlo shell model". In: *Phys. Rev. C* 82 (2010), p. 061305. DOI: 10.1103/PhysRevC.82.061305.
- [Shi+12] N. Shimizu et al. "Variational procedure for nuclear shell-model calculations and energy-variance extrapolation". In: *Phys. Rev. C* 85 (2012), p. 054301. DOI: 10.1103/PhysRevC.85.054301.
- [Sim+17] J. Simonis et al. "Saturation with chiral interactions and consequences for finite nuclei". In: *Phys. Rev. C* 96 (2017), p. 014303. DOI: 10.1103/PhysRevC.96.014303.
- [Sim84] H. D. Simon. "The Lanczos algorithm with partial reorthogonalization". In: *Math. Comput.* 42 (1984), p. 115. DOI: 10.1090/S0025-5718-1984-0725988-X.

- [SIS90] Y. Suzuki, K. Ikeda, and H. Sato. "New Type of Dipole Vibration in Nuclei". In: *Prog. Theo. Phys.* 83 (1990), p. 180. DOI: 10.1143/PTP.83.180.
- [SJ03] I. Stetcu and C. W. Johnson. "Tests of the random phase approximation for transition strengths". In: *Phys. Rev. C* 67 (2003), p. 044315. DOI: 10.1103/PhysRevC.67.044315.
- [Sla29] J. C. Slater. "The Theory of Complex Spectra". In: *Phys. Rev.* 34 (1929), p. 1293. DOI: 10.1103/PhysRev.34.1293.
- [SMY18] N. Shimizu, J. Menéndez, and K. Yako. "Double Gamow-Teller Transitions and its Relation to Neutrinoless $\beta\beta$ Decay". In: *Phys. Rev. Lett.* 120 (2018), p. 142502. DOI: 10.1103/PhysRevLett.120.142502.
- [SO96] A. Szabo and N. S. Ostlund. *Modern Quantum Chemistry: Introduction to Advanced Electronic Structure Theory*. Dover Publications Inc., 1996.
- [Spe91] J. Speth. *Electric And Magnetic Giant Resonances In Nuclei*. International Review Of Nuclear Physics. World Scientific Publishing Company, 1991.
- [Spi+16] M. Spieker et al. "The pygmy quadrupole resonance and neutron-skin modes in ^{124}Sn ". In: *Phys. Lett. B* 752 (2016), p. 102. DOI: 10.1016/j.physletb.2015.11.004.
- [SS99] H. Sagawa and T. Suzuki. "Pigmy and giant dipole states in oxygen isotopes". In: *Phys. Rev. C* 59 (1999), p. 3116. DOI: 10.1103/PhysRevC.59.3116.
- [SSH03] T. Suzuki, H. Sagawa, and K. Hagino. "Electromagnetic moments and electric dipole transitions in carbon isotopes". In: *Phys. Rev. C* 68 (2003), p. 014317. DOI: 10.1103/PhysRevC.68.014317.
- [SSM14] J. R. Stone, N. J. Stone, and S. A. Moszkowski. "Incompressibility in finite nuclei and nuclear matter". In: *Phys. Rev. C* 89 (2014), p. 044316. DOI: 10.1103/PhysRevC.89.044316.
- [Ste+05] I. Stetcu et al. "Effective operators within the ab initio no-core shell model". In: *Phys. Rev. C* 71 (2005), p. 044325. DOI: 10.1103/PhysRevC.71.044325.
- [Str+16] S. R. Stroberg et al. "Ground and excited states of doubly open-shell nuclei from ab initio valence-space Hamiltonians". In: *Phys. Rev. C* 93 (2016), p. 051301. DOI: 10.1103/PhysRevC.93.051301.
- [Str+17] S. R. Stroberg et al. "Nucleus-Dependent Valence-Space Approach to Nuclear Structure". In: *Phys. Rev. Lett.* 118 (2017), p. 032502. DOI: 10.1103/PhysRevLett.118.032502.
- [Stu13] C. Stumpf. "Importance-truncated large-scale shell model". Master Thesis. TU Darmstadt, 2013.
- [Suh07] J. Suhonen. *From Nucleons to Nucleus*. Theoretical and Mathematical Physics. Berlin, Heidelberg: Springer Berlin Heidelberg, 2007. ISBN: 978-3-540-48859-0. DOI: 10.1007/978-3-540-48861-3.
- [Sur+04] P. Surján et al. "Partitioning in multiconfiguration perturbation theory". In: *Ann. Phys. (Leipzig)* 13 (2004), p. 223. DOI: 10.1002/andp.200310074.

- [SWR17] C. Stumpf, T. Wolfgruber, and R. Roth. *Electromagnetic Strength Distributions from the Ab Initio No-Core Shell Model*. 2017. arXiv: 1709.06840.
- [Tal52] I. Talmi. "Nuclear spectroscopy with harmonic oscillator wave-functions". In: *Helv. Phys. Acta* 25 (1952), p. 185.
- [TBS11] K. Tsukiyama, S. K. Bogner, and A. Schwenk. "In-Medium Similarity Renormalization Group For Nuclei". In: *Phys. Rev. Lett.* 106 (2011), p. 222502. DOI: 10.1103/PhysRevLett.106.222502.
- [TBS12] K. Tsukiyama, S. K. Bogner, and A. Schwenk. "In-medium similarity renormalization group for open-shell nuclei". In: *Phys. Rev. C* 85 (2012), p. 061304. DOI: 10.1103/PhysRevC.85.061304.
- [Tic+18] A. Tichai et al. *Natural orbitals for ab initio no-core shell-model calculations*. in preparation. 2018.
- [TL11] N. Tsoneva and H. Lenske. "Pygmy Quadrupole Resonance in skin nuclei". In: *Phys. Lett. B* 695 (2011), p. 174. DOI: 10.1016/j.physletb.2010.11.002.
- [Ton+10] A. P. Tonchev et al. "Spectral Structure of the Pygmy Dipole Resonance". In: *Phys. Rev. Lett.* 104 (2010), p. 072501. DOI: 10.1103/PhysRevLett.104.072501.
- [Tri16] R. Trippel. "Collective Excitations with Chiral NN+3N Interactions from Coupled-Cluster and In-Medium SRG". PhD thesis. Technische Universität Darmstadt, 2016.
- [Tse07] V. I. Tselyaev. "Quasiparticle time blocking approximation within the framework of generalized Green function formalism". In: *Phys. Rev. C* 75 (2007), p. 024306. DOI: 10.1103/PhysRevC.75.024306.
- [Tse13] V. I. Tselyaev. "Subtraction method and stability condition in extended random-phase approximation theories". In: *Phys. Rev. C* 88 (2013), p. 054301. DOI: 10.1103/PhysRevC.88.054301.
- [Usm+11] I. Usman et al. "Fine structure of the isoscalar giant quadrupole resonance in ^{40}Ca due to Landau damping?" In: *Phys. Lett. B* 698 (2011), p. 191. DOI: 10.1016/j.physletb.2011.03.015.
- [VMK88] D. A. Varshalovich, A. N. Moskalev, and V. K. Khersonskii. *Quantum Theory of Angular Momentum*. World Scientific Publishing Co. Pte. Ltd., 1988. ISBN: 978-9971-5-0107-5.
- [VR16] K. Vobig and R. Roth. private communication. 2016.
- [Weg94] F. Wegner. "Flow-equations for Hamiltonians". In: *Ann. Phys. (Leipzig)* 506 (1994), p. 77. DOI: 10.1002/andp.19945060203.
- [Wei79] S. Weinberg. "Phenomenological Lagrangians". In: *Physica A* 96 (1979), p. 327. DOI: 10.1016/0378-4371(79)90223-1.
- [Whi+77] R. R. Whitehead et al. "Computational Methods for Shell Model Calculations". In: *Adv. Nucl. Phys.* 9 (1977), p. 123.

-
- [Whi02] S. R. White. "Numerical canonical transformation approach to quantum many-body problems". In: *J. Chem. Phys.* 117 (2002), p. 7472. DOI: 10.1063/1.1508370.
- [Whi80] R. R. Whitehead. *Theory and Applications of Moment Methods in Many-Fermion Systems*. Ed. by B. J. Dalton et al. Boston, MA: Springer US, 1980. ISBN: 978-1-4613-3122-3. DOI: 10.1007/978-1-4613-3120-9.
- [WSS95] R. B. Wiringa, V. G. J. Stoks, and R. Schiavilla. "Accurate nucleon-nucleon potential with charge-independence breaking". In: *Phys. Rev. C* 51 (1995), p. 38. DOI: 10.1103/PhysRevC.51.38.
- [Yan87] C. Yannouleas. "Zero-temperature second random phase approximation and its formal properties". In: *Phys. Rev. C* 35 (1987), p. 1159. DOI: 10.1103/PhysRevC.35.1159.
- [Zha+04] H. Zhan et al. "Extrapolation method for the no-core shell model". In: *Phys. Rev. C* 69 (2004), p. 034302. DOI: 10.1103/PhysRevC.69.034302.

Danksagung

Schreiben musste ich meine Dissertation zwar alleine—doch zu ihrem Gelingen haben auch andere Menschen wesentlich beigetragen. An dieser Stelle möchte ich dafür herzlich Danke sagen.

Meinem Doktorvater Prof. Robert Roth danke ich für die Möglichkeit diese Dissertation anzufertigen und für die vielen Ratschläge und physikalische Intuition, mit denen er jederzeit zur Verfügung stand. Insbesondere die Unterstützung und die aufbauenden Worte in schwierigeren Phasen habe ich nie als selbstverständlich angesehen. Von ihm habe ich viel für die Zukunft gelernt.

Prof. Gabriel Martínez-Pinedo danke ich für das Übernehmen des Zweitgutachtens und die wertvollen Diskussionen während meiner Promotion.

Meiner Arbeitsgruppe danke ich für die Wohlfühlatmosphäre. Insbesondere danke ich Alex Tichai, Eskendr Gebrerufael, Klaus Vobig, Laura Mertes, Roland Wirth, Stefan Alexa, Stefan Schulz und Thomas Hüther für konstruktive Kritik für meine Arbeit und die Zeit, die wir auch außerhalb der Uni miteinander verbracht haben, zum Beispiel bei einem Spieleabend oder während ein paar Tage Urlaub vor oder nach Konferenzen.

Besonderer Dank geht an Roland Wirth, ohne dessen Hilfe bei Verständnis- und technischen Problemen ich wahrscheinlich noch ein paar Jahre länger an dieser Arbeit sitzen würde. Danke auch an alle, die mindestens ein Kapitel meiner Dissertation korrekturgelesen haben.

Weiterhin danke ich meiner ganzen Familie, insbesondere meinen Eltern, Klaus und Angelika Stumpf, und meiner Schwester, Steffi Stumpf, dafür, dass sie immer für mich da sind.

Schließlich möchte ich Benjamin Bastida Virgili danken, der mir immer zur Seite steht, mich zum Lachen bringt und der mir auf vielen Reisen immer wieder zeigt, dass es auch außerhalb der Physik viel zu entdecken gibt.

Werdegang

Zur Person

Name	Christina Stumpf
Geburtsdatum	24. Juli 1987
Geburtsort	Aschaffenburg
Nationalität	Deutsch

Bildungsweg

1994-1998	Grundschule , Grundschule Glattbach
1998- 2007	Gymnasium , Karl-Theodor-v.-Dalberg-Gymnasium, Aschaffenburg
2007-2010	Bachelorstudium Physik , TU Darmstadt
2010-2013	Masterstudium Physik , TU Darmstadt
2013-2018	Promotionsstudium , TU Darmstadt

Publikationen

- J. Langhammer, R. Roth, C. Stumpf: Spectra of Open-Shell Nuclei with Padé-resummed Degenerate Perturbation Theory. Phys. Rev. C 86, 054315 (2012)
- J. Beller, C. Stumpf, M. Scheck, et al.: Separation of the $1+/1-$ Parity Doublet in ^{20}Ne . Phys. Lett. B 741, 128 (2015)
- C. Stumpf, J. Braun, R. Roth: Importance-Truncated Large-Scale Shell Model. Phys. Rev. C 93, 021301(R) (2016)
- T. D. Morris, J. Simonis, R. S. Stroberg, et al.: Structure of the Lightest Tin Isotopes. Accepted for publication in Phys. Rev. Lett., arXiv:1709.02786 (2017)
- C. Stumpf, T. Wolfgruber, R. Roth: Electromagnetic Strength Distributions from the ab initio No-Core Shell Model. Submitted to Phys. Lett. B, arXiv:1709.06840 (2017)

Erklärung gemäß §9 Promotionsordnung

Hiermit versichere ich, dass ich die vorliegende Dissertation selbstständig angefertigt und keine anderen als die angegebenen Quellen und Hilfsmittel verwendet habe. Alle wörtlichen und paraphrasierten Zitate wurden angemessen kenntlich gemacht. Die Arbeit hat bisher noch nicht zu Prüfungszwecken gedient.

Datum

Ort

(Christina Stumpf)

